Version 1.4

The MultiPurpose Detector – MPD

to study Heavy Ion Collisions at NICA
(Conceptual Design Report)

Project leaders: A.N. Sissakian, A.S. Sorin, V.D. Kekelidze

Editorial board:
V.Golovatyuk, V.Kekelidze, V.Kolesnikov, D.Madigozhin, Yu.Murin, V.Nikitin, O.Rogachevsky

Internal referee board:
N.Gorbunov, V.Kolesnikov, I.Meshkov, A.Olshevski, Yu.Potrebenikov, N.Topilin, I.Tyapkin, Yu.Zanevsky, A.Kurepin

The MPD Collaboration:[1]

Kh.U.Abraamyan, S.V.Afanasiev, V.S.Alfeev, N.Anfimov, D.Arkhipkin, P.Zh.Aslanyan, V.A.Babkin, S.N.Bazylev, D.Blaschke, D.N.Bogoslovsky, I.V.Boguslavski, A.V.Butenko, V.V.Chalyshev, S.P.Chernenko, V.F.Chepurnov, Vl.F.Chepurnov, G.A.Cheremukhina, I.E.Chirikov-Zorin, D.E.Donetz, K.Davkov, V.Davkov, D.K.Dryablov, D.Drnojan, V.B.Dunin, L.G.Efimov, A.A.Efremov, E.Egorov, D.D.Emelyanov, O.V.Fateev, Yu.I.Fedotov, A.V.Friesen, O.P.Gavrischuk, K.V.Gertsenberger, V.M.Golovatyuk, I.N.Goncharov, N.V.Gorbunov, Yu.A.Gornushkin, N.Grigalashvili, A.V.Guskov, A.Yu.Isupov, V.N.Jejer, M.G.Kadykov, M.Kapishin, A.O.Kechechyan, V.D.Kekelidze, G.D.Kekelidze, H.G.Khodzhibagiyan, Yu.T.Kiryushin, V.I.Kolesnikov, A.D.Kovalenko, N.Krahotin, Z.V.Krumshtein, N.A.Kuz'min, R.Lednicky, A.G.Litvinenko, E.I.Litvinenko, Yu.Yu.Lobanov, S.P.Lobastov, V.M.Lysan, L.Lytkin, J.Lukstins, V.M.Lucenko, D.T.Madigozhin, A.I.Malakhov, I.N.Meshkov, V.V.Mialkovski, I.I.Migulina, N.A.Molokanova, S.A.Movchan, Yu.A.Murin, G.J.Musulmanbekov, D.Nikitin, V.A.Nikitin, A.G.Olshevski, V.F.Peresedov, D.V.Peshekhonov, V.D.Peshekhonov, I.A.Polenkevich, Yu.K.Potrebenikov, V.S.Pronskikh, A.M.Raportirenko, S.V.Razin, O.V.Rogachevsky, A.B.Sadovsky, Z.Sadygov, R.A.Salmin, A.A.Savenkov,W. Scheinast, S.V.Sergeev, B.G.Shchinov, A.V.Shabunov, A.O.Sidorin, I.V.Slepnev, V.M.Slepnev, I.P.Slepov, A.S.Sorin, O.V.Teryaev, V.V.Tichomirov, V.D.Toneev, N.D.Topilin, G.V.Trubnikov, I.A.Tyapkin, N.M.Vladimirova, A.S.Vodop'yanov, S.V.Volgin, A.S.Yukaev, V.I.Yurevich, Yu.V.Zanevsky, A.I.Zinchenko, V.N.Zrjuev, Yu.R.Zulkarneeva
Joint Institute for Nuclear Research, Dubna, RF

V.A.Matveev, M.B.Golubeva, F.F.Guber, A.P.Ivashkin, L.V.Kravchuck, A.B.Kurepin, T.L.Karavicheva, A.I.Maevskaya, A.I.Reshetin, E.A.Usenko
Institute for Nuclear Research, RAS, Troitsk, RF

[1]The list of participating Institutes is currently a subject of update.

E.E.Boos, V.L.Korotkikh, I.P.Lokhtin, L.V.Malinina, M.M.Merkin, S.V.Petrushanko, L.I.Sarycheva, A.M.Snigirev, A.G.Voronin
Skobeltsyn Institute of Nuclear Physics Moscow State University, Moscow, RF

O.A.Denisovskaia, K.R.Mikhailov, P.A.Polozov, M.S.Prokudin, G.B.Sharkov, A.V.Stavinskiy, V.L.Stolin, S.S.Tolstoukhov
Institute for Theoretical Experimental Physics, Moscow, RF

S.Igolkin, G.Feofilov, V.Zherebchevskiy, V.Lazarev
St.Petersburg State University, St.Petersburg, RF

O.I.Batenkov
Radium institute, St.Petersburg, RF

G.M.Zinovjev, K.A.Bugaev
Bogolyubov Institute for Theoretical Physics, NAS, Kiev, Ukraine

K.K.Gudima, M.I.Baznat
Institute of Applied Physics, AS, Chisinau, Moldova

D.Tonev, I.Geshkov
Institute for Nuclear Reseach & Nuclear Energy BAS, Sofia, Bulgaria

V.D.Tcholakov, P.S.Geraksiev, L.S.Yordanova, M.S.Kolchevska, D.A.Suvarieva, B.R.Marinova
Plovdiv University "Paisii Hilendarski", Plovdiv, Bulgaria

D.A.Bliznyuk, B.V.Grinyov, P.N.Zhmurin
Institute for Scintillation Materials, Kharkiv, Ukraine

V.N.Borshchov, O.M.Listratenko, M.A.Protsenko, I.T.Tymchuk
State Enterprise Scientific & Technology Research Institute for Apparatus construction, Kharkiv, Ukraine

N.M.Shumeiko, F.Zazulia
Particle Physics Center of Belarusian State University, Minsk, Belorussia

Yi Wang, Yuanjing Li, Yinong Liu, Zhi Deng, Guanghua Gong, Xianglei Zhu, Weicheng Ding
Department of Engineering Physics, Tsinghua University, Beijing, China

Cheng Li, Hongfang Chen, Ming Shao, Xiaoliang Wang, Yongjie Sun, Zebo Tang
Center of Particle Physics and Technology (CPPT) of the University of Science and Technology of China (USTC) Hefei, China

M. Apostol, I. Cruceru, M. Cruceru, G. Nicolesku, L. Ciolacu
Horia Hulubei National Institute of Physics and Nuclear Engineering (IFIN-HH), Bucharest, Romania

O.Abdinov, M.Suleimanov
Physics Institute Az.AS, Baku, Azerbaijan

T. Czopowicz, K. Dynowski, W. Peryt, J. Pluta, D. Wielanek, M. Piwek
Warsaw University of Technology, Faculty of Physics, Warsaw, Poland

Togoo Ravdandorj, Baatar Tseepeldorj, Khurelbaatar Begzsuren, Batgerel Baatar, Sovd Maamuu
Institute of Physics and Technology Mongolian Academy of Sciences, Ulan Bator, Mongolia

T.K.Koshurnikov
"Neva-Magnet" S&E, ltd, St.Petersburg, RF

Abstract

A conceptual design of the MultiPurpose Detector (MPD) is proposed for a study of hot and dense baryonic matter in collisions of heavy ions over the atomic mass range A = 1–197 at a centre-of-mass energy up to $\sqrt{s_{NN}} = 11\ GeV$ (for Au^{79+}). The MPD experiment is foreseen to be carried out at a future JINR accelerator complex facility for heavy ions – the Nuclotron-based Ion Collider fAcility (NICA) which is designed to reach the required parameters with an average luminosity of $L = 10^{27}\mathrm{cm}^{-2}\mathrm{s}^{-1}$.

Contents

Introduction

Investigation of hot and dense baryonic matter is a challenging task in modern physics. It provides information on the in-medium properties of hadrons and nuclear matter equation of state, allows a search for possible manifestations of the deconfinement and/or chiral symmetry restoration, phase transition, mixed phase and critical end point, and sheds light on the evolution of the Early Universe and formation of neutron stars.

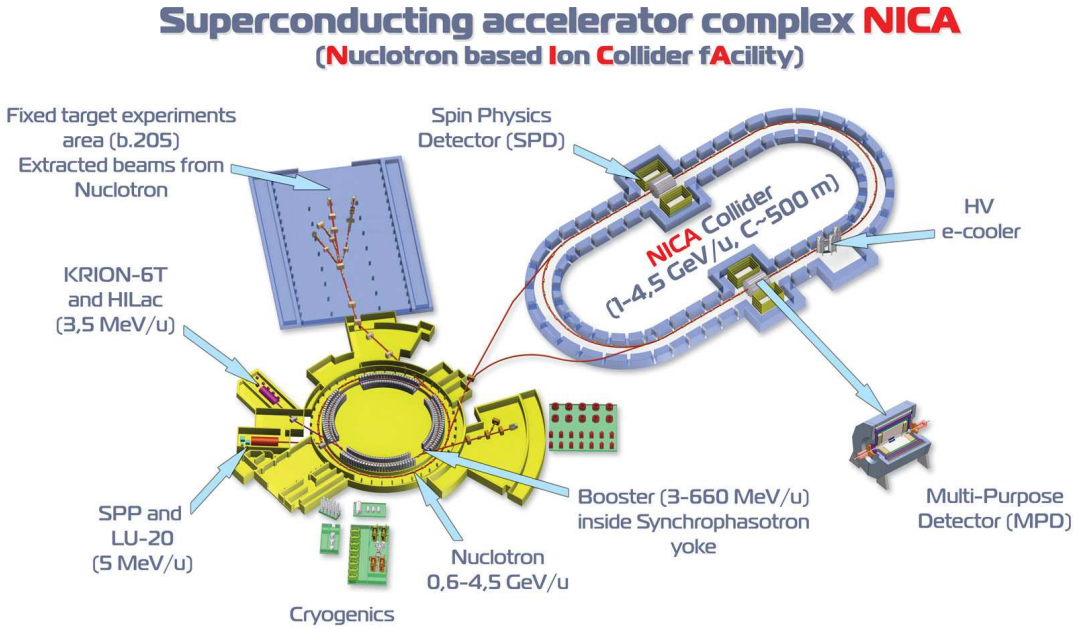

Fig. 1: The NICA accelerator complex at JINR.

A vast research program in this branch of basic science has been carried out over last 20 years. The main centers equipped with high energy ion accelerators are: GSI (Germany), $E_{lab} = 1 - 2$ AGev, equivalent nucleon - nucleon c.m.s. energy $\sqrt{s_{NN}} = 2 - 2.5$ GeV; CERN - SPS (Geneva), $E_{lab} = 20 - 158$ AGeV, $\sqrt{s_{NN}} = 6 - 17$ GeV; BNL - RHIC, (USA), $\sqrt{s_{NN}} = 20 - 200$ GeV; JINR - SPh - Nuclotron, (Russia), $E_{lab} = 1 - 6$ AGev, $\sqrt{s_{NN}} = 2 - 3.5$ GeV. The most intensive exploration has been performed recently in the high energy domain $\sqrt{s_{NN}} = 20 - 200$ GeV. A number of new phenomena were discovered in relativistic nuclei collisions: strong stopping power of colliding nuclei, collective flow of secondary particles, unexpectedly large broadening of transverse momentum distributions, irregularities in the beam-energy behaviour of the K/π ratio, drastic enhancement of multistrange hyperon production, essential broadening of the spectral function maximum for ρ-mesons in the experiments with leptons instead of the expected shift toward the lower lepton-pair invariant mass, strong in-medium modification of produced fast hadrons, jet quenching during propagation through the excited nuclear medium.Thus, recent observations bear witness to creation of a new kind of QCD matter, the strongly

interacting quark-gluon plasma (SQGP). But the theoretical comprehension of these data is far from being complete, which pushes different laboratories to undertake new efforts in the domain of heavy-ion physics. It was realized recently that picture is not complete for lack of data from the pilot experiments in the lower energy domain $\sqrt{s_{NN}} = 2 - 10$ GeV. According to recent theoretical considerations, it is in this energy range that a formed excited system enters into a new phase, and transition between different phases of nuclear matter may be observed. As a response to this quest, GSI declared construction of a big accelerator complex FAIR with the extracted ion beam with $E_{lab} = 5 - 35$ AGeV, $\sqrt{s_{NN}} = 3 - 10$ GeV. A big international project "Compressed Baryon Matter" at FAIR has been launched. The BNL-RHIC is also planning to reduce the collider energy from $\sqrt{s_{NN}} = 200$ GeV to 5 GeV.

An essential part of the JINR scientific program resulted from many discussions in view of the Dubna Nuclotron upgrade is dedicated to the study of hot and dense baryonic matter [1, 2, 3, 4]. Realization of this ambitious goal is related to the construction of a new JINR accelerator complex – the Nuclotron-based Ion Collider fAcility (NICA) [5] to provide collisions of heavy ions over a wide range of atomic masses, from Au+Au collisions at a centre-of-mass energy of $\sqrt{s_{NN}} = 11\ GeV$ (for Au^{79+}) and an average luminosity of $L = 10^{27}\mathrm{cm}^{-2}\mathrm{s}^{-1}$, to proton-proton collisions with $\sqrt{s_{pp}} = 20\ GeV$ and $L \approx 10^{30} cm^{-2} s^{-1}$. The NICA collider complex is shown on Fig. 1. Two interaction points are foreseen at the NICA collider, which provide a possibility for two detectors to operate simultaneously. One of these detectors, the MultiPurpose Detector (MPD), is optimized for the study of properties of hot and dense matter in heavy-ion collisions and, in particular, for the search a manifestation of possible deconfinement and/or chiral symmetry restoration phase transitions, critical end-point and mixed quark-hadron phase.

The NICA complex is aimed at the basic science research, yet beams of particles intended for physics experiments may find another applications. In particular, JINR has already accumulated essential experience in conducting biomedical research and in performing cancer therapy. The complex includes a complete chain of accelerators - a linac, a buster and Nuclotron. They will produce extracted proton and ion beams within the energy range of $E_{lab} = 0.5 - 3$ AGeV well suited for applications. This future facility will greatly enhance considerable JINR capability in many important areas of applied sciences, radiation technology and medicine.

Chapter 1

MPD Physics Goals

1.1 Introduction

This document presents the NICA/MPD concept for the international heavy-ion research facility proposed by the Joint Institute for Nuclear Research to investigate the basic Quantum Chromo Dynamics (QCD) structure of matter. The facility takes into account the broadened scope of the physics of strong interaction and related problems in the fundamental many-body systems and provides particle beams from protons to gold nuclei. The range of colliding energy of nuclei is $\sqrt{s_{NN}} = 4 - 11$ GeV, and that for protons $\sqrt{s_{pp}} = 4 - 20$ GeV.

The global scientific goal of the NICA/MPD Project is to explore the phase diagram of strongly interacting matter in the region of highly compressed and hot baryonic matter. Such matter exists in neutron stars and in the core of supernova explosions, while in the early Universe we meet the opposite conditions of very high temperature and vanishing baryonic density. In terrestrial experiments, high-density nuclear matter can transiently be created in a finite reaction volume in relativistic heavy ion collisions. In these collisions, a large fraction of the beam energy is converted into newly created hadrons, and new color degrees of freedom [6, 7] may be excited. The properties of excited resonances may noticeably be modified by the surrounding hot and dense medium. At very high temperature or density, this hadron mixture melts and their constituents, quarks and gluons, form a new phase of matter, the quark-gluon plasma. Different phases of strongly interacting matter are shown in the phase diagram of Fig. 1.1.

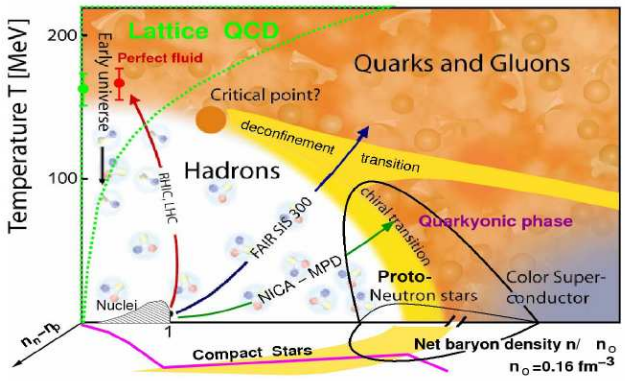

Fig. 1.1: The phase diagram of strongly interacting QCD matter. Phase boundaries, critical end-point, and conjectured dynamical trajectories for an expansion stage are plotted as well.

As it is seen from the phase diagram, the heavy-ion experiments at BNL-RHIC as well as the coming CERN-LHC experiments probe the region of high temperature and low net baryon density where circumstantial evidence has been obtained for a new phase, strongly interacting quak-gluon matter existing above a critical temperature $T_c \approx 160 - 170$ MeV.

In the other corner of the phase diagram, at lower temperature and moderate baryonic density, the GSI-SIS experiments definitely show no hint at a phase transition but certainly point to in-medium modification effects. At still higher density and low temperature the matter is deconfined and, as predicted, correlated quark-antiquark pairs form a color superconductive phase. Such phase may be created in the interior of neutron stars. We are interested in an intermediate region of the phase diagram, where essential evidence was obtained by the NA49 collaboration within the CERN-SPS energy scan program that the system enters a new phase at a beam energy of about 30 AGeV. The fascinating particularity of this energy range is the critical end point located according to the recent lattice QCD calculations at $T_E = (162 \pm 2)$ MeV and baryon chemical potential $\mu_E = (360 \pm 40)$ MeV [8], whereas model predictions are strongly scattered throughout the regions of $T_E \sim 50-170$ Mev and $\mu_E \sim 200-1400$ MeV [9] The importance of this finding was well understood at GSI where the CBM (Compressed Baryon Matter) experiment was proposed within the FAIR project. This understanding was recently shared by the BNL-RHIC which suggested to decrease its beam collider energy to reach this domain of the phase diagram. The low-energy RHIC at BNL[10], CBM at FAIR (GSI) [11] and the proposed NICA/MPD at JINR [5, 12], as well as the CERN-SPS [13] working with lighter systems, may be considered as complementary basic facilities aimed at the study of relevant physics problems of hot and dense baryonic matter.

The phase diagram translates the properties of strong interactions and their underlying QCD theory into a visible pattern. In particular, the fundamental QCD phenomena, such as confinement and broken chiral symmetry, quantitative understanding of which is still lacking, are a challenge for future heavy-ion research. As it is demonstrated in Fig. 1.2, the domain of excited dense baryonic matter accessible in the planned NICA/MPD Project is located roughly between the dynamical trajectories presented at limiting colliding energies covering the range of quasi-equilibrium states with the baryon density up to $n_B \approx 10 n_0$. The hadronic phase at high net baryon density and moderate temperature, as well as new states of matter beyond the deconfinement, chiral transition, and in a mixed phase may be reached in this sector of the phase diagram. With the lattice data of [8] the critical point location in baryon density may be recalculated from Fig. 1.1 into this representation as $n_E \approx 1.5 - 2.0 n_0$. **Therefore, the major goal of the NICA/MPD Project is the study of in-medium properties of hadrons and the nuclear matter equation of state, including a search for possible signals of deconfinement and/or chiral symmetry restoration phase transitions and the QCD critical endpoint** in the region of the collider energy $\sqrt{s}_{NN} = 4 - 11$ GeV. Due to the high complexity of this task and large uncertainty in the predicted signals, an accurate scanning of the considered phase diagram domain in collision energy, impact parameter, and system size is utterly needed.

To reach this goal, the envisaged experimental programme includes the simultaneous measurement of the observables which are presumably sensitive to high density effects and phase transitions. The obsevables measured on event-by-event basis are particle yields and ratios, correlations and fluctuations. Different species probe different stages of the nucleus-nucleus interaction due to their differences in mass, energy and interaction cross sections. The hadrons containing heavy strange quarks are of particular interest. These strange heavy hadrons are created in the early high-temperature and high-density stage but may quickly decouple due to their low interaction cross section with surrounding matter. Among various characteristics, the elliptic flow deserves special attention because this

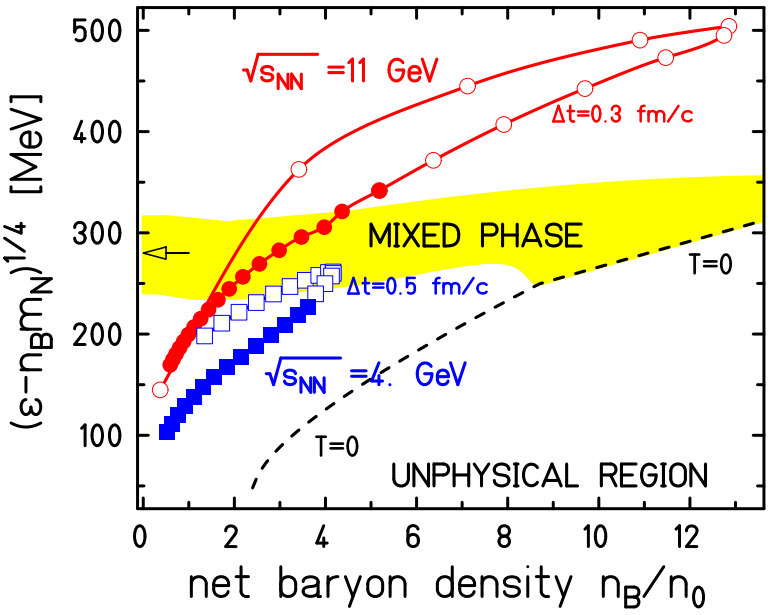

Fig. 1.2: The phase diagram in terms of extensive variables, the reduced energy density versus the net baryon density. The dynamical trajectories are shown for central ($b = 2$ fm) Au + Au collisions at two limiting NICA energies. The highly non-equilibrium part of trajectories, starting from the still not interacting two counter streaming flows, are calculated within the kinetic Quark Gluon String Model (open symbols). The subsequent locally equilibrium evolution is considered within the 3D relativistic hydrodynamics (filled ones). The results obtained correspond to the Lorentz-contracted cylinder of the radius $R = 5$ fm and the length $L = 2R/\gamma$ where γ is the center-of-mass gamma-factor. Time differences between points are 0.3 and 0.5 fm/c for $\sqrt{s}_{NN} = 8.8$ and 4 GeV, respectively. The highlighted region is a quark-hadron mixed phase estimated according to the phenomenological two-phase equation of state [14]. The dashed curve separates the unphysical region by condition $T = 0$.

collective motion is formed mainly in the early stage of the collision. The spatio-temporal information on the particle freeze-out source, which depends on the preceding evolution of the system, is provided by the measurement of identical particle's interference. Certainly, the direct information on hot and dense transient matter is provided by penetrating probes, photons and leptons. In this respect, the vector mesons which contain information on chiral symmetry restoration are very attractive. Measurement of the positive/negative pion asymmetry with respect to the reaction plane as a function of centrality of heavy-ion collisions opens a possibility to probe such fundamental problem as spontaneous violation of CP parity in strong interactions.

In the first stage of the Project we consider

- Multiplicity and spectral characteristics of the identified hadrons including strange particles, multi-strange baryons and antibaryons characterizing entropy production and system temperature at freeze-out.
- Event-by-event fluctuations in multiplicity, charges, transverse momenta and K/π ratios as a generic property of critical phenomena
- Collective flow effects (directed, elliptic and higher ones) for hadrons including strange particles.

- Femtoscopy with identified particles and particle correlations

In the second stage, the electromagnetic probes (photons and dileptons) will be measured.

The suggested Project allows one to collide mass asymmetric beams including pA collisions. In addition to proper physics meaning, it is quite important as a reference point for comparison with heavy ion data. In future, as a next stage of the Project, the NICA keeps a possibility for electron-ion collisions. It could add to the NICA program a unique feature to perform measurements of nucleon and nuclei electro-magnetic form factors to large momenta, such as the investigation of the spatial distribution of charge and magnetization in nuclei and the nucleon, including the determination of the valence quark generalized parton distribution, which reveal the correlation of spatial and momentum distributions. The study of color transparency provides a new insight into the behavior of QCD matter at zero temperature.

The MPD detector will be operated at an interaction rate of about $7 \cdot 10^3$ interactions per second with multiplicities of up to $\sim$1500 charged particles per central $Au + Au$ collision at the maximal energy. This interaction rate provides more than two orders of magnitude advantage over the low-energy RHIC . The intensity of the planned fixed target CBM experiment is higher by almost three orders of magnitude, however it will have non-homogeneous acceptance depending on the beam energy, while the MPD acceptance is homogeneous in the whole energy range. The short-lived vector mesons decay into lepton pairs with a branching ratio of $10^{-4} - 10^{-5}$. At $\sqrt{s}_{NN} = 11$ GeV, with a mean multiplicity of ρ_0-mesons of $N_\rho \sim 10$ we get about one dilepton pair per second from this channel. The major issue is suppressing the physical background of electron-positron pairs from Dalitz decays and gamma conversion.

An estimate of the multi-strange hyperons is strongly model-dependent. For example, the multiplicity of Ω^- baryons at the maximal colliding energy is approximately 0.6 and 0.1 in central and minimal-bias events, respectively. It results in the production rate of $200/s$ and $700/s$ for 5% centrality and the minimal-bias collision, respectively. Proceeding to the lowest colliding energy $\sqrt{s} = 4$ GeV results in changing of both values by two orders of magnitude. So, a decrease of luminosity at this energy more than by order of the magnitude may be quite crucial.

Note that using these numbers gives only a first feeling. In estimating beam time needed, MPD geometrical acceptance, trigger, efficiency, particularities of the channel considered should be taken into account. All these issues will be considered below.

It is proposed that along with heavy ions the NICA will provide proton and light ion beams with a unique possibility of using polarized beams. This will allow JINR to continue its traditional investigations on a new level. In particular, the door is opened for studying nuclear quark-gluon structure in the processes with large momentum transfer as well as in the measurements with target/projectile polarization, for experimental verification of quark counting rules [15], clarification of the abnormal behavior known as the color nuclear transparency [16], and for comprehension of large spin effects in production of mesons and hyperons.

By this time, the accelerators available at JINR have provided good possibilities for a wide spectrum of radiobiological research in the field of cellular and molecular biophysics. A new heavy ion facility will allow one to conduct a deeper research in this field.

1.2 Observables and requirements

Since the global physics goal of the NICA/MPD Project is to explore the phase diagram of strongly interacting matter in the region of highly compressed and hot baryonic matter, the MPD experimental program includes simultaneous measurements of observables that are presumably sensitive to high nuclear density effects and phase transitions. In central collisions of heavy nuclei at NICA energies the nuclear matter goes through the substantial compression and moderate heating followed by a maximum energy density stage which then turns into expansion and cooling. As estimated by different models, net baryon

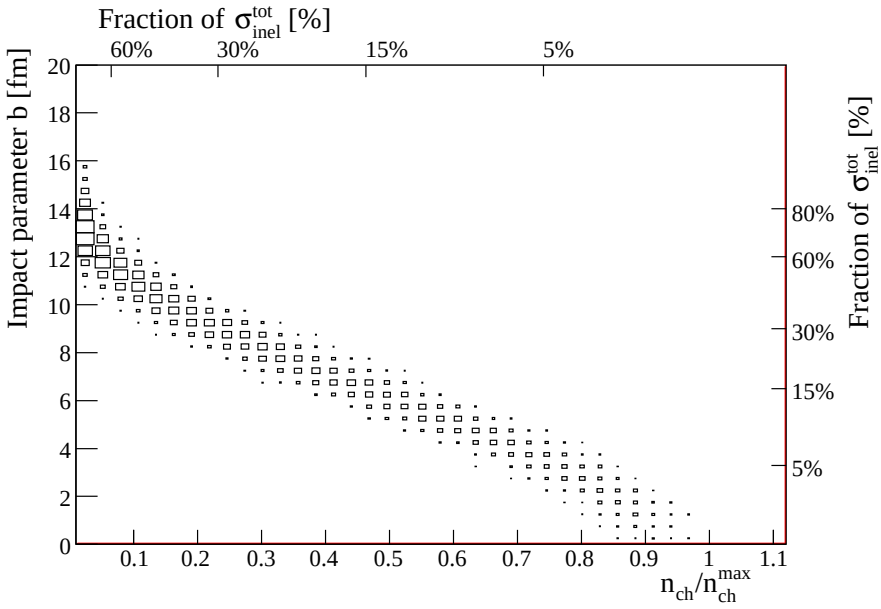

Fig. 1.3: The interrelation between multiplicity, impact parameter, and centrality in the events simulated by the UrQMD code.

densities achieved in heavy-ion collisions at NICA energies are more than 10 times that of the standard nuclear matter density. This energy range covers a broad region in the phase diagram, including the locations of the predicted **critical endpoint** (CP) in the QCD $\mu_B(T)$ phase diagram (second order point, where the line of the first order transition ends). The existing numerical techniques in lattice QCD calculations meet difficulties for $\mu_B > 0$ thus leading to theoretical uncertainties in the prediction of the location of the critical point. If the QCD CP exists, substantial critical phenomena such as large non-statistical fluctuations and correlations in the particle yield and kinematical spectra are expected. An experimental program is planned to search for the CP location by decreasing collision energies ($\sqrt{s}_{NN}$=5–50 GeV, corresponding to μ_B= 0.6–0.15 GeV) , modernization of the existing experimental set-up at SPS (NA49, NA61) ($E_{\rm lab}$=20–158 AGeV, corresponding to $\sqrt{s}_{NN}$=6.3–17.3 GeV), construction of the new facilities FAIR (CBM) ($E_{\rm lab}$=5–35 AGeV) and NICA (MPD) ($\sqrt{s}_{NN}$=4–11 GeV). The main physics goal of NICA is to locate the critical point via experimental detection of its signatures. Various theories agree on the following main signatures of the critical point:

1. non-monotonic behavior of some observables;

2. the increase of fluctuations near the CP, i.e. their rise and then fall as energy increases and $\mu_B(T)$ passes the CP;

3. non-equilibrating final state expected after cooling throughout a 1^{st} order phase transition, leading to the non-Gaussian fluctuations.

Several unexpected results at lower energies were obtained in the NA49 experiment at SPS: non-monotonic K^+/π^+ behavior, "horn" at $\sqrt{s}_{NN} = 7$ GeV, and the "collapse"of proton direct flow. The energy scan which will be undertaken by RHIC, FAIR, NICA, SPS aim to study the evolution with beam energy of the unusual medium properties found at RHIC: do any of the partonic properties change or "turn off"? The following observables are planned for studying by all these collaborations during the energy scan:

1. yields and particle ratios,

2. particle spectra (p_t, rapidity...),

3. strangeness production (K/π...),

4. different types of fluctuations and correlations ($\langle p_t \rangle$, femtoscopy),

5. flow (v_1, v_2, v_4...) with identified particles.

The signature would be a change in the behavior of the observable from rise to fall off with the increase of μ_B. It is expected that a number fluctuations will better survive during the hot matter evolution at the late stage of hadron gas, so that, e.g., K/π fluctuations will have higher propability to survive than $\langle p_t \rangle$ fluctuations.

A study of the multiplicity fluctuations, femtoscopic correlations, and collective flows of identified hadrons allows one to extract information on **the nuclear equation of state** for baryonic matter at high density. Primarily, an analysis of the measured yields and kinematical characteristics of particles produced in both peripheral and central collisions will be performed. These particles include charged hadrons ($\pi^+, \pi^-, K^+, K^-, p, \overline{p}$) measured directly and various neutral and charged strange particles (${K_s}^0, \Lambda, \Xi^-, \Omega^-$) identified via charged particle decay modes. A study of the corresponding particle yields and spectra as a function of the impact parameter (size of the reaction volume) will provide additional information about the signature for the formation of the dense nuclear matter. The important observable for a sign of **chiral symmetry restoration** is the modification of the properties of vector mesons at high baryon density. Their in-medium properties can be studied by measuring the dileptonic decay channels.

In order to obtain a complete picture of heavy-ion collisions, the reference data from elementary collisions are required, so a comprehensive set of observables should be measured in proton-nucleus and nucleus-nucleus collisions over the full NICA energy range. To get quantitative estimates of the expected particle yields and spectral shapes, the samples of events for the central and minimum bias Au+Au collisions at energies $\sqrt{s_{NN}} = 4, 5, 7, 9, 11\ GeV$ were simulated with the UrQMD [17] and FASTMC [18] codes. Interrelation between the event multiplicity, impact parameter, and centrality calculated by UrQMD is shown in Fig. 1.3.

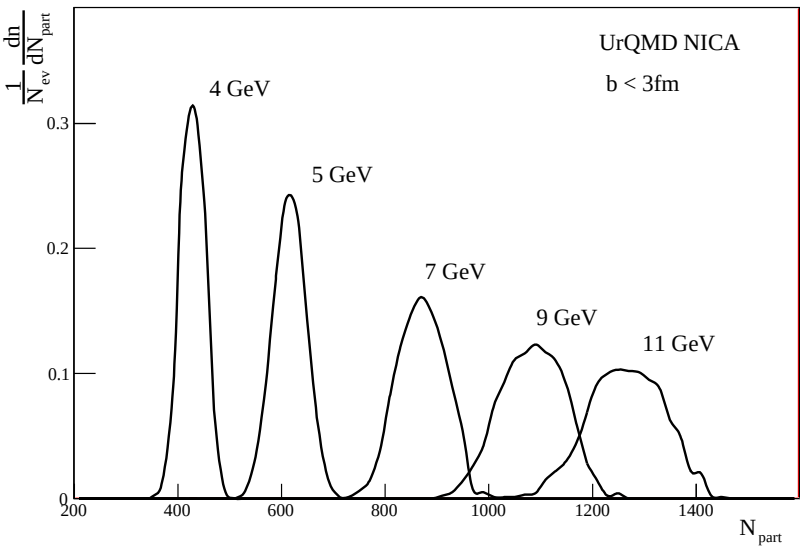

Fig. 1.4: Charged multiplicity distributions in central Au + Au collisions ($b < 3$ fm) calculated by UrQMD.

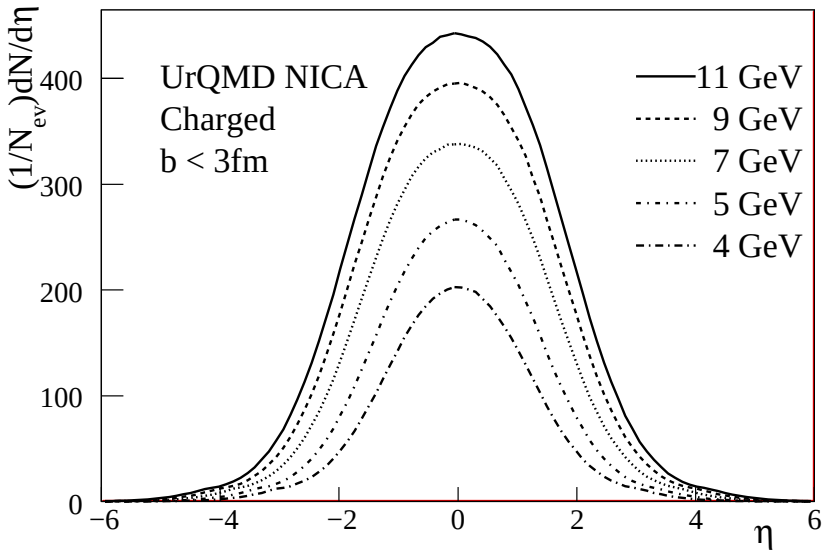

Fig. 1.5: Pseudorapidity distributions of charged particles in central Au + Au collisions ($b < 3$ fm) calculated by UrQMD.

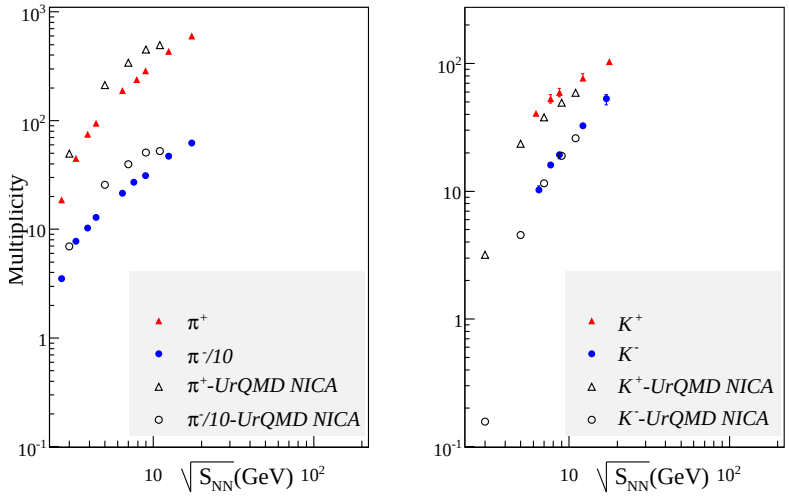

Fig. 1.6: Meson multiplicities in central ($b < 3$ fm) Au+Au (Pb+Pb) collisions at the energy range from AGS ($\sqrt{s} = 2.4 - 5.5GeV$) [19] to SPS ($\sqrt{s} = 6.3 - 17.8GeV$) [20] energies. The UrQMD calculation is plotted by open circles and triangles; the data - by corresponding filled symbols.

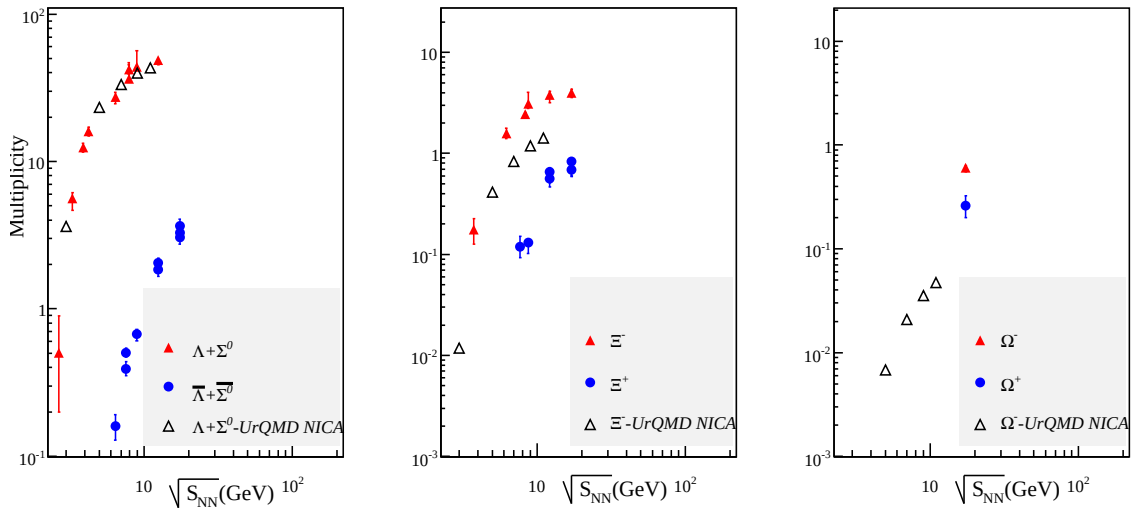

Fig. 1.7: Hyperon multiplicities in central ($b < 3$ fm) Au+Au (Pb+Pb) collisions at the energy range from AGS ($\sqrt{s} = 2.4 - 5.5GeV$) [19] to SPS ($\sqrt{s} = 6.3 - 17.8GeV$) [20] energies. The UrQMD calculations are depicted by open triangles; the data - by filled symbols.

Table 1.1: The mean particle multiplicity in central Au+Au events (impact parameter $b < 3$ fm) calculated by UrQMD.

Part.	4 GeV		7 GeV		11 GeV	
	4π	$\|\eta\| < 1$, $p > 100$ MeV/c	4π	$\|\eta\| < 1$, $p > 100$ MeV/c	4π	$\|\eta\| < 1$, $p > 100$ MeV/c
charged	430	250	870	430	1300	550
p	170	91	160	63	160	49
n	200	110	180	68	170	53
π^+	110	65	310	160	470	230
π^-	120	78	340	170	520	240
π^0	120	72	340	180	510	240
K^+	12	7.6	38	19	57	24
K^-	1.3	0.82	12	6.2	26	12
K^0	12	7.7	38	19	57	26
Λ	10	6.2	26	12	31	12
Σ^+	3.4	2.1	8.0	3.7	9.2	3.6
Σ^-	4.0	2.4	8.8	4.0	10	3.8
Σ^0	3.2	1.9	7.9	3.6	9.4	3.8
Ξ^-	0.16	0.11	0.87	0.42	1.7	0.66
Ξ^0	0.13	0.077	0.86	0.42	1.3	0.62
Ω^-	0.003	0.002	0.022	0.011	0.038	0.015

Particles yield

Mean multiplicity of different species in the UrQMD simulated central Au+Au events ($b < 3$ fm) for three collision energies are given in Table 1.1. The multiplicities in the kinematic region restricted by midrapidity ($|\eta| < 1$) and typical acceptance limitation of $p_T < 100$ MeV/c, are shown as well. Figures 1.4 and 1.5 represent the multiplicity and pseudorapidity distributions of charged particles in 4π geometry for central events at five collision energies: $\sqrt{s_{NN}} = 4, 5, 7, 9, 11$ GeV. Meson and hyperon multiplicity versus the collision energy in comparison with the AGS and SPS data are given in Fig. 1.6 and Fig. 1.7. Experimental data are represented by excitation function of particle multiplicities in Au+Au collisions at energy range E_{Lab} = 2 - 15 AGeV at AGS and in Pb+Pb collisions at E_{Lab} = 20 - 160 GeV at SPS. As seen in Fig. 1.6, the theoretical calculations depicted by open symbols overestimate the measured pion multiplicities and underestimate the kaon multiplicities (filled symbols). The yield of multistrange hyperons is underestimated by the UrQMD code as well (Fig. 1.7).

In the NICA energy range, one of the most promising observables that could serve as a sensitive diagnostic probe of two phases of matter created in the high energy heavy ion collisions is the strangeness-to-entropy ratio which can be estimated through the kaon-to-pion and/or Lambda-to-pion ratios. A pronounced peak of the K^+/π^+ ratio, the so-called "horn" effect, was found by the CERN-NA49 collaboration in central $Pb+Pb$ collisions at a beam energy of 30 AGeV. The $(\Lambda+\Sigma^0)/\pi$ ratio exhibits a similar maximum at the same beam energy. Transport models, HSD (Hadron String Dynamics) and UrQMD, fail to

describe these experimental data. Details and requirements of K/π ratio measurements at NICA/MPD are given below.

Strange baryons

In connection with the discovery of anomalous behavior of the K^+/π^+ ratio, it is of interest to analyze the behavior of the other strangeness carrying particles such as hyperons. Because of the associated production the hyperons is sensitive to the baryon density (characterized by the baryochemical potential μ_B) which decreases with increasing energy. Therefore, hyperon reconstruction is essential for understanding of the heavy ion collision dynamics. Only those hyperons which have charged decay vertices are measurable. Typical reconstruction efficiencies for hyperons defined mainly by the hyperon lifetimes and the vertex reconstruction cuts are 5-20%. Simulated track reconstruction and secondary vertex finding for Λ and ${K_s}^0$ are given in Section 5.2.

Particle Spectra

Despite the relatively good agreement of data and transport calculations in the longitudinal direction, significant deviations are found in the transverse direction. In addition to the enhanced relative yield of positive kaons, the measured transverse mass spectra of both positive and negative kaons around the center-of-mass rapidity at AGS and SPS energies show a substantial hardening in central Au + Au collisions relative to *pp* interactions. The m_t-distributions of kaons in nucleus-nucleus interactions can be treated as thermal; the inverse slope parameter (T) from an exponential in m_t fit is a measure of the effective temperature of the source:

$$\frac{1}{m_t}\frac{dN}{dm_t} = C\exp(-\frac{m_t - m}{T}) \tag{1.1}$$

Fig. 1.8 displays the inverse slopes of transverse spectra of kaons in Au + Au and Pb + Pb collisions measured at AGS and SPS compared with UrQMD calculations, which considerably deviate from the data. Transport calculations [21] showed that at high AGS and low SPS energies the hardening of the transverse mass spectra should be attributed neither to the presence of collective flow (initial pressure) nor to the initial state semi-hard scattering of fast quarks in a dense medium (Cronin effect).

The NICA/MPD detector combining the large phase space coverage and excellent PID capabilities offer the exciting possibility to study in great detail transverse mass (m_t) and rapidity (y) dependence of hadron production. Detailed measurements of the excitation function of the effective temperature of the kaon spectra in different colliding systems (from p+p to central A+A) may help to identify a possible phase transition. In addition, an analysis of the m_t-spectra of several particle species (π, K, p) within hydrodynamics-motivated blast-wave approaches will provide valuable information on collective expansion of the colliding system. Measurements of multiplicity and transverse energy distributions is important to characterize the thermodynamic properties of hot dense nuclear matter (μ_B, T, entropy and energy density, EoS). The midrapidity $m_t(p_t)$ spectra of baryons and antibaryons are particularly interesting for determining the baryo-chemical potential and the nuclear matter stopping power. The difference between the p_t-distributions for p and $\bar{p}$ or Λ and $\bar{\Lambda}$ will reflect the redistribution of valence quarks from the target and projectile nucleons in phase space.

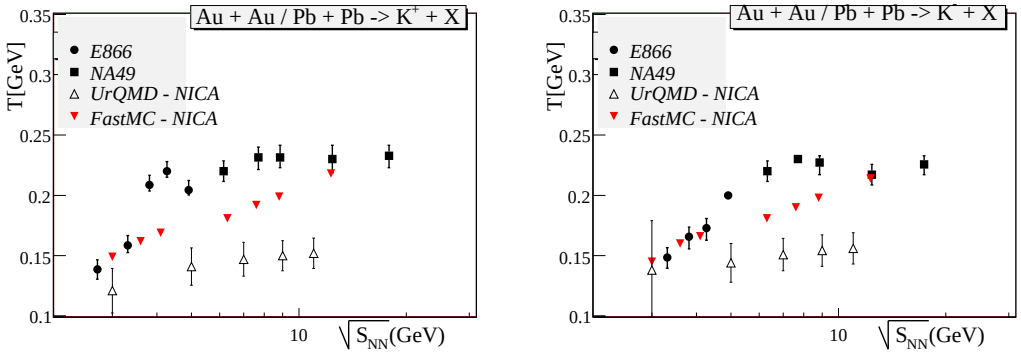

Fig. 1.8: Inverse slopes of transverse momentum distributions for K^+ and K^- in central Au + Au and Pb + Pb collisions. UrQMD points are given for Au + Au collisions.

Multiplicity and transverse momentum fluctuations

Multiplicity and transverse momentum fluctuations are expected to be modified when the system approaches the phase boundary between hadron gas and quark-gluon plasma (QGP). It has been also argued that significant transverse momentum and multiplicity fluctuations should appear for the systems hadronizing near the second-order critical QCD end-point [22]. For a quantitative measure of the particle number fluctuations it is convenient to use the scaled variances,

$$\omega^i = \frac{\langle {N_i}^2 \rangle - \langle N_i \rangle^2}{\langle N_i \rangle}, \tag{1.2}$$

where $< \cdots >$ denotes event-by-event averaging and the index i means '-', '+', and 'ch', i.e negative, positive, and all charged final state hadrons, respectively. In a superposition model ω is the same in A + A collisions as in nucleon-nucleon interactions at the same energy per nucleon, provided the number of particle-producing sources does not fluctuate from event to event. At NICA energies, multiplicity of charged particles at midrapidity reaches 400 – 500 (Fig. 1.5) which allows one to perform the event-by-event analysis. Scaled variances of the positive, negative and all charged particles for the UrQMD simulated events at the zero impact parameter of $Au + Au$ collisions are shown in Fig. 1.9 together with the experimental measurements. No significant increase of ω, as expected from the predictions with the critical point is observed in the data. The scaled variance for low transverse momentum particles shows neither significant non-monotonic structure nor excess over the UrQMD baseline.

Nevertheless, it is believed that event-by-event fluctuations of particle ratios related to the hadro-chemical composition of the particle source could provide a direct probe of the existence and nature of the phase transition. The proposed mechanisms that can lead to such event-by-event fluctuations are manifold. They range from the overheating-supercooling fluctuations due to a first order phase transition with large latent heat, over-fluctuations caused by a phase of coexisting confined and deconfined matter (mixed phase) in varying relative abundances, to true critical fluctuations in the vicinity of the critical point in the QCD phase diagram [23, 24, 25]. Analysis of the kaon-to-pion ratio measured in the NA49 experiment in central Pb+Pb collisions at energies near $\sqrt(s) = 7\ GeV$ indicates that dynamical (non-statistical) fluctuations in the event-by-event K/π ratio are

larger than those predicted by the transport model UrQMD [26]. These observations have generated a speculation that a phase transition from hadronic matter to quark-gluon matter may take place at incident energies around $\sqrt(s) = 7\ GeV$ [20]. The study of dynamic fluctuations in the event-by-event K/π ratio may provide information concerning QCD phase transitions such as the order of transition and its location, or lead to observation of the critical point of QCD [22, 27]. The detailed analysis of these dynamical fluctuations and requirements for NICA/MPD to observe them are given in the section below.

Another important non-statistical fluctuations are the event-by-event transverse momentum dynamical fluctuations defined as

$$\Phi_{p_t} = \sqrt{\frac{\langle Z^2_{p_t} \rangle}{\langle N \rangle}} - \sqrt{\overline{z^2_{p_t}}}, \tag{1.3}$$

where $Z^2_{p_t} = \sum^{N} (p_{t_i} - \overline{p_t})$, and $z_{p_t} = p_t - \overline{p_t}$. Here Φ_{p_t} quantifies a difference between the event-by-event fluctuations of transverse momentum in the data and the corresponding fluctuations in the 'mixed' events. There are two important properties of the Φ_{p_t} measure. If the system consists of independently emitted particles (no inter-particle correlations) Φ_{p_t} equals to zero. On the other hand, if A+A collision can be treated as an incoherent superposition of independent N+N interactions (superposition model), then Φ_{p_t} is a constant, the same for A+A and N+N interactions. As was shown by the NA49 collaboration, no significant energy dependence of the Φ_{p_t} measure is observed, both for data and for the UrQMD events (Fig. 1.10). The interpretation of these results requires sufficient theoretical understanding, whereas the major advance of the measurements of these observables with the multi-purpose MPD detector will be a considerable minimization of the systematic uncertainties in the fluctuation signal measurements.

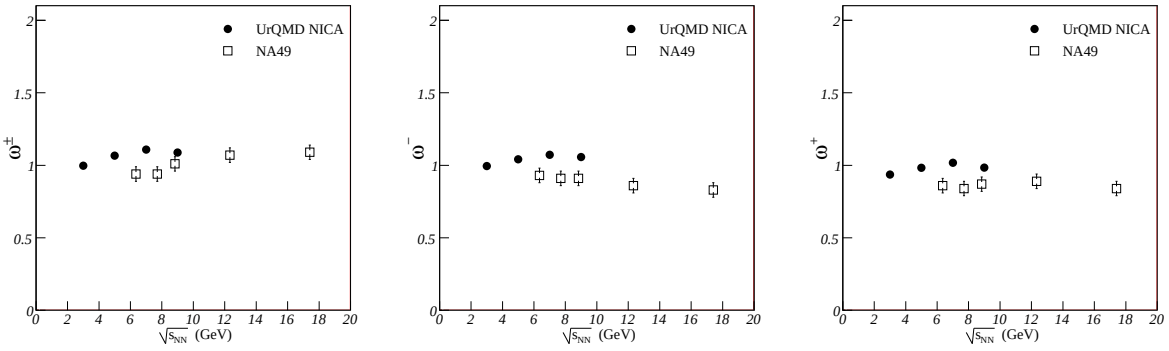

Fig. 1.9: Scaled multiplicity variances of the charged, positive and negative particles in the central Au+Au/Pb+Pb collisions. UrQMD calculations are compared with NA49 results [28].

Chiral Magnetic Effect

The system created in a noncentral relativistic nucleus-nucleus collision possesses large angular orbital momentum. Along with large angular orbital momenta the noncentral collisions may create magnetic fields due to relative motion of electrically charged ions and the products of the collision. The magnetic fields lead to other unusual effects due

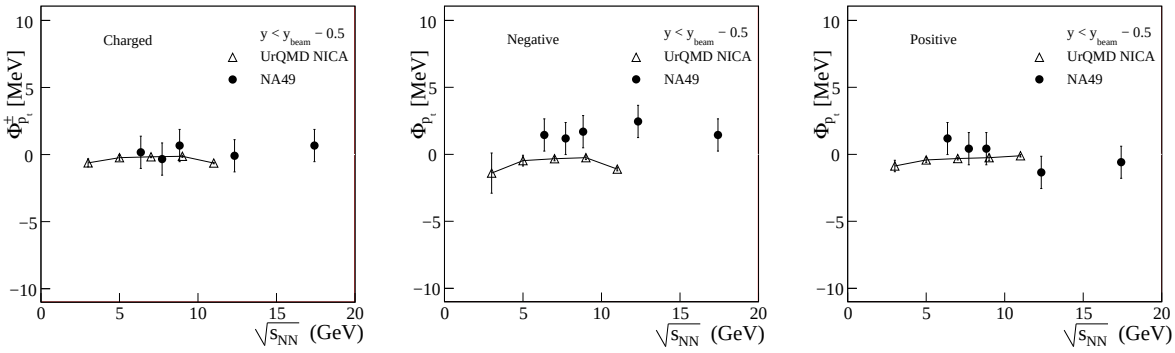

Fig. 1.10: The collision energy dependence of transverse momentum dynamical fluctuations for charged, negative and positive particles. UrQMD calculations are compared with NA49 results [29].

to nontrivial topological structure of QCD [30, 31, 32, 33]. One of the most interesting effects, called the Chiral Magnetic Effect (CME), generates a spatial separation of positive and negative electric charges along the direction of the magnetic field. In the noncentral collisions the magnetic field is perpendicular to the reaction plane, therefore a charge separation can be observed in heavy-ion collisions as a non-statistical asymmetry in the number of positively and negatively charged particles emitted on different sides of the reaction plane [34]. This effect is also called event-by-event P- and CP-violation because this asymmetry implies that the difference of the numbers of quarks of different chiralities is created in a particular event due to quantum fluctuations of the topological charge. However, since there is no CP - violation in strong interactions in the usual sense, this effect vanishes after averaging over all events. The only way to observe it experimentally is by studying CP-even correlations of reaction products [34]. The magnetic field grows with the impact parameter of the collision, therefore this asymmetry should depend strongly on the centrality of the collision. The CME is expected to work effectively in the chirally restored phase [30, 31]: the chiral condensate, which breaks the chiral symmetry, provides a direct coupling between left-handed quarks to the right-handed ones thus leading to an efficient mechanism to suppress any asymmetry between them. Therefore the CME should work effectively in the high temperature case, where the chiral condensate is suppressed and the chirality fluctuations are strong. There are preliminary indications that this effect has been indeed observed by the STAR collaboration at RHIC [35]. The physical explanation of the CME is as follows [30, 31, 36]. At high energy scales of the collisions, the light u and d quarks may be considered as approximately massless particles. The massless fermions are characterized by right- or left-handed helicity (i.e., positive or negative projection of fermions spin on the momentum, respectively), so that the magnetic moment of (anti)quark is always collinear to its momentum. The strong enough external magnetic field makes the magnetic moment to be parallel to the direction of the field so that the motion of the quarks is essentially collinear to the magnetic field. The helicity is related to chirality: the quarks have the same helicity and chirality while for the antiquarks the helicity is opposite to chirality. In the equilibrium ensembles the total chirality is vanishing, so that the total electric current along the magnetic field is zero (the left-handed and right-handed quarks move in opposite directions and compensate each other). However, if there is a difference between the (anti)quarks with left- and

right-handed chirality then the balance is broken and the total electric current along the magnetic field becomes nonzero.

Since the angular momentum of the system is perpendicular to the collision reaction plane, the effects under consideration can be studied by the methods and techniques developed for anisotropic flow analysis. So, parity violation implies charge asymmetry in the particle emission along the system orbital momentum. Such asymmetry fluctuates event by event but its relative sign for the opposite charge particles stays constant. This results in the following azimuthal distribution [37]:

$$\frac{dN_{\pm}}{d\phi} \propto 1 + 2a_{\pm}\sin(\phi - \Psi_{RP}), \tag{1.4}$$

where ϕ is the particle emission azimuthal angle relative to the reaction plane, $a_{\pm} = (4/\pi)Q/N_{\pm}$ is the asymmetry in charged particle production defined by the ratio of topological charge $Q(|Q| \geq 1)$ to the corresponding charged particle multiplicity $N_{\pm}$. One can measure charged particle anisotropy by using the mixed harmonic method applied in a

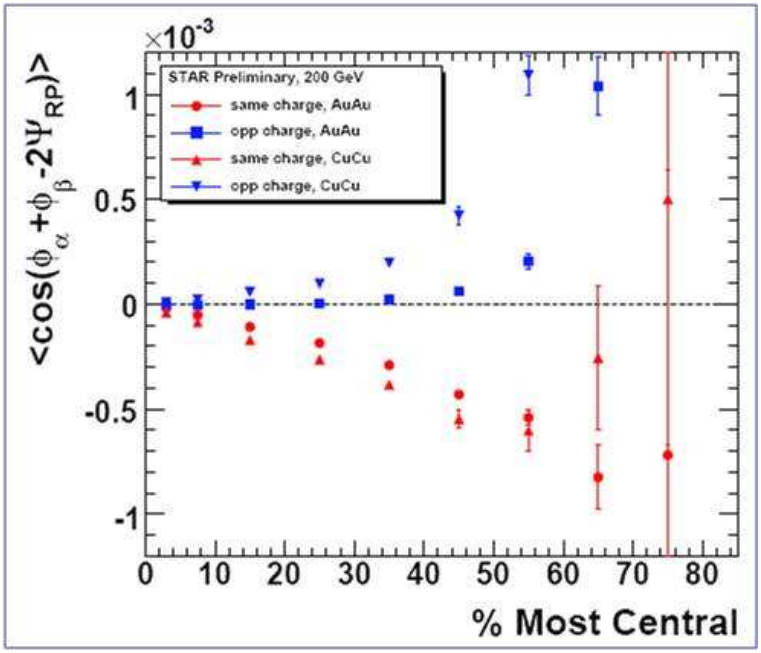

Fig. 1.11: Charged particle asymmetry parameters as a function of standard STAR centrality bins selected on the basis of charged particle multiplicity in the $|\eta| < 0.5$ region [35].

symmetric pseudo-rapidity region:

$$a_i a_j = -\langle cos(\varphi_i - \varphi_j + 2\Psi_{RP})\rangle, \tag{1.5}$$

where $\varphi_{i,j}$ is the azimuthal angle of particles/antiparticles (for example, π^+ and π^-), and Ψ_{RP} is the collision reaction plane angle. The CME implies an imbalance between total electric charge observed above and below the reaction plane which is indeed seen in preliminary data published by STAR collaboration at RHIC. Fig. 1.11 shows the charged particle asymmetry parameter (symmetric pseudo-rapidity range $|\eta| < 0.5$) for different centrality of the collision. Points represent the STAR preliminary results from the experimental data for the Au+Au collisions at $\sqrt{s_{NN}} = 62$ GeV. Note that the correlator

(1.5) contains contributions from other effects not related to parity violation. Could one expect that this strong CP effect be observed at NICA energies? A careful analysis of such a contribution is obviously needed before any strong conclusion can be drawn from these measurements. At least, to measure this possible charged particle asymmetry at NICA, the detecting system should provide geometrical 4π coverage.

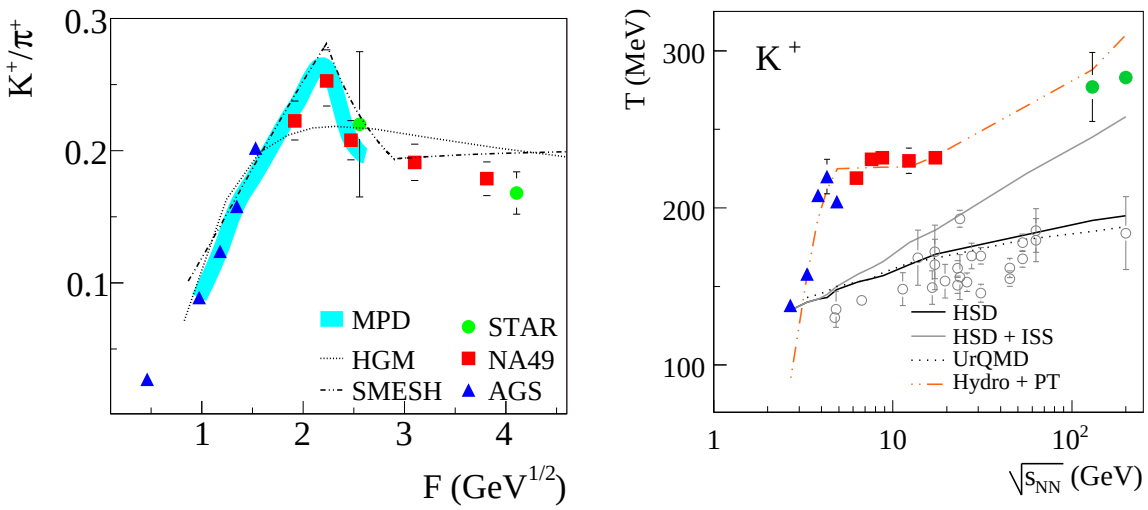

Fig. 1.12: (left)Energy dependence of the K^+/π^+ ratio in central A+A collisions compared to the predictions of HG models with (dosh-dotted) and without (dotted curve) phase transition . The blue band represents the 5% uncertainty limits (could be accomplished at the NICA/MPD). (right) Slope parameter of K^+ transverse spectra (A+A collisions are compared to the $N+N$ data and models). Only the hydrodynamic model with phase transion (dot-dashed line) is capable to reproduce the trend.

1.3 The K/π (strangeness to entropy) ratio

Among the numerous particle species to be measured with the MPD, strange particles are of particular interest, since strangeness production has already proven to be a valuable diagnostic tool for investigating the QGP phase [38]. It has been argued [39] that the onset of deconfinement in central heavy-ion collisions may manifest itself in a non-monotonic energy dependence of the strangeness-to-entropy ratio. As the K^+ yield is proportional to the overall strangeness production and the total entropy produced in the reaction can be associated with the pions, the K^+/π^+ ratio was proposed as the key observable. The experimental data, indeed, show an anomaly in the energy dependence of the strangeness to entropy ratio. Recent results on the relative strangeness yield is shown in Fig. 1.12 (left panel) as a function of the Fermi variable ($F = \frac{(s-2m_N)^{3/4}}{s^{1/4}}$, where s is the centre-of-mass energy and m_N denotes the proton mass). The rapid increase of the relative kaon-to-pion multiplicity changes dramatically at $\sqrt{s_{NN}} \approx 8$ GeV, – the ratio drops down sharply (by about 30%) and then reaches some kind of saturation.

Another very intriguing finding is seen in Fig. 1.12 (right panel), which shows AGS, SPS and RHIC data on the apparent temperature of the midrapidity transverse mass distributions for kaons [20]. Such an anomaly in the energy dependence of the effective temperature of the source (slope parameter T of the transverse mass spectra reflects a superposition of the effect of thermal motion and collective transverse expansion at the decoupling time) might be an indication of the phase transition at the early stage of the collisions and appearance of a mixed phase system in which temperature and pressure are independent of energy density [40]. The pressure saturation in the early stage of the reactions can also be (indirectly) confirmed by the combined analysis of the 2-pion HBT correlations and transverse hadron spectra within a hydrodynamic motivated

approach [41], which results in the nearly constant value of the collective transverse flow velocity ($v_{surface} \approx 0.7c$) and emission duration ($\approx 3.5\ fm/c$) in central Pb+Pb reactions at $\sqrt{s_{NN}}$ from 7 to 17 GeV.

These properties of hadron production can not be described satisfactory in the framework of traditional dynamical string-hadronic models which include rescattering but not consider a phase transition (predictions of the most popular models are shown in Fig. 1.12). However, within the scenario with the onset of deconfinement (OD) at the early stage of the reaction [39] the non-monotonic energy dependence can be reproduced (dot-dashed curve in Fig. 1.12).

We have to emphasize, however, that a traditional statistical thermal model can not be excluded from the interpretation of the experimentally observed "horn" effect. The predictions of such a model [42] with the updated in 2008 hadron mass spectrum and inclusion of the σ meson are shown in Fig. 1.12 (left, dotted line). However, even that requires using of the Hagedorn's limiting temperature concept [43] which contains a phase transition and, as the authors of the paper [42] emphasized in the Summary: "Our results strongly imply that the hadronic observables near and above the horn structure at a beam energy of 30 AGeV provide a link to the QCD phase transition".

It is clear now that the most fundamental constrains in justification of the onset of deconfinement in the NICA energy domain are the experimental measurement uncertainties of the existing data. In particular, in order to prove or disprove any scenario (HG or QGP), it is of highest priority to continue studying the K/π observable with the goal of minimizing the overall uncertainty of the measurements.

The ultimate goal of the future MPD investigation of the relative strangeness production is the overall uncertainty of 5% in the measured K/π ratio shown as the blue band in Fig. 1.12(left panel).

1.4 Anisotropic collective flow

Measurements of collective flow phenomena are the important tools for studying the properties of dense matter created in relativistic heavy ion collisions (such as the equation of state — EOS, formation conditions, etc.). In non-central collisions, the beam direction and the impact parameter vector define a reaction plane for each event. The azimuthal anisotropy of particle production with respect to the reaction plane is an important signature of the physics dynamics at the early stages of non-central heavy ion collisions [44, 45]. An initial nuclear overlap region has an "almond" form at the non-zero impact parameter. If the produced matter interacts and thermalizes, pressure is built up within the almond shaped region leading to anisotropic pressure gradients. This pressure pushes against the outside vacuum and the matter expands collectively. The expansion goes faster along the largest pressure gradient, i.e. along the shortest axis of the almond. This results in the anisotropic azimuthal angle distribution of the detected particles. One can expand this azimuthal angle distribution in a Fourier series

$$dN/d\psi \propto 1 + 2v_1 \cos(\psi) + 2v_2 \cos(2\psi). \tag{1.6}$$

Here the first coefficient, called the directed flow v_1 is defined as

$$v_1 =< \cos(\psi) - \Phi_{RP}) >, \tag{1.7}$$

and the second coefficient is elliptic flow

$$v_2 =< \cos 2(\psi) - \Phi_{RP}) >, \tag{1.8}$$

where ψ is the azimuth angle of particle emission with respect to the reaction plane, Φ_{RP} is the azimuth angle of the reaction plane. The directed flow measures the total amount of transverse flow. It is most pronounced in semi-central interactions around target and projectile rapidities where the spectators are deflected away from the beam axis due to a bounce-off from the compressed and heated matter in the overlap region. Three different interesting properties of the directed flow have been proposed [46].

- The time scales probed by the directed flow are set by the crossing time of the Lorentz-contracted nuclei. Thus, it serves as a keyhole to the initial, probably non-equilibrium, stage of reaction.
- The softening of the equation of state in a first order phase transition leads to decrease of the directed flow.
- The space-momentum correlation of the emitted particles can be addressed experimentally via the v_1 rapidity distributions of nucleons and pions.

The slope of $v_1(y)$ of protons around midrapidity measured at AGS and SPS is shown on the left panel of Fig. 1.13. Going down from the AGS energy range, at SPS energies the data develops even negative values. This behavior cannot be reproduced within the cascade model. To reproduce the data, one should include the mean field with hard EoS, its momentum dependence and medium-modified nucleon-nucleon potential [47].

The elliptic flow deserves special attention because this collective motion is formed mainly at an early stage of the collision. According to the typical hydrodynamic scenario,

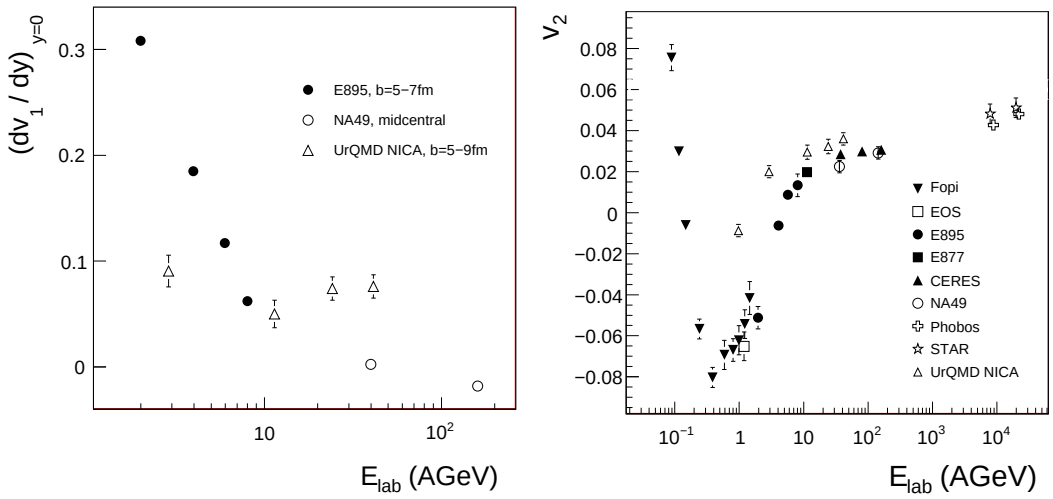

Fig. 1.13: Left: Slope of v_1 of protons around midrapidity. The data are taken from E895 (filled circles)[47] and NA49 (open circles) [48]. Right: v_2 near midrapidity versus collision energy.

the values $v_2(p_T)$ at relatively low transverse momenta ($p_T < 2$ GeV/c) are determined mainly by the internal pressure gradients of the expanding fireball during the initial high density phase of the reaction. The ideal hydrodynamics predicts non-monotonic $\sqrt{s}$-dependence of v_2 as a result of EOS softening near the critical temperature of quark-hadron phase transition [49]. In principle, the elliptic flow of hadrons at low transverse momenta can be related to the degree of thermalization, viscosity, and EoS of the produced matter. However, the elliptic flow of the high p_t particles is related to the jet fragmentation and energy loss of the primordially produced hard antiquark-quark pair traveling through the hot QCD medium. At moderate p_t the experimental data indicate a gradual increase of v_2 with p_t. Thus, an accurate v_2 measurement might allow a deeper insight into the bulk properties of the produced matter. The elliptic flow was measured in a wide range of heavy ion beam energies (AGS, SPS, RHIC). As is seen on Fig. 1.13, the elliptic flow demonstrates rather complicated behavior, being negative at the beam energy $E_{beam} < 2$ AGeV, positive at $E_{beam} > 6$ AGeV, and near zero at $E_{beam} = 4$ AGeV. At the NICA/MPD energy v_2 strongly depends on the collision energy and changes its sign. Positive values of v_2 correspond to a preferential in-plane enhancement of the emitted particles, whereas negative values describe the preferred emission perpendicular to the reaction plane. Clearly, large differences are seen between the results of calculations with and without potentials. On one hand, cascade calculations only show in-plane enhancement of the emitted particles. On the other hand, calculations including nucleonic potentials show a transition from the in-plane to the out-of-plane emission with increasing bombarding energy, which is seen by current experiments. This dependence serves as an important constraint for discriminating between various EoS for high-density nuclear matter, providing an important insight into the interplay between the collision geometry and expansion dynamics. However, the experimental measurement of the elliptic flow is not a trivial task because of the uncertainty in the orientation of the reaction plane and various non–flow contributions such as the transverse momentum conservation, small angle azimuthal correlations (final state interactions), resonance decays, jet production, and quantum statistical correlations (HBT effect).

Besides the integral elliptic flow, differential measurements of v_2 (e.g. as a function of particle transverse momentum p_T for various hadron species) are of a great interest. In particular, one of the most striking features of the RHIC experimental data for Au+Au collisions at $\sqrt{s} = 200$ and 62.4 GeV per nucleon pair is the so-called constituent quark scaling, approximate independence of v_2/n_q as a function of p_T/n_q on hadron species up to $p_T/n_q \sim 1$ GeV/c (where n_q is the number of constituent quarks for the given hadron type), which can be explained in terms of the elliptic flow formation on a partonic level [50]. The breaking of such scaling at lower energies may carry information on the changes in the properties of created dense matter. In particular, the decrease of the baryon flow and increase of the meson flow are predicted as signals of the first order quark-hadron phase transition in the presence of critical point [51, 52]. Since at SPS energies the energy dependence of v_2 for baryons is not established, more detailed measurements (including p_T-dependence of v_2 up to high $p_T \sim 2-3$ GeV/c) are required for the SPS energy range.

It is expected that the high-accuracy and high-luminosity measurements of differential anisotropic flow for various hadron types over the full MPD/NICA energy range will provide important constraints on the early dynamics of heavy ion reactions under conditions where a first order quark-hadron phase transition may occur.

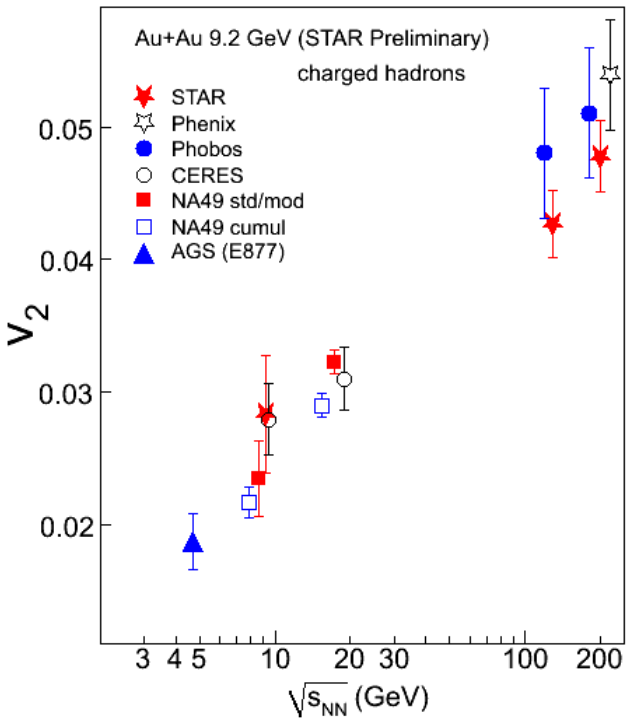

Fig. 1.14: The elliptic flow coefficient v_2 in minimum bias Au+Au and Pb+Pb collisions as a function of c.m.s energy of colliding beams. [53].

1.4.1 Methods to measure anisotropic flow

There exists a wealth of anisotropic flow measurement methods, each having its own advantages and limitations. The three wide-spread methods to calculate the v_2 coefficient are 1) event plane angle determination, 2) cumulant, and 3) Lee-Yang zero methods.

Reaction plane determination. The event plane angle, Ψ_n, can be determined from the measured n-th harmonics via the standard method [54, 55]:

$$\tan n\Psi_n = \frac{\sum\limits_i w_i \sin(n\varphi_i)}{\sum\limits_i w_i \cos(n\varphi_i)}, \qquad n \geq 1, \quad 0 \leq \Psi_n < 2\pi/n, \tag{1.9}$$

where φ_i is the azimuthal angle of the i-th particle and w_i is the weight. The sum runs over all particles in a given event. A procedure to optimize the weights is usually needed in order to achieve the best accuracy, e.g. using the particle transverse momentum, $\omega_i = p_{\mathrm{T}i}$.

If the azimuthal distribution of particles is described by an elliptic form, as in the case of non-central collisions where the initial state is characterized by an anisotropic distribution in the coordinate-space region given by the lens- or almond-like shape of the overlapping zone, then

$$\frac{dN}{d\varphi} = \frac{N_0}{2\pi}\left[1 + 2v_2 \cos 2(\varphi - \Psi_0)\right], \qquad N_0 = \int\limits_{-\pi}^{\pi} d\varphi \, \frac{dN}{d\varphi}, \tag{1.10}$$

where N_0 is the total particle multiplicity in the event, and the reaction plane angle Ψ_0 can be determined via the second harmonic, $n = 2$ in Eq. (1.9). Then the observed value of v_2^{obs} is calculated using the event plane (EP) method by the formula:

$$v_2^{\mathrm{obs}}\{EP\} = \langle \cos 2(\varphi - \Psi_2) \rangle, \tag{1.11}$$

where the event plane angle Ψ_2 is the estimate of the true reaction plane angle Ψ_0, the mean is taken over all charged particles in a given event and then over all events. Usually, the true elliptic flow coefficient is evaluated by dividing v_2^{obs} by the correction factor R [55], which accounts for the event plane resolution:

$$v_2\{EP\} = \frac{v_2^{\mathrm{obs}}\{EP\}}{R} = \frac{v_2^{\mathrm{obs}}\{EP\}}{\langle \cos 2(\Psi_2 - \Psi_0) \rangle}. \tag{1.12}$$

To avoid the trivial autocorrelation of particles, the event plane angle Ψ_2 and hence R are calculated in one angular distribution sample of event, and v_2 in another sample with the same multiplicity. The samples may be selected in two regions of pseudo-rapidity, $\eta < 0$ and $\eta > 0$.

The distribution of the difference, $\Delta\Psi_n$, between the measured angle, Ψ_n, and the "true" angle, Ψ_0, is independent of Ψ_0 if non-flow particle correlations are neglected, and has the form [54, 55]

$$\frac{dw}{d(n\Delta\Psi_n)} = \frac{1}{2\pi}\left[e^{-\frac{\xi^2}{2}} + \xi\sqrt{\frac{\pi}{2}}\cos\left(n\Delta\Psi_n\right)\left[e^{-\frac{\xi^2 \sin^2\left(n\Delta\Psi_n\right)}{2}}\left(1 + \mathrm{erf}\left(\frac{\xi\cos\left(n\Delta\Psi_n\right)}{\sqrt{2}}\right)\right)\right]\right], \tag{1.13}$$

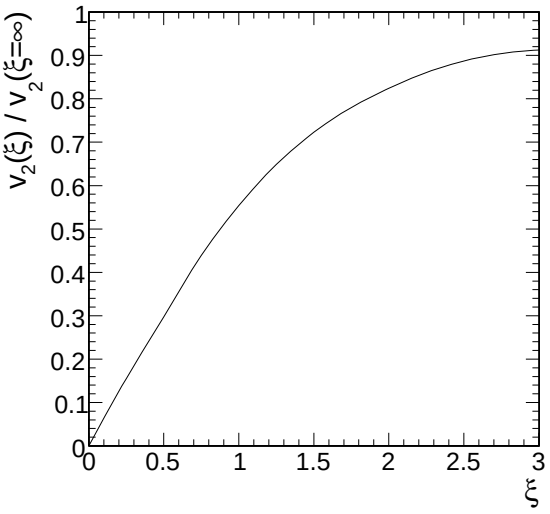

Fig. 1.15: The resolution of the determination of the elliptic flow coefficient, $v_2(\xi)/v_2(\xi \to \infty)$, as a function of the parameter ξ.

where w is the weighting variable. The dimensionless parameter ξ depends on particle multiplicity and strength of the anisotropy, and determines the resolution of the reaction plane: $\Psi_n(\xi \to \infty) = \Psi_0$.

Figure 1.15 shows the resolution of the v_2 determination, defined as the ratio ($\equiv R$) of the "measured" value, $v_2(\xi) = \langle \cos 2(\varphi - \Psi_2) \rangle$, to the "true" value, $v_2(\xi \to \infty) = \langle \cos 2(\varphi - \Psi_0) \rangle$ [54, 55]. This dependence has a universal form for different absolute values of v_2.

The cumulant method for flow studies. Anisotropic flow can be measured without any direct reconstruction of the reaction plane angle. Since all particles are correlated with the reaction plane, they are also indirectly correlated with each other [55, 56, 57]. In the case that the particle azimuthal distribution can be well described by an elliptic form, Eq. (1.10), and there are no other particle correlations besides those due to flow (or other correlations can be neglected), the azimuthal anisotropy coefficient can be determined using the two-particle azimuthal correlator without the event plane angle Ψ_0,

$$\langle \cos 2(\varphi_1 - \varphi_2) \rangle = \frac{1}{N_0^2} \int_{-\pi}^{\pi} d\varphi_1 \int_{-\pi}^{\pi} d\varphi_2 \; \cos 2(\varphi_1 - \varphi_2) \; \frac{d^2N}{d\varphi_1 d\varphi_2}$$

$$= \frac{1}{N_0^2} \int_{-\pi}^{\pi} d\varphi_1 \int_{-\pi}^{\pi} d\varphi_2 \; \cos 2((\varphi_1 - \Psi_0) - (\varphi_2 - \Psi_0)) \; \frac{dN}{d\varphi_1} \frac{dN}{d\varphi_2} = v_2^2 \; . \quad (1.14)$$

The advantage of this method is that it automatically corrects for the detector anisotropies. Thus, the correlation-function method is more robust than the event-plane based approaches. On the other hand, in this procedure each harmonic of the azimuthal distribution is determined independently, without taking into account that the different harmonics are related to each other through the reaction plane. In the event-plane method these relations provide useful consistency checks which are absent here. The statistical

uncertainties, as well as those arising from non-flow effects, are the same in the event-plane methods and in the correlation function approach, because all these methods rely on the two-particle azimuthal correlations.

Note that the event plane and two-particle correlation methods for the analysis of the azimuthal anisotropies rely on the assumption that collective elliptic flow is the dominant source of particle correlations. However, there exist alternative physical sources of azimuthal correlations, such as global momentum conservation, resonance decays (where the decay products are correlated), final state Coulomb, strong or quantum interactions, (mini)jet production [58]. The sensitivity to non-flow contributions in the two particle azimuthal correlation methods motivated the development of new techniques which make use of the fact that anisotropic flow correlates all particles in the event. It was thus proposed to measure the flow with multi-particle azimuthal correlations by performing a cumulant expansion where the collective source of correlations can be disentangled from other sources [57]. The main advantage of the higher order cumulant analysis lies in the fact that, if the flow is larger than the non-flow correlations, the contribution of the latter to v_2, extracted from higher order correlators, is suppressed by powers of the particle multiplicity in the event, N_0.

Thus, for example, the fourth order cumulant for the elliptic particle flow is defined as

$$\begin{aligned} c_2[4] \;\equiv\; & \langle \cos 2(\varphi_1 + \varphi_2 - \varphi_3 - \varphi_4) \rangle \\ - \langle \cos 2(\varphi_1 - \varphi_3) \rangle \, \langle \cos 2(\varphi_2 - \varphi_4) \rangle - & \langle \cos 2(\varphi_1 - \varphi_4) \rangle \, \langle \cos 2(\varphi_2 - \varphi_3) \rangle \; . \end{aligned} \tag{1.15}$$

If there are only correlations with the reaction plane (i.e. the multi-particle distributions factorize as in Eq. (1.14)), then

$$c_2[4] \;=\; -\, v_2^4 \quad . \tag{1.16}$$

If the coefficient v_2 is defined by the two-particle correlator (1.14), then the contribution of non-flow correlations is of the order of $1/\sqrt{N_0}$. The non-flow contributions to v_2, extracted from the fourth-order correlator,

$$v_2 \;=\; (-c_2[4])^{1/4} \quad , \tag{1.17}$$

scale as $1/N_0^{3/4}$, suppressed by the extra factor $1/N_0^{1/4}$.

The Lee-Yang zeroes method for flow studies. The Lee-Yang zeroes method [59] refers to the Generation function as a complex function of variable r:

$$G^{\theta}(ir) = \langle e^{irQ^{\theta}} \rangle, \tag{1.18}$$

where Q^{θ} is the flow vector and θ is arbitrary angle.

$$Q^{\theta} = \sum_{j}^{N} \cos 2(\varphi_j - \theta). \tag{1.19}$$

The p_T-integrated v_2 value is connected with the first minimum r_0^{θ} of module of the Generation function $|G^{\theta}(ir)|$,

$$v_2^{\theta}\{\infty\} \equiv \frac{j_{01}}{N_0 r_0^{\theta}}, \tag{1.20}$$

and the differential value is given by the more complex expression:

$$\frac{{v_2}^{\theta}(p_T)\{\infty\}}{N_0 v_2\{\infty\}} \equiv Re\left(\frac{\langle \cos 2(\varphi-\theta) e^{ir_0^{\theta}Q^{\theta}}\rangle}{\langle Q^{\theta} e^{ir_0^{\theta}Q^{\theta}}\rangle}\right) . \tag{1.21}$$

Here, $j_{01} = 2.405$ is the point of the first minimum of the Bessel function $J(x)$. The advantage of the Lee-Yang zeroes method is that it is the best to reconstruct v_2 in the presence of large non-flow correlations. However, the efficiency of the method drops significantly at low event multiplicities.

1.4.2 Estimation of statistical p_T-reach for elliptic flow measurements

The estimation of statistical reach for elliptic flow measurements at MPD has been done with the HYDJET++ heavy ion event generator [60]. The final hadronic state in the HYDJET++ represents a superposition of soft and hard components. These parts are independent and their contribution to the total multiplicity production depends on collision energy, and centrality, and is tuned by model input parameters. The hard component of the model accounts for the medium-modified partonic jet fragmentation. The soft component of the model accounts for the "thermal" hadronic state where multiplicities are determined under the assumption of thermal equilibrium. Hadrons are produced on the hyper-surface represented by parametrization of relativistic hydrodynamics with epy preset freeze-out conditions. Feed down of hadronic resonances is taken into account. Although the HYDJET++ is optimized for very high energies of RHIC and LHC colliders, in practice it can also be used for studying particle production in a wider energy range down to $\sqrt{s_{NN}} \sim 10$ GeV. As one moves from the very high to moderately high energies, the contribution of the hard part of the event becomes smaller, while the soft part turns into a multi-parameter fit to the data. For NICA energies, input parameters of the HYDJET++ soft component were tuned using SPS data on pion spectra and femtoscopic correlation radii in Pb+Pb collisions. The normalization of the p_T-integrated elliptic flow coefficient on the value $v_2 = 0.027$ was done basing on the experimental data (Fig. 1.14).

Figure 1.16 shows the p_T-dependence of the elliptic flow coefficient v_2 for charged pions, kaons and protons at pseudo-rapidity $\mid \eta \mid < 1$ in Au+Au collisions at $\sqrt{s_{NN}} = 9$ GeV simulated with the HYDJET++ . The number of entries and the statistical errors correspond to various generated event rates: 10^3, 10^4, 10^5, and 10^6 minimum bias events. The estimated statistical p_T reach of v_2 measurements within first 10^4 events is ~ 1.5 GeV/c for protons and ~ 1 GeV/c for pions and kaons. For the first 10^5 events, the p_T reach can be extended up to ~ 2 GeV/c for protons and ~ 1.5 GeV/c for pions and kaons. The reasonable statistical reach to measure the v_2 of identified hadrons up to $p_T/n_q = 1$ GeV/c (where n_q is the number of constituent quarks for a given hadron type, so it corresponds to $p_T = 3$ GeV/c for protons and $p_T = 2$ GeV/c for pions and kaons) can be achieved within the first 10^6 events. In order to measure v_2 of pions and kaons with small statistical error at $p_T = 3$ GeV/c, MPD will need $\sim 10^7$ events.

The estimated event rates correspond to the "first day" of MPD physics at a designed NICA luminosity. Thus, at long time scale measurements, the statistical error in differential v_2 determination (not only for pions, kaons and protons, but also for most of other hadrons like ρ, ω and ϕ mesons, Λ, Ξ and Ω baryons, etc.) is expected to be much less than the systematic error. The main systematic uncertainties are expected due

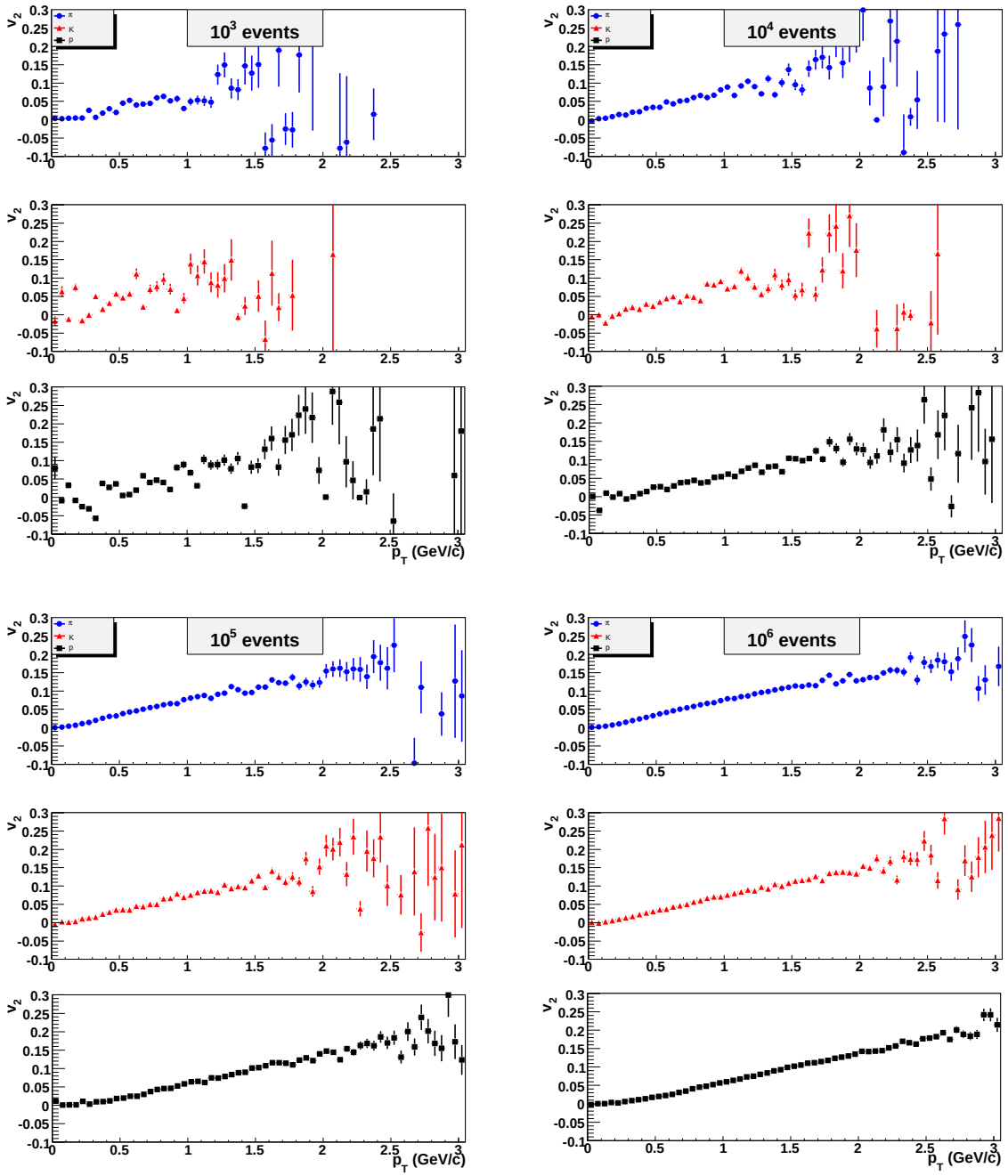

Fig. 1.16: The p_T-dependence of the elliptic flow coefficient v_2 for charged pions, kaons, and protons at a pseudo-rapidity of $|\eta| < 1$ in Au+Au collisions at $\sqrt{s} = 9$ GeV per nucleon pair. From left to right and from bottom to top: 10^3, 10^4, 10^5 and 10^6 minimum bias HYDJET++ events.

to the uncertainties of methods for elliptic flow reconstruction (see the previous section 1.4.1). Figure 1.17 shows the event plane resolution parameter $\xi \sim \sqrt{2N_0}v_2$ in Eq. (5.6) as a function of multipilicity of hadrons used for the analysis at different values of epy p_T-integrated v_2. At the expected values of $v_2 \sim 0.02 - 0.03$ and mean multiplicities of charged hadrons in an MPD acceptance of $N_0 \sim 100 - 200$ (dependent on event centrality), the estimated range of ξ is $\sim 0.3 - 0.6$. It corresponds to the typical resolution of the

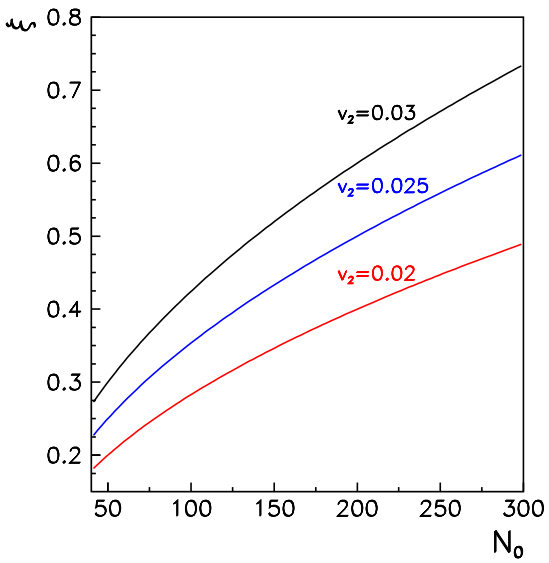

Fig. 1.17: The event plane resolution parameter ξ in Eq. (5.6) as a function of multipilicity of hadrons used for analysis at the p_T-integrated $v_2 = 0.03$, 0.025 and 0.02 (from top to bottom).

v_2 measurement (the ratio of the measured v_2 to the "true" v_2) on the level of $\sim 0.2 - 0.3$ (see Fig. 1.15), which should be taken into account as a corresponding correction factor in Eq. (1.12). Thus, in order to reduce the total systematic uncertainty, the combination of all effective methods to measure the anisotropic flow is strongly preferable.

1.4.3 Conclusions

The azimuthal collective flow measurements in relativistic nuclear collisions have recently generated a very strong interest. One of the most striking observables related to azimuthal correlations in a wide energy range of heavy ion beams is the p_T-dependence of the elliptic flow coefficient v_2 for identified hadrons, which carries information abouton the changes in the properties of created dense matter. The high-accuracy and high-luminosity measurements of differential anisotropic flow for various hadron types over the full NICA energy range will provide important constraints on the early dynamics of heavy ion reactions under the conditions where the first order quark-hadron phase transition may occur.

The anisotropic flow can be measured independently by different analysis methods. Since each method has its own advantages and limitations, combination of all wide-spread methods (event plane reconstruction, cumulant and the Lee-Yang zeroes methods) allows the systematic uncertainties for the v_2 measurements to be reduced. For MPD acceptance, the statistical p_T reach up to $p_T/n_q = 1$ GeV/c ($p_T = 3$ GeV/c for protons and $p_T = 2$ GeV/c for pions and kaons) is expected to be achieved within the first million minimum bias Au+Au events at the NICA energy of $\sqrt{s} = 9$ GeV per nucleon pair.

To summarize, at a central rapidity ($|\eta| < 1$), MPD will be able to measure the anisotropic flow of identified hadrons in the early NICA running for a reasonable range of particle multiplicity and elliptic flow magnitudes with a high statistical reach.

1.5 Femtoscopy (momentum correlations)

1.5.1 Introduction

The momentum correlations of two or more particles at small relative momenta in their center-of-mass (c.m.) system are widely used to study space-time characteristics of the production processes on a level of fm = 10^{-15} m, so serving as a correlation femtoscopy tool (see reviews [61, 62, 63, 64, 65, 66, 67, 68]).

In fact, the femtoscopic correlations due to the Coulomb final state interaction (FSI) between the emitted electron or positron and the residual nucleus in beta-decay are known for more than 70 years (see [69] for a discussion of the similarity and difference between the femtoscopic correlations in beta-decay and multiparticle production). The femtoscopic correlations due to the quantum statistics (QS) of produced identical particles were observed almost 50 years ago as an enhanced production of pairs of identical pions with small opening angles (GGLP effect). The basics of the modern correlation femtoscopy were settled by Kopylov and Podgoretsky in the early seventies of the last century. Besides the space-time characteristics of particle production, the femtoscopic correlations yield also a valuable information on the low-energy strong interaction between specific particles, which can hardly be achieved by other means [67].

1.5.2 Formalism

The ideal two-particle correlation function $\mathcal{R}(p_1, p_2)$ is defined as a ratio of the measured two-particle distribution to the reference one, which would be observed in the absence of the effects of QS and FSI. In practice, the reference distribution is usually constructed by mixing the particles from different events with similar selection criteria, normalizing the correlation function to unity at sufficiently large relative velocities. This procedure is well justified for high-energy collisions involving nuclei since they are characterized by sufficiently large multiplicity of produced particles and, in the absence of QS and FSI, the particle correlations at small relative velocities are negligibly influenced by kinematic constraints and production dynamics.

Usually, it is assumed that the correlation of two particles emitted with a small relative velocity is only influenced by the effects of their mutual QS and FSI and that the momentum dependence of the one-particle emission probabilities is inessential if the particle four-momenta p_1 and p_2 are varied by the amount characteristic for the correlation due to QS and FSI (*smoothness assumption*). As for the former assumption, besides the rare events with a large phase-space density fluctuations, it may not be justified also in the low energy heavy ion reactions in which the particles are produced in a strong Coulomb field of residual nuclei; to deal with, this field a quantum adiabatic (factorisation) approach can be used [70, 71, 72]. The latter assumption, requiring the components of the mean space-time distance between the particle emitters much larger than those of the space-time extent of the emitters, is well justified for ion collisions.

The correlation function is then given by a square of the properly symmetrized Bethe-Salpeter amplitude in the continuous spectrum of the two-particle states, $\Psi^{S(-)}_{p_1p_2}(x_1, x_2)$, averaged over the four-coordinates $x_i = \{t_i, \mathbf{r}_i\}$ of the emitters and over the total spin S of the two-particle system [73, 74, 75, 76]. On the assumption of the quasi-free propagation of the low-mass two-particle system, one can separate the free c.m. system motion in the unimportant phase factor. As a result, this amplitude practically reduces to the one,

$\psi^{S(-)}_{\widetilde{q}}(\Delta x) = [\psi^{S(+)}_{\widetilde{q}}(\Delta x)]^*$, depending only on the relative four-coordinate $\Delta x \equiv x_1 - x_2 = \{t, \mathbf{r}\}$ and the generalized relative momentum $\widetilde{q} = q - P(qP)/P^2$, where $P = p_1 + p_2$, $q = p_1 - p_2$ and $qP = {m_1}^2 - {m_2}^2$; in the two-particle c.m. system, $\mathbf{P} = 0$, $\tilde{q} = \{0, 2\mathbf{k}^*\}$, and $\Delta x = \{t^*, \mathbf{r}^*\}$.

At equal emission times of the two particles in their c.m. system ($t^* \equiv t^*_1 - t^*_2 = 0$), the reduced non-symmetrized Bethe-Salpeter amplitude $\psi^{S(+)}_{\widetilde{q}}(\Delta x)$ coincides with a stationary solution $\psi^{S(+)}_{-\mathbf{k}^*}(\mathbf{r}^*)$ of the scattering problem having at large distances r^* the asymptotic form of a superposition of the plane and outgoing spherical waves (the minus sign of the vector $\mathbf{k}^*$ corresponds to the reverse in time direction of the emission process; also, the intermediate and detected channels should be interchanged, the latter should be considered as the entrance scattering channel).

Note that, to simplify the calculations, the reduced Bethe-Salpeter amplitude is usually substituted by the equal-time amplitude $\psi^{S(+)}_{-\mathbf{k}^*}(\mathbf{r}^*)$. For non-interacting particles, the reduced non-symmetrized Bethe-Salpeter amplitude coincides with the plane wave $\mathrm{e}^{i\tilde{q}x/2} \equiv \mathrm{e}^{-i\mathbf{k}^*\mathbf{r}^*}$ which is independent of the relative time in the two-particle c.m. system and so, coincides with the corresponding equal-time amplitude. On the contrary, the amplitude of two interacting particles contains an explicit dependence on t^* – the interaction effect vanishes at $|t^*| \to \infty$. However, it can be shown [73, 74] that the effect of non-equal times can be neglected on the condition $|t^*| \ll m(t^*)r^{*2}$, where $m(t^* > 0) = m_2$ and $m(t^* < 0) = m_1$. This condition is usually satisfied for heavy particles like kaons or nucleons. But even for pions, the $t^* = 0$ approximation merely leads to a slight overestimation (typically less than a few percent) of the strong FSI effect and, doesn't influence the leading zero-distance ($r^* \ll |a|$) effect of the Coulomb FSI [73, 74, 75, 76].

In the *equal time* approximation, the correlation function is as follows:

$$\mathcal{R}(p_1, p_2) \doteq \sum_S \widetilde{\rho}_S \langle |\psi^{S(+)}_{-\mathbf{k}^*}(\mathbf{r}^*)|^2 \rangle_S. \tag{1.22}$$

For identical particles, the amplitude in Eq. (1.22) enters in a symmetrized form:

$$\psi^{S(+)}_{-\mathbf{k}^*}(\mathbf{r}^*) \to [\psi^{S(+)}_{-\mathbf{k}^*}(\mathbf{r}^*) + (-1)^S \psi^{S(+)}_{\mathbf{k}^*}(\mathbf{r}^*)]/\sqrt{2}. \tag{1.23}$$

The averaging in Eq. (1.22) is done over the four-coordinates x_1, x_2 of the emitters according to the two-particle emission function $G_S(x_1, p_1; x_2, p_2)$ at a given total spin S of the two particles; $\widetilde{\rho}_S$ is the corresponding population probability, $\sum_S \widetilde{\rho}_S = 1$. For the unpolarized particles with spins s_1 and s_2 the probability $\widetilde{\rho}_S = (2S+1)/[(2s_1+1)(2s_2+1)]$. Generally, the correlation function is sensitive to particle polarization. For example, if two spin-1/2 particles are initially emitted with polarizations $\boldsymbol{\mathcal{P}}_1$ and $\boldsymbol{\mathcal{P}}_2$ then [73, 74] $\widetilde{\rho}_0 = (1 - \boldsymbol{\mathcal{P}}_1 \cdot \boldsymbol{\mathcal{P}}_2)/4$, $\widetilde{\rho}_1 = (3 + \boldsymbol{\mathcal{P}}_1 \cdot \boldsymbol{\mathcal{P}}_2)/4$.

1.5.3 Femtoscopy techniques

Identical particles

For identical pions or kaons, the effect of the strong FSI is usually small and the effect of the Coulomb FSI can be in first approximation simply corrected for (see [77] and references therein). The corrected correlation effect is then only determined by the QS symmetrization, i.e. the Bethe–Salpeter amplitudes have to be substituted by the properly symmetrized combinations of the plane waves. As a result, $\mathcal{R}(p_1, p_2) = 1 + \langle \cos(q\Delta x) \rangle$.

Assuming, for example, that for a (generally momentum dependent) fraction λ of the pairs, the particles are emitted by independent one-particle emitters that are at rest and differ only in the four-coordinates of their centers characterized by the Gaussian space-time dispersions r_0^2, τ_0^2, whereas for the remaining fraction $(1-\lambda)$, related to very long-lived emitters (η, K_s^0, Λ, ...), the relative distances r^* between the emission points in the pair c.m. system are extremely large and lead to extremely narrow unobservable momentum correlation, the correlation function can be written as follows:

$$\mathcal{R}(p_1,p_2) = 1 + \lambda \exp\bigl(-{r_0}^2\mathbf{q}^2 - {\tau_0}^2 q_0^2\bigr)\,. \tag{1.24}$$

We see that the characteristic feature of the correlation function of identical spin-0 particles is the presence of an interference maximum at small $|\mathbf{q}|$, followed by a horizontal plateau at sufficiently large $|\mathbf{q}|$, as compared with the inverse characteristic space-time distance between the particle's emission points.

The on-shell constraint $q_0 P_0 = \mathbf{qP}$ makes the q-dependence of the correlation function essentially three-dimensional (particularly, in pair c.m. system, $q\Delta x = -2\mathbf{k}^*\mathbf{r}^*$) and thus makes impossible the unique Fourier reconstruction of the space-time characteristics of the emission process. However, within realistic models, the directional and velocity dependence of the correlation function can be used to determine both the duration of the emission and the form of the emission region [61, 62], as well as to reveal the details of the production dynamics (such as collective flows; see, e.g., reviews [65, 66, 67, 68]). For this, the correlation functions can be analyzed in terms of the out (x), side (y), and longitudinal (z) components of the relative momentum vector $\mathbf{q} = \{q_x, q_y, q_z\}$ [78, 79, 80, 81, 82, 83]; "out" and "side" denote the transverse components of the vector $\mathbf{q}$, the out direction being parallel to the transverse component of the pair three-momentum. The corresponding correlation widths are usually parameterized in terms of the Gaussian correlation (interferometry) radii r_i, e.g., for spin-0 bosons

$$\mathcal{R}(p_1,p_2) = 1 + \lambda \exp(-r_x^2 q_x^2 - r_y^2 q_y^2 - r_z^2 q_z^2 - 2r_{xz}^2 q_x q_z), \tag{1.25}$$

and the radii dependence on pair rapidity and transverse momentum is studied. The correlation strength parameter λ can differ from unity due to the contribution of very long-lived emitters, particle misidentification, and coherence effects. Equation (1.25) assumes azimuthal symmetry of the production process. Generally, e.g. in case of the correlation analysis with respect to the reaction plane, all three cross terms $q_i q_j$ contribute.

It is well known that particle correlations at high energies usually measure only a small part of the space-time emission volume, being only slightly sensitive to its increase related to the fast longitudinal motion of particle emitters. In fact, due to limited emitter decay momenta of a few hundred MeV/c, the correlated particles with nearby velocities are emitted by almost comoving emitters and, and so, at nearby space-time points. The dynamical examples are resonances, colour strings or hydrodynamic expansion. To substantially eliminate the effect of longitudinal motion, the correlations can be analyzed in terms of the invariant variable $Q = 2k^* \equiv (-\widetilde{q}^2)^{1/2}$ and components of the three-momentum difference in the pair c.m. system ($\mathbf{q}^* \equiv \mathbf{Q} = 2\mathbf{k}^*$) or in the longitudinally comoving system (LCMS) [84]. In LCMS, each pair is emitted transverse to the reaction axis, so that the generalized relative three-momentum $\widetilde{\mathbf{q}}$ coincides with $\mathbf{q}^*$, except for the *out*-component $\widetilde{q}_x = \gamma_t q_x^*$, where γ_t is the LCMS Lorentz factor of the pair.

Nonidentical particles

The FSI effect allows one to access the space-time characteristics of particle production also with the help of correlations of non-identical particles.

The correlation function of non-identical particles, as compared with the identical ones, contains a principally new piece of information on the relative space-time asymmetries in particle emission [85]. Since this information enters in the two-particle FSI amplitude through the terms odd in $\mathbf{k}^*\mathbf{r}^* \equiv \mathbf{p}_1^*(\mathbf{r}_1^* - \mathbf{r}_2^*)$, it can be accessed from studying the correlation functions $\mathcal{R}_{+i}$ and $\mathcal{R}_{-i}$ with positive and negative projection k_i^* on a given direction $\hat{i}$ or, the ratio $\mathcal{R}_{+i}/\mathcal{R}_{-i}$. For example, $\hat{i}$ can be either the direction of the pair velocity or any of the out (x), side (y), or longitudinal (z) directions. In LCMS, we have $r_i^* = r_i$, except for $r_x^* \equiv \Delta x^* = \gamma_t(\Delta x - v_t \Delta t)$, where γ_t and v_t are the pair LCMS Lorentz factor and velocity. One may see that the asymmetry in the out (x) direction depends on both space and time asymmetries $\langle \Delta x \rangle$ and $\langle \Delta t \rangle$. In case of a dominant Coulomb FSI, the intercept of the correlation function ratio is directly related with the asymmetry $\langle r_i^* \rangle$ scaled by the pair Bohr radius a:

$$\mathcal{R}_{+i}/\mathcal{R}_{-i} \approx 1 + 2\langle r_i^* \rangle / a. \tag{1.26}$$

The difference between the correlation functions $\mathcal{R}_+$ and $\mathcal{R}_-$ yields a robust estimate of the asymmetry $\langle r_i^* \rangle$ though its statistical error is not minimized. The lowest possible statistical error is achieved by giving the weight $|\hat{k}_i^*| = |\cos\psi_i|$ to each pair contributing to $\mathcal{R}_+$ or $\mathcal{R}_-$. This corresponds to the least squares fitting or moment method (yielding $2\langle r_i^* \rangle / a = \langle \hat{k}_i^* \rangle / 3$) and decreases the statistical error of the $\mathcal{R}_+$ vs $\mathcal{R}_-$ method by a factor of $(4/3)^{1/2}$ (corresponding to a 33% gain in statistics) [86].

Besides the asymmetry information in the first order moments $\langle \hat{k}_i^* \rangle$, useful information on the anisotropy of the $\mathbf{r}^*$-separation of particle emitters can be extracted also from the higher order moments. Thus, a systematic expansion of the correlation function in terms of Cartesian or spherical harmonics and a study of the corresponding $(2l+1)$ real Q-dependent angular-moment coefficients for each order $l = 0, 1, \ldots$ has been suggested [87, 88].

It appears that the "out" correlation asymmetries between pions, kaons and protons observed in heavy ion collisions at CERN and BNL are in agreement with the practically charge independent meson production and, assuming $m_1 < m_2$, with a negative $\langle \Delta x \rangle = \langle x_1 - x_2 \rangle$ and/or positive $c\langle \Delta t \rangle = c\langle t_1 - t_2 \rangle$ on the level of several fm [67, 89]. In fact, they are in quantitative agreement with the RQMD transport model, as well as with the hydro-motivated blast wave parametrization, both predicting the dominance of the spatial part of the asymmetries generated by large transverse flows.

In the thermal approach, the mean thermal velocity is smaller for heavier particle, which washes out the positive spatial shift due to the flow to a lesser extent. As a result, $\langle x_\pi \rangle < \langle x_K \rangle < \langle x_p \rangle$. The observation of the correlation asymmetries in line with the mass hierarchy of the shifts in the "out" direction may thus be considered as one of the most direct signals of the universal transversal collective flow [67].

Correlation measurement of strong interaction

The correlation measurements can be used to improve the knowledge of strong interaction for various two-particle systems. In the collisions involving sufficiently heavy nuclei, the effective radius r_0 of the emission region can be considered much larger than the range

of the strong interaction potential. The FSI contribution is then independent of the actual potential form [90]. At the small $Q = 2k^*$ values and at a given total spin S, it is determined by the s-wave scattering amplitude $f^S(k^*)$ [73, 74]. In case of $|f^S| > r_0$, this contribution is of the order of $|f^S/r_0|^2$ and dominates over the effect of QS. In the opposite case, the sensitivity of the correlation function to the scattering amplitude is determined by the linear term f^S/r_0.

The possibility of the correlation measurement of the scattering amplitudes has been demonstrated [67] in a preliminary analysis of the NA49 $\pi^+\pi^-$ correlation data within the RQMD transport model. For this, besides the r^*-scale s_r, the strong interaction scale s_f has been introduced in the RQMD correlation function $\mathcal{R}(Q; s_r, s_f)$, rescaling the original s-wave $\pi^+\pi^-$ scattering amplitude: $f(k^*) \to s_f f(k^*)$; it approximately corresponds to the rescaling of the original scattering length $f_0 = 0.23$ fm. The fitted parameter $s_f = 0.6 \pm 0.1$ appears to be significantly lower than unity (see [75, 76] for the discussion of possible systematic errors). To a similar but somewhat weaker rescaling (~ 0.8) point also the recent experimental data on pionium lifetime, K_{l4} and $K^\pm \to \pi^\pm\pi^0\pi^0$ decays, as well as the two-loop calculation in the chiral perturbation theory with a standard value of the quark condensate [75, 76]. The correlation technique was also used to estimate the singlet $\Lambda\Lambda$ and $p\bar{\Lambda}$ s-wave scattering lengths [67, 91].

1.5.4 Role of femtoscopy in interpretation of the phase transition and critical point signatures.

Experiments at RHIC demonstrated that hot and dense matter with partonic collectivity, the so called "strongly coupled quark-gluon plasma", were formed in ultra-relativistic heavy ion collisions at $\sqrt{s}_{NN} = 200$ GeV [92, 93, 94, 95]. There are such effects as jet-quenching, charmonium suppression, elliptic flow quark-number scaling, strangeness enhancement etc, which are usually considered as signals of phase transition to the deconfined phase. Information on the space-time evolution of hot and dense matter created in heavy ion collisions can only be extracted with the help of femtoscopy correlations. The correlations depend on the space-time distance separating the emission points and on the particle relative momentum. The space-time relative distances are "measured" at the points where the particles stop to interact, and are set free. This moment comes at a very late stage of collisions, long after the QGP or any other exotic state of matter was created and disappeared, except the direct photons which can originate from the QGP. Yet, such signals as geometric growth of the reaction zone and the specific features of the collective flow generated by QGP pressure gradients are imprinted in the final state as the very specific space-momentum correlations influencing particle spectra and correlation radii. It was demonstrated [96] that the particle spectra, interferometry volumes (correlation radii), and averaged phase-space densities, measured at any time of the expansion of hadron-resonance gas, are approximately conserved upon isentropic and chemically frozen evolution. Studying femtoscopic correlations thus allows one to constrain the model predictions for early stages and fireball evolution. It was expected that the first order phase transition strongly delays the fireball evolution [97]. However, the pion correlation radii measured in a wide energy range (from AGS to RHIC energies) demonstrated surprisingly weak energy dependence ("RHIC HBT puzzle", Fig. 1.18) and did not demonstrate any discontinuities [98, 99, 100, 101, 102, 103, 104, 105, 106, 107]. The attempts to describe the correlation radii together with momentum observables (v_2 in particular) stimulated

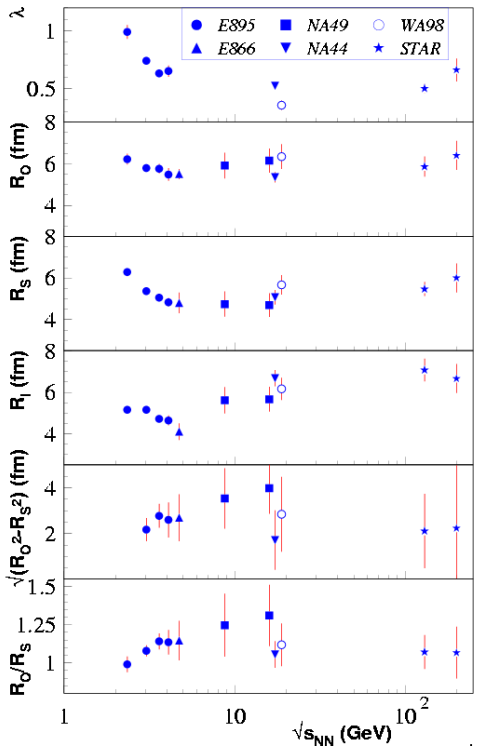

Fig. 1.18: Energy dependence of correlation radii for central Au+Au (Pb+Pb) collisions at midrapidity.

development of hydrodynamic models. Thus, according to recent hydrodynamic calculations, the femtoscopic radii, particle spectra and elliptic flow can be described either by using the initial Gaussian density profile [108] or by including the combination of: pre-thermal acceleration, a stiffer equation of state, and adding viscous corrections [109]. Further development is related to the use of continuous freeze-out scenario within the new hydro-kinetic model [110].

The regime obtained in heavy ion collisions at highest RHIC energies seems to correspond to the lattice QCD calculations for the phase transition of the 2nd order: a rapid, but smooth, crossover at large temperature T and vanishing baryonic chemical potential μ_B [111, 112, 113]. Various models predict a strong 1st order transition at $T \sim 0$ and large μ_B [25, 114].

The increase of emission time due to the first order phase transition should be reflected in the increase of the R_{out}/R_{side} ratio. However, such an increase was observed (Fig. 1.18) neither at RHIC energies nor at AGS-SPS energies. The reasons for the absence of this effect at RHIC energies were discussed above, the possible reasons at lower energies can be as follows:

1. the decrease of relative contribution of QGP phase at small energies;

2. the dominance of the small space-time separations of the particle emitters over the large ones in the visible femtoscopic correlations (in the fitted Gaussian correlation radii).

These reasons indicate that more complicated techniques than those used in the past experiments are necessary to extract information on the large sizes associated with QGP.

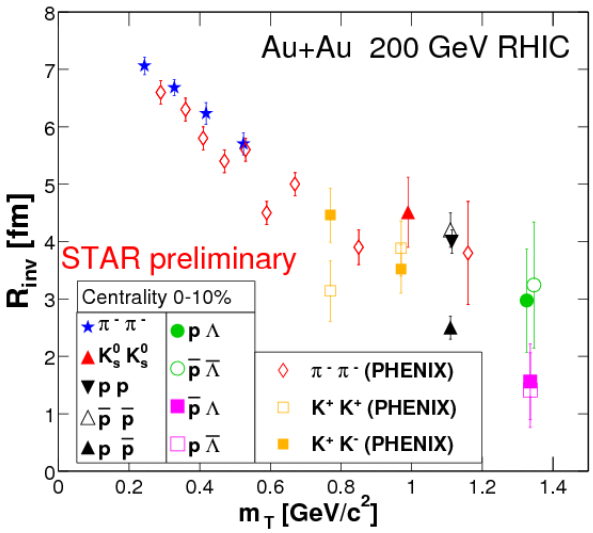

Fig. 1.19: The m_t dependence of the invariant correlation radius for central Au+Au collisions at midrapidity obtained for different particle pairs.

It may be the "imaging technique" [115] or the multiparametric fits substituting the simple 3D-Gaussian ones, both requiring very large statistics. Important information can be also obtained from a detailed angular correlation analysis with respect to the reaction plane [65] and spherical harmonic decomposition [116]. These measurements will give a detailed information about the space-time structure of the emitting system. Requiring large statistics, such experiments will be only possible for the most numerous particle species. The large luminosity planned in the NICA project will be crucial for these tasks.

The femtoscopy correlations can now be studied with new more precise sets of detectors providing large statistics data. The particle yields measured in the SPS experiments are presented in Table 1.2. The Gaussian correlation radii were determined for various combinations of identical and non-identical particles (see, e.g., Fig. 1.19). Note that the kaon correlations are less affected by resonance decays and thus allow one to access smaller space-time scales in a more direct way than the pion ones. A list of two-particle systems which will be potentially available for femtoscopy studies in the NICA energy range is presented in Table 1.3.

What are the specific features of the MPD proposal for femtoscopy studies as compared with SPS(NA61), RHIC(STAR) and FAIR(CBM)?

1. The acceptance and occupancy in the collider experiments (STAR, MPD) are nearly constant and energy independent contrary to the fixed target experiments (NA61, CBM), where they strongly change with energy (at a fixed target geometry). One more advantage of collider experiments is smaller detectors. Particularly, the measured particle momenta and the corresponding time of flight base for the TOF system in the fixed target CBM experiment are about ten times larger than those in the MPD experiment, with obvious impact on the detector cost.

2. The planned luminosity at maximal energy of NICA will be by about two orders of magnitude larger than that at RHIC. It will allow to measure the wider spectrum of particle combinations and carry out wider spectrum of physics experiments than at the lowest RHIC energies.

Table 1.2: Mean multiplicities of charged mesons at 20, 30 and 40 AGeV from SPS experiments. Central (7%) Pb+Pb interactions.

$E_{\rm lab}, AGeV$	20	30	40
$\sqrt{s_{NN}}$, GeV	6.3	7.6	8.8
$\langle\pi^+\rangle$	$184.5 \pm 0.6 \pm 13$[117]	$239 \pm 0.7 \pm 17$[118]	$293 \pm 3 \pm 15$[119]
$\pi^+, \frac{dn}{dy}_{y\approx 0}$	–	-	$96.6 \pm 0.4 \pm 6$[119]
$FMC: \pi^+, \frac{dn}{dy}_{y\approx 0}$	63.0 ± 1.0	79.0 ± 1.0	$98 \pm 1.0 \pm 6$
$\langle\pi^-\rangle$	$217.5 \pm 0.6 \pm 15$[117]	$275 \pm 0.7 \pm 19$[118]	$322 \pm 3 \pm 16$[119]
$\pi^-, \frac{dn}{dy}_{y\approx 0}$	81.0 ± 0.35[117]	94 ± 0.37[118]	$106.1 \pm 0.4 \pm 6$[119]
$FMC: \pi^-, \frac{dn}{dy}_{y\approx 0}$	81.0 ± 1.0	94 ± 1.0	$106. \pm 0.5$
$\langle\pi^0\rangle$	–	-	-
$\pi^0, \frac{dn}{dy}_{y\approx 0}$	-	-	
$FMC: \pi^0, \frac{dn}{dy}_{y\approx 0}$	76.0 ± 1.0	92.0 ± 1.0	100.0 ± 0.5
$\langle K^+\rangle$	$40.0 \pm 0.8 \pm 2.0$[117]	$55.3 \pm 1.6 \pm 2.8$[118]	$59.1 \pm 1.9 \pm 3$[119]
$K^+, \frac{dn}{dy}_{y\approx 0}$	15.2 ± 0.45[117]	19.4 ± 0.51[118]	$20.1 \pm 0.3 \pm 1$[119]
$FMC: K^+, \frac{dn}{dy}_{y\approx 0}$	15.0 ± 0.5	19.0 ± 0.5	20.0 ± 0.5
$\langle K^-\rangle$	$10.4 \pm 0.12 \pm 0.5$[117]	$16.1 \pm 0.2 \pm 0.8$[118]	$19.2 \pm 0.5 \pm 1.0$[119]
$K^-, \frac{dn}{dy}_{y\approx 0}$	4.80 ± 0.055[117]	6.8 ± 0.15[118]	$7.58 \pm 0.12 \pm 0.4$[119]
$FMC: K^-, \frac{dn}{dy}_{y\approx 0}$	4.0 ± 0.05	7.5 ± 0.5	$8.0 \pm 0.0.5$
$\langle\phi\rangle$	1.91 ± 0.45[117, 120]	1.65 ± 0.17[117, 120].	2.50 ± 0.25[117, 120]
$\phi, \frac{dn}{dy}_{y\approx 0}$	0.0010 ± 0.0005[117, 120]	0.055 ± 0.012[117, 120]	0.07 ± 0.01[117, 120]
$\langle p\rangle, \frac{dn}{dy}_{y\approx 0}$	-	-	-
$p, \frac{dn}{dy}_{y\approx 0}$	-	-	41.3 ± 1.1[121]
$\langle\overline{p}\rangle, \frac{dn}{dy}_{y\approx 0}$	-	-	-
$\overline{p}, \frac{dn}{dy}_{y\approx 0}$	–	–	0.32 ± 0.03[122]
$\langle\Lambda\rangle$	28.0 ± 1.5[123, 120]	$41.9 \pm 2.1 \pm 4.0$[123, 120]	$43.0 \pm 1.9 \pm 3.4$[124]
$\Lambda, \frac{dn}{dy}_{y\approx 0}$	-	16.5 ± 0.2[123, 120]	$14.4 \pm 0.6 \pm 1$[124]
$\langle\overline{\Lambda}\rangle$	0.16 ± 0.03[125]	0.50 ± 0.04[123, 120]	$0.66 \pm 0.04 \pm 0.06$[124, 120]
$\overline{\Lambda}, \frac{dn}{dy}_{y\approx 0}$	-	-	$0.37 \pm 0.04 \pm 0.04$[124, 120]
$\langle\Xi^-\rangle$	1.5 ± 0.13[120]	2.48 ± 0.19[120]	$2.41 \pm 0.15 \pm 0.24$[126, 127, 120]
$\Xi^-, \frac{dn}{dy}_{y\approx 0}$	0.93 ± 0.13[120]	1.17 ± 0.13[120]	1.07 ± 0.06[126, 127, 120]
$FMC: \Xi^-, \frac{dn}{dy}_{y\approx 0}$	0.75 ± 0.10	1.0 ± 0.1	1.2 ± 0.1
$\langle\Omega + \overline{\Omega}\rangle$	-	-	$0.14 \pm 0.03 \pm 0.04$[128]

The final state interactions (FSI) between pairs of non-identical particles provide information about the average relative space-time separation between the emission points of two particle species in the pair rest frame [85]. It is interesting to study the particles which freeze-out in very different conditions, e.g., multistrange baryons Ξ, Ω - which are expected to freeze-out during the early stages of evolution, and pions - which freeze-out at the late stage.

The measurement of inclusive signatures, e.g., K/π ratio, can be effectively extended by studying the femtoscopy correlations of various particle species. If a peculiarity is observed in the momentum space, some unusual behavior should reflect this peculiarity in coordinate space. The low temperature, large μ_B part of the QCD-diagram, is characterized by large baryon density (which may trigger the phase transition). This large density should be reflected in the coordinate space and is potentially observable by femtoscopy studies. The femtoscopy radii can be used to estimate particle densities, as well as to search for completely new effects (see Section 1.7 for more details).

Table 1.3: Two-particle systems which, in principle, can be measured in the NICA energy range.

	π^+	π^-	π^0	K^+	K^-	K^0	p	n	Λ	$\overline{\Lambda}$	Ξ
π^+	+	+	+	+	+	+	+	+	+	+	+
π^-		+	+	+	+	+	+	+	+	+	+
π^0			+	+	+	+	+	+	+	+	+
K^+				+	+	+	+	+	+		
K^-					+	+	+	+	+		
K^0						+	+	+	+		
p							+	+	+		
n								+	+		
Λ									+		
$\overline{\Lambda}$											
Ξ											

1.6 Electromagnetic probes

Electromagnetic probes — virtual (appearing as e^+e^- or $\mu^+\mu^-$ pairs) and real photons — are an important and powerful tool to diagnose the hot and dense matter produced in relativistic heavy-ion collisions. They are sensitive probes of the two fundamental properties that characterize the QGP and are predicted by lattice QCD numerical calculations, the deconfinement transition into quarks and gluons and the restoration of chiral symmetry [129, 130, 131]. Since dileptons and photons interact only electromagnetically, their mean free path is large compared to the size of the system formed in these collisions. They are thus not distorted by final state interactions and once produced can escape unaffected the interaction region, carrying to the detectors information about the conditions and properties of the medium at the time of their creation. Electromagnetic probes are emitted over the entire space-time evolution of the collision, from the primordial nucleon-nucleon collisions in the early stage till the hadron decays well after freeze-out. They are thus very rich in information content but this wealth is also a challenge for the measurement and subsequent analysis that need to disentangle the various sources — virtual or real photons in thermal equilibrium. Such radiation is a direct fingerprint of the matter formed [132, 133]. Two well distinct sources are considered:

a) thermal radiation emitted by the strongly interacting QGP in the early phase of the collision. The elementary processes involved are the quark annihilation into virtual photons ($q\bar{q} \rightarrow l^+l^-$) or the annihilation ($q\bar{q} \rightarrow g\gamma$) and QCD Compton ($qg \rightarrow q\gamma$ or $qg \rightarrow \bar{q}\gamma$) channels producing real photons. The identification of this signal serves as a proof of deconfined phase and also provides a direct measurement of one of the most basic plasma properties, the temperature, readily given by the inverse slope of its expected exponential spectral shape. Theory has singled out dileptons in the mass range $m_{l^+l^-}$ = 1-3 GeV/c^2 [134, 135] or real photons in the p_T range p_T = 1-3 GeV/c [136] as the most appropriate windows to observe the thermal radiation from the Quark-Gluon Plasma phase.

b) thermal radiation is also emitted by the high-density hadron gas in the later phase of the collision. The main elementary process here is the pion annihilation into dileptons, having the shortest life-time and mediated through vector meson dominance by the ρ meson ($\pi^+\pi^- \rightarrow \rho \rightarrow \gamma* \rightarrow l^+l^-$). This component, controlled by the pole at the ρ mass of the pion electromagnetic form factor, contributes primarily to the low-mass region ($m_{l^+l^-} < 1$ GeV/c^2), around and below the ρ mass [136]. It must always be present since ultimately the system ends in the hadronic phase and was readily identified in the enhancement of low-mass dileptons discovered at the SPS in the mid-nineties [137, 138]. The measurement of dileptons is notoriously difficult. There are two main difficulties. The first one is the huge combinatorial background of uncorrelated lepton pairs. It arises from the fact that, since single leptons do not preserve any information about their parent particle, all leptons are paired with all anti-leptons in the same event to form the invariant mass spectrum. This background therefore depends quadratically on the particle multiplicity and strongly increases as the coverage moves to low-p_T leptons. In the measurement of e^+e^- pairs, the combinatorial background mainly comes from π^0 Dalitz decays and conversions. The second difficulty is the physics background. Photons and dileptons can be emitted by a variety of sources and therefore before claiming observation of any new effect, it is mandatory to have a thorough understanding of the expected contribution from all known sources. A lot of gammas is created due to electromagnetic decays of hadrons after the freeze-out. These gammas or leptons carry no information

about excited system and usually should be subtracted ("hadronic cocktail").

Thermal photons

The unambiguous identification of thermal photons from the QGP is a very strong signal of deconfinement and provides a direct measurement of the plasma temperature. The absolute yields, obtained by integrating the emission rate over the space-time evolution of the collision, have been calculated by several authors and considerable progress has been achieved [139, 140, 141]. The results point to rather well established features. At temperatures close to the phase transition, thermal photons from partonic and hadronic processes have similar production rates in close analogy to the behavior of dilepton production rates, perhaps another manifestation of quark-hadron duality. In an elaborate calculation, the transverse momentum range p_T = 1-3 GeV/c appears as the most promising window where the QGP radiation could shine over other contributions in central $Au+Au$ collisions.

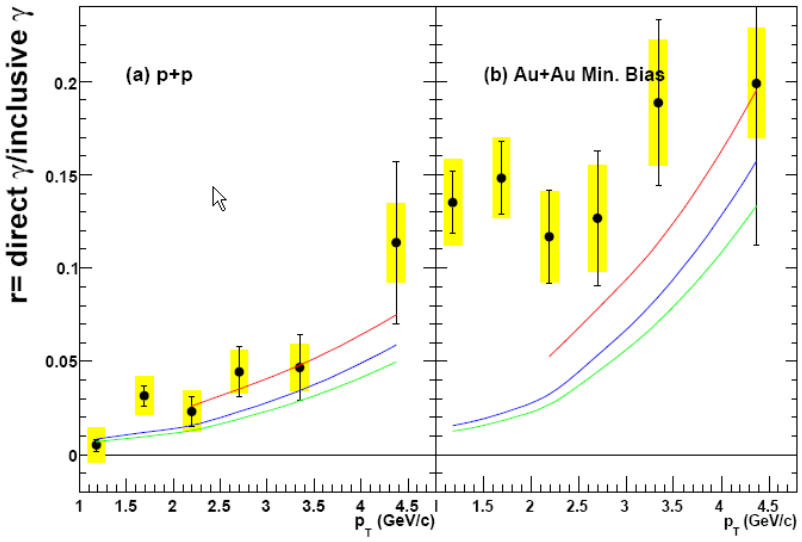

Fig. 1.20: The fraction of the direct photon component as a function of p_T in (a) $p+p$ and (b) $Au+Au$ (min. bias) at $\sqrt{s_{NN}}$ = 200 GeV. The error bars and the error band represent the statistical and systematic uncertainties, respectively. The curves are from a NLO pQCD calculation [142]

The initial measurements of WA80 and CERES with a S beam at 200 AGeV yielded only upper limits of 15% of the total photon yield for any source beyond the known hadron decays. In later measurements, the WA98 experiment observed a photon excess in $Pb+Pb$ collisions at 158 AGeV . An interesting and original analysis has recently been presented by PHENIX at RHIC. The PHENIX experiment at RHIC has measured direct photon production in $p+p$ and $Au+Au$ collisions at 200 GeV over a wide transverse momentum (p_T) range. Figure 1.20 shows the obtained fractions of the virtual direct photon component as a function of p_T in $p+p$ and $Au+Au$ collisions. A clear excess above the NLO pQCD calculation is seen in $Au+Au$ collisions while the result in $p+p$ collisions is consistent with the NLO pQCD calculation.

Dilepton yield

The in-medium spectral functions of short-lived vector mesons which are expected to be sensitive to partial chiral symmetry restoration can be studied in dense nuclear medium via their decay into lepton pairs. Since leptons interact only electromagnetically and hence are very little affected when passing through high-density matter, they provide a penetrating probe of almost undistorted information on conditions in the interior of the collision zone. Spectra of dielectrons from decays of pseudoscalar and vector mesons created in central Au + Au collisions generated by the QGSM code [143] are shown in Fig. 1.21. The experimental task is to reduce the combinatorial background due to gamma conversion, Dalitz decays of pions and eta mesons.

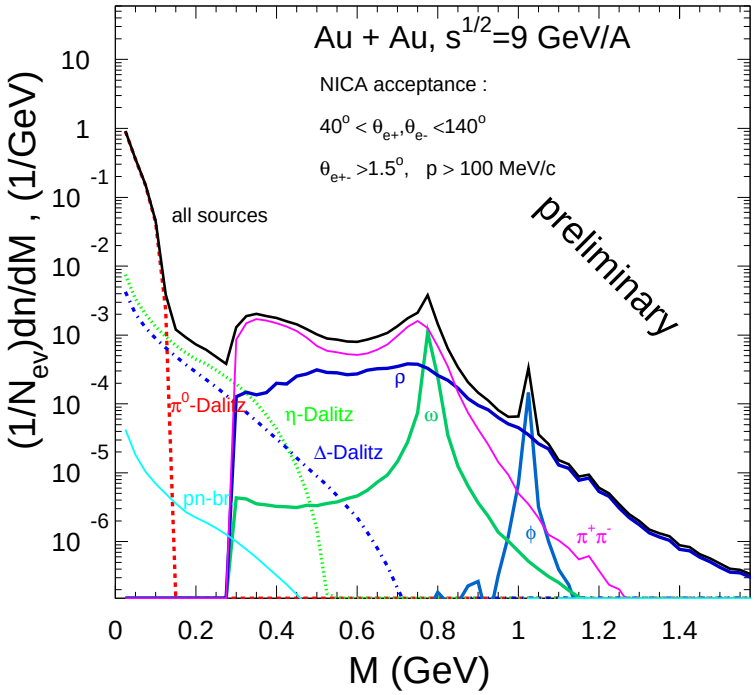

Fig. 1.21: Dielectron spectrum in central Au + Au collisions at $\sqrt{s_{NN}}$ = 9 GeV. Calculations are made by the QGSM code.

Low-mass dileptons in nuclear collisions were measured in three diferent energy ranges: 1-2 AGeV at the DLS (BEVALAC) and HADES (GSI), 40 and 158 AGeV at the CERN SPS as well as $\sqrt{s_{NN}}$ = 200 GeV at RHIC. The three experiments that measured lepton pairs at the CERN SPS in the early nineties, CERES, HELIOS-3 and NA38, reported almost simultaneously an enhanced production of dileptons (either e^+e^- or $\mu^+\mu^-$) in S induced reactions over a very broad invariant mass range from m_{ll} ∼200 MeV up to the J/ψ [144].

Since then an enhancement of low-mass dileptons has been observed at all energies and all systems studied although it is not clear that the enhancement reflects the same physics in all cases.

At the two lower energies, measurements were done by two different experiments at least, with consistent results. At RHIC energies, PHENIX is presently the only experiment capable of measuring low-mass dileptons (Fig. 1.22).

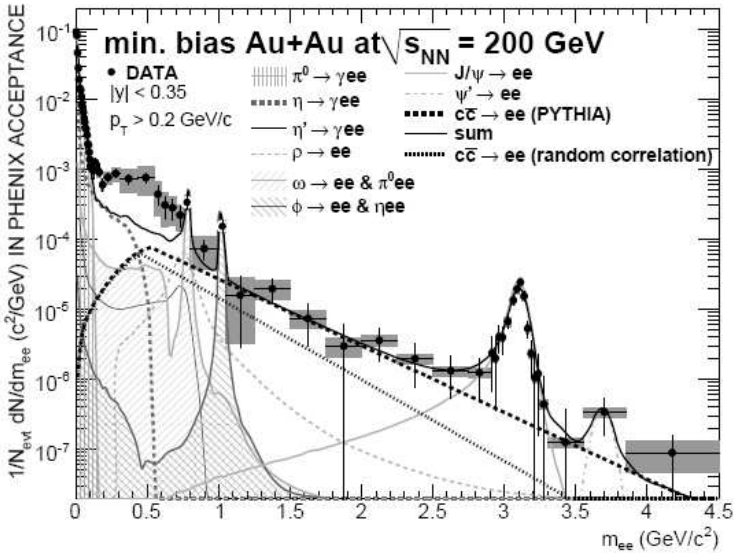

Fig. 1.22: Invariant mass e^+e^- spectrum measured by PHENIX in p $\sqrt{s_{NN}}$ = 200 GeV minimum bias Au + Au collisions at mid-rapidity. The data are compared to the expected yieldsfrom light mesons and semileptonic open charm decays. Statistical (bars) and systematic (boxes) errors are plotted separately [145].

The capability of MPD to study electromagnetic probes is presented in Section 6.3.

1.7 Other studies with MPD

1.7.1 Dense cold matter at NICA

One of the main goals of the experiments on heavy ion beams is to discover and study a new form of QCD matter, the quark-gluon plasma (QGP) [146]. In recent years advances in theory led to a significant complication of the QCD phase diagram, in particular, to the appearance of a critical point [147]. The discovery of critical point at intermediate temperature and density is considered as one of the most important goals of FAIR and NICA projects. The region of low temperature and extreme baryon density is considered as hardly achievable in laboratory conditions, whreas it is probably realized in nature, in neutron stars. At high density and low temperature the first order phase transition and existence of color superconductivity phase [148] are expected. It is hard to achieve this region due to small number of tools to move points over the phase diagram. One can change the initial energy and masses of colliding nuclei, or select the impact parameters to move over a relatively small area determined by small area $T \pm dT(\rho \pm d\rho)$, but not over the whole phase diagram.

The cumulative effect, discovered in the 1970's [149], has been considered as density fluctuations of nuclear matter. Some properties of cumulative processes, such as strangeness increase, are similar to the expected evidence of QGP. However, the association of cumulative processes with QGP seems to be questionable for the following reasons. Firstly, the high densities could only be realized in cumulative processes in the form of short-lived fluctuations, "fluctons", (the term coined by D.I.Blokhintsev [150]). Secondly, particles in such fluctuations can be highly virtual and have large relative momenta. Thirdly, these multinucleon fluctuations are local and and can not be considered as a media (although the existence of plasma droplets is possible [151]). By overcoming these objections we will obtain an effective trigger for extreme dense nuclear matter.

This prospecting experiment will give us the first taste of how to reach phase diagram region of interest by selection of special criteria. In that sense it can be considered as a pilot experiment the results of which can lead to a more extensive experimental program. The garanteed outcome of proposed experimental program will be the study of properties of the practically unknown flucton-flucton interaction.

Basic idea

We propose to create a trigger on a photon (pion, kaon) at midrapidities and maximal transverse momenta by colliding light nuclei (from Helium to Carbon), see Fig.1.23. Due to kinematical limits such trigger selects mainly flucton-flucton (FF) interactions.

We should stress that production of even high cumulative particle is neither necessary nor sufficient condition for selection of dense baryon system. However, such selection increases signal (the flucton-flucton interaction product) to background (the other participants of the ion-ion interaction) ratio by several orders of magnitude. The closer the energy of trigger particle to the maximal one for the colliding nuclei, the lower should be the internal energy of the available secondary baryon system. Therefore, the lifetime of this system will be longer.

This consideration waives the objection of short lifetime and large relative momenta. And, after all, at high density much smaller system size is enough to speak about medium because free path length decreases with the density increase. After realization of the

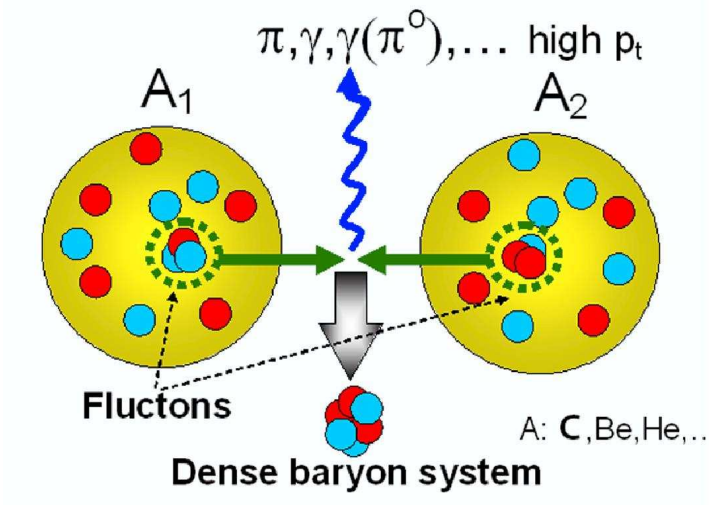

Fig. 1.23: Scheme of the flucton-flucton interaction process

proposed trigger we suggest to proceed with a bright research program focused on the properties of dense multibaryon final state system. The theoretically predicted properties (like, for example, superconductivity [148] or strangeness enhancement [38]) of dense baryon systems should be checked experimentally. The list of these properties will become more specific but it is clear nowadays that isospin system's states, space-time characteristics, search for exotic particles such as dibaryons, strange quark presence in trigger etc. should be studied. In this connection it is important to mention the research programs discussed in mid 80's related to cumulative processes [152]. Some of these proposals (though with modifications) and a list of considerations are the problems of today. The proposed below list of tasks could be divided into the following subsections. The first two points are trigger efficiency check; the next three ones are consequences of different symmetries, restoration; and the last two points are devoted to absolutely new phenomena in dense matter.

Proposed measurement program and general detector requirements

The detector should be equipped with a trigger on flucton-flucton interaction. The possibility to make such effective trigger was experimentally proven in a test made in ITEP on the FLINT (FLuctonINTeraction) experimental setup. The realization is based on registration of high p_t photons in a midrapidity range. The maximum value of cumulativeness magnitude achieved at the first stage of the experiment is $X_1 + X_2 \sim 5$, see Fig.1.24. Here X_1 and X_2 are the nucleon minimal numbers of projectile and target, respectively.

In general, pion, kaon or ϕ-meson trigger is possible. Detector subsystems for different program tasks are listed in Table 1.4.

1. *clusterization*

   One of the expected effect is baryon clusterization in the momentum space. If the lightest nuclei are colliding and most of the nucleons are involved in fluctons, then the relative momentum distribution of participanting baryons should be narrower than the total pair momentum distribution of a baryon pair.

   For heavier nuclei, e.g. CC, a bend should be seen in the relative momentum spectrum. This bend separates baryon pairs participating in the dense and cold

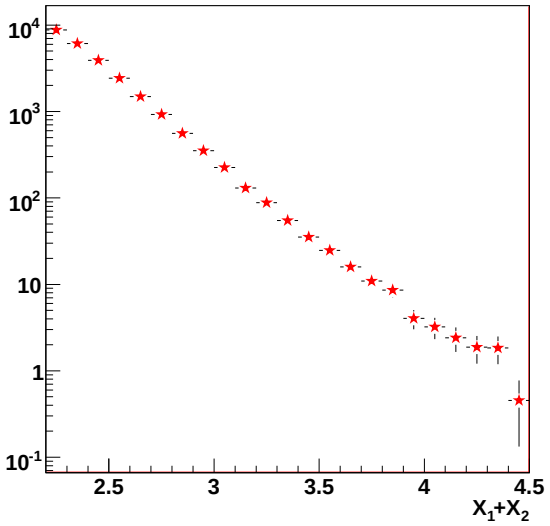

Fig. 1.24: Photon spectrum vs $X_1 + X_2$.

baryon system from other pairs, similarly to the bend in the spectra of nucleons, in which regions of spectators and participants are seen. The spectators of colliding nuclei (those for which clusterization is trivial) should be excluded from this analysis. Cluster position in the momentum space is model dependent.

The cluster is expected to be in the midrapidities range. Thus, one should identify and measure baryon momenta at $y \sim 0 \;\; 0 < p_t < p_{trig}$.

2. *femtoscopy*

   The second consequence expected is clusterisation of baryons in the coordinate space and the increase of the cluster existence time in comparison with the emission time of the particles which are not in cluster. These consequences could be experimentally tested using the correlation method (femtoscopy). The differences in π, K, ϕ, γ correlation functions allow us to look at the quark matter evolution in a new way. Femtoscopy measurement in the proposed studies is needed to control the density and lifetime of the formed baryonic system. Dividing secondary baryons into participants of the dense cluster formed in flucton-flucton interaction (N_c) and other participants (N_p) (spectators are out of consideration), one can expect hierarchy of sizes $r(Nc1, Nc2) < r(Np, Np) < r(Nc, Np)$.

3. *isotopic symmetry*

   In dense fermions, a rich system with broken symmetries should tend to restore. In particular, ratios of cross sections of production of particles-components of the same isomultiplet, should be close to unit [153]. This conclusion is trivial for isosymmetric nuclei, but becomes non-trivial for $He^3 + He^3$ collisions and for an asymmetric trigger (e.g. charged pion or kaon). Therefore, the detector should be able to measure $p/n, \pi^+/\pi^-$ ratios.

4. *strangeless*

Another broken symmetry (SU(3)) should also tend to restore in high baryon density conditions. This could cause the equalization of producing different components of the baryon octet. However, increase in production c.s., e.g. Λ-baryons, should be accompanied by increased production of additional kaons (strangeness conservation) . At colliding nuclei energies of several GeV/nucleon the energy deficit could be regulated by varying the minimal target mass (cumulative number) [154]. Strange particle production is more probable than that of the not strange one at the same kinematical conditions (the same cumulative number). The case in which the additional kaon brings the cumulative number to a value exceeding the sum of colliding nuclei masses, is of special interest. In such case Λ production is only possible if light pentaquarks e.g. $(qqqq\bar{s})$ or (and) dibaryons $(qqqqqq\bar{s})$ exist. Strangeness increase is considered as one of the signatures of quark-gluon plasma onset due to the processes like $gg \to s\bar{s}$ [38]. The vertex of weak decay identification plays an important role by strange baryons (Λ, Ξ^-) registration. The typical distance between the primary vertex and the decay point is $\sim$ 1cm. This specifies the requirements to the vertex detector. For Σ^0 identification (Σ^0 and Λ separation) one needs to identify the photon. Σ^- identification requires neutron identification, and Σ^+ requires identification of neutral pions.

5. *vector mesons*

   An increased production of resonances and high spin particles is expected in cumulative processes. In particular, the vector- to scalar- mesons ratio should increase with cumulative number (the effect was predicted by A.M. Baldin) [155].

6. *exotic*

   As a consequence of the the requirements of the Pauli principle, the role of exotic states is expected to be increased in the dense fermionic medium conditions. In particular, diquark medium will favour the dibaryonic resonances production. Light pentaquarks like (4qs) or dibaryons like (7qs) must decay into nucleons and photons.

7. *multifermion correlations*

   Multiboson and multifermion effects could appear in dense medium. [156]

Counting rates estimate

The trigger rate (see Tab. 1.5) was estimated from the experimental data accumulated by the FLINT collaboration in ITEP assuming 4π detector geometry at a luminosity of about $10^{30} cm^{-2} s^{-1}$.

The estimated size of data sample size needed to measure the source size (femtoscopy) with the statistical errors less than 10% is $\sim 2 \cdot 10^3$ events.

1.7.2 Strange multibaryon states

Observation of strange multi-baryonic clusters is an exiting possibility to explore the properties of cold dense baryonic matter and non-perturbative QCD [157, 158, 159, 160, 161, 162, 163, 164, 165, 166, 167, 168, 169].

The experimental data from heavy ion collisions show that the K^+/π^+ ratio ([168, 169]) is larger at BNL−AGS energies than at the highest CERN−SPS energies

Table 1.4: Detector subsystems for different program tasks (++) nessesary, (+) disarable

	ECAL	Vertex	Tracking	TOF	Neutron
Trigger	++				
Cluster	++		++	++	+
Femto	++		++	++	+
IsoSym	++	+	++	++	++
Strange	++	++	++	++	+
Vector	++	+	++	++	
Exotics	++	+	++	++	+
Multy	++	+	++	++	+

Table 1.5: Expected number of accumulated events as a function of baryonic content for a 106-sec run

$X_1 + X_2$	5	6	7
NICA	10^5(CC); 10^4(HeHe)	$3 \cdot 10^3$(CC); $3 \cdot 10^2$(HeHe)	10^2(CC); 10(HeHe)
RHIC	10^3(CC); 10^2(HeHe)	30 (CC)	

and even those at RHIC. The experimental Λ/π^+ ratio in the pC reaction is approximately two times larger than this ratio in pp reactions or in pC reactions within the FRITIOF model at the same energy [170]. However, there are no sufficient experimental data on strange hyperon production in hadron−nucleus and nucleus-nucleus collisions over the 4−50 GeV/c momentum range.

Recently, the existence of discrete nuclear bound states of $\overline{K}^0$p has been predicted within the phenomenological Kaonic Nuclear Cluster (KNC) model based on the experimental information on the $\overline{K}^0$N scattering lengths, kaonic hydrogen atom, and the $\Lambda^*(1405)$ resonance[162, 163, 164, 165].

Although such states were predicted by Wycech [166] some time ago, only recently the availability of experimental facilities (KEK [164, 165, 171], DISTO [172], FOPI [173], DAFNE [174, 175], and OBELIX [176], in particular for studying these kind of exotic nuclei, has delivered first experimental results which triggered a vivid discussion and project of AMADEUS [177].

As was shown [178], the strangeness production in antiproton annihilation on nuclei and on hydrogen are related to the possible quark-gluon plasma formation in hadronic matter.

Following [168, 169], we assume that the above experimental fact is due to the formation of a 'blob' of QGP.

Experimental evidence for exotic dibaryons in the (Λp) system first came from the observation of S = -1 narrow resonances by the propane bubble chamber method [179, 180, 170] at the beam momenta of 7 GeV/c [181], [182] and 10 GeV/c [183, 184], respectively.

According to A. Gal [167], the issue of $\overline{K}^0$ nuclear states is yet far from being experimentally resolved and more dedicated, systematic search is necessary

1.7.3 (Λ, π^+) and (Λ, p) spectra

(Λ, π^+)spectra The $\Lambda\pi^+$ effective mass distribution for all 19534 combinations with a bin size of 17 MeV/c^2 at 10 GeV/c is shown in Fig.1.25, a) [182, 183, 184, 185, 186, 187, 188]. The bin size is consistent with the experimental resolution. The upper dashed curve (Fig.1.25, a) is the sum of the background and 1 Breit-Wigner function. The background (lower dashed curve) is the 8th-order polynomial function. The dashed histogram in the figures is the background simulated by the FRITIOF model. The mass resolution is $\Delta M/M = 0.7\%$, the decay width is $\Gamma \approx 45$ MeV/c^2. The cross section of $\Sigma^{*+}(1382)$ production is approximately 1.1 mb (600 events in the peak, 13σ) for the p+C interaction, which is 1.5 times larger than the estimated cross section. This observed resonance $\Sigma^{*+}(1382) \to \Lambda\pi^+$ was a good test of this method. The geometrical efficiency for the hyperon decays results in an overall detection probability of 25 % for Λ and $\Sigma^{*+}(1382)$ hyperons.

Figure 1.25, b) shows the same $\Lambda\pi^+$ spectrum for 14102 combinations with the geometrical acceptance of MPD(TPC) detector[189] and 16 MeV/c^2 bin size at a momentum of $\sqrt{s}$=4.4 GeV/c for p+C reactions. The dashed curve is the sum of the eight-order polynomial and 1 Breit-Wigner functions (350 events in the peak, 7.2σ). The geometrical efficiency for the hyperon decays results in an overall detection probability of 19 % for Λ and 15.0 % for $\Sigma^{*+}(1382)$ hyperons. These acceptance values already contain the decay branching ratios too.

(Λ, p) spectra In the are published reports [182, 183, 184, 185, 186, 187, 188] the (Λp) invariant mass with identified protons is given for the momentum range of $0.350 < P_p < 0.900$ GeV/c. The solid curve is the sum of the background obtained by the polynomial method and 4 Breit-Wigner resonance(BW) curves (Fig.1.26, *a*). There are significant enhancements in the mass regions of 2100($6.9\ \sigma$), 2175($4.9\ \sigma$), and 2285(3.8σ)MeV/c^2. There are also small peaks at masses of 2225(2.2σ) and 2353(2.9σ) MeV/c^2.

Figure 1.26, b) shows the invariant mass of 4669(Λp) combinations with a bin size of 14 MeV/c^2 for stopped protons in the momentum range of $0.14 < P_p < 0.30$ GeV/c. The dashed curve is the sum of the eight-order polynomial and 4 Breit-Wigner curves with $\chi^2 = 30/25$ from fits. There are significant enhancements in the mass regions of 2100($5.7\ \sigma$), 2150(5.7σ), 2220(6.1σ), 2310(3.7σ), and 2380(3.5σ)MeV/c^2. The significant peak in the mass range of 2220 MeV/c^2 (6.1σ), B_K 120 MeV is conformed by the KNC model prediction [162] in the $K^- pp \to \Lambda p$ channel.

The Λp effective mass distribution for 4523 combinations with relativistic protons over a momentum range of P > 1.5 GeV/c is shown in Figure 1.27, a), where the events with the undivided (ΛK_s^0) are removed. The solid curve is the 6-order polynomial function(χ^2/n.d.f = 271/126). The background for the analysis of the experimental data is based on the FRITIOF and the polynomial method. There are significant enhancements in the mass regions of 2150(4.4σ), 2210(3.8σ), 2270($3.4\ \sigma$), 2670 (3.1σ), and 2900(3.1σ) MeV/c^2. The observed peaks for the combinations with relativistic P > 1.5 GeV/c protons agree with the peaks for the combination with the identified protons ($0.350 < P_p < 0.900$ /c) and with stopped protons $0.14 < P_p < 0.30$ /c.

Figure 1.27, b) shows the Λp spectrum for 1421 combinations over the momentum range of $0.350 < P_p < 0.900$ GeV/c with the geometrical acceptance of MPD(TPC) detector [189] at a momentum of $\sqrt{s}$=4.4 GeV/c for p+C reactions. Then there is only one peak at the mass of 2165 MeV/c^2(4.5σ).

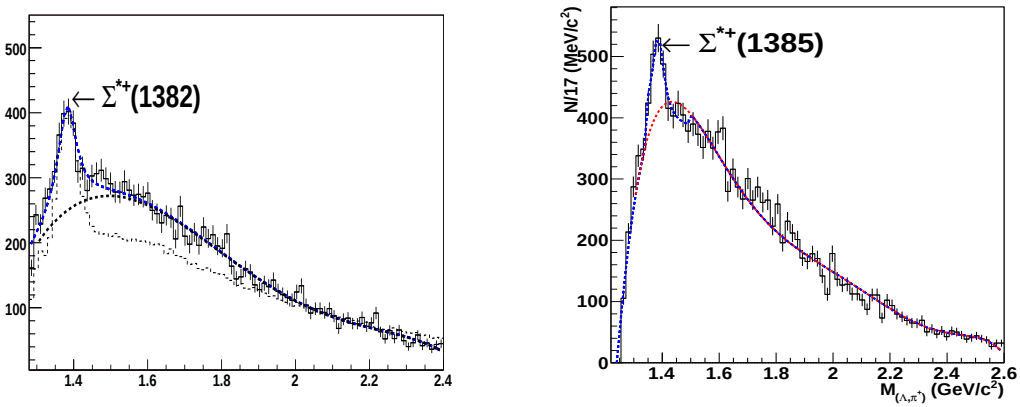

Fig. 1.25: a)The $\Lambda\pi^+$ - spectrum for all combinations with bin size of 12 MeV/c^2 b) $\Lambda\pi^+$ - spectrum in acceptance for MPD with bin size of 17 MeV/c^2. The dashed curve is the experimental background by polynomial function.

Figure 1.27, c) shows Λp spectrum for 14102 combinations with relativistic protons over the momentum range of $P_p > 1.5$ GeV/c with the geometrical acceptance for MPD(TPC) detector [189] at momentum of $\sqrt{s}$=4.4 GeV/c for p+C reactions, where the events with the undivided (ΛK_s^0) are incuded. Then there are significant enhancements in the mass range of 2145 and 2270 MeV/c^2(4.5σ). Therefore, the MPD(TPC) acceptance allows us to observe significant signals in the mass range of $M_{\Lambda p}$ >2130 MeV/c^2 at a momentum range of $P_p > 0.35$ GeV/c.

Proposal

A number of important peculiarities were observed in the effective mass spectrum of exotic states with the decay modes [184, 185, 186, 187, 188] $(\Lambda, \pi^{\pm})$,(Λ, γ), (Λ, π^+, π^-), (Λ, p), (Λ, p, p), (Λ, Λ), (Λ, p, π^-), (Λ, K_s^0), $(K_s^0\pi^{\pm})$ and $(K_s^0 p)$. The observed well-known resonances Σ^0, $\Sigma^{*+}(1385)$ and $K^{*\pm}(892)$ from PDG are good tests of this method. There are enhancement signals from all observed hyperons.

The search for and study of exotic strange multibaryon states with Λ and K_s^0 s subsystems at MPD(NICA, JINR), CBM(FAIR, GSI), p07(JPARC, KEK), OBELIX(CERN) and AMADEUS(DAFNE, INFN) can provide information on their nature and properties and will be a test for the observed PBC data. Higher statistics experiments with the mass resolution ≈1% are needed.

1.7.4 Diphoton production

The two-photon decay of light mesons represents an important source of information. In particular, the $\gamma\gamma$ decay of light scalar mesons was considered as a possible tool to deduce their nature. Also the scalar-isoscalar sector is question at issue presently, since more states are known (including possible glueball candidates) than can be fitted into a single multiplet. Unfortunately, the existing experimental information from $\pi\pi$ scattering has many conflicting data sets at intermediate energies and no data at all close to the interesting threshold region. For many years this fact has made it very hard to obtained conclusive results on $\pi\pi$ scattering at low energies or in the sigma region. Interest in the

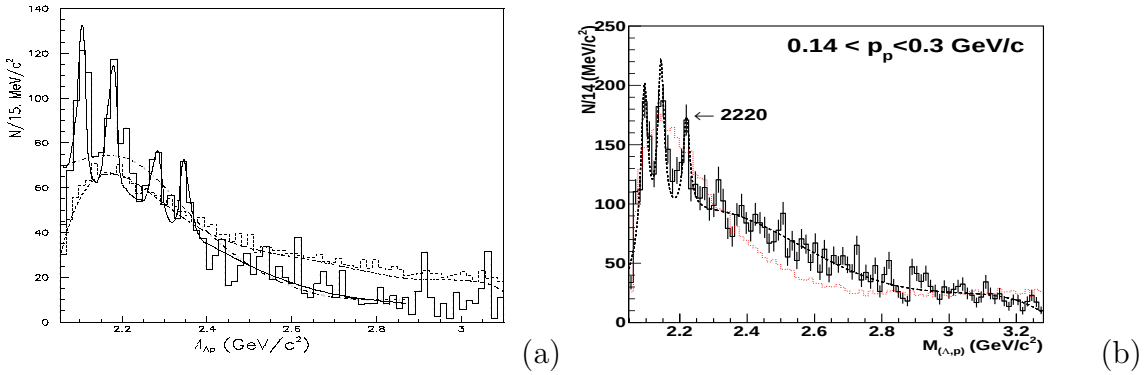

Fig. 1.26: (a) (a) the Λp spectrum with identified protons in the momentum range of 0.35< P_p <0.90 GeV/c;(b) the Λp spectrum with stopped protons in the momentum range of 0.14 < P_p *<0.3 GeV/c. The dashed histogram is events simulated by FRITIOF.*

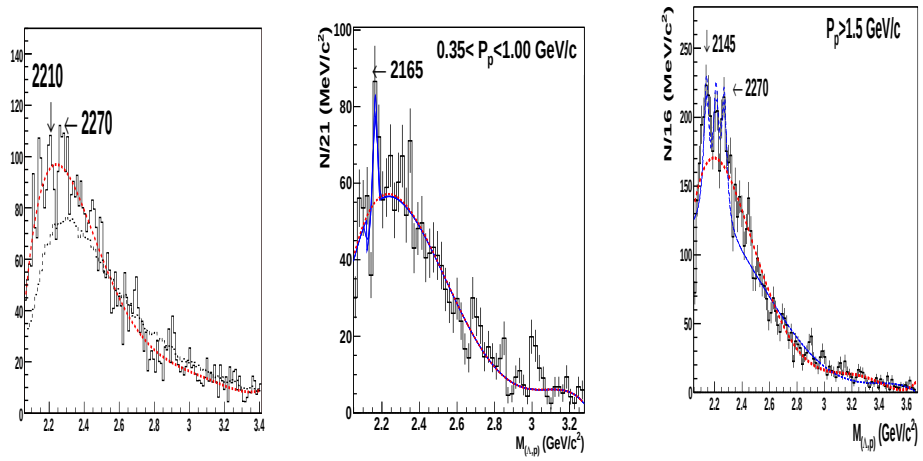

Fig. 1.27: (a)Λp spectrum for relativistic protons over momentum P_p >1.5 GeV/c with bin size of 11 MeV/c^2.(b) the Λp spectrum with identified protons in the momentum range of 0.35< P_p <0.90 GeV/c for MPD acceptance.(c)Λp spectrum with relativistic protons over momentum P_p > 1.5 GeV/c for MPD acceptance. The dashed histogram is simulation by FRITIOF.

investigation of the photon pair production is bound up with set of problem:

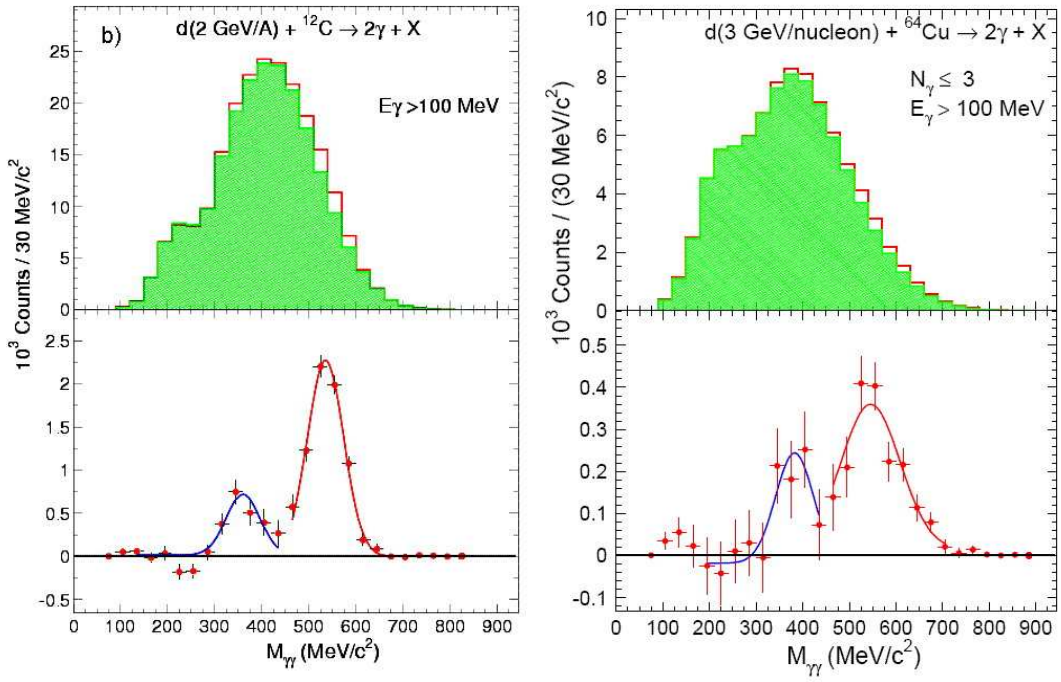

Fig. 1.28: Invariant mass distributions of $\gamma\gamma$ pairs without (upper panels) and with (bottom panels) the background subtraction. The left and right figures are obtained for the dC- and dCu-interactions at 2.75 GeV/c and 3.83 GeV/c per nucleon respectively. The curves are the Gaussian approximation of experimental points.

1. To clarify of the nature and further investigations of the resonance observed in the invariant mass spectrum of $\gamma\gamma$-pairs in dC-interactions at 2.75 GeV/c per nucleon and dCu-interactions at 3.83 GeV/c per nucleon (see Fig.1.28) [190]. The collider NICA allows to scan energy and mass dependencies of the resonance production in ion collisions.

2. To search for some features in the invariant mass spectrum of $\gamma\gamma$-pairs in the interval of 270-750 MeV bounding up with the chiral symmetry restoration [2, 3].

3. Due to the strangeness ($s\overline{s}$) in η-mesons, comparison η and π^0-productions allows to clarify the mesons production mechanism. The indication on the difference between the π^0- and η-mesons production mechanisms was obtained from the comparison of the mesons spectra in the near-threshold region [191, 192, 193, 194].

4. Investigations of π^0-mesons is interest in view of the NICA possibilities. The scan of the π^0 spectra in the nuclear-nuclear collision allows to detect signals of the π-condensate state: the pion vacuum breaking at the strong QCD field in dense nuclear matter.

Chapter 2

MPD Concept

2.1 General Design

The design concept of a detector which would be capable to exploit the broad physics potential of the high luminosity NICA collider is a challenging task. The detector to explore phase diagram of strongly interacting matter in a high track multiplicity environment has to cover a large phase space, be functional at high interaction rates and comprise high efficiency and excellent particle identification capabilities. It must also be based on the recent detector developments in order to meet the ambitious physics requirements, and to be of comparatively reasonable cost. None of the existing and planned so far experimental facilities can fulfill all these demands. The MPD detector concept matching these requirements is shown in Fig. 2.1. It comprises the central detector (CD) and two forward spectrometers FS-A and FS-B (optional) situated along the beam line symmetrically with respect to the centre of MPD. The detector design parameters follow from several technical constrains and guided by good detector performances versus a reasonable budget compromise. The MPD length along the beam axis is limited by a 800 cm gap between the collider optics elements. The diameter of 4 m is chosen as a compromise between the time of flight requirements to length of tracks to be sufficient for good particle identification and track reconstruction precision on one hand, and the needs in homogeneous magnetic field and reasonable cost of the magnet on the other hand. The chosen dimensions of the CD are presened in Fig.2.2.

The CD consits of a barrel part and two endcaps located inside the magnetic field. The barrel part is a shell-like set of various detector systems surrounding the interaction point and aimed to reconstruct and identify both charged and neutral particles in the pseudorapidity region of $|\eta| \leq 1.2$. The endcaps are aimed for precise tracking over pseudorapidity range ($1.2 < |\eta| < 2$). Two forward magnet spectrometers (FS-A and FS-B) which are considered as an option situated on both sides of MPD barrel and cover the pseudorapiduty region from 2.0 to 3.0 (detailed overview of MPD pseudorapidity coverage is shown in Fig. 2.3).

The ion beams pass through the whole detector inside the beam pipe located along the z axis with the central interaction point at $z = 0$ in the centre of the detector. The interaction region covers an interval of $|z| \leq 25$ cm.

The barrel part shown in Fig.2.2 consists of tracker and particle identification system. The principal tracker is the time projection chamber (TPC) supplemented by the inner tracker (IT) surrounding the interaction region. Both subdetectors (IT and TPC) has to provide precise track finding, momentum determination, vertex reconstruction and pattern recognition.

The inner tracker is a silicon strip detector (as a baseline) representing a barrel of double sided position sensitive layers around the interaction region. The energy loss (dE/dx) measurements in the TPC gas will give us an additional capability for particle

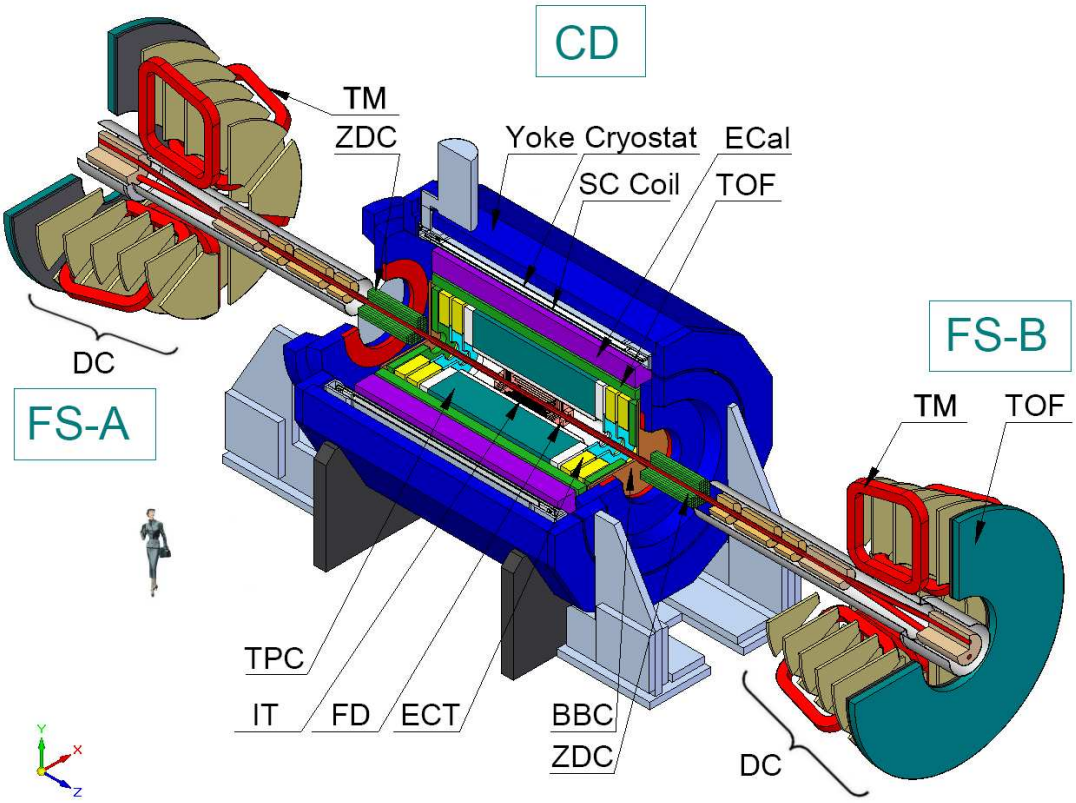

Fig. 2.1: General view of the MPD detector with end doors retracted for access to the inner detector components. The detector is represented by three major parts: CD-central parts, and (FS-A, FS-B) - two forward spectrometers (optional). The subsystems are indicated: superconductor solenoid (SC Coil) and magnet yoke, inner detector (IT), straw-tube tracker (ECT), time-projection chamber (TPC), time-of-flight stop counters (TOF), electromagnetic calorimeter (EMC), fast forward detectors (FFD), beam-beam counter (BBC), and zero degree calorimeter (ZDC).

identification in low momentum region.

The high performance time-of-flight (TOF) system must be able to identify charged hadrons and nuclear clusters in the broad rapidity range and up to total momentum of 2 GeV/c. The fast forward detectors (FD) will provide the TOF system with the start signal.

The main goal of electromagnetic calorimeter (EMC) is to identify electrons, photons and measure their energy with high precision. High granularity of the EMC together with excellent energy resolution and good timing performances will enhance the overall efficiency and particle identification capabilities of the MPD detector. The layout of the EMC is shown in fig 1.2 Two possible options of the EMC are considered: the first one is based on the crystals and the other one is a “shashlyk” type calorimetr.

Two ECTs are located on both sides of the TPC along the z axis. The current design includes wheel-like tracking detectors based on straw tubes supplemented by two cathode pad chambers (CPC). The ECT is designed to provide tracking information for particles travelling at small radii and for which the TPC has poor reconstruction ability. Thus a supplementary principle is exploited for tracking of the charged particles in the

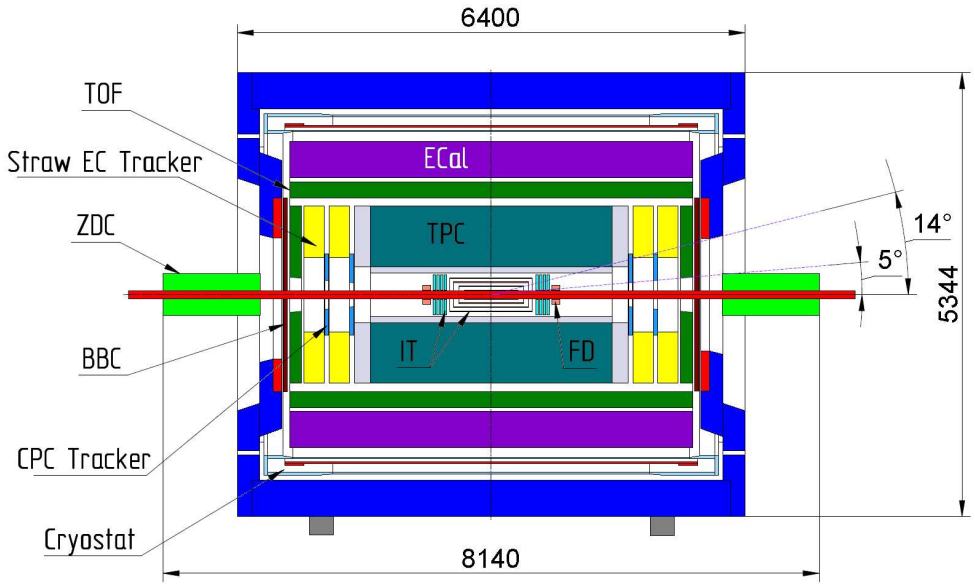

Fig. 2.2: Cutaway side view of the Central Detector of MPD with based dimensions.

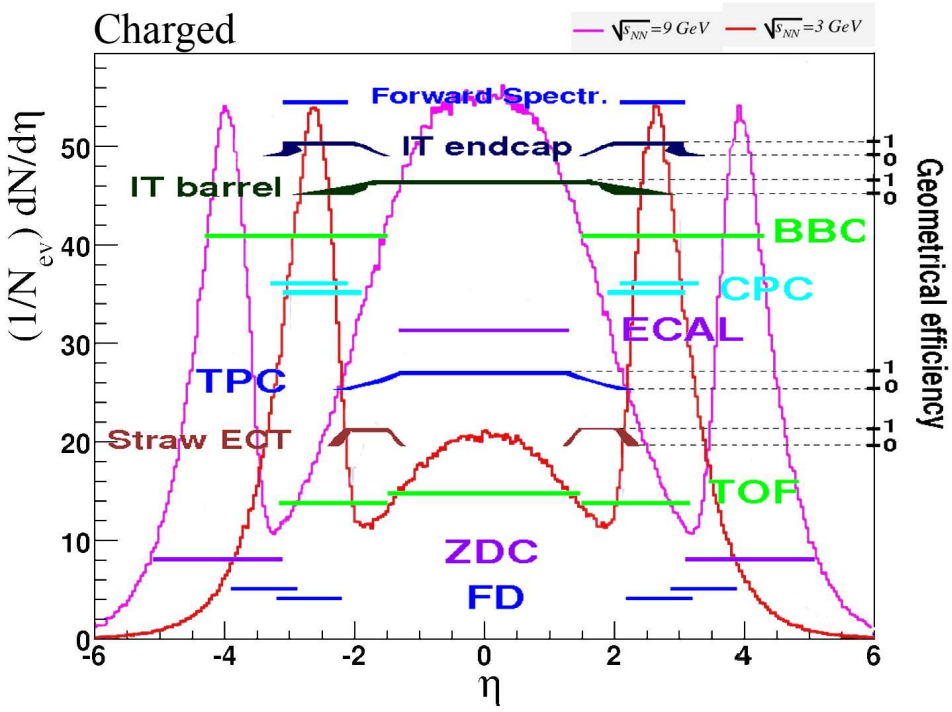

Fig. 2.3: MPD pseudorapidity coverage.

pseudorapidity range up to $\eta = 2.0$. It allows a precise definition of an azimuthal angle for charged tracks and momentum reconstruction with a sufficient precision. Particles emitted in very forward/backward directions are detected by fast forward detectors (FD), beam-beam counters (BBC) and zero degree calorimeters (ZDC). They are used for trigger definition, centrality determination and reconstruction of the position of the interaction

point.

In the proposed detector composition one may define three regions connected with capability of observables measurement; the central part $|\eta| < 1.2$, forward part $1.2 < |\eta| < 2$ and region of pure momentum reconstruction $2 < |\eta| < 3$ (Fig. 2.4).

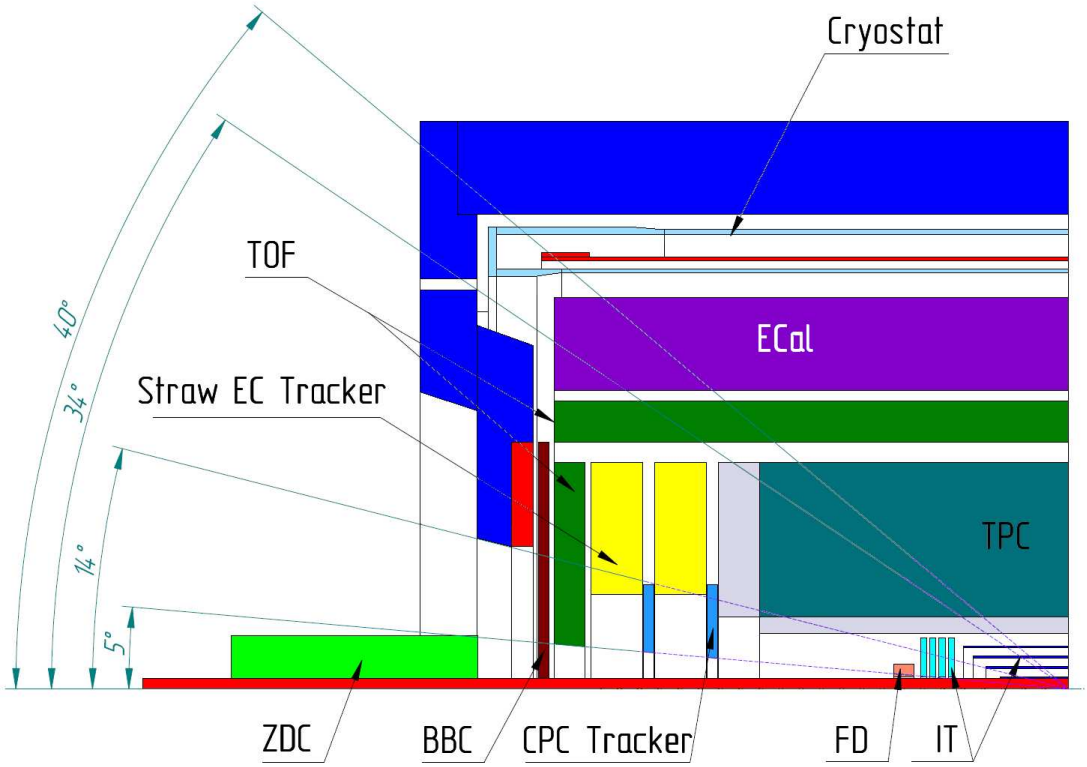

Fig. 2.4: Cutaway of quarter of the MPD. Three regions of pseudorapidity are defined: $|\eta| < 1.2$ *is covered by inner tracker, TPC, TOF barrel and Ecal, the region* $1.2 < |\eta| < 2.0$ *– partly TPC, Straw ECT, TOF; in the region* $2 < |\eta| < 3$ *we have Si discs, CPC tracker and TOF; ZDC, FD, BBC extend over region* $|\eta| < 3$.

The FS-A and FS-B are considered as optional because the necessity of their construction will be decided at the latest stage depending on the physics requirements and reached CD performance.

2.2 Magnet of MPD

The magnet of MPD (See Fig.2.1) is intended to provide a homogeneous magnetic field of 0.5 T in its aperture. It has to ensure the required resolution for transverse momenta over the range 0.1-3 GeV/c. The magnet will be designed as a superconducting solenoid with a flux return iron yoke. Diameter of the aperture of this magnet is 4 m, the distance between pole tips is 5.24 m and the magnet weight is 440 ton. The field inhomogeneity in the tracker area of the detector is about 0.1%.

As it follows from Table 2.1, where parameters of the similar magnet systems are listed, the magnet system of MultiPurpose Detector cannot be considered as unique equipment with regard to technical characteristics. Nevertheless, the design and construction of such a magnet system is connected with some technical problems because of required low level of field inhomogeneity in the tracker area, high weight and large overall dimensions of the system.

Table 2.1: Comparison of solenoids similar to the MPD solenoid

	DELPHI [195] (CERN)	ALEPH [196] (CERN)	BABAR [197] (SLAC)	CDF [198] (Fermilab)	MPD (JINR)
Year completed	1988	1986	1997	1984	2014
Central field, T	1.2	1.5	1.5	1.5	0.5
Field inhomogeneity in the tracker area, %	0.1	0.4	2	1	0.1
Stored energy, MJ	110	137	25	30	7.8
Total Amp.Turns, MA	7.6	8.56	5.12	5.75	2.19
Current density, A/mm^2	46.3	40	47	64	65
Current, kA	5.0	5.0	4.6	5.0	1.36
Aluminum stabilized conductor cross section, mm^2	4.5×24	3.6×35	4.9×20	3.89×20	3×7
Inner bore, m	5.2	4.96	2.8	2.86	4
Coil length, m	6.8	7	3.46	5	5.3
Yoke incircle outer diameter, m		9.36	5.84	9.5	5.34
Yoke length, m		10.6	6	7	6.4
Total magnet weight, t		2640	580	2000	440
Cold mass, kg		25000	4900	5570	4100
Thermal load at 4.5 K, W	150 W +1.25 g/sec	100 W +1.25 g/sec	52	35	30 W +0.156 g/sec

2.2.1 Requirements and Constraints for the Solenoid

The issues related to the detector magnet integration and services are discussed in the Chapter 4.1. The MPD layout is shown in Fig. 2.1. The inner dimensions of the solenoid cryostat and its length are defined by the arrangement of the central detectors (TPC, TOF, Straw EC Tracker, BBC, EMC). The solenoid forms the reference frame for all the detectors placed inside. This picture specifies the magnet volumes necessary to allow safe location of all detectors inside the magnet without interference with the detectors that it supports.

As it can be seen from the picture, all detectors of the MPD are placed inside the solenoid coil. Thus the requirement of the cryostat radiation transparency is not established.

The main requirements for the solenoid in respect to the detector systems are:

- Rated value of the axial component of magnetic field in the area of the tracker is 0.5 T.
- Homogeneity of the radial components of the magnetic field induction is defined by integrals of a result obtained by dividing radial component by axial component in the volume of Charged Particle Tracker (TPC). These field requirements are summarized in Table 2.2.
- The stray field outside the barrel part of the yoke: < 5 mT.

Due to the symmetry of the magnet, the azimuthal component of magnetic induction is negligible.

Table 2.2: Homogeneity over a cylindrical layer of TPC

Radial magnetic field component $z \geqslant 0$, $z_{max} = +1500\ mm$ $350\ mm < r < 1100\ mm$	$Int = \int_{z}^{z_{max}} \frac{B_r}{B_z}\ dz$	$\lvert Int \rvert < 0.775\ mm$
Radial magnetic field component $z \leqslant 0$, $z_{min} = -1500\ mm$ $350\ mm < r < 1100\ mm$	$Int = \int_{z}^{z_{min}} \frac{B_r}{B_z}\ dz$	$\lvert Int \rvert < 0.775\ mm$

There are some additional requirements:

- The iron yoke should hold the cryostat weight.
- The frame of Electromagnetic Calorimeter (EMC) and other inner detectors must be fixated on the iron yoke.
- The superconducting solenoid must be assembled at the first place to provide support of all inner detectors.
- The unbalanced axial forces applied to the coil should be transmitted to an iron yoke support ring.

- The solenoid has to be mounted on a movable rail-guided carriage to be transported from the assembly area to its operational position.

2.2.2 Superconducting Solenoid

Solenoid Concept

The MPD solenoid is a magnet with a thin superconducting NbTi winding and flux return yoke, as shown in Fig. 2.5.

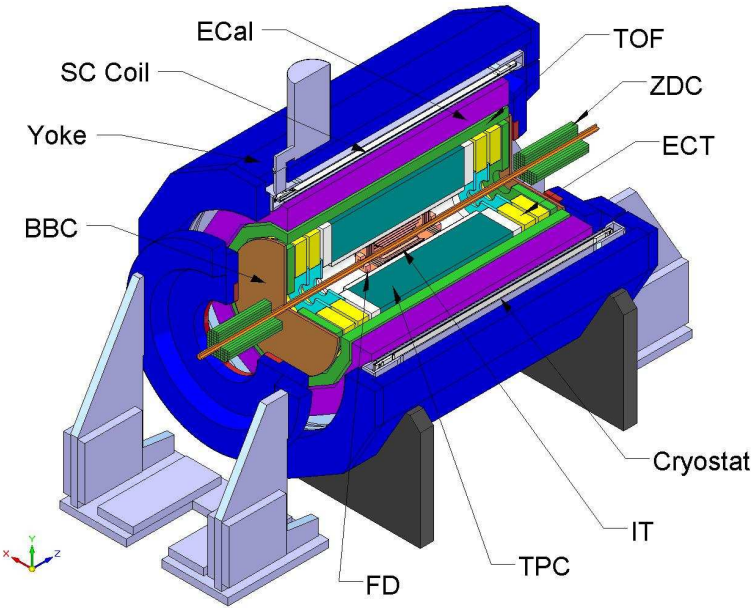

Fig. 2.5: 3D view of the MPD solenoid with the withdrawn pole

The flux return yoke of the magnet consists of a dodecahedral barrel and two end caps. The yoke design is similar to the STAR magnet yoke design [199] - two supporting rings secure structural magnet stiffness. The rings control the azimuth and radial location of each flux return bar and provide minimal deflections in the magnet structure under action of gravity and magnetic forces which is required for magnetic field quality. The weight of the cryostat and inner detectors is being transmitted to the supporting rings. Two end caps installed within the supporting rings form the magnet poles. Both end caps with pole tips and trim coils can be promptly withdrawn in axial direction to provide access to the detectors.

In spite of some economic benefits of water cooled winding for the MPD magnet, because of variety of reasons a superconducting technology has been chosen. The coil design is based on an aluminium stabilized, indirectly cooled superconductor cable internally wound in an aluminium alloy mandrel to support the magnetic hoop stresses. The technology of internal winding of aluminium stabilized conductor has been chosen and successfully tested for many spectrometer solenoids from CELLO in the early 80s to ATLAS and CMS at LHC today [200]. Internal winding and indirect cooling simplify the cryostat design and minimize the amount of liquid helium in it and ipso facto the overpressure hazard for the cryostat is eliminated. Two correcting coils with higher linear current density at each end of the SC coil are to compensate the gap between the coil

and end caps (supporting rings) of the yoke and to suppress the radial component of the magnetic field in the tracker area.

The absence of requirement on the radiation transparency allows using a conservative coil design and inexpensive stainless steel cryostat. Furthermore, we don't need to minimize material of the support cylinder and of the vacuum vessel.

The cold mass of the cryostat is supported by 6 axial ties and 2×12 radial struts.

Aluminium stabilized conductor gives high stability against quenches due to the large electrical conductivity of aluminium at low temperature. It is able to withstand large thermal perturbations (energy releases) before a normal conducting zone starts to spread. Thermal stresses after a quench are much even in such kind of windings and potentially are not so dangerous for the magnet.

Combination of pole tip trim coils and shaping the pole tip enables attainment of high TPC field homogeneity, $\int_{z}^{z_{max}} \frac{B_r}{B_z}\, dz \approx 0.3\ mm$.

Fig. 2.6 shows the longitudinal cross-section of the MPD superconducting solenoid. The main dimensions of the magnet are summarized in Table 2.3.

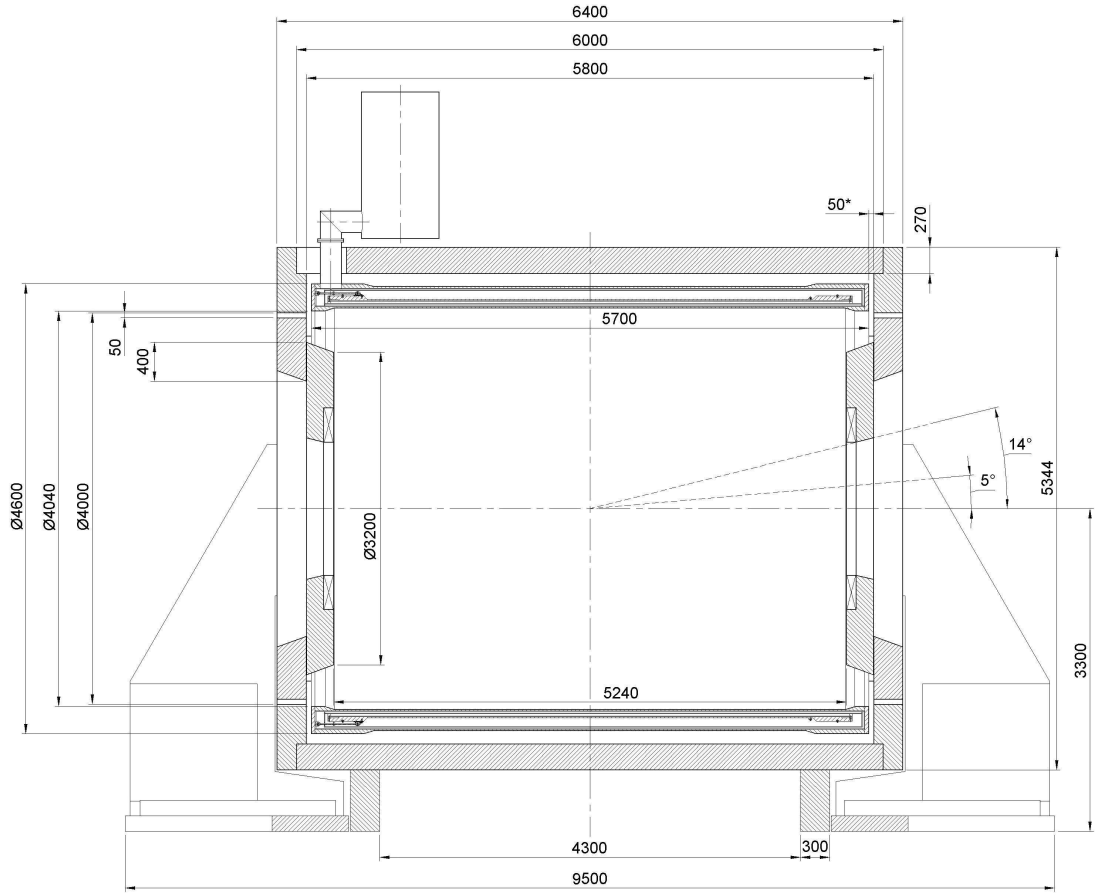

Fig. 2.6: MPD SC solenoid longitudinal cross-section

Magnetic Field and Forces

The superconducting coil with an average linear current density of $4.01 \cdot 10^5$ A/m was designed to achieve the required magnetic flux density of 0.5 T in the tracker area. The

Table 2.3: Main Dimensions of the Cryostat and of the Iron Yoke

Cryostat	
Inner radius (warm bore), m	2.0
Outer radius, m	2.3
Length, m	5.7
Iron Yoke	
Incircle radius of the yoke, m	2.4
Circumcircle radius of the yoke, m	2.67
Distance between pole tips, m	5.24
Length of the yoke, m	6.4

distribution of magnetic induction in the magnet structural parts and in the area of the tracker is presented in Fig. 2.7. The peak of magnetic field induction in the SC coil ends is 0.65 T. The trim coils placed in the recesses on the inner faces of the poles have to compensate the local magnetic field inhomogeneity resulting from central holes in the end caps and possible shifts in the axial position of the coil. A level of general field inhomogeneity of $|\triangle B|/|B_0| \sim 10^{-3}$ in the tracker area is provided.

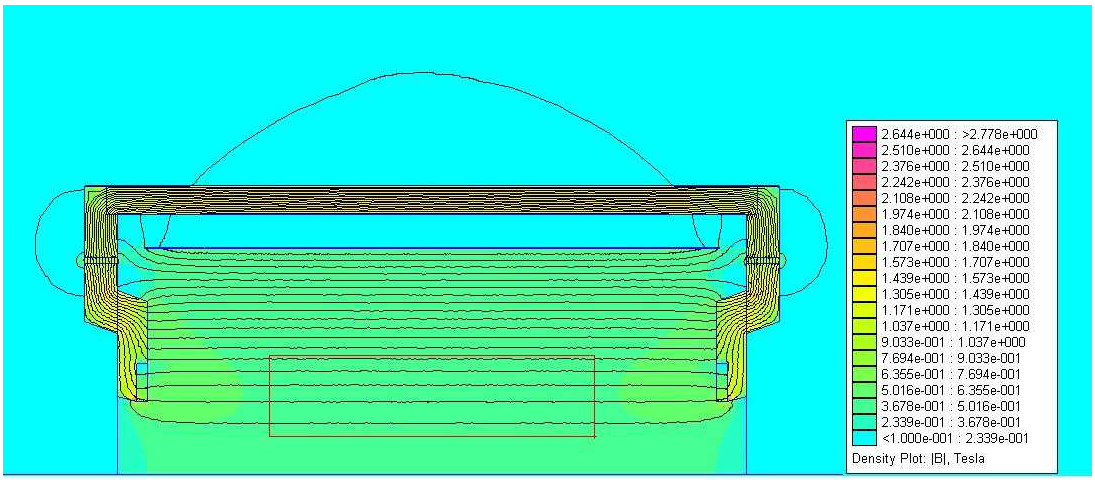

Fig. 2.7: Distribution of the magnetic induction in the magnet structural parts

The plot of the radial component of magnetic induction B_r in the area of tracker is shown in Fig. 2.8 in dependence on the axial coordinate Z for three values of the radius R. The maximum value of B_r in this region is $|B_r| < 9.5 \times 10^{-4}$ T. The average value of the ratio $|B_r/B_z|$ in the tracker region is 2.4×10^{-4}.

The contour plot of the field inhomogeneity $\delta = \frac{B-B_0}{B_0}$ in the tracker region is shown in Fig. 2.9. The maximum value is $|\delta| = 1.2 \times 10^{-3}$.

Distribution of the integral of the radial component over the region of the Charged Particle Tracker (TPC)

$$Int = \int_{z}^{z_{max}} \frac{B_r}{B_z}\, dz$$

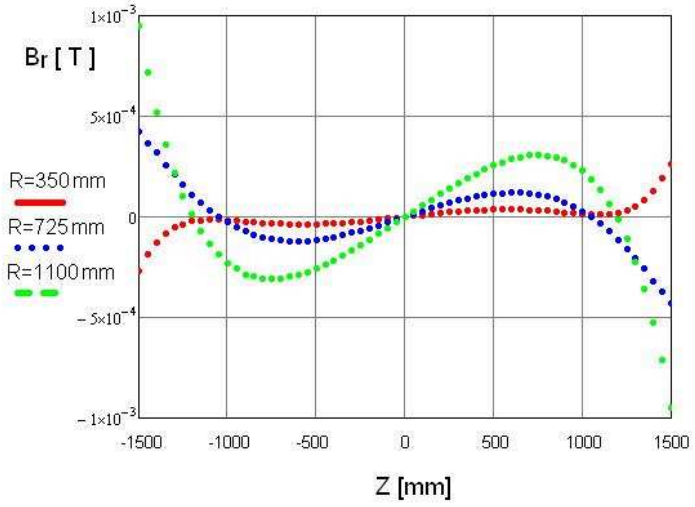

Fig. 2.8: Distribution of the radial component of magnetic induction in the area of tracker

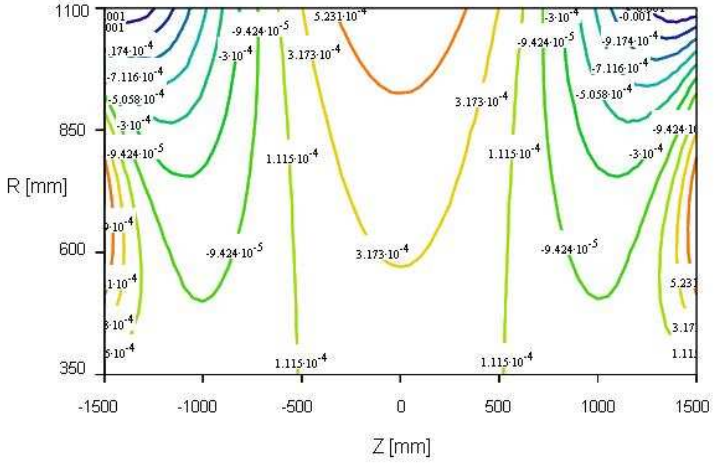

Fig. 2.9: Distribution of the inhomogeneity of magnetic induction in the area of tracker

is presented in Fig. 2.10. It can be seen from the pictures that the normalized integral is much below 0.775 mm.

The integral of the radial component of the magnetic field as well as the axial component of the magnetic force applied to the coil are very sensitive to the axial position of the coil with respect to the return yoke. The axial force acting on the solenoid coil and the integral of the radial component in the tracker area versus the axial coil displacement are shown in Fig. 2.11.

The nominal value of the axial force F_z due to symmetry of the magnet system is zero. An axial displacement of the coil by 1 cm results in the following deviations: $\Delta Fz = \pm 37\ kN$, $|\Delta\delta| = 2.8 \times 10^{-3}$ and $|\Delta Int| = 1.5\ mm$. A radial displacement of the coil produces the radial offset force of 10.6 kN/cm.

The increase of the radial component integral, appearing due to the axial coil displacement, can be compensated by restoration of the magnetic field symmetry using the trim coils placed at the magnet poles. The dependence of trim coils current density on the

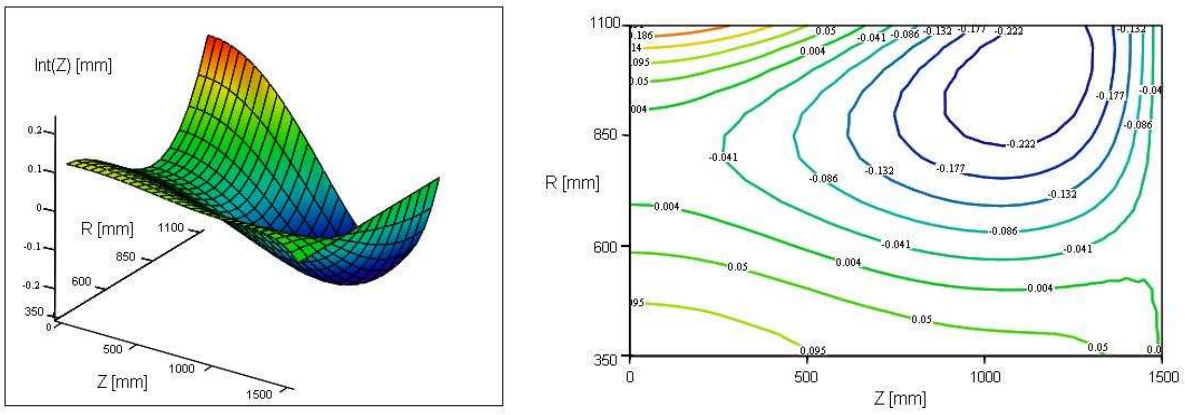

(a) (b)

Fig. 2.10: Surface (a) and contour (b) plots of the radial component integral. $|Int|_{max} = 0.27mm$

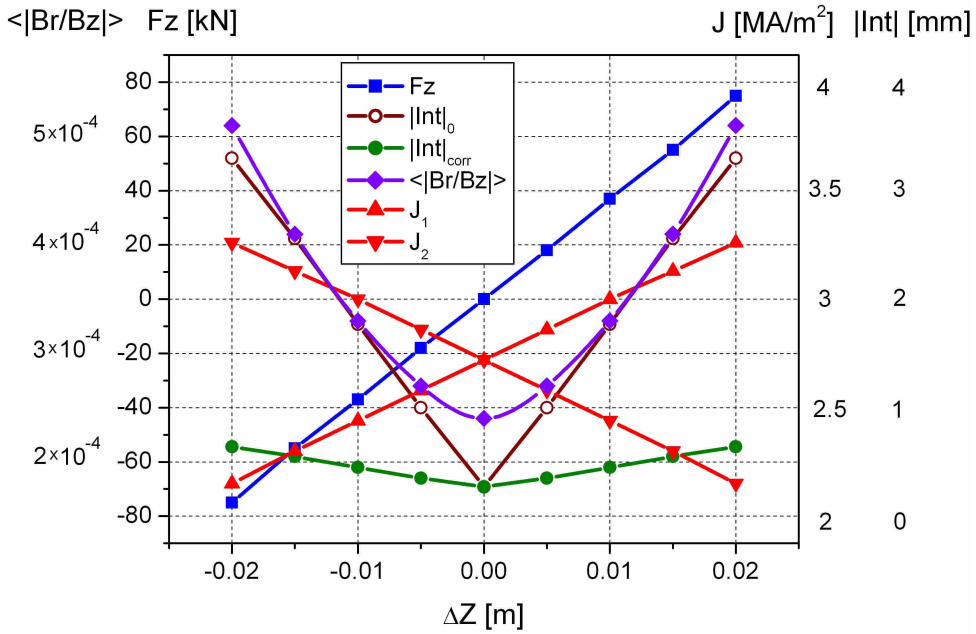

Fig. 2.11: Axial force F_z, maximal absolute value of integral of the radial component in the tracker area without additional correction $|Int|_0$, that with correction $|Int|_{corr}$ and the average ratio $|B_r/B_z|$ with correction using the trim coil currents J_1 and J_2 versus axial coil displacement

axial coil displacement is shown in Fig. 2.11. The maximal trim coil current density for compensation of a 2 cm deviation is about 3.3 MA/m^2. The maximum absolute value of integral of the radial component of magnetic induction and the average ratio $|Br/Bz|$ with current correction are also shown in Fig. 2.11. The maximum values at $\Delta Z = 0.02\,m$ are: $|Int|_{corr} = 0.64\ mm$, $|\triangle B|/|B_0| = 4 \times 10^{-3}$ and $< |Br/Bz| >= 5.1 \times 10^{-4}$ that are within the allowable limits. The force applied to each of the trim coils is about 10 kN. The tractive magnetic forces applied to the yoke end caps are 980 kN.

Distributions of the equivalent radial magnetic pressure and of the axial force density characterizing concentration of the axial magnetic force along the coil axis are shown in Fig. 2.12. The maximal radial pressure, 0.137 MPa, is generated in the regions at the ends of the coils. The maximal axial force of 0.31 MN is generated in the central region.

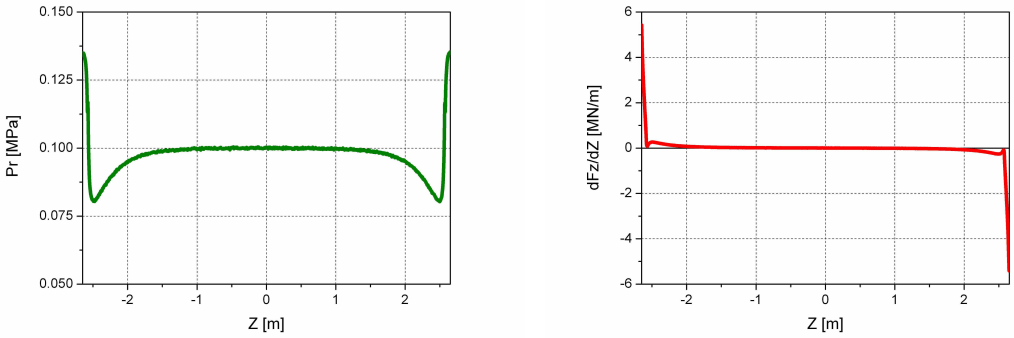

(a) (b)

Fig. 2.12: Distributions of the equivalent radial pressure (a) and of the axial force density (b) along the coil axis

The magnetic circuit of the solenoid is not saturated. The magnetic field in the flux return yoke is 1.45 T for the central magnetic field of 0.5 T.

If the magnet should provide the average induction in the tracker region $< |B| >$ other than 0.5 T, the current density in the main SC coil may be defined proportionally to this average induction. The values of the SC coil current I and the values of the trim coils currents $J = J_1 = J_2$ in the units of the nominal currents I_0 and J_0 and the characteristics of the field homogeneity in dependence of the central magnetic induction $B_0 =< |B| >$ are given in Table 2.4.

Table 2.4: Dependence of the field parameters on the solenoid current

$< \|B\| >$, T	I/I_0	J/J_0	$\|\Delta B/B\|_{max}$	$< \|Br/Bz\| >$	$Int(B_r/B_z)$, mm
0.2	0.40	0.40	1.1×10^{-3}	1.9×10^{-4}	0.10
0.5	1.00	1.00	1.2×10^{-3}	2.4×10^{-4}	0.27
0.7	1.42	1.62	2.1×10^{-3}	4.1×10^{-4}	0.63

The normalized integral of radial field component and filed inhomogeneity grow up for higher inductions due to nonlinearity of the magnet circuit. Nevertheless, the field integral remains within acceptable limits up to central induction of 0.7 T (this value of induction is considered as a calculated case only and it is well beyond the magnet operation limits). As it can be seen from the table 2.4, the yoke is considerably saturated for the central induction of 0.7 T. The induction in the barrel part is up to 1.85 T and the stray field at a radial distance of 1 m from the magnet system at the central plane Z=0 is increasing from 1.5 mT (for $B_0 = 0.5\ T$) up to ten times higher for $B_0 = 0.7\ T$. Besides that, the solenoid current and trim coil currents are not growing up linearly for this induction.

Certain redundancy of steel thickness in the yoke parts for the rated value of the central magnetic field 0.5 T is explained by the requirement of the yoke mechanical stability.

The main parameters of the solenoid are given in Table 2.5.

Table 2.5: Main parameters of the solenoid

Ampere-turns of the solenoid coil, MA	2.186
Nominal operational current, kA	1.36
Design current density, MA/m^2	64.5
Stored energy, MJ	7.53
Self inductance, H	8.01
Maximal induction in the superconducting winding, T	0.65

Aluminium Stabilized Conductor

The choice of operating current 1360 A is a compromise between low heat generation in the current leads and secure protection of the coil for larger conductor. In addition, the larger conductor is easier for handling in the coil winding process. The stability of the coil is based on high specific heat and thermal conductivity of the high purity aluminum stabilizer and on a conservative margin of the superconductor critical current, which is well over the operating current of the magnet. The aluminum stabilized superconductor is composed of a round multifilament NbTi/Cu wire 1.6 mm in diameter embedded in a pure aluminum matrix by a coextrusion process. The cross-section of the bare cable is $3 \times 7 mm^2$. The current density in the conductor of $64.5 A/mm^2$ is quite safe for such kind of superconducting windings. The coil winding can be made using several lengths of the conductor. It takes several electrical joints for it. The main parameters of the conductor are listed in Table 2.6.

Table 2.6: Main parameters of the conductor

Superconductor	NbTi/Cu
Stabilizer	Pure Al
RRR of stabilizer	> 500
Configuration (NbTi/Cu/Al)	1:0.9:12.3
NbTi/Cu wire diameter, mm	1.6
Bare conductor outer dimensions, mm^2	3×7
Edge radius, mm	0.3
Insulated conductor dimensions, mm^2	3.4×7.4
Insulation material	Half lapped prepreg fiberglass tape of 0.1 mm (after compression)
Critical current (0.65 T), kA	> 5
Nominal operation current density, A/mm^2	64.5
Nominal operation current, kA	1.36
Maximal field in the coil, T	0.65
Number of turns in the winding	$1559 + 2 \times 22 = 1603$
Length of the conductor, km	21
Weight of the conductor, kg	850

Electrical Insulation

Two kinds of insulation are required: turn-to-turn insulation and ground plane insulation between the coil and support cylinder. The design of the quench protection systems is based on a maximum voltage to ground of 500 V. The ground plane insulation will be made of a 1 mm layer of fiberglass prepreg cloth deposited between the support cylinder and the winding layer. Turn-to-turn conductor insulation will be prepared by half lapped prepreg fiberglass tape during winding to give an insulation thickness of 0.2 mm compacted. The resulting turn-to-turn insulation will be fully bonded after the heat treatment process and its thickness is 0.4 mm.

Mechanical Analysis of the Solenoid Coil and Iron Yoke

The coil thickness is defined by using the following way. After a quench when protective circuit fails the whole energy is dissipated into the coil itself believing that the support cylinder can't contribute a heat capacity to the load, because of low thermal conductance of the ground plane insulation. For the E/M ratio around 6 kJ/kg (it corresponds to the average coil temperature about 70 K after a quench) the required thickness of the conductor becomes about 7 mm.

Next, the coil has to withstand hoop force F_θ induced by the magnetic pressure P_m

$$F_\theta = P_m \; R = \frac{B_z^2}{2\mu_0},$$

where B_z is the axial magnetic field component. The hoop force is supported by the support cylinder and by the coil. Since the radial magnetic pressure is very low for this magnet (0.1 MPa) it would be quite enough to have a restraining cylinder of 3-4 mm in thickness. The practical cylinder thickness of 12 mm is decided in consideration of manufacturing and handling during the manufacturing.

The hoop stress inside the coil induced by the magnetic pressure will be shared between the aluminum support cylinder and the aluminium stabilized conductor. The maximal hoop stress for the coil is 10.5 MPa according to FE computations.

The axial compressive stress in the coil and support cylinder induced by the magnetic forces is approximately -2.7 MPa.

Plastic deformation in the large detector magnet coils is usually expected to occur during the first charge. But if the amount of these deformations is small, it ensures that the pure aluminum stabilizer will not be stressed beyond the elastic limit in the subsequent charges. This prevents premature quenches during the coil energizing. The winding of MPD detector is much better secured from quenches and other instabilities in comparison with the other magnet coils because of lower level of stresses. Equivalent stress (Von Mizes) for the aluminium conductor of this coil is $\sigma_{EQ} = 12.5$ MPa $< [\sigma] = 20$ MPa. It means that the plastic deformation of the conductor is not anticipated and the stresses will remain within the elastic range during the subsequent charges.

The shear stress between the winding and outer supporting cylinder induced by the magnetic force is ~ 0.5 MPa $< [\tau] = 2$ MPa.

Keeping the cylindrical shape of the coil. The ratio of the coil and support cylinder overall thickness to the coil diameter is very small (~ 0.5 %). So, this shell is very flexible and can be easily deformed by the gravity and magnetic forces. By-turn, the loss of the coil circularity can flaw to the magnetic field homogeneity disturbance. To keep the

coil circularity there are two thickening on both ends of support cylinder of 45 mm in thickness where the radial support ties are fixated. The choice of an appropriate number of ties provides stability of the coil support shape in operation conditions. In Fig. 2.13 the shape and radial deviation of the coil and support cylinder shape are shown for their fixation by 2×12 radial ties. The coil is loaded by gravity, magnetic pressure and radial decentering force for the coil vertical displacement of -20 mm (21 kN). The maximal radial deviation of the coil shape doesn't exceed 0.48 mm. The results of stresses computation are obtained by means of FE code COSMOS [201].

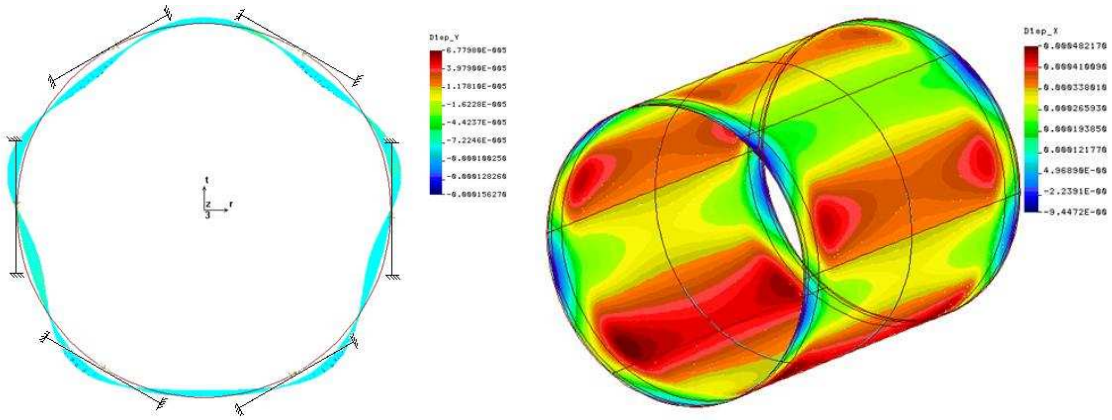

(a) (b)

Fig. 2.13: The shape in the cross-section (a) and the radial displacements (b) of the coil loaded by gravity, magnetic pressure and radial decentering force for vertical displacement of 20 mm. The coil is fixated by 2×12 *radial ties.*

Stresses in the coil due to handling and transportation with maximum acceleration of 2 G in vertical direction and 0.5 G in horizontal direction are: hoop stress 11 MPa, axial stress 1 MPa. Maximal radial deformation of the coil is 0.3 mm.

Results of FE stress computations for the superconducting coil are summarized in Table 2.7.

Thermal contraction makes support cylinder and coil shorter after cooling down by ~ 22 mm (and below the initial diameter by ~ 9 mm). In the drawings of this paper the dimensions of the cold mass after cooling down are indicated. The coil supports are to be adjusted such that the cold coil position aims at the cryostat centre.

The outer and inner cryostat shells are 17 and 14 mm in thicknesses respectively. As it follows from the performed computations, the operation stresses in the cryostat shells don't exceed the allowable stresses under normal operation and emerging conditions.

The Iron Yoke becomes deformed under action of the gravity, magnetic forces and weight load of the cryostat and inner detectors. According to FE computations, the vertical deflection of the upper part of the support rings and the upper barrel beam deflection would be -0.6 mm and -2.3 mm respectively if the magnet rests on the bottom beam without supports. Accounting of the supporting cradles, which join five bottom beams and provide general rigidity of the bottom part, gives maximal vertical deflection of the upper beam -1.9 mm, that of the bottom beam +0.9 mm and horizontal deflection of the side beams 0.13 mm. The deformations of the Iron Yoke are shown in Fig. 2.14.

Table 2.7: Results of stress computations in the coil and support cylinder

Magnetic forces	
Hoop stress, MPa	10.5
Axial stress, MPa	-2.7
Equivalent stress (Von Mises), MPa	12.5
Shear Stress, MPa	~ 0.5
Gravity and Decentering Force	
Hoop stress, MPa	2.5
Axial stress, MPa	0.6
Equivalent stress (Von Mizes), MPa	2.9
Magnetic forces + Gravity and Decentering Force	
Hoop stress, MPa	10.5
Axial stress, MPa	+0.8 -3.0
Equivalent stress (Von Mizes), MPa	11.7
Stresses in the coil due to handling and transportation	
Hoop stress, MPa	11
Axial stress, MPa	+1.0 -3.1
Equivalent stress (Von Mizes), MPa	11.7

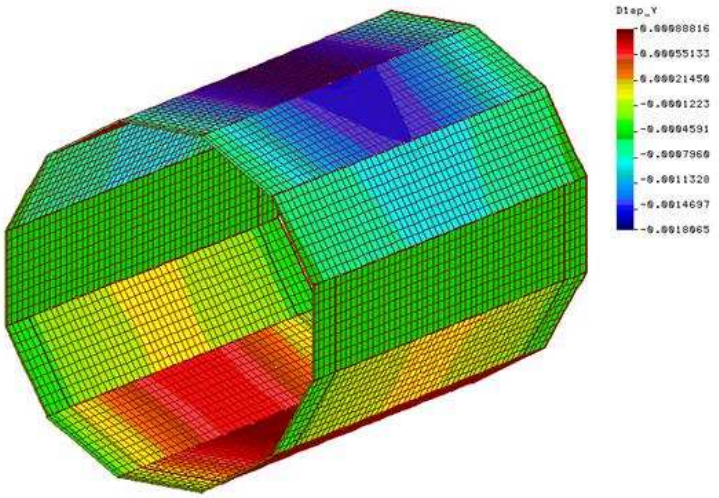

Fig. 2.14: Vertical deflections of the yoke barrel parts under action of the gravity, magnetic forces and weight load of the cryostat and inner detectors

Thermal Design of the Cryostat

To obtain the assured thermal stabilization of the conductor, the cold mass is to be installed in the space between inner and outer cryostat vacuum shells and supported by high thermal resistance ties and struts. The coil is indirectly cooled by two-phase liquid helium flowing through an aluminum cooling tube, which is welded to the outside surface of the support cylinder. The cold volume is surrounded by the thermal shield supported from the side of the vacuum chamber, which is cooled by helium gas at 40-80 K.

Thermal shield

The cryostat is equipped with radiation shield inserted between the coil and the cryostat outer can. The shield surface is covered by high purity aluminum foil to reduce radiation heat loads. About 30 layers of superinsulation separate the vacuum vessel walls from the shields. The data of the thermal load at the thermal shield multiplied by the safety factor 2 are presented in Table 2.8. The overall heat load at the level 77 K is expected not to exceed 734 W in the operational mode.

Table 2.8: Heat Loads on the cold volume and on thermal shield

T=4.2 K (safety factor 2)	Load, Watt
Radiation	11.5
Support conduction	8
Cryogenic chimney conduction	10
Conductor joints and wires	2
Eddy current losses in the Al cylinder	12
Total (normal/transient regime):	31.5/43.5
T=77 K (safety factor 2)	
Radiation	388
Shield supports conduction	300
Heat intercepts of the coil supports	118
Total:	806
Current leads (safety factor 1.5)	
Operation current	0.156 g/sec
Zero current	0.094 g/sec

Cold mass support

Six axial tension-compression ties are located on the chimney end of the cryostat. 12×2 low-heat-conduction radial struts support the cold mass of the cryostat at the ends. The conductivity load for the stainless steel supports multiplied by the safety factor 2 is presented in Table 2.8.

Cold mass

The cold mass surface is covered with high purity aluminum foil to reduce radiation heat loads. A radiation specific load of 40 mW/m^2 has been estimated for the cold mass. The data of the heat load at 4.5 K multiplied by the safety factor 2 are summarized in Table 2.8. The value is obtained for 146 m^2 of cold mass surface. The thermal load due to the eddy currents in the aluminum support cylinder is presented there as well. A time interval for energizing the coil is 1 hour. The overall heat load at the level of 4.5 K is expected not to exceed 31.5 W in the operational mode and about 43.5 W - in the transient mode.

Current leads

Helium vapor cooled current leads of normal conductor will be used to provide maximal reliability of the solenoid operation. Leads of this type evaporate up to 3.2×10^{-3} liters per hour per ampere for each lead pair when operate at the design current (40% less at zero current) [202]. For operation current 1360 A they will consume $\sim$ 4.5 l/hour (or 0.156 g/sec).

Coil and Support Cylinder Design

Detail of the cross-section of the coil is shown in Fig. 2.15.

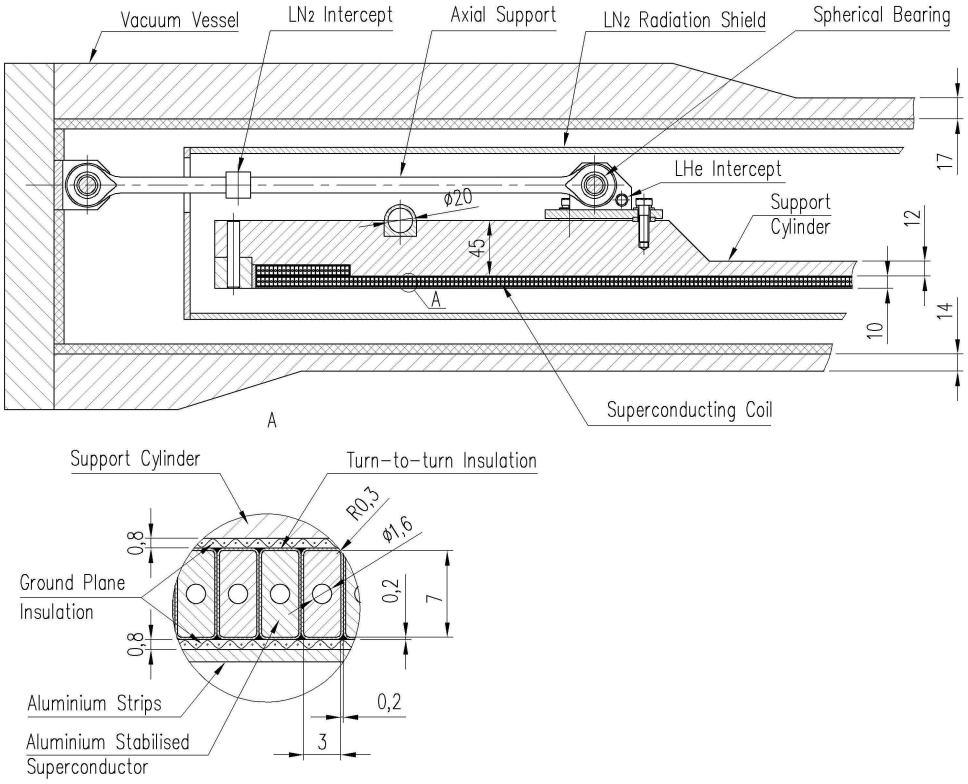

Fig. 2.15: Detail of cross-section of the coil and superconductor

The coil consists of a single layer of aluminium stabilized conductor NbTi/Cu within an outer support cylinder made of aluminium alloy. This cylinder is considered as a secondary dump turn for quench protection as well.

The winding layer helps to bear the hoop stress. The thickness of the coil is based on amount of aluminum stabilizer required to limit the temperature of the coil if all of the energy were absorbed by the stabilizer.

Manufacturing of the aluminium support cylinder of 12 mm in thickness and 4.2 m in diameter is not an easy task and will demand a lot of auxiliaries. The inner diameter of support cylinder is machined for coil winding. Before final machining the helium cooling tubes and support attachments can be welded onto the outer surface of the cylinder. To prepare the plane insulation, a layer of fiberglass-epoxy insulation several millimeters thick is built up on the inner surface of the cylinder, using prepreg sheets, compressed to high glass fraction and cured. The insulated surface of the cylinder is then machined. The final thickness of the insulation is about 1 mm.

During operation the solenoid should not quench or exhibit other instabilities. This implies that the winding structure must be tight and rigid so that it is everywhere free from inelastic conductor motion that can cause quenching. It must be bonded securely to the support cylinder so that the axial stresses do not cause debonding between the coil and the cylinder. The winding preload and the integrity of the epoxy used to bond the turns to one another and to the support cylinder has to ensure that the coil will perform as intended.

The coil conductor will be internally edge wound in compression on the inside of the aluminium support cylinder, slowly rotating turn table. Several stations along the conductor path will prepare the conductor (shot blasting, degreasing, drying, and taping by turn-to-turn prepreg insulation). The last station is a caterpillar feed and runway to push the conductor onto previous turn. During the winding the conductor is to be pressed in the axial direction with rollers. After depositing some turns an axial pressure load is applied for a brief period to keep a newly wound coil section tight. At every half meter of completed winding each new section has to be cured keeping axial pressure to provide high homogeneity of the turns.

Design of Iron Yoke

Barrel and end caps design
The Solenoid iron yoke is a cylindrical steel structure consisting of 12 flux return bars, two supporting end rings, two pole tips and support structures. The 6 m long flux return bars are trapezoidal in cross-section, and weigh 17.2 ton each. They form the barrel part of the yoke, which contains the cryostat with the superconducting coil.

The supporting rings have a 4 m I.D., 5.34 m incircle O.D. and twelve chord surfaces on the 4.8 m diameter to control the azimuth and radial location of each flux return bar, with an axial thickness of 270 mm. A support ring weighs 20.9 ton each.

Each pole piece weighs 28.4 ton and is fixated relative to the supporting ring. They have a conical 14 grad inner diameter, whole axial thickness 600 mm, a 3.9 m O.D. and a recess on the inner face surface for the trim coil. A 50 mm annular gap between supporting ring inner diameter and pole piece outer diameter is provided for passage of cables and tubing of internal detectors. To simplify manufacturing and transportation the poles are divided in axial direction on two parts consolidated by bolts which weigh about 14 ton each.

The solenoid support structure consists of two cradles weighing 17.5 ton each. They embrace the five lower flux return bars of the yoke barrel part. The support structure is placed on a transport carriage guided by two rails. The magnet traveling section (the magnet without both poles) can be moved between experimental hall and assembly area as required.

Two pole piece support structures weighing 31.7 tons each rest on rails so that the poles may be withdrawn to provide access to the ends of internal detector elements.

All magnet yoke material is specified as Steel 10 which has a minimum yield strength of 210 MPa with an annealed heat treatment.

The magnetic field quality required that deflections in the magnet structure are to be minimized to less than 1 mm. This can be accomplished with precise fabrication of magnet components and the use of high strength bolted and pinned connections between mating components.

Yoke supports have to fixate the magnet at the foundation rigidly and to provide adjustment of the detector systems relative to the beam axis. To minimize the yoke deformations, five bottom beams will be welded-in to the yoke supports.

Poletip Trim coils
The trim coils are to improve the magnetic field homogeneity in the tracker area. They are embedded in the recesses on each poletip. The coils are wound with hollow aluminum conductor and insulated with fiberglass cloth vacuum impregnated with epoxy resin. Each coil has 4 layers and is wound two-in-hand (bifilar)-fashion giving 56 turns per coil. Each

coil contains two separate water circuits. The water circuits are of approximately 151 m long. The conductor measures 23 mm square with a 13.3 mm in diameter central water hole. Each coil is 1.36 m I.D. by 2.06 m O.D., it has an axial thickness of 0.1 m and weighs about 0.32 tons. At the nominal magnet field 0.5 T the currents of the trim coils will be 1625 A. Each coil consumes 65 kW and is cooled by demineralized water at the pressure drop 6 Bar. Water consumption per one trim coil is 0.52 liter/sec. Flexible copper cables and pressure water hoses make it possible to withdraw a pole pieces without their preliminary detaching.

Transportation of the magnet parts to Dubna will not make much trouble. The weights and sizes of the most yoke parts (see Table 2.9) are within acceptable limits for standard transportation procedure and it will not be necessary to obtain special permissions from road services. Overall dimensions of the support rings are beyond permitted limits and for their transportation it will be necessary to obtain a special permission and to have a special track escorted by the road police. For transportation of the assembled cryostat a special track is necessary.

Table 2.9: Weights and overall dimensions of the magnet constituent parts

Item	Dimensions, m	Part count	Weight	Sum
Iron Yoke				
Support ring, ton	4.0 I.D., 5.34 O.D., t=0.3	2	20.9	41.8
Barrel beam, ton	$6.0 \times 1.43 \times 0.27$	12	17.2	206.4
Pole tip inner ring, ton	1.36 I.D., 3.4 O.D., t=0.28	2	14	28
Pole tip outer ring, ton	2.6 I.D., 3.9 O.D., t=0.3	2	14.4	28.8
Yoke support, ton	$5.9 \times 2.49 \times 0.3$	2	17.5	35
Pole support, ton	$3.8 \times 3.96 \times 2.28$	2	31.7	63.4
Trim coil, ton	1.36 I.D., 2.06 O.D., t=0.1	2	0.32	0.64
Total (weight of the yoke):				404
Cryostat & coil				
Vacuum vessel, ton	4.04 I.D., 4.6 O.D., l=5.7	1	25.3	25.3
Thermal shield, ton	4.19 I.D., 4.46 O.D., l=5.49	1	2.8	2.8
Coil+Support cylinder, ton	4.24 I.D., 4.35 O.D., l=5.36	1	4.1	4.1
Total (cryostat+coil)				33
Auxiliary ironware, ton				3
Grand total (magnet weight)	440 ton			

Assembly

The first assembly of the return yoke will be done by the manufacturer at his place.

The experimental Building 205 at LHEP JINR has an assembly area in which the detector will be assembled and tested prior to the transportation to the experimental area. Assembly begins with the installation of the transport carriage on the rails in a concrete floor running from the assembly area to the experimental hall. The carriage has to be mounted on temporary supports to provide stability of the construction during the assembly. The support cradles are set atop the carriage. The lower five flux return bars are installed, aligned, and fixated to the support cradles to form a monolithic support for the remaining magnet yoke and detector elements: Fig. 2.16(a). Each supporting ring is

being then installed in the cradle formed by the five chord surfaces of each flux return bar: Fig. 2.16(b). Then they will be locked to the ends of the lower five flux return bars, using taper pins and bolts. With end rings in place an additional two flux return bars were installed to mid plane to form the lower part of the magnet yoke cylinder. The cryostat with the superconducting coil is then installed into the lower magnet yoke part, aligned and fixated to the supporting rings: Fig. 2.17(a).

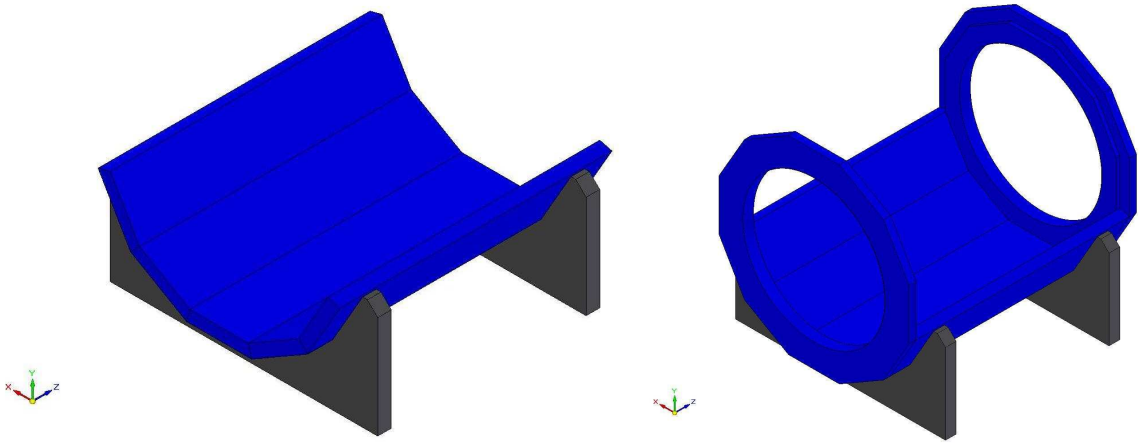

(a) *Assembly began* (b) *Supporting rings installed*

Fig. 2.16:

When the cryostat has been aligned and locked in the place, the remaining five upper flux return bars are installed to complete the assembly of the magnet core: Fig. 2.17(b). Traveling solenoid section (assembled solenoid without both poles) is ready to be transported to the operation area of Bd.205. Before transportation of the traveling section the temporary supports under the carriage will be removed by means of jacking.

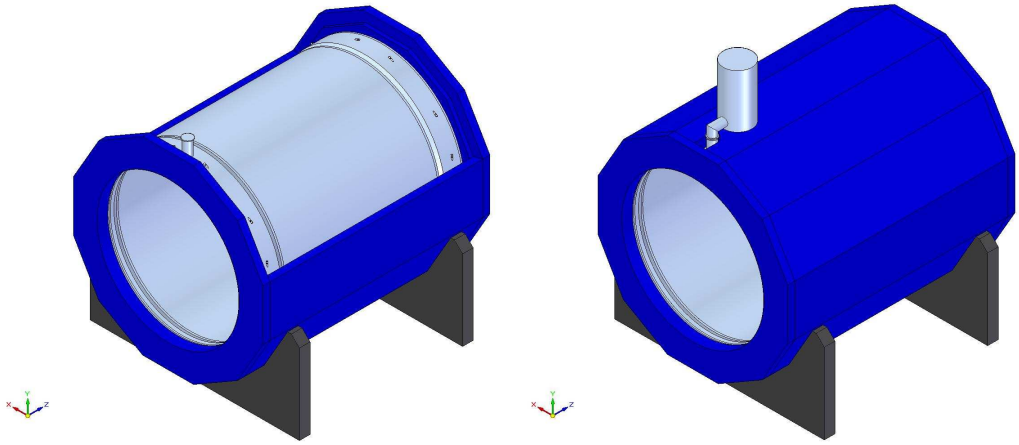

(a) *Cryostat installation* (b) *Assembled Yoke barrel part with cryostat*

Fig. 2.17:

The two pole pieces on their supports will be individually installed to complete the magnet assembly in the operation area.

Adjustment of the solenoid to the beam line

The central line of the coil has to be adjusted with respect to the cryostat axis within the precision of ±5 mm by correction of the radial support ties lengths. The axial position of the coil with respect to the chimney side cryostat flange has to be adjusted within ±5 mm by correction of the axial ties lengths. Adjustment of the coil central line relative the return yoke central line will be fulfilled at the stage of the final assembly. Finally, the assembled solenoid has to be adjusted to the beam line. The hydraulic jacks and supports embedded into the floor allow the magnet to be adjusted relative the collider beam. It will be done by means of adjusting shims under the solenoid supports. Expected precision of the solenoid coil and beam axes alignment is to be within ±10 mm.

Design of the Cryostat

Vacuum vessel

Stainless steel was chosen as the material of the vacuum vessel of the cryostat to ensure its mechanical stability. The cryostat will be designed, fabricated and inspected according to the intent of the RF code [203]. The ends of the shells are thickened to provide means for anchoring the rods supporting the coil (Fig. 2.5). Wall thickness of the inner and outer shells of the vacuum vessel is 14 mm and 17 mm respectively. At the top of the upstream part of the outer shell there is a flanged branch where the chimney for liquid and gaseous helium inlets and outlets are mounted. The diagnostic wires connectors, relief valves and flanges for vacuum pumping are located on this flange as well. The weight of the vacuum vessel is 25.3 tons.

Thermal shield

The cryostat is equipped with radiation shield inserted between the coil and the cryostat outer can, which is cooled by helium gas at 40-80 K. The material of the thermal shield is stainless steel covered by aluminium foil. The shield is broken electrically in the circumferential direction to eliminate eddy currents induced by charging/discharging of the coil. The weight of the thermal shield is 2.8 tons.

Cold mass supports

The forces acting on the solenoid cold mass are its own weight (41 kN), offset axial and radial forces 37 kN/cm and 10.6 kN/cm respectively. The coil suspension system consists of 24 stainless steel radial ties (03Cr20Ni16NMn6) fixed at the ends of the outer vacuum shell. They center the cold mass with respect to the outer vacuum shell. The axial decentering magnetic force is carried by six stainless steel rods. The position of the coil has to be adjusted taking into account thermal shrinkage of the coil and its supports as well as the yielding of the support ties. To take into account the acceleration during the transportation and installation, the supports are designed to carry the maximum load of 2 G in vertical direction and 0.5 G in horizontal direction. The solenoid cold mass is cooled by helium in tubes attached to the coil support cylinder. The volume of helium in a tubular cooling system is small. During a quench this amount of helium will be expelled and returned to the refrigerator. The tubes can withstand high pressures during a quench.

2.2.3 Cryogenic and Vacuum Systems

Solenoid Proximity Cryogenics

To compensate the cryogenic losses of the solenoid, a refrigeration power is required.

The largest part of the losses is defined by radiation load, heat conduction along the mechanical supports and current leads boil-off. Besides that, the cryogenic system has to compensate the eddy current heating of the coil during the ramp up of the magnet to the operation field. The MPD solenoid needs cryogenic supplies from a satellite refrigerator for the operation amounting to (including the quoted safety factors) ~ 50 W refrigeration at 4.5 K, ~ 800 W refrigeration at 50 K and 0.16 g/sec liquid helium (liquefaction) for the operation of the copper counter flow current leads.

It is foreseen that the magnet will be cooled by forced flow of two-phase helium. Closed loop helium satellite refrigerator provides adequate refrigeration power both at ~ 50 K for the intermediate temperature shields and at 4.5 K for the forced flow refrigeration of the coil cold mass. Flow for the magnet cooling circuit comes from the J-T circuit of the helium refrigerator. Two-phase helium from the refrigerator J-T circuit flows through a heat exchanger that is cooled in a bath of liquid helium at the suction pressure of the cold end of the refrigerator. The temperature of the helium bath is the lowest temperature in the two phase flow circuit. Within the heat exchanger, helium in the gas phase is condensed to liquid so that the helium leaving the heat exchanger is either on saturated liquid line or slightly sub-cooled. As a result, the average density of the helium in the flow circuit maximized, which will cause the flow pressure drop through the flow circuit to be reduced a factor of two or three as compared to the same flow circuit without heat exchanger in the helium bath. The use of the heat exchanger in the control Dewar allows the operation of the cooling circuit with a heat flow into the magnet that exceeds the capacity of the refrigerator by as much as fifty percent. Under this condition, the magnet can be kept cold as long as the heat exchanger in the control Dewar is kept covered with liquid helium. This solution, integrating a quite larger control Dewar, is used also for the refrigeration of the current leads, allowing a limited thermo-siphon operation of the coil in case of sudden failure of the refrigerator.

The control Dewar is the interface between the helium satellite refrigerator and the cryostat. The control Dewar has couplings to the supply and return lines for gaseous and liquid helium, connections to the power leads. The superconducting leads from the coil enter the helium reservoir through insulating feed troughs and connect with vapor cooled current leads. In the helium bath of the control Dewar the helium exchanger is accommodated. The vacuum vessel of the control Dewar is made of stainless steel. The chimney contains a pair of superconducting current leads, supply and return helium lines.

Vacuum System

The pumping system consists of a forepump and a turbo-molecular pump to ensure an ultimate pressure of $\sim 10^{-5}$ torr (at room temperature). The pressure drop up to $\sim 10^{-7}$ torr has to be reached by means of cryo-pumping of the vapors onto the cryogetter charcoal panels after cooling down. A relieve valve for an overpressure of 0.2 bar must be provided in the vacuum system to avoid pressure increasing in the cryostat caused by cryo-pumped gases while quick temperature rising.

2.2.4 Protection System and Power Supplies

A quench protection system is based on extracting energy from the series-connected main superconducting coil and two correcting subcoils L_s to an external dump resistor R_d and to the secondary dump turn (the Al coil support cylinder) (L_c, R_c) (see Fig. 2.18). When a quench is detected by the control system of the protection circuit, the protective breakers

(S_1 and S_2) are opened to a fast discharge in the circuit made up by the solenoid, the dump resistor and the aluminium support cylinder.

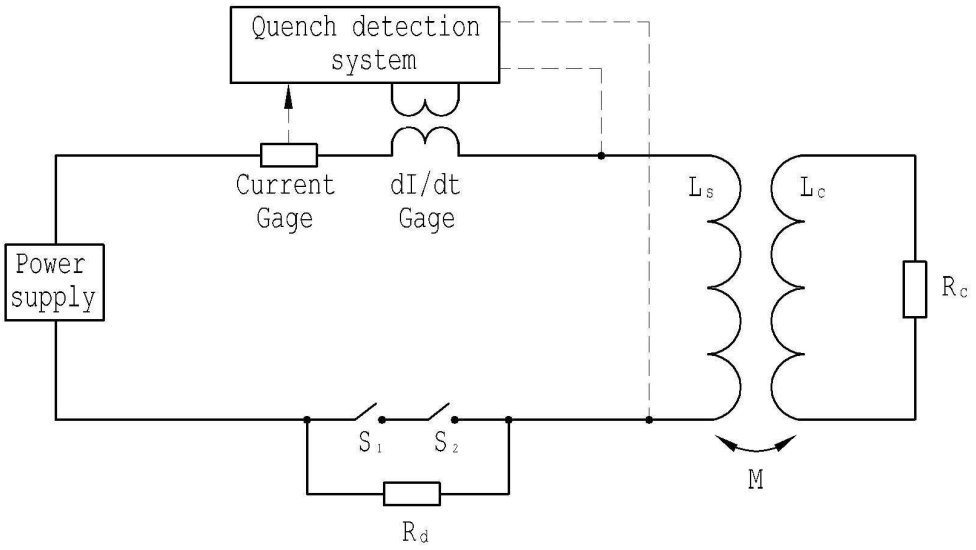

Fig. 2.18: The coil protection circuit

If the quench is propagated to entire coil slower than the power decay time constant and the mutual inductivity of the solenoid coil with aluminium support cylinder is not taken into consideration, the temperature rise after a quench in the hottest point of the superconductor would be up to 140 K. The dump resistor (R_d = 0.37 Ohm) reduces the maximum voltage on the solenoid leads to 500 V. This rise is rather high for glue connections of dissimilar materials in the winding.

The presence of the support cylinder ensures quench safety by the rapid spreading of the normal zone in the event of a quench (the "quench-back" effect) and it is a typical feature of magnets of this type. It is planned to additionally enhance quench safety by improving effective thermal conductance in axial direction by bypassing the thermal insulation by pure aluminium strips of 1 mm in thickness glued inside the coil surface. These strips help to increase the quench propagation in axial direction as well.

Transient process of the energy dump in the superconducting coil of the MPD detector is shown in Fig. 2.19 when after a quench the entire coil conductor is in normal state. The maximal average temperature of the coil is about 50 K, the temperature of the Al cylinder ($L_c = 4 \times 10^{-6}$ H, $M = 4.8 \times 10^{-3}$ H) is about 50 K as well. The maximum voltage on the coil leads ($I_1(t) \times R_d$) is limited to 500 V. These values are quite acceptable for the coil materials.

The circuit breakers and dump resistors are used to protect solenoid against a failure from overheating after a quench. The circuit breaker is made of two independent switches to increase safety redundancy.

The power supplies must operate with stability of $\pm 0.01\%$ and have to be connected to the solenoid current leads by insulated flexible copper cables. The cables should be air cooled.

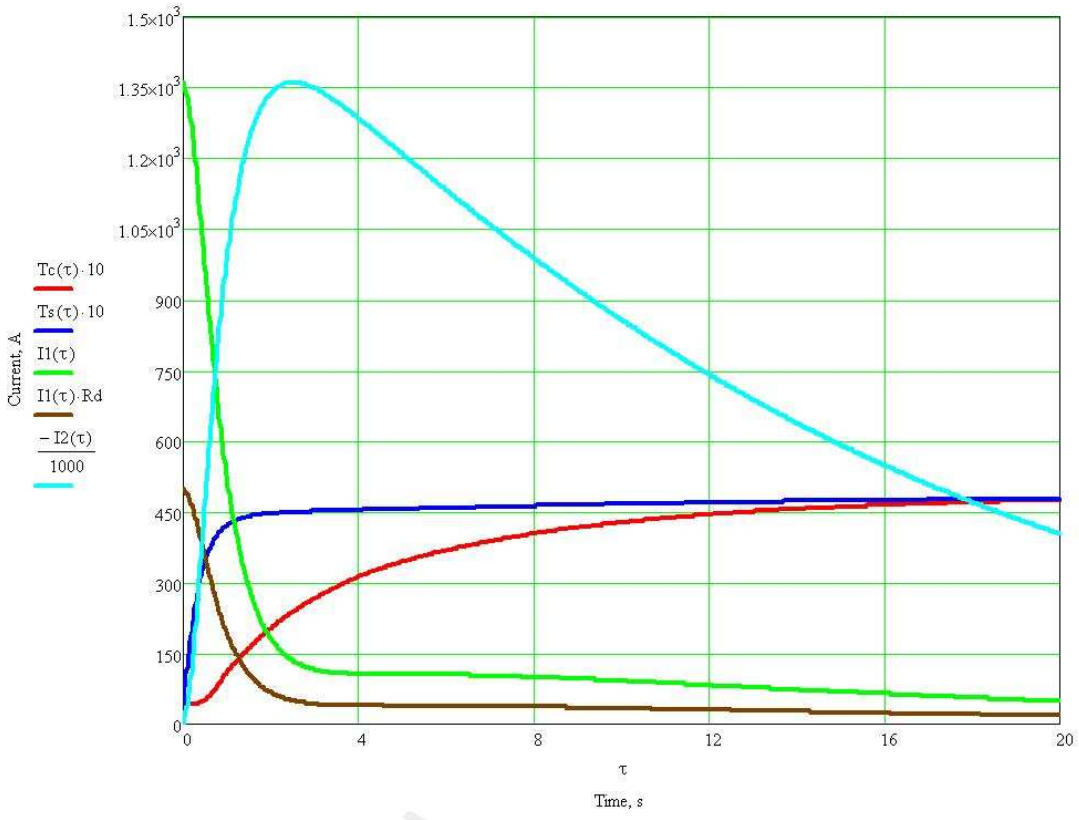

Fig. 2.19: Fast discharge of the solenoid current $I_1(t)$ on external resistor 0.37 Ohm and behavior of the induced current in the support cylinder $I_2(t)$. The average temperatures of the coil and support cylinder are indicated as $T_s(t)$ and $T_c(t)$ respectively.

2.2.5 Quality Assurance and Manufacturing

It is planed that the iron yoke, the solenoid coil and the cryostat will be produced under general responsibility of a European firm, which has positive experience in producing such kinds of magnet systems. This firm will be charged for the final parameters of the magnet system. It is planed that Russian producers of steel and manufacturers of metal constructions will be involved in the magnet production as subcontractors. Final assembly of the magnet, its commissioning and preparation of user instruction must be fulfilled by the prime contractor. The prime contractor of the MPD solenoid will have to provide a written Manufacturing Plan, which describes the overall process sequence and details of critical process steps in fabrication, assembly and inspection.

The prime contractor will have to provide a written Quality Assurance Plan or Manual, generally in accordance with the requirements of ISO 9001. The Plan will describe as a minimum the QA organisation, authorities and responsibilities, requirements for the design and procedural documentation, requirements for control of manufacturing, procurement and inspection operations; requirements for record keeping and audits.

Supplier will prepare as minimum the following QA records:

- materials input test reports;
- inspections reports during the coils manufacturing;

- acceptance test reports.

JINR LHEP engineering division has to carry out preliminary work to accommodate the power supplies, Helium and Nitrogen supply, cooling water supply and other engineering systems. To maintain compatibility with this work, the Interface Document will define minimum and maximum limits for many of the engineering parameters or indicate fixed parameters.

When the return yoke and the cryostat are manufactured, assembled and tested at the producer places, they will be transported to JINR where the magnet will be finally assembled and commissioned. Field mapping will be included in the acceptance test procedures.

2.3 Time projection chamber

2.3.1 Technical requirements

The MPD time projection chamber (TPC) is the main tracking detector of the central barrel and, together with the internal tracking system, time of flight system and electromagnetic calorimeter has to provide charged particles momentum measurement with sufficient resolution, particle identification and vertex determination, two track separation and dE/dx measurement for hadronic and leptonic observables at pseudorapidities $|\eta|$ <1.2 and p_t >100 MeV/c.

The electromagnetic calorimeter will provide, in conjunction with the data from the TPC, reliable electron identification to study dielectron processes. TPC has to provide the high dE/dx resolution in the high multiplicity environment of a $Au + Au$ central collision to identify electrons with an efficiency of over 90% and reject pions at the level of 10^3.

The track reconstruction in the region of pseudorapidity beyond 1.2 is provided by both TPC and End cap straw tracker. In order to have excellent momentum resolution and identification capability in this region the end plate elements of the TPC and readout electronics which is mounted on them have to be minimized for material budget. Thus material budget of endplate and readout electronics is about 15%.

The requirements to the TPC performance following from the physics described above are as follows:

— provide efficient tracking up to pseudorapidity region $|\eta|$ =1.2.

— the momentum resolution for charge particles about 2% at the transverse momentum of 300 Mev/c.

— the two-track resolution has to be about 1 cm in order to provide interference measurements with a resolution in relative momentum of a few MeV/c.

— for hadron and lepton identification a dE/dx resolution better than 8% is desirable [204].

All these requirements must be satisfied at a design luminosity of $10^{27}\text{cm}^{-2}\text{s}^{-1}$ for $Au + Au$ collisions at NICA collider, which corresponds to an interaction rate of about 7 kHz. The particle multiplicities are ∼1000 for the central collision at $\sqrt{s_{NN}} = 9$ GeV.

TPC is shown schematically in Fig. 2.20. It is 3 m long and 2.2 m in diameter. The TPC design is "conventional" in the overall structure widely used in other experiments [204, 205, 206, 207]. The active gas volume of the TPC is bounded by coaxial field cage cylinders with instrumented pad-plane end-caps at both ends. The uniform electric field in the active volume required for drift electron chambers is created by a thin Central Electrode at the center of TPC, concentric field cage cylinders and the readout end-caps. The electric field uniformity is critical since track reconstruction precision required is a fraction of mm and electron drift paths are up to 1.5 m.

The TPC readout system is based on Multi-Wire Proportional Chambers (MWPC) with cathode readout pads. Image charges are induced on an array of pads and are recorded as a function of time. The image charge is measured by a preamplifier/shaper/ waveform digitizer system. For each track segment, the drift time provides a coordinate along the TPC axial line, while the induced signals on the pad provide the coordinates in the plane of the MWPC. The charge induced on the pads is shared between several adjacent pads, so the original track position can be reconstructed to a small fraction of pad width.

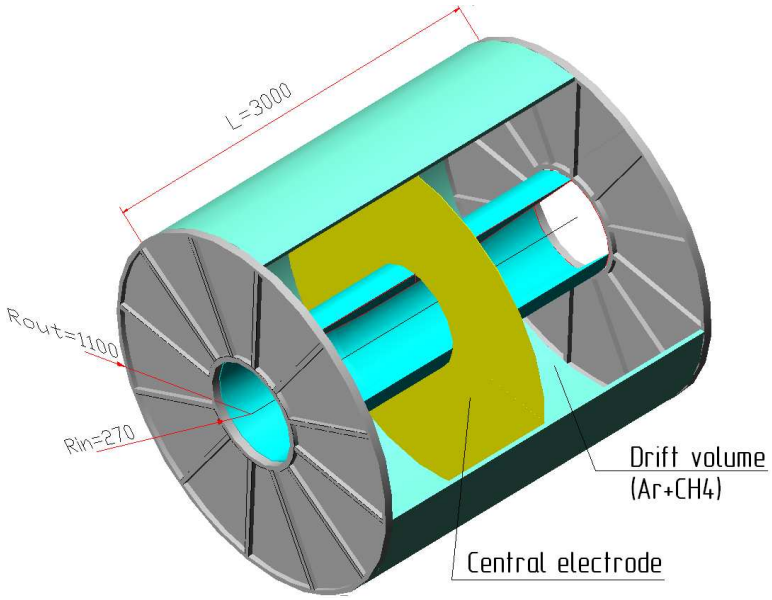

Fig. 2.20: Schematic view of the MPD TPC.

Each end-cap is comprised of 12 sectors of MWPC (24 sectors at both sides). The overall area to be instrumented is about 8.0 m^2. The chambers are modular units mounted on aluminum end-plates and on special support wheels adjacent to the end-plates. To reach a reasonable value of occupancy and to ensure the necessary dE/dx and position resolution, there will be about 80 000 readout pads of two different sizes. The pads are arranged in two subsectors. The inner subsector covers the region of highest track density near the inner TPC radius and has to be optimized for good two-track resolution. The outer subsector is optimized for dE/dx measurements which provide good particle identification. The basic parameters of TPC are summarized in Table 2.10.

Drift volume

The radial dimensions of the TPC have to be balanced with the strength of magnetic field. Momentum resolution is a strong function of the measured charge particle path length, i.e. as small inner radius and as large outer radius as possible are feasible. In addition, for the present MPD design a small inner radius is desirable for accurate matching the tracks from the inner tracking system. The expected track density within the TPC acceptance in the central $Au + Au$ collisions allows us to conclude the inner radius of 35 cm will be acceptable. The tracks length in the TPC will be sufficient to obtain adequate momentum resolution up to transverse momentum about 3 GeV/c at 0.5 T.

Drift gas

The TPC active volume is filled with 90% argon and 10% methane gas mixture (P10) at 2 mbar above atmospheric pressure. The over-pressure has to be as small as possible to reduce the multiple scattering in the TPC gas.

This gas mixture has long been used in TPCs [205, 206, 208]. Its primary attribute is fast drift velocity which peaks at a low electric field. Operating on the peak of the voltage-velocity curve makes the drift velocity stable and insensitive to small variations in temperature and pressure. Low voltage greatly simplifies the field cage design.

Table 2.10: Basic parameters of the MPD TPC.

Item	**Dimension**
Length of the TPC	340cm
Outer radius	110cm
Inner radius	27cm
Outer radius of the drift volume	100cm
Inner radius of the drift volume	35cm
Length of the drift volume	150cm (of each half)
Cathode	Membrane at the center of the TPC
Electric field strength	∼140 V/cm
Magnetic field strength	0.5 Tesla
Drift gas	90% Ar+10% Methane at Atmospheric + 2 mbar
Drift velocity	5.45 cm/μs
Drift time	$\sim 28\mu$s
Transverse diffusion	230 μm/$\sqrt{cm}$ at magnetic field 0.5 Tesla
Longitudinal diffusion	360 μm/$\sqrt{cm}$
Number of readout chambers	24 (12 per end plate)
Multiplisity (central collision)	~ 800
Number of pads	~ 80000
Pad numbers after zero suppression	$< 10\%$
Pad size	4x10 mm in inner sector area 6×12 in outer sector area
Spatial resolution	$\sigma z \sim 1$ mm, $\sigma x \sim 0.6$ mm, $\sigma y \sim 0.8$ mm
$\Delta E/dX$ resolution	$\sim 8\%$ (75 samples× 2 cm)
Maximum rate	$\sim 5-6$ kHz (Lum. 10^{27}cm^{-2}s^{-1})
Electronics shaping time	∼180 ns (FWHM)
Signal to noise ratio	20:1
Signal dynamical range	10 bits
Sampling rate	12.5 MHz
Sampling depth	350 time buckets

The another suitable gas mixture based on neon (90% Ne, 10% CO_2) is used in ALICE TPC [206]. It provides better momentum resolution because of reduced multiple Coulomb scattering within the drift volume. However, this gas is more expensive, a higher drift voltage is needed to keep the drift velocity above 2 cm/μs, and the primary ionization is lower.

Fig. 2.21 shows the drift velocity as a function of the field for the P10 gas mixtures [209]. The drift velocity peaks to 5.5 cm/μs at 140 V/cm. The dependences of the drift velocity and the diffusion coefficient against Ar fraction in the gas mixture are shown in figures 2.22 —2.24. The longitudinal diffusion coefficient in Ar/CH_4 only weakly depends on Ar fraction for argon fractions below 90%. Its value is about 360 μm/$\sqrt{cm}$ at a drift field of 140 V/cm. The time constant of the shaping amplifier has to be equal to the time dispersion in the collection of the ionization cloud which traverses the maximal drift

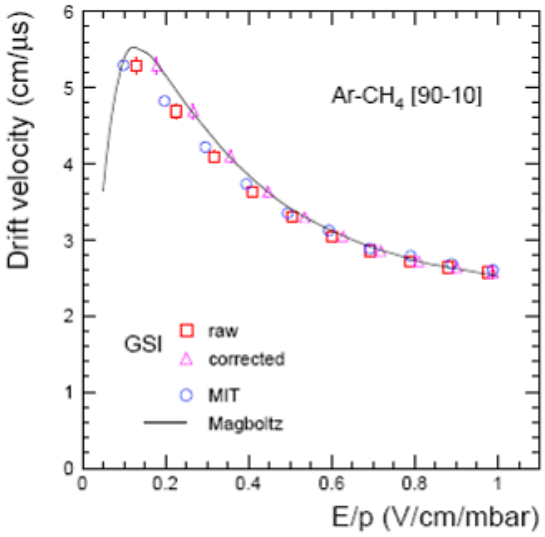

Fig. 2.21: Drift velocity as a function of the electric field.

length of the TPC. Electronics shaping time constant (full width at half maximum) has to be about 180 ns. The transverse diffusion depends on magnetic field. For magnetic field 0.5 T the value of 230 $\mu m/\sqrt{cm}$ was found [204].

The drift velocity of electrons in TPC can vary with changes in temperature, pressure and gas composition. An active feedback system will be used for stabilizing the drift velocity. It is based on monitoring the drift time of photoelectrons emitted from the TPC high voltage membrane under UV laser pulse.The variations in the electrons drift time can be consistently measured with an accuracy of 1 ns, which corresponds to a position accuracy of 55 μm. The STAR results [205] show that a 1 volt change on the field cage causes 0.5 ns change in the drift time over a distance 80 cm. The drift velocity for the electrons in the gas must be known with a precision of 0.1% in order to convert the measured time into position with sufficient accuracy. This corresponds to about 25 ns variation in the arriving time of electrons. Therefore, the desired high voltage stabilization should be better than $\pm$25 V.

Gas pressure

One could advance arguments in favor of atmospheric or higher pressure. However, MPD will be used to detect relatively low energy particles, therefore minimum material budget of TPC field cage walls and minimum multiple scattering is of the highest priority. Consequently, the increase of pressure and thickness of the field cage and outer cage walls are not acceptable. We propose 2 mbar overpressure in the drift volume and both containment sections.

B and E field requirements

The TPC is used to measure the momentum and emission angle of charged particles. The z coordinate is obtained from the drift time and the known drift velocity. The $r\varphi$

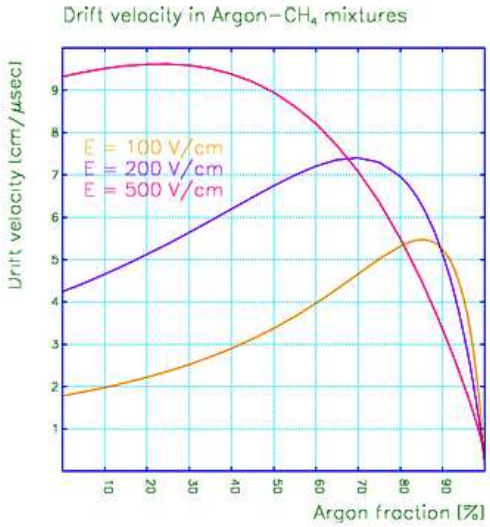

Fig. 2.22: Drift velocity in Argon-CH4 mixture as a function of Argon fraction.

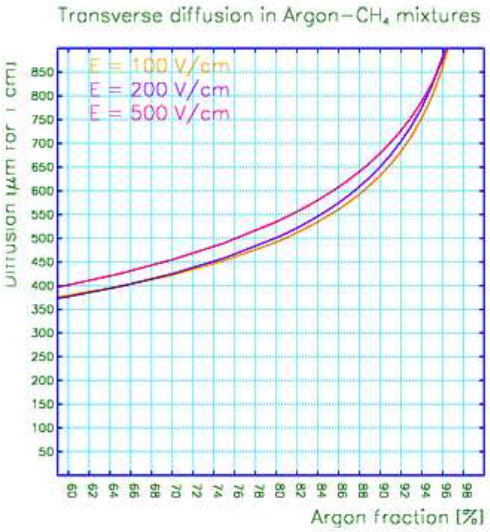

Fig. 2.23: Transverse diffusion in Argon-CH4 mixture as a function of Argon fraction.

coordinate is defined by interpolating signals induced on the cathode pads. The TPC will register spacial coordinates of 50 points for each track traversing the inner and outer field cages.

The trajectory of a charge particle in the TPC is a helix; and its projection onto the end plate is an arc of a circle. Measurement of the sagitta of this arc yields the curvature radius which is proportional to the transverse momentum of the particle. The transverse momentum resolution is related to the resolution in the measurement of the sagitta δs[mm] as $\Delta p/p = 0.027 p \delta s/(l^2 B)$, where B[T] is the modulus of the magnetic field and l[m] is the length of the projected trajectory. For MPD requirements the corresponding error in the sagitta is 280 μm.

The drift velocity of electrons in a gas is described by the Langevin equation as function of electric field E and magnetic field B:

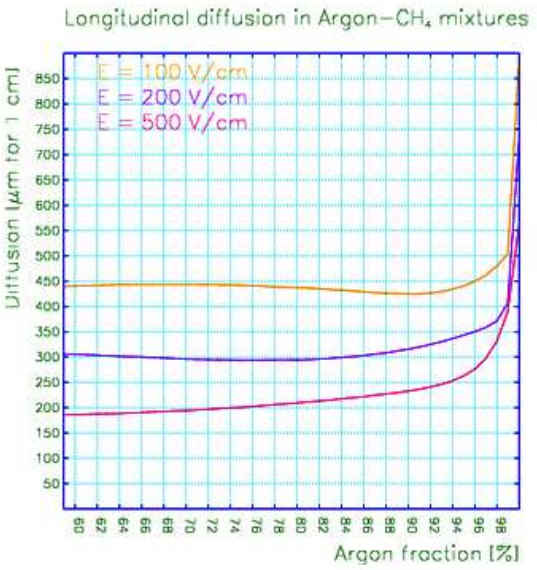

Fig. 2.24: Longitudinal diffusion in Argon-CH4 mixture as a function of Argon fraction.

$$\vec{\nu}_d = \frac{\mu}{1+(\omega\tau)^2}\left(\vec{E} + (\omega\tau)\frac{\vec{E}\times\vec{B}}{|\vec{B}|} + (\omega\tau)^2\frac{(\vec{E}\cdot\vec{B})\vec{B}}{|\vec{B}|^2}\right)$$

where μ is the electron mobility, ω is the cyclotron frequency and τ is the mean drift time between two collisions with gas molecules. In the ideal TPC, E and B are exactly parallel. In reality there are deviation due to field inhomogeneities and a global angle between E and B caused by the tilt of the TPC field cage in the magnet.

The radial fields components are dominant in producing azimuthal shifts since the azimuthal field components are constrained by the cylindrical symmetry of the TPC and the magnet. The azimuthal shift at the end cap due to radial magnetic field component is then

$$\Delta r\varphi = \frac{\omega\tau}{1+(\omega\tau)^2}\int_z^{z_{max}}\left(\frac{B_r}{B_z}\right)dz$$

A quantitative estimate of the allowable field inhomogeneities can be found by setting the above expression equal to the permitted sagitta error.

$$\int_z^{z_{max}}\left(\frac{B_r}{B_z}\right)dz = \Delta s\frac{1+(\omega\tau)^2}{\omega\tau} = 0.775mm$$

$\omega\tau$=2.34 for $90\%Ar + 10\%CH_4$ mixture and B=0.5 T
This corresponds to an average value of

$$\left|\frac{B_r}{B_z}\right| = 5.2\cdot 10^{-4}.$$

The allowable uncertainly in the electric field has the same value

$$\left|\frac{E_r}{E_z}\right| = 5.2\cdot 10^{-4}.$$

TPC field cage and cathode

The tracking volume of the TPC is confined by a 2.2 m outer diameter outer field cage (OFC), 0.54 m diameter inner field cage (IFC), and pad planes spaced 1.5 m from of the central high voltage membrane. The basic TPC configuration is shown in Fig. 2.25. The tracking volume is divided into two chambers by a high voltage membrane placed at the center of the outer field cage. A high negative potential is applied to this membrane which, with the two field cages, defines a region of constant electric field.

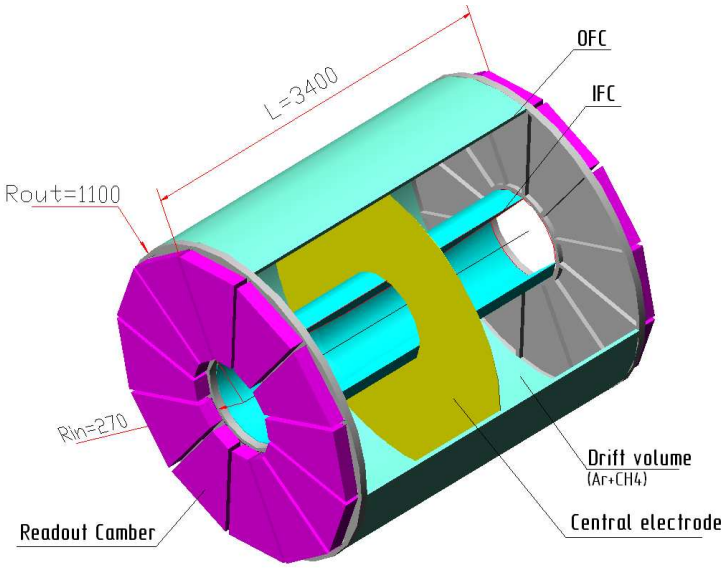

Fig. 2.25: Schematic view of TPC. The gas filled volume between the outer (OFC) and the inner (IFC) field cages with one thin central electrode, endplates and readout pads ensures minimal particle scattering.

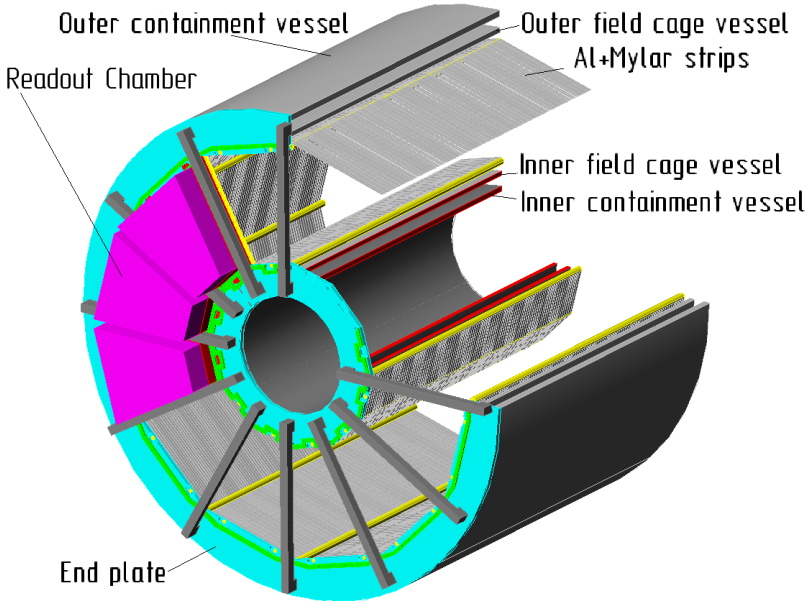

Fig. 2.26: The outer (OFC) and inner field cages (IFC) opened to show the narrow 3-5cm gap between field cages and insulating gas containments.

The main task of the TPC field cage is to provide a uniform electrostatic field in a cylindrical high-purity gas volume to transport the primary charges over long distances (1.5 m) towards the readout end-plates. For reasons of symmetry in colliding beam experiments, two such field configurations are chosen, back-to-back in a common gas volume, with a common high-voltage (HV) electrode located at the axial center of the cylinder.

The central electrode and two opposite axial potential degraders provide uniform drift fields. The drift field value should be chosen from the intrinsic properties of the drift gas affecting the drift velocity and the diffusion of primary ionization electrons. Thus, for the maximum drift path 1.5 m and P10 drift gas, the HV at the central electrode should be as high as 20 kV to provide the electron drift velocity of 5.5 cm/μs. In general, our design is similar to that of the TPCs used in STAR [205] and ALICE [206] experiments, except for the size. The actual field cage is surrounded by an insulating gas envelope (containment) as shown in Fig. 2.26. The containment provides personnel and operation safety with minimum material traversed by particles. The outer containment surface is coated with thin *Al* foil screen.

The main function of the OFC is to constrain the electric potential along one boundary of the active volume of the TPC with homogeneous electric field at one side and zero fields at the other side of the OFC. The OFC should be airtight to minimize drift gas contamination with oxygen and water. To have minimal material budget around the beam interaction point, the outer field cage should serve as a main structural support for the TPC itself. The OFC is a 3.00 m long cylinder with a 2.2 m outer diameter. Figure 2.27 shows the overall configuration and some details of the OFC.

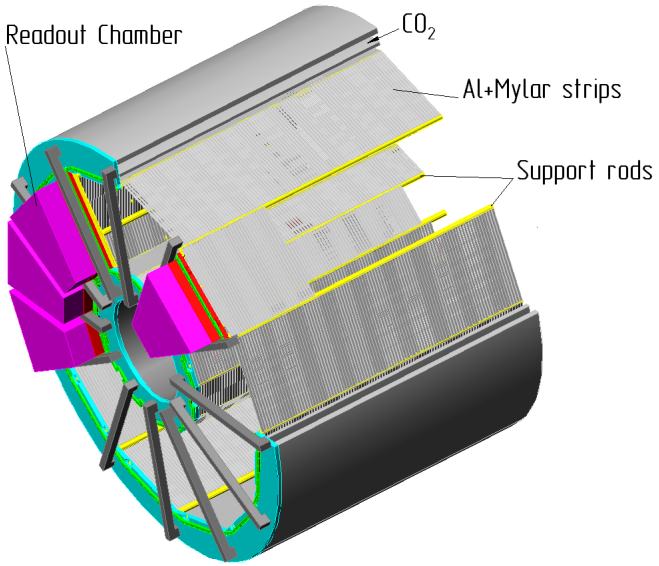

Fig. 2.27: The field cage volume is surrounded by 2 insulated gas envelopes. 12 rods along the OFC and IFC circumferences support the aluminized Mylar stripes forming the electric field boundary and provide minimum field distortion.

The primary function of IFC is defining the electrical potential along the inner radius of the active volume of the TPC; its secondary function is that of gas containment. Its support structure is not as substantial as that of the OFC to be required only for self support. The space between the field cage IFC and the containment vessel is filled with a dry gas such as nitrogen or CO_2. This configuration is shown in Figure 2.27. The IFC must

perform its functions and at the same time has the minimum radiation length for particles passing through it into the TPC's tracking volume. Therefore, minimum radiation length materials should be used to fabricate the IFC itself and the inner containment vessel. Fabrication of the IFC will be slightly easier than that of the OFC due to the smaller diameter (70 cm against 2.2 m).

As it was mentioned, our design is similar to that of the TPCs used in STAR and ALICE experiments but, considering vessels forming drift gas and containment volumes of the TPC, we investigate a possibility to produce all four cylinders as monolithic carbon fiber plastic constructions. Such an approach allows one to minimize problems with gluing of parts and fragments. Moreover, we suppose to mount field cages, central electrode and end plates as an independent precisely adjusted construction what will be inserted between carbon fiber vessels and fixed mechanically and with epoxy. Calculations show that walls of vessels will be rather thin (1-3 mm).

In our design of the central membrane we take advantage of the experience of STAR TPC in fabrication of the central membrane using 70 μm Kapton films bonded with a double sided tape. The carbon-loaded Kapton film of 200–250 Ω surface resistance provides sufficient current for voltage dividers and gives possibility to use aluminum stripes for laser calibration. A membrane, stretched over the hoop mounted in OFC and not glued to IFC, allows one to avoid problems of connection with the thin (6–7 mm) IFC wall [204]. 12 rods will be placed along the outer and inner field cage circumferences similar to those used in the ALICE TPC (see Fig. 2.28). These rods are used to support the mylar strips (13 mm wide, 30 μm thick, aluminum covered) of the potential degrader; 4 rods serve as a UV pipeline for laser calibration system, one is the voltage degrader and one provides high voltage supply for the central membrane. We shall investigate a possibility to design rods 25–30 mm in diameter which should be mounted near the IFC.

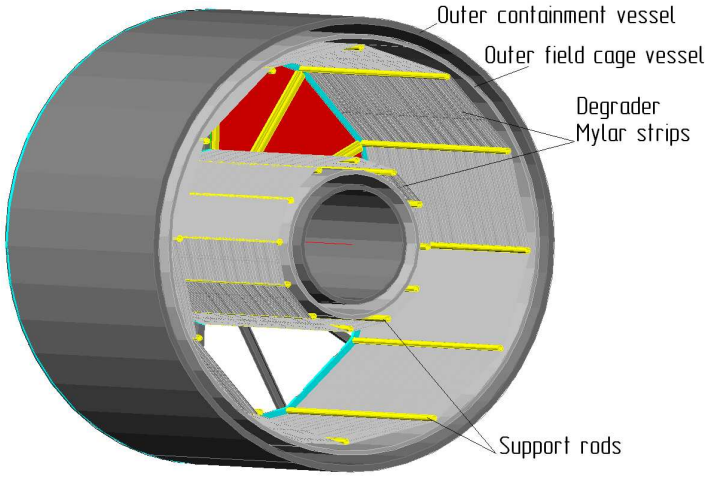

Fig. 2.28: The half of TPC volume viewed from central membrane. Rods supporting potential degrader Mylar strips are shown.

Detailed studies of the reliability of the MPD TPC design choice have been performed by means of computation of internal forces and deformations within the elements of the TPC mechanical structure. The results of calculations of the mechanical deformation profile in the TPC wall performed with the ANSYS code are shown in Fig.2.29. The largest deformation is not greater than 95 μm for a 2 m long Kevlar tube.

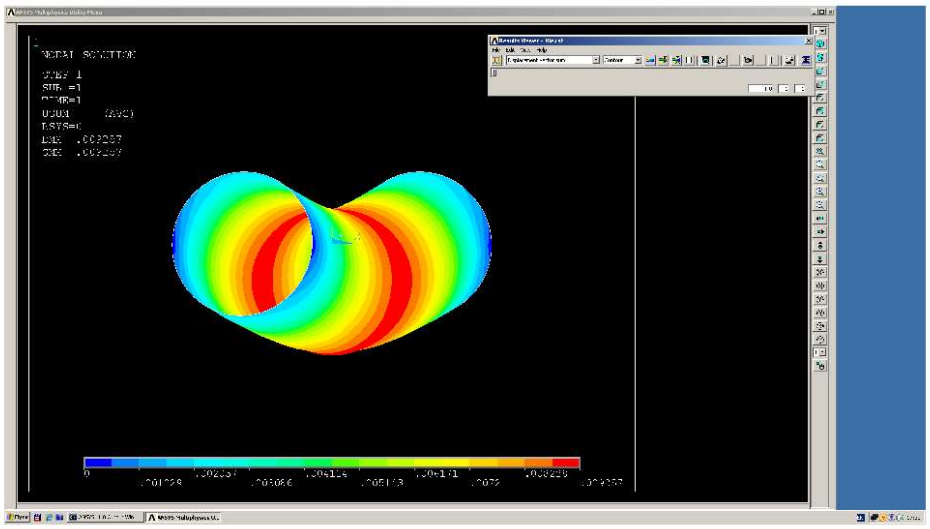

Fig. 2.29: The deformation profile in the TPC cylinder wall as calculated with the ANSYS code.

TPC readout chambers

The readout system is based on the Multi-Wire Proportional Chambers (MWPC) with readout pads. The end-cap readout plane is similar in design to that used in other TPCs such as of STAR and ALICE. The readout planes, MWPCs with pad readout, are modular sectors. 12 such trapezoidal sectors, each covering 30° in azimuth, are mounted into the sector cutouts of the end-plates.

The readout chambers are patterned after the scheme of design commonly used in a TPC. The chambers consist of a pad plane and three wire planes. The amplification/readout layer is composed of the anode wire plane with the pad plane on one side and the ground wire plane on the other. The third wire plane is a gaiting grid. This grid is a shutter to control the entry of electrons from the TPC drift volume into the MWPC and block the positive ions produced in the MWPC, keeping them from entering into the drift volume where they would distort the drift field.

All wires and pad rows run in the azimuthal direction for most precise determination of momenta of the highest transverse momentum particles whose tracks are nearly straight radial lines. The sagitta of the high transverse momentum tracks is most accurately determined by setting the anode wires roughly perpendicular to the straight radial tracks because position resolution is best along the direction of the anode wires. In the other direction the resolution is defined by the spacing between the anode wires.

The dimensions of the rectangular pads have to be optimized to provide the best position resolution for stiff tracks and dE/dx resolution. The optimum pad width in the azimuthal direction is defined by the distance from the anode wire to the pad plane. The avalanche signal should be spread over two or three adjacent pads for more accurate determination of the centre of the distribution. This condition is met if the pad width is two times larger than the gap between the anode wires and the pad plane [206, 210]. The

position reconstruction accuracy depends on the signal-to- nose ratio and track angle. Typically, it is better than 20% of the pad width.

For hadron and electron identification a dE/dx resolution of better than 8% is desirable. It depends on the pad length. The pad length in radial direction for a given value of dE/dx resolution can be estimated using the empirical relation of Allison and Cobb [211]

$$\frac{\Delta dE/dx}{dE/dx} = \frac{0.96}{2.35} N^{-0.46} l^{-0.32}$$

where l is the pad length and N is the number of points per track. The value of dE/dx resolution consist with ~7% for the number $N = 40$ of pad rows and $l = 1.2$ cm the pad length. The readout chamber will have a symmetrical geometry as shown in Fig. 2.30.

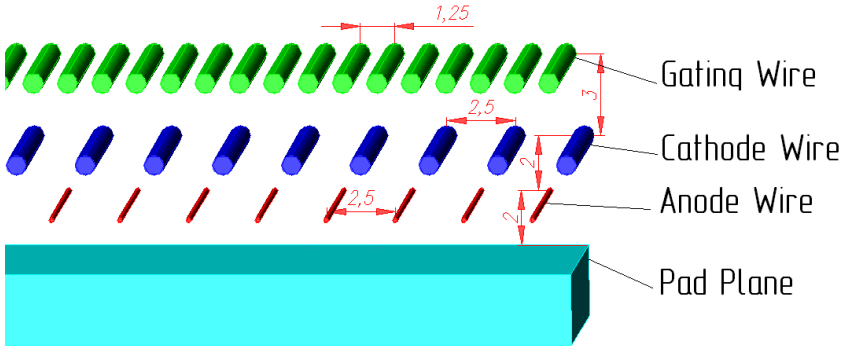

Fig. 2.30: Schematic view of TPC readout chamber.

The gap between the anode wire grid and the pad plane, as well as the distance between the anode wire and cathode wire grids, is 2 mm. The gaiting grid is located 3 mm above the cathode wire plane. To reduce the accumulated charge per unit length of the anode wire and thus the gas condition, the anode wire pitch has to be small enough. It is matched with the pad length and is set equal to 2.5 mm. The same pitch value is set for the cathode wire grid. The gaiting grid wire pitch is two times smaller. The anode wire and gaiting grid wires are staggered with respect to the cathode wire.

From the proportional chamber geometry described above, the pad width in the azimuthal direction has to be about 4 mm.

The gas amplification must be high enough to give adequate position resolution and provide the signal-to-noise ratio at a level of more than 20:1. On the other side, the gain must be low enough to be well within the proportional mode to maintain dE/dx resolution. Typically, the gain is a few units of 10^3.

The tracks in the TPC simulated with the UrQMD code for central $Au + Au$ collision at $\sqrt{s_{NN}} = 9$ GeV are shown in Fig. 2.31. About 1000 charged particles tracks are registered in the TPC, 16% of which correspond to the particles with transverse momenta less than 100 MeV/c. These tracks occupy the about 10 cm area around the inner field cage wall. Using short pads in this area will provide better two track separation of low momentum tracks with large crossing angles.

The pad plane is a trapezium with the bases of 200mm and 520mm and the height of 600 mm. It will contain 14 rows of 4×10 mm^2 pads and 40 rows of 6×12 mm^2 pads in the inner and outer area, respectively. The total number of pads in the TPC will amount to 80000.

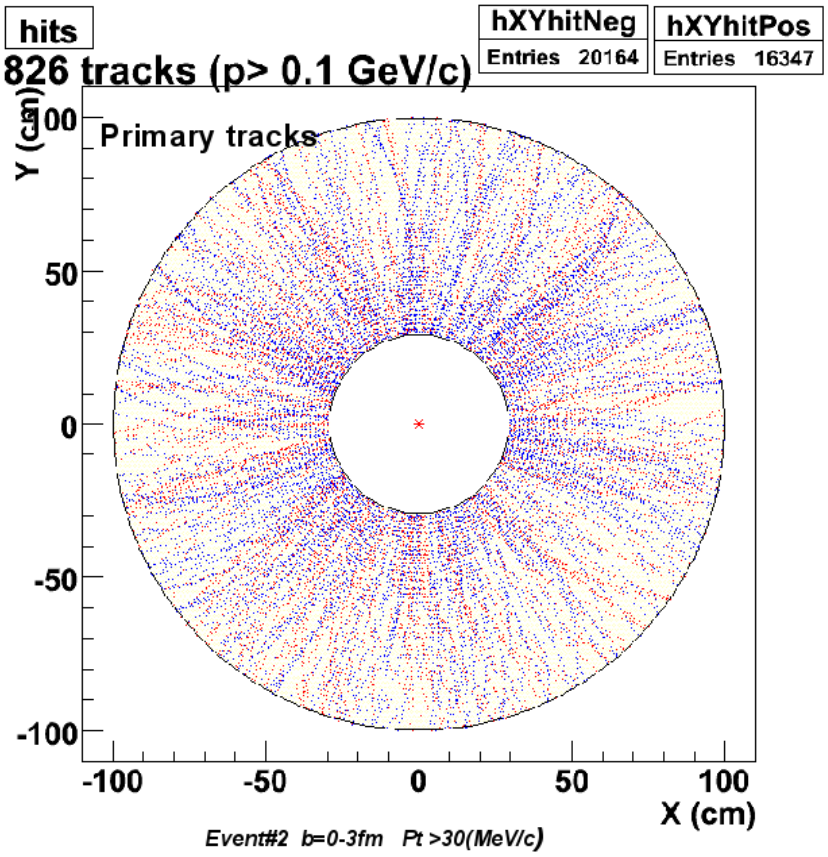

Fig. 2.31: Simulated charge tracks in the TPC for a central Au + Au collision.

The relative pad pulse height distribution is not entirely determined by the pad response function. It depends on the diffusion in the gas and on the large variations in track qualities such as dip angle, drift distance and crossing angle. It is not possible for a TPC to focus the design on a particular condition and optimize its performance only by simulation. The experience of other TPC teams shows that none of the simulated parameters such as dE/dx resolution, momentum resolution and two track resolution shows any dramatic dependence on the design parameters because a lot gained through oversampling and averaging. In addition to simulation, a prototype of the pad readout chamber has to be build and studied to verify charge coupling parameters.

TPC testing and calibration

The UV laser system is a part of the test and calibration procedure designed to produce a set of tracks at well defined angles and positions. The system will provide on-line measurements of drift velocity to evaluate effects of gas pressure changes (caused by changes of atmospheric pressure), temperature and contribution of $\mathbf{E}\times\mathbf{B}$ and space charge effects. The beams follow the paths of stiff tracks emerging from the interaction region and can be used for correcting the sagitta of such stiff tracks.

In order to minimize the error in the absolute position measurement by TPC, it is necessary to account for both static and time-dependent distortions in the drift path of the ionization cloud. The static distortions are the result of non-uniformities in the B and E fields. A calibration system that provides absolute positional references is needed so

that a deconvolution procedure, which determines the absolute spatial position from the row pad and time bucket information, can be developed. The time-dependent distortions can result from the changes in gas performance, in environmental variables (temperature or atmospheric pressure), or from spontaneous failures. A calibration system that can reproduce fiducial tracks is needed to monitor the TPC performance. The positional accuracy of the calibration system must be significantly better than the spatial resolution of the TPC. Taking into account experience of STAR and ALICE, we hope to obtain similar values.

The system selected to perform these functions consists of two pulsed 20 mJ 5-10 ns Nd:YAG lasers with 10 Hz repetition rate. The 20 mm wide beams from each laser are split to four beams and then, through 4 rods inside the drift volume of TPC, directed to 1 mm diameter micro mirrors to form 112 narrow calibration beams within the half of active volume of the TPC (224 beams in whole TPC). This number of beams is of the same order as in STAR [212, 213] and ALICE [206] TPCs and is sufficient to calibrate the TPC at different η and φ.

A carbonized kapton membrane with a pattern of 3 mm wide aluminum stripes glued on is proposed for the central electrode. The electron clouds emitted from the stripes in a one-photon ionization process induce signals similar to those induced by the laser beams in the TPC volume. The membrane pattern covers all the TPC sectors at the maximum drift distance and will be used to align all TPC readout sectors at both sides of the membrane. This is the easiest method to align the opposite readout sectors [214].

In addition to the laser calibration, the TPC is supposed to be tested with cosmic rays prior to mounting inside of the MPD magnet. During these tests TPC should be rotated around its axis on the service wheel. Changing gravitational deformations allows one to check the performance of laser beam position monitoring system, based on CMOS cameras, as well as remote mirror adjusting devices with piezoelectric picomotor drivers. The position of two detectors with the high coordinate resolution — TPC and Inner Tracker (IT), should be measured precisely in the process of mounting to align them with the NICA collider and MPD magnet systems. To take into account the mechanical deformations due to magnetic field, displacement monitoring system like that of ALICE [206] will be used with collimated laser diodes and CMOS position detectors mounted on the TPC end plate, and spherical mirrors mounted on IT. The system provides displacement measurements with a 10 μm accuracy.

The calibration of the readout channels (with a spread of $\sim$20%) can be also performed by injecting of ^{83}Kr gas into the TPC volume. Dedicated krypton runs can be arranged periodically during the normal data taking. This radioactive krypton isotope decays with emission of Auger electrons within the 10 to 50 keV interval. The normalization of the channels is based on the fact that the illumination of the chamber is homogeneous.

Gas system

Taking into account that the volume-to-surface ratio for MPD TPC is close to that of NA49 and only twice lower than that of ALICE, and the total volume of MPD TPC is 10 m^3, we propose gas mixture circulation flow rate to be 2-3 m^3/h for the chosen sealing methods. This flow rate is 10 times lower than that used in the STAR TPC. This difference is essential because, in this experiment, like in STAR, the P10 gas mixture ($90\%Ar + 10\%CH_4$) will be used. Therefore, it seems to be reasonable to base our design on the results obtained at STAR experiment [215] with no significant changes. All other

systems (P10 mixture preparing, pressure control, mixture control, purification, filling and refilling, temperature control, computer control and gain control) are planned to be similar. Obviously, the lower gas flow slightly simplifies the task but, nevertheless all control systems should be elaborated, tested and tuned.

	Volume/surface[m]	O_2[ppm]
ALEPH	0.55	20
NA49 MTPC	0.47	1-2
ALICE	0.70	<5
STAR	0.56	<25
MPD	0.3	1-2

Table 2.11: Volume-to-surface ratios for different TPCs

2.3.2 Capabilities of the TPC

TPC readout simulation

In order to study the performance of the TPC a simulation program chain was implemented into the MPD ROOT software package. It contains different codes to generate detector geometry and ion collision events. These events are tracked and processed consequently through all subdetectors of MPD by the GEANT code. The TPC geometry used in the simulation is shown in fig. 2.32. It includes the high voltage membrane placed in the center of the TPC volume halved by membrane field cage and two readout endplates. Each endplate contains 12 sectors of pad readout proportional wire chambers. The size of pads is 4×7.5 mm over the entire sector. The pads are placed continuously in the rows along the azimuthal direction perpendicularly to the sector axial line.

The electromagnetic interactions of the primary particles with the gas lead to the release of primary electrons. (The mean number of primary electrons is about 100 per cm for a MIP in P10). The primary electrons ionize gas atoms and produce secondary electrons, creating electron clusters. The clusters are assumed to be point-like. The total number of electrons in the cluster is given by

$$N = (E_{tot} - I_{pot})/W_i + 1$$

where E_{tot} is the energy loss in a given collision, W_i is the electron-ion pair production effective energy, and Ipot is the first ionization potential. The distribution of a number of electrons in the clusters is shown in Fig. 2.33. Since the distribution appears to be rather wide, it should be remembered in choosing the dynamic range of the ADCs used.

Each electron is traced to the pad readout plane. During the drift, the electrons are subject to diffusion. The electron cloud, after drifting over a distance L_{drift}, can be described by the 3-D Gaussian distribution:

$$P(x,y,z) = \frac{1}{\sqrt{2\pi}\sigma_T}\exp\left[-\frac{(x-x_0)^2}{2\sigma_T^2}\right]\cdot\frac{1}{\sqrt{2\pi}\sigma_T}\exp\left[-\frac{(y-y_0)^2}{2\sigma_T^2}\right]\cdot\frac{1}{\sqrt{2\pi}\sigma_L}\exp\left[-\frac{(z-z_0)^2}{2\sigma_L^2}\right],$$

where (x_0, y_0, z_0) is the electron creation point, D_T and D_L are the coefficients of the transverse and longitudinal diffusion, $\sigma_T = D_T\sqrt{L_{drift}}$, and $\sigma_L = D_L\sqrt{L_{drift}}$. The values

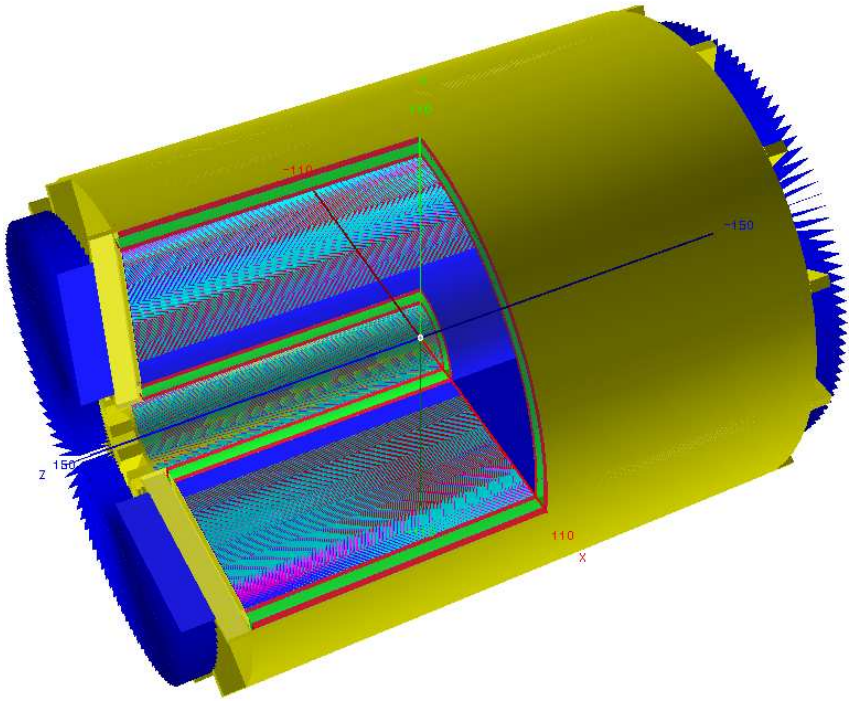

Fig. 2.32: Simulation view of TPC in the MPD ROOT.

of $185\mu\text{m}/\sqrt{cm}$ and $320\mu\text{m}/\sqrt{cm}$ for the transverse and longitudinal diffusion respectively were used in the simulation.

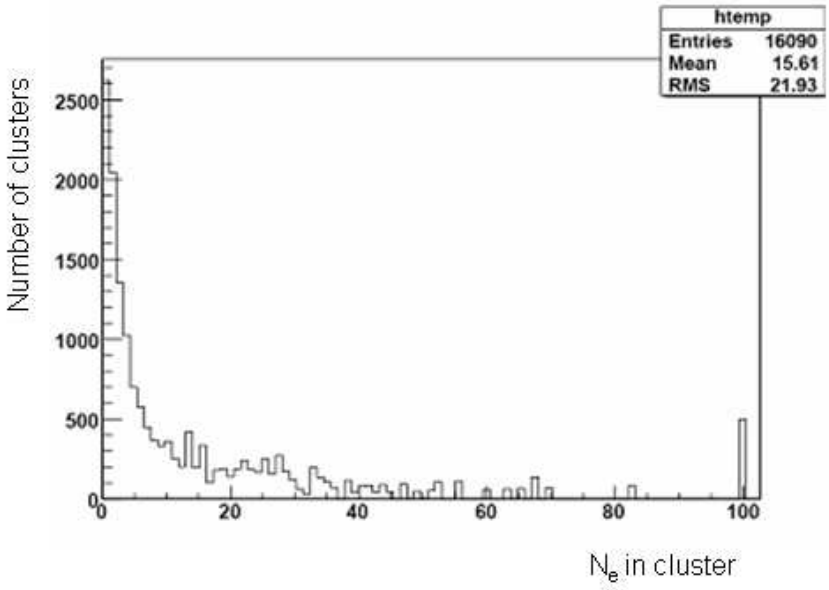

Fig. 2.33: Distribution of the number of secondary electrons in the cluster.

In Fig. 2.34 the distribution of electrons in the cloud as a function of drift time is shown for a large electron cluster after 80 cm drift. The time spread width of the cloud is about 55 ns (∼3 mm). At least 3 time buckets have to cover the cloud spread to find the arrival time with a precision of ∼20% of a bucket. The spread of the electron cloud after the maximal drift length, with allowance made for the pad response function, is equal

to σ ∼4.8 mm (0.089 μs). The requirement to have at least three time buckets for one electron cloud is consistent with ∼280 time buckets depth. For a two-track resolution of ∼1 cm (0.183 μs) the designed sampling depth has to be about 500 time buckets.

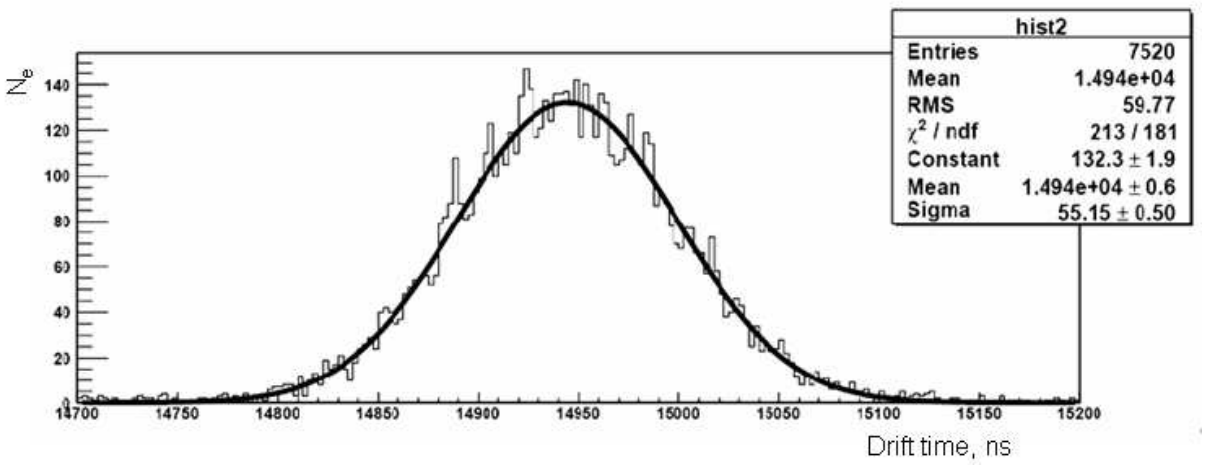

Fig. 2.34: The longitudinal diffusion of an electron cluster.

The electron collected on the anode wire of the readout chamber induce charges on the pad plane. The distribution of these charges over the pad area is the pad response function which is a distinctive characteristic of the readout chamber which determines its intrinsic resolution. It is approximately the Gaussian distribution

$$PRF(x,y) = A \cdot e^{-(x-x_0)^2/2\sigma^2}$$

where x_0 is the center of the pad and σ is the intrinsic resolution. In the simulation, the value of intrinsic resolution was taken equal to σ=1.97 mm. Each electron from the cloud induces charges on the pads according to the pad response function. Then this charge is passed trough a preamplifier/shaper chain with an amplification of about 10^4 and shaping constants T_{diff}=50 ns and T_{int}=50 ns. The total response is the convolution of the charge spreads induced by each cloud electron. The signal is then processed by a 10 bit ADC with a threshold corresponding to 500 electrons and 40 MHz sampling rate.

Fig. 2.35 shows charge particle tracks in the TPC volume traced by GEANT for a central $Au + Au$ collision at $\sqrt{s_{NN}} = 9$ GeV.

The signals induced on the pad plane obtained by the method described above are shown in fig. 2.36 and fig. 2.37 for the 5-th and the 905-th time sample respectively.

The set of the induced pad signals taken as a whole in the pad-time space is used then to find a set of three dimension hits (clusters) which are used for reconstruction of the corresponding space points. The K-mean clustering algorithm [216] commonly used in the computer vision as a form of image segmentation was applied. Then the center of gravity of cluster pads is taken as the reconstructed position of the corresponding three dimension space point.

Distribution of clusters found as described above is shown in Fig. 2.38 for a TPC half. Concerning the actual space-point errors, they are approximately proportional to the dispersions (second central moments) of the corresponding clusters at least for stiff tracks which cross the entire TPC [206]. The precision of the reconstruction of the cluster position depends on the track parameters and then on the cluster size. The distribution

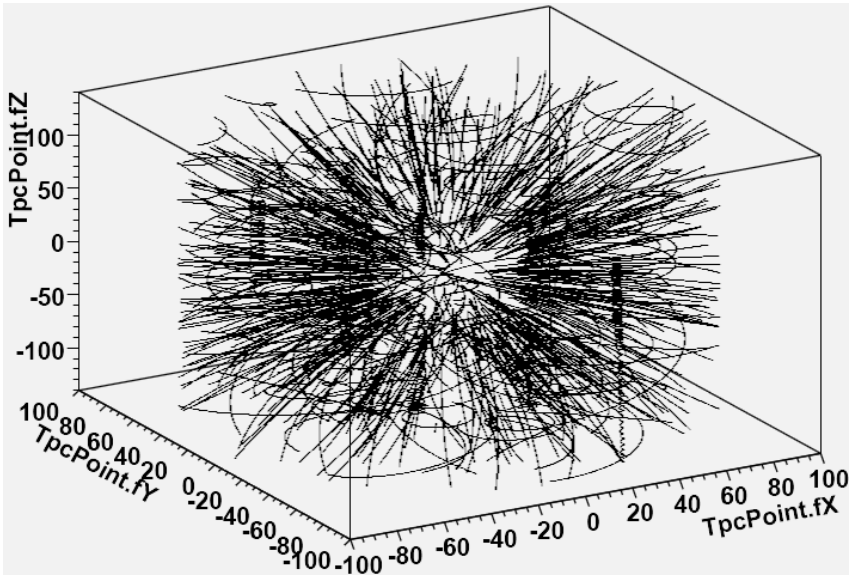

Fig. 2.35: Charge particle tracks in the TPC volume for a central Au + Au collision.

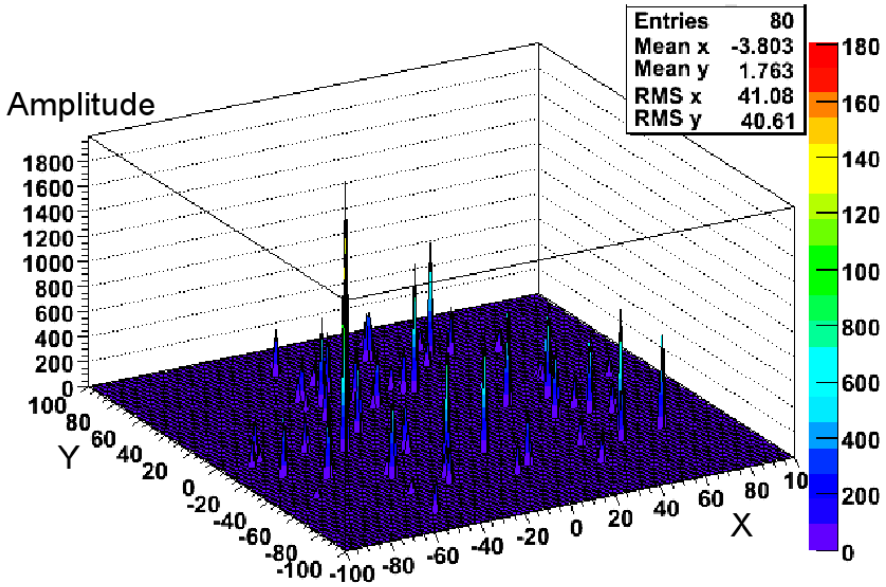

Fig. 2.36: The signal induced on the pad for the 5-th time sample.

of the second central moments for the clusters along pad row in one time bucket is shown in Fig. 2.39. The dispersion of the size for most of the clusters is about 3 mm, i.e. the signal is induced on three pads.

The spatial resolution

The azimuthal position resolution $\sigma_{r\varphi}$ of a single space point required to achieve a given momentum resolution is determined by the relation:

$$\frac{\Delta p_t}{p_t^2} = \frac{\sigma_{r\varphi}}{0.3 \cdot B \cdot L^2} \sqrt{\frac{720}{N+4}}$$

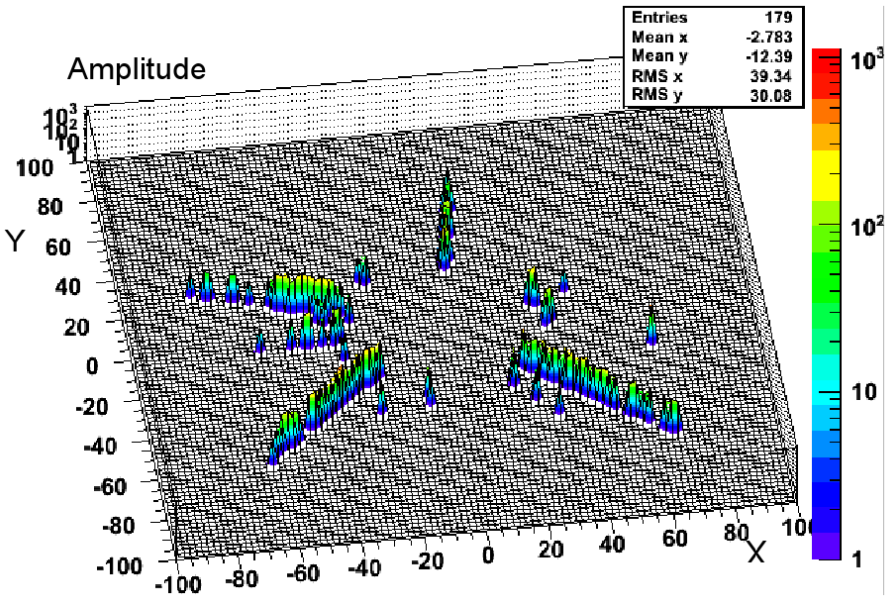

Fig. 2.37: The signal induced on the pad for 905-th time sample.

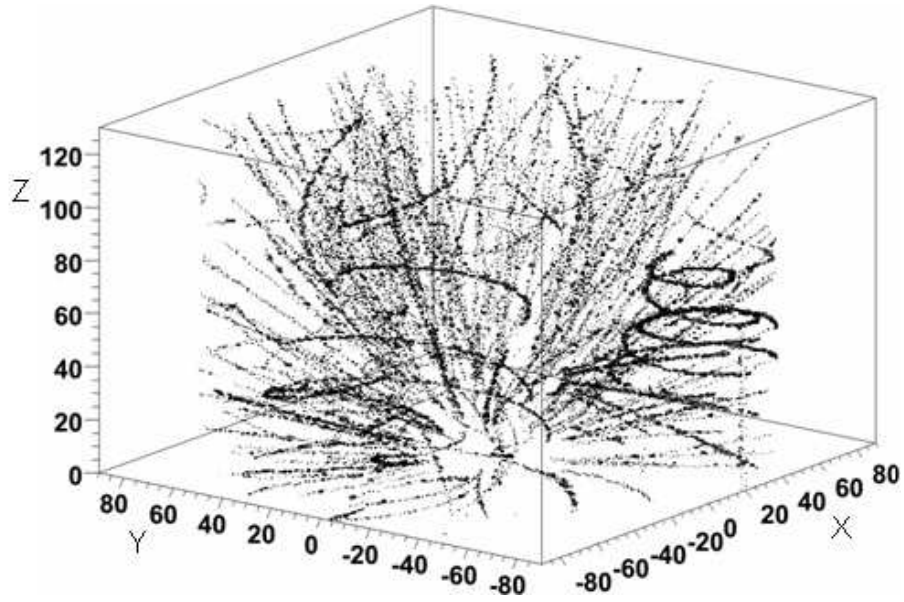

Fig. 2.38: TPC clusters for Au + Au central collision (half TPC view).

where L is the total visible track length, N is the number of space points on the trajectory and B is the magnetic field. The contributions from the multiple scattering and energy loss are not included here. For our momentum resolution requirement, $\sigma_{r\varphi}$ must be about 620μm.

The $r\varphi$ resolution is given by: [217, 218]

$$\sigma^2_{r\varphi} = \sigma^2_0 + \sigma^2_d/\cos^2\alpha + \sigma^2_\alpha(tg\alpha - tg\psi)^2 + \sigma^2_\alpha tg^2\alpha\cos^2\alpha,$$

where σ_0 is the intrinsic pad response resolution, $\sigma^2_d = \sigma^2_t/(N_e h)$, $\sigma^2_\alpha = d^2/(12N_{eff}h)$, σ_t is the electron transverse diffusion after a drift to pad, h is the pad length, d is the wire pitch, N_e is the effective number of electrons per unit length, N_{eff} is the effective number

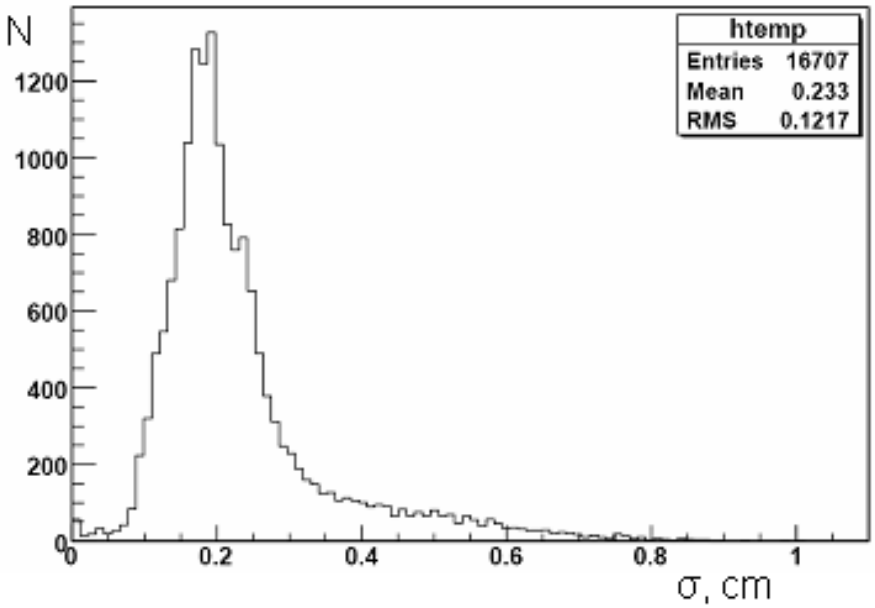

Fig. 2.39: The second moments distribution of cluster sizes along the pad row.

of electron clusters in a given sample, and ψ is the average Lorenz angle.

The three terms correspond to an intrinsic resolution, determined by the TPC readout chain and by the limited mechanical precision of the chamber geometry, the diffusion term, and the term which accounts for the crossing angle of the track relative to the normal of the pad row. For the signal-to-noise ratio of the readout chain 20:1, the noise contribution is small [204]. For the P10 gas mixture at atmospheric pressure, the mean ionization for minimum ionizing particle is about 100 electrons per cm [219]. The effective number of electrons sampled by the wire depends on the electron transverse diffusion over a drift length via declustering effect. This effect tends to increase N_{eff} and to improve the resolution until it is equal to the total number of electrons per track unit length. For our design parameters, the estimations give σ_d=201 μm , σ_α=152 μm, σ_0= 200μm, and total $\sigma_{r\varphi}$=320 μm for tracks perpendicular to the pad row, without considering the $\mathbf{E}\times\mathbf{B}$ effect near anode wires.

The position resolution along the pad rows was measured for the STAR TPC [204]. The pad geometry to be applied in our design is similar to that used in the inner sectors of the readout chamber of STAR. We believe that in our design the position resolution will be a little bit better because the anode wires pitch is decreased to 2 mm. The STAR TPC results are shown in Fig. 2.40c for a 0.5 T magnetic field. In these data the sigma was extracted from a Gaussian fit to the residuals distribution, i.e. to the distribution of distances between the hit position and the track extrapolation points.

Fig. 2.40d shows the position resolution along the z-axis. The position resolution depends on the dip angle θ (the angle between the particle momentum and the drift direction) and on the drift distance. The position resolution dependence on the dip angle is determined by the spread of ionization electrons over a distance along the drift direction. The resolution is best for short drift distances and small dip angles. The position resolution depends on the drift distance but the dependence is weak because of the large shaping time in the readout electronics. The resolution deteriorates, however, with the increase of dip angle because the time needed for electrons to reach the pad

becomes greater than the shaping time.

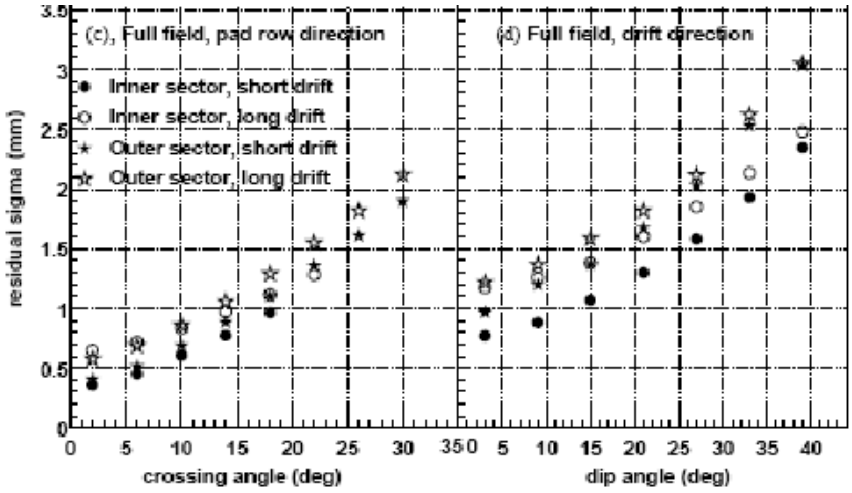

Fig. 2.40: Position resolution across the pad row for STAR TPC. The crossing angle is the angle between the particle momentum and pad row direction. The dip angle is the angle between the particle momentum and the drift direction.

dE/dX and particle identification

The energy loss method dE/dx, i.e. measuring the mean specific energy lost through the charged particles in the TPC gas, is a valuable tool for the particle identification. It works especially well for low momentum particles; but as the particle energy increases the energy loss becomes less mass-dependent, which significantly reduces the resolving power of the method. The measured energy loss depends on many factors such as gas gain, the readout electronics response variations and the ionization fluctuations. All these effects have to be controlled by monitoring and calibration. The same gas mixture as in the TPC of STAR detector $90\%Ar + 10\%CH_4$ will be used in our TPC.

The estimated dE/dx resolution for TPC depends on the track length. It has been shown [220] that resolution $\sigma\left(\frac{dE}{dx}\right)/\frac{dE}{dx} = 5.7\% \cdot L^{-0.37}$. Based on this formula, dE/dx resolution of MPD TPC with a depth of 75 cm is expected to be 6,3%. Using a sample of events from the central $Au - Au$ collision at $\sqrt{s_{NN}}$=9 GeV/c we reconstructed ionization loss per track using the truncated mean method. The number of samples per track in the TPC was 56 and the upper truncation level 70%. Fig. 2.41 shows ionization energy loss as a function of momentum for different types of particles.

Space charge effect

The position of a secondary electron at the pad plane can be distorted by non-uniformities in the electric and magnetic fields of the TPC as well as by the space charge of positive ions in the drift volume. There are two sources of the positive charge in the drift volume of the TPC: the ionization created by charge particles in the gas mixture and the positive ions backflow from the readout chamber. The backflow of positive ions can be reduced by implementation of a gaiting grid (the reduction factor has to be not lower than 10^4). The ion drift velocity is four orders of magnitude less than that of the electrons and so a permanent positive charge is built in the TPC drift volume, affecting the drift field.

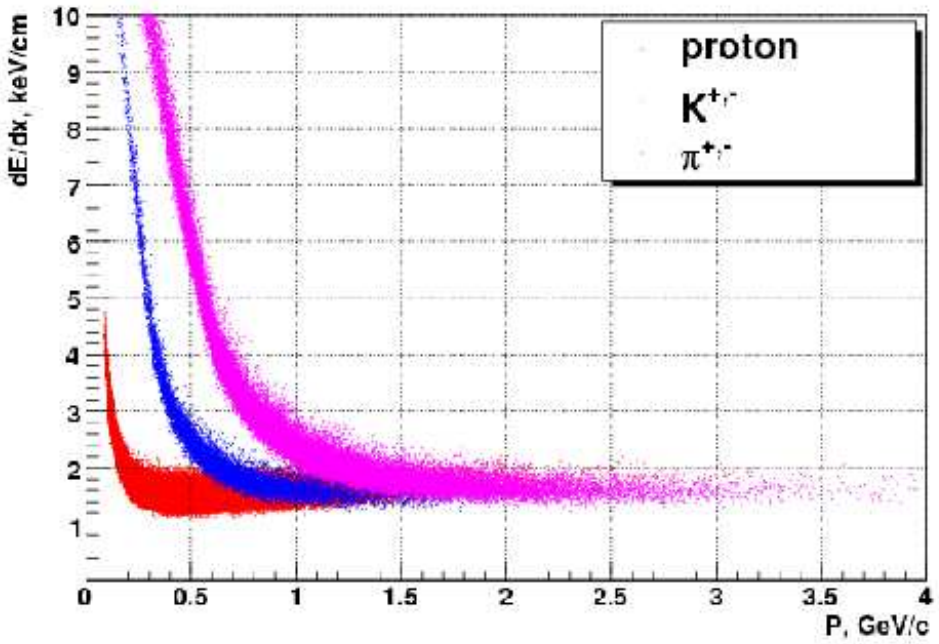

Fig. 2.41: Separation of particles in the TPC by ionization loss in the region of pseudorapidity $|\eta| < 1.2$

To estimate the space charge effect in the TPC we will use the formalism developed by S.Palestini et al [221, 222]. This formalism is applied for detector with the geometry of a parallel-plate capacitor with electrode planes perpendicular to the x axis and separation D between anode and cathode. The ionization is created uniformly over the volume of the detector at a volume rate of K ion pair/volume/s. The field E and the space charge ρ (due to positive ions) are determined by the continuity equation

$$\frac{\partial \rho}{\partial t} + \mu E \frac{\partial \rho}{\partial x} + \frac{\mu}{\epsilon}\rho^2 = K,$$

where ϵ is the dielectric constant, μ is the positive-ion mobility. If K is constant, E and ρ evolve toward a stationary case. The stationary solution is

$$E(x) = E_0 \sqrt{\frac{(E_A)^2}{(E_0)^2} + \alpha^2 \frac{x^2}{D^2}},$$

where E_A is the electric field at the anode, E_0 is the nominal electric field in the absence of space charge, α is the dimensionless parameter

$$\alpha = \frac{D}{E_0}\sqrt{\frac{K}{\epsilon\mu}}$$

Fig. 2.42 shows the ratio E_A/E_0 as a function of α. The solution of space charge problem is completely described by the parameter α.

The drift velocity of a positive ion is $\nu_{ion} \approx 0.213 \cdot 10^3$cm/s for the P10 gas mixture and the mobility is $\mu = 1.64 \cdot 10^{-4}$m^2/V/s. The maximal ion drift time is ~0.704 s.

The mean value of positive ion space charge in the $Au + Au$ event was determined using the STAR experimental data [223] on charge particle multiplicity at $\sqrt{s_{NN}}$ =9 GeV

for $1.2 \cdot 10^6$ positive ions created in the simulated central collision. The mean value of the positive ion space charge in the TPC is $2.4 \cdot 10^9$ ions for the event rate of $6 \cdot 10^3$ events/s, the effective injected charge density rate is $\sim 1.3 \cdot 10^{-10}$ C/m^{3}s. The stationary conditions would be reached after 0.7 s from the beginning of the beam exposure.

The corresponding value of the scaling parameter α is equal to 0.035 for an electric field E_0 of 130 V/cm, so the effects of positive charges will be negligible. Nevertheless, we have to take its effect into account and implement correction for the introduced distortions [224].

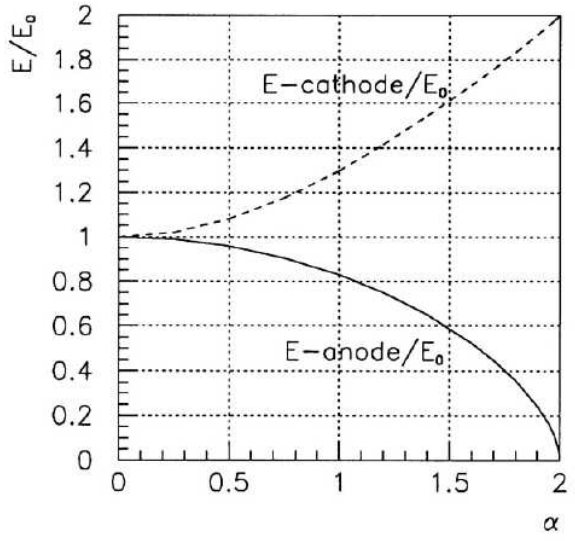

Fig. 2.42: Normalized electric field values at anode and cathode as a function of α.

2.3.3 Front-end electronics and readout.

General requirements

The front-end electronics has to read out the charge collected by about 80000 pads located in the readout chambers at the TPC end caps. These chambers deliver on their pads the current signals with a fast rise time and a long tail due to the motion of positive ions.

The main requirements to the front-end electronics are listed in Table 2.12.

System overview

The front-end electronics of MPD TPC includes about 80000 channels. A single readout channel consists of three basic units (Fig. 2.43): a charge sensitive preamplifier/shaper(PASA), a 10-bit low power 10–20 MSPS ADC, and FPGA logic unit which is a digital signal processor circuit.

The charge induced on the TPC pads is amplified and integrated by the PASA. It is based on the charge-sensitive amplifier followed by a semi-Gaussian pulse shaper. These analog functions are realized by a custom integrated circuits unit (ASIC) which contains 16 channels with a power consumption below 20 mW per channel. The circuit has a conversion gain of about 10 mV/fC and an output dynamic range of 2 V matched to the proposed ADC. It produces a pulse with a shaping time of ∼180 ns. The single channel noise is equivalent to ∼1000e$^-$ (RMS).

Table 2.12: The main requirements to the front-end electronics

Parameter	**Value**
Number of channels	80000
Signal-to-noise ratio	20:1
Dynamic range	∼1000
Noise (ENC)	< 1000 e$^-$
Conversion gain	∼10 mV/fC
Crosstalk	$< 0.3\%$
Shaping time	∼180 ns
Sampling rate	12.5 MHz
Signal dynamical range	10 bits
Sampling depth	350 time buckets
Tail correction after 1 μs	$\sim 0.1\%$
Event size	∼1 MB
Transfer data rate	∼5 GB/s $\rightarrow$ 50 MB/s
Power consumption	∼50 mW/channel

To measure a charge particle track, each pad of the TPC will be read out by a sampling ADC. If the system takes several samples for an ionization cluster reaching the pad, a 3-point fit can be used to localize the hit to within a fraction of a time sample. The number of digitized samples is determined by the diffusion spreading and two-track resolution requirement. If the signal is spread over 3 buckets, then the arrival time can be determined with an accuracy of ∼20% of a bucket length.

Since the dynamic range of the signals from the amplifier/shaper should be about 1000, one has to use a sampling 10-bit ADC running at a rate of 10÷20 MSPS (the corresponding period is 50-100 ns). The ADCs with the required conversion time, dynamic range, power consumption, and precision are commercially available.

Front-end basic components

Amplifier/Shaper The basic requirements for the amplifier/shaper are similar to the ones applied for PCA16 (developed at CERN) and PASA/ALICE, both are 16-th ASICs, which are used in the ALICE or STAR TPCs.

Programmable Charge Amplifier (PCA 16). Specification[225, 226]:

Power consumption < 8 mW/channel
16 channel charge amplifier + anti-aliasing filter
Fully differential output amplifier
Both signal polarities
Power down mode (wake-up time = 1 ms)
Programmable peaking time (30 ns - 120 ns)
Programmable gain in 4 steps (12 - 27 mV/fC)
Tunable time constant of the preamplifier
Chip dimensions = 1.5 mm $\times$ 4mm

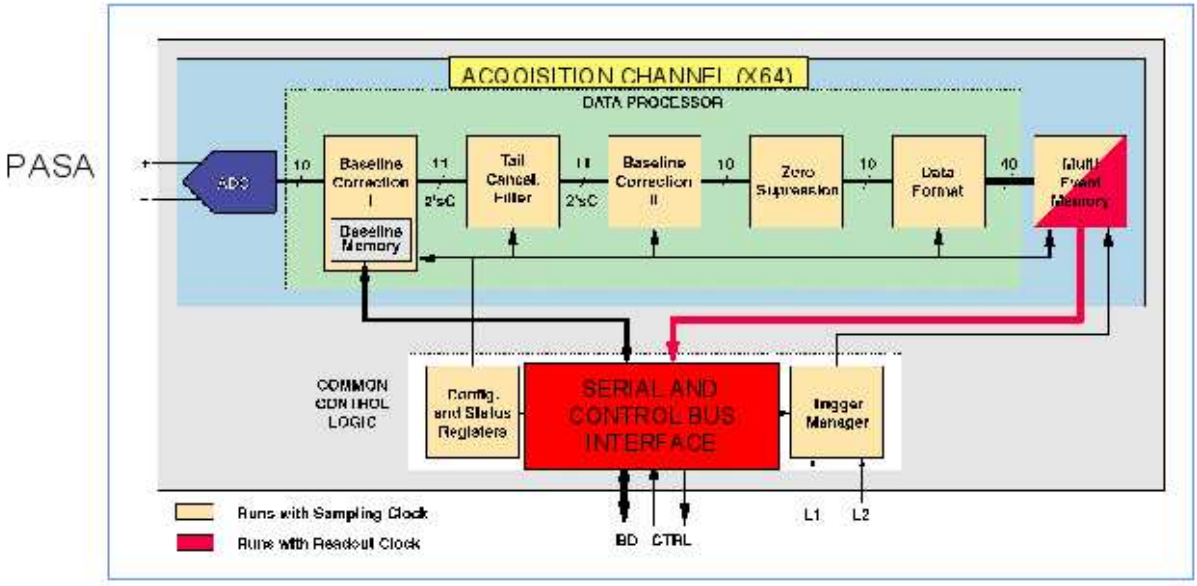

Fig. 2.43: Readout channel architecture.

PASA/ALICE specification[227]:

Equivalent Noise Charge (electrons)< 1000 e$^-$
Conversion Gain . . . . . 12 mV/fC
Shaping time (FWHM) . . . . . 180 ns
Channel-to-Channel crosstalk . . . . . $< 0.3\%$
Power consumption . . . . . $<$ 20 mW/channel
Both chips are intended to be tested at R&D stage.

Analog-to-Digital conversion The analog signal output of preamplifier/shaper circuits is sampled by an analog-to-digital converter with a 10-bit dynamic range at a rate of 10–20 MHz. Now we have a wide assortment of such ADCs. Power consumption and a number of channels in one chip become the basic requirements.

At the present time several custom ADCs can be considered as candidates for implementation in the NICA/TPC. One of them is the ADS5287 (Texas Instruments), which has suitable resolution, power dissipation, and sampling rate [228]. The ADC has a serialized output that allows to connect a large number of channels to one FPGA chip.

Main parameters of ADS5287:

Resolution . . . . . 10 bit
Channels . . . . . 8 Channels
Max Sample Rate . . . . . 65 MSPS
Min Sample Rate . . . . . 10 MSPS
Power Dissipation$\sim$40 mW/channel
Package . . . . . 9 mm$\times$9 mm

Digital Signal Processor based on FPGA Main functions which are similar to the ones used at TPC/ALICE are the following:

- interfacing ADCs channels
- tail cancellation
- baseline subtraction
- zero suppression
- formatting
- buffering
- high speed serial interface to data concentrator
- trigger manager function

After digitization during signal processing a baseline correction scheme removes systematic perturbations of the baseline by subtracting a pattern stored in a memory. A self-calibration (between triggers) can correct baseline shifts due to temperature, drift or low-frequency perturbations. Later on, the baseline correction can remove the non-systematic perturbations of the baseline that are superimposed on the clusters. The tail cancellation filter is a digital filter that removes the long ion tail of the detector signal and undershoot caused by pileup. This procedure improves the clusters identification. Eventually, the Zero Suppression procedure removes all data that are below the threshold and reduces the amount of transferred information.

Allocation of Front-End Electronics

Each Front-end board (FEB) contains a full set of the analog and digital components needed to read out pad signals. The high channel density of up to 0.4 channel/sm^2 in the inner area of the pad plane and the requirement to provide a minimal material budget from electronics force us to use a very compact electronics components as well as the boards population. The FEB should be placed in parallel to the pad plane of Readout chambers (Fig. 2.44) to get a minimal material budget. The modern FPGAs [229] are considered to realize such approach instead of digital ASICs such as ALTRO [227, 230]. A most powerful FPGA Spartan-6 and Virtex-6 series will be used.

Among the very important factors are the capacity of the inbuilt memory, quantity of fast data links and accordingly - cost.

The most suitable devices are the Spartan-6 LX(T) FPGAs. These devices support up to 150 K logic density, 4.8 Mb memory, integrated memory controllers, and easy-to-use and high-performance system IP such as DSP blocks, with an innovative open standards-based configuration.

Five versions of FEBs are supposed to be used (Fig.2.45). Each of them is divided into cells, which include one FPGA/Spartan-6 LX, 64 ADC channels (8 ch $\times$ 8 chip = 64 chs), 64 PASA channels (16 chs $\times$ 4 chips = 64 chs), and provide data transmission via serial interface to "data concentrator" FPGAs based on the Virtex-6 LXT with a rate of around 100 Mbps.

All cells are synchronized through the Trigger, Timing, Control (TTC) bus. In addition, FEB1 and FEB2 have one chamber powerful FPGA chip, which provides data receiving from all the FEB cells and transmitting them via optical lines with a speed of ∼2.0 Gbps. It provides a total speed of data transmission from TPC of ∼5 GB/sec.

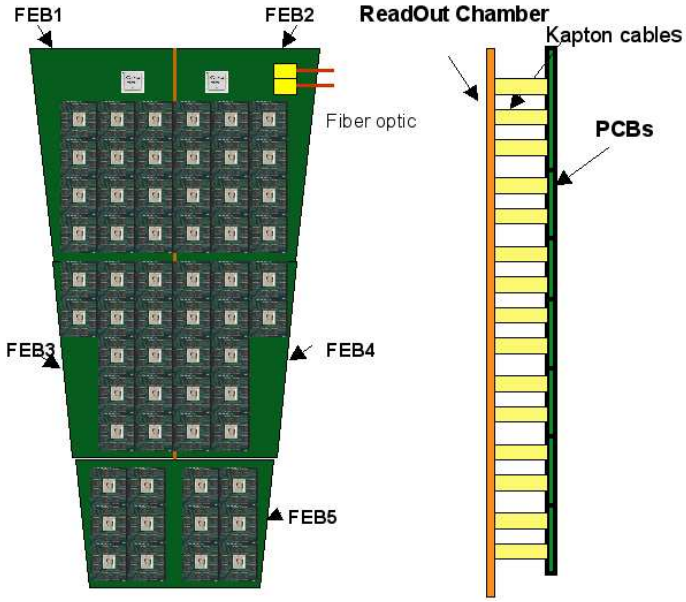

Fig. 2.44: The layout of the segment of front-end electronics (power consumption 200 W).

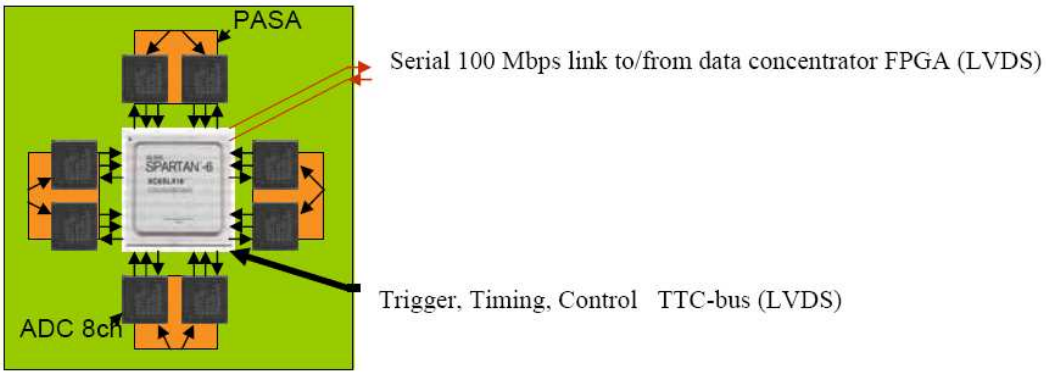

Fig. 2.45: FEE 64 channel cell.

Data flow (rate)

The data flow structure for one readout chamber is shown in Fig.2.46 . The large granularity of TPC (80000 × 400 time bins) leads to the event size of about 1 MB after zero suppression. At a trigger rate of ∼5 kHz the maximum count rate is ∼50 Gbps, which corresponds to ∼2.0 Gbps per one readout chamber and around 40 Mbps per one FEE Cell (64 channel).

Each FEE cells has a 0.5 Mb inbuilt memory (4 KSamples per channel) which can provide buffering of 4–8 events (that will allow to eliminate data loss due to DAQ dead

time) and a fast communication link with the data concentrator FPGA which provides data collection and transmission to DAQ MPD.

From the experience of STAR (upgraded version), data size could be reduced on-line (in DAQ) by a factor of 100, i.e. up to 50 MB/s.

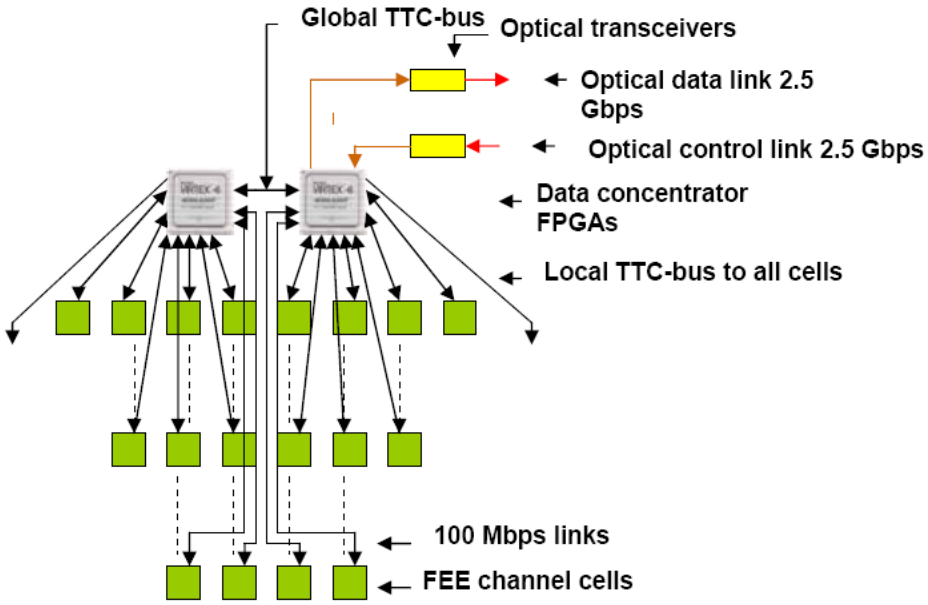

Fig. 2.46: Data flow structure.

2.3.4 Infrastructure for gas detector construction and prototyping

For constructing and testing of the chambers at the LHEP JINR, a new Detector Laboratory was equipped with modern tools and "clean" rooms (total area of ∼120 m^2). Usually the construction of a chamber is divided into 3 major steps:

a)gluing of chamber frames (and pad-planes),

b)winding and transfer of cathode and anode wires,

c)assembling and testing of the chamber.

Several precision assembling tables are used for chamber frames gluing. The transfer of wire planes on a chamber frames is carried out in the "clean" rooms equipped with the climate control, which makes possible to maintain a constant temperature of 23-24° and humidity below 35%. The wire planes are prepared for each chamber on a computer controlled winding machine, which makes it possible to wind wires with different tension and pitch. Additional air filters are installed over each table where the wire planes are transferred on chamber planes to provide a purity class of better than 10000. The position of wire planes on a chamber is corrected with the microscopes (Fig. 2.47) to an accuracy of up to 20 microns [231].

Having been assembled, the chamber is tested on a computer control test stand. This stand is equipped with a collimated X-ray tube (10 keV) which can be positioned with a high accuracy (∼50 μm in the X/Y directions); this makes it possible to scan the full

area of the chamber to measure the uniformity of efficiency (or amplification factor) over the full area of the chamber.

Fig. 2.47: Wire planes transfer on the chamber frames.

A small Prototype with one TPC sector and 256 sensitive pads (6×12 mm^2) is planned to be constructed (Fig. 2.48) to test its performance with different gas mixtures, to measure the spatial resolution, and to check the parameters of FEE.

The first prototype of cylindrical TPC for the MPD detector constructed in industry is shown in Fig. 2.49. It is of 95 cm long and 90 cm in diameter. The prototype wall of 2 mm thickness is made of Kevlar laminated by Tedlar films. It is equipped with one readout chamber based on conventional MWPC with pads of 6x10 and 4x12 mm size. The TPC prototype was filled with an argon plus methane gas mixture (80% Ar + 20% CH4). Some basic prototype's performance are testing with an ^{55}Fe source, namely: gas gain, pad response function, energy and space resolution, operational stability.

The GEM based detectors are also under study to use them as the readout chambers. Several versions of GEM detectors with 10×10 cm^2 active areas and 1-D and 2-D readout have been developed and tested in the LHEP, JINR. A prototype of 10x10 cm based on a triple GEM setup with 2-D strip read-out (800 μm pitch, see Fig.2.51) is shown in Fig.2.50. The energy and space resolution for this prototype was measured with an radioactive source. The energy resolution of 18% (FWHM) was achieved with an accuracy in (x, y)-image reconstruction of about 100 μm for each coordinate[232]. The GEM-based detectors should be further tested for spark resistivity.

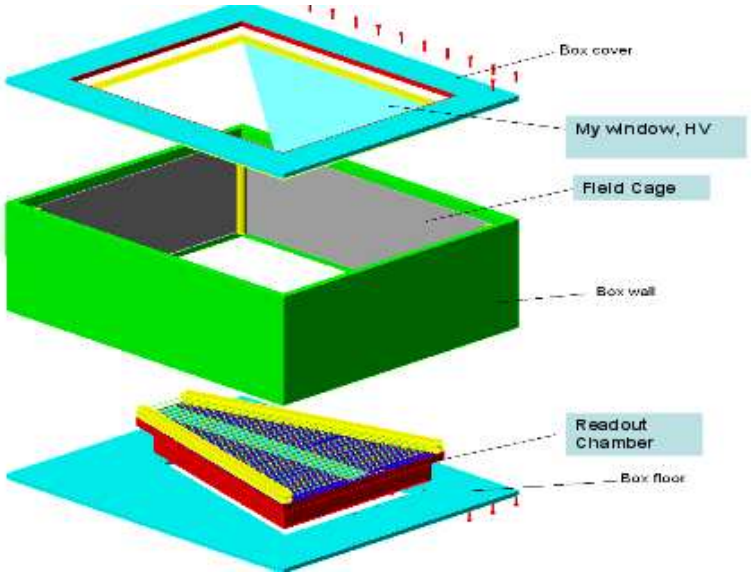

Fig. 2.48: One TPC sector prototype

Fig. 2.49: The first prototype of the MPD TPC constructed in industry.

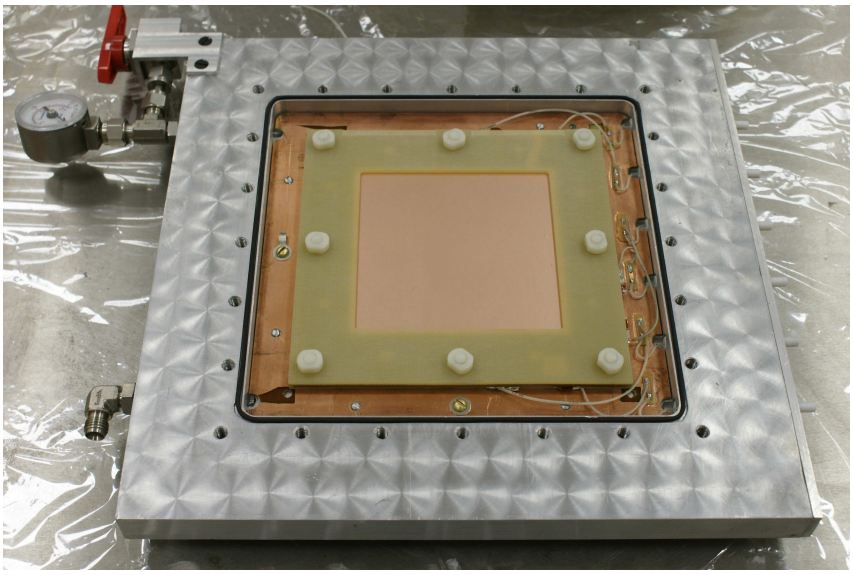

Fig. 2.50: GEM module of 100 cm^2

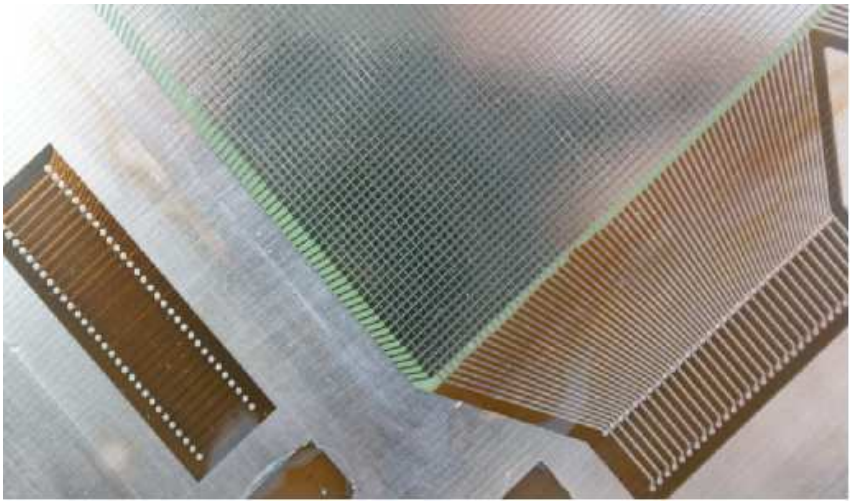

Fig. 2.51: The GEM 2-D readout plate

Table 2.13: Major hyperon decay modes suitable for detection with the ITS and TPC sequence.

♯	Decay mode	Branching	Range, cm.	Comment
1.	$\Lambda \to \pi^- p$	0.64	3.2	
2.	$\Sigma^0 \to \Lambda\gamma$	1.	0	Unaccessible, $c\tau = 2 \cdot 10^{-9}\ cm$
3.	$\Sigma^0(1385) \to \Lambda\pi$	0.9	0	Resonance, $\Gamma = 36\ MeV$
4.	$\Sigma^0(1385) \to \Sigma^{\pm}\pi^{\mp}$	0.1	0	Resonance, $\Gamma \approx 30\ MeV$
5.	$\Sigma^- \to n\pi^-$	0.99	3.0	
6.	$\Sigma^+ \to n\pi^+$	0.48	1.9	
7.	$\Sigma^+ \to p\pi^0$	0.5	1.9	Unaccessible
8.	$\Xi^0 \to \Lambda\pi^0$	0.99	5.0	Unaccessible
9.	$\Xi^0(1690) \to \Lambda K^0$	?	0	Resonance, $\Gamma \approx 30\ MeV$
10.	$\Xi^- \to \Lambda\pi^-$	0.99	2.5	
11.	$\Omega^- \to \Lambda K^-$	0.68	0.7	
12.	$\Omega^-(2250) \to \Xi^- K^- \pi^+$	?	0	Resonance, $\Gamma \approx 50\ MeV$

2.4 Inner Tracker System

The tasks to be performed by the silicon ITS are twofold.

Firstly, it shall enhance track reconstruction for particles registered with all other subsystems. Here the role of the ITS seems to increase with the decrease of the scattering angle of the particles. Within the TPC acceptance of 40-140^o the IT is able to restore tracks of particles with momentum less than 100 MeV/c, a region not covered by the TPC. The track reconstruction power of the TPC degrades for particles emitted at smaller angles and here the role of ITS which is free of this disadvantage would be of great help. For particles registered by the MPD Forward Spectrometer (FS) the ITS is simply a must since the FS is situated far from the interaction region and tracking of the origin of particles with the primary vertex is quite a problem. On the other hand, this is a region of great importance because the particles emitted at small angles carry vital information on the reaction plane which is in the list of the highest priority observables of the MPD.

Secondly, there is a specific task for the ITS of great importance for the whole physics program of the MPD. This task is to identify relatively rare events with production of hyperons, especially the multistrange ones. These particles are believed to be one of the most effective probes of the nuclear matter density variations realized in nucleus-nucleus collisions and, therefore, their yields could signal on the density fluctuations growth in the critical point the NICA-MPD is to search for. We are about to make use of the ITS ability to identify very short-range tracks of hyperons located close to the primary interaction vertex.

Table 2.13 provides a compilation of major hyperon decay modes suitable for detection with the MPD ITS.

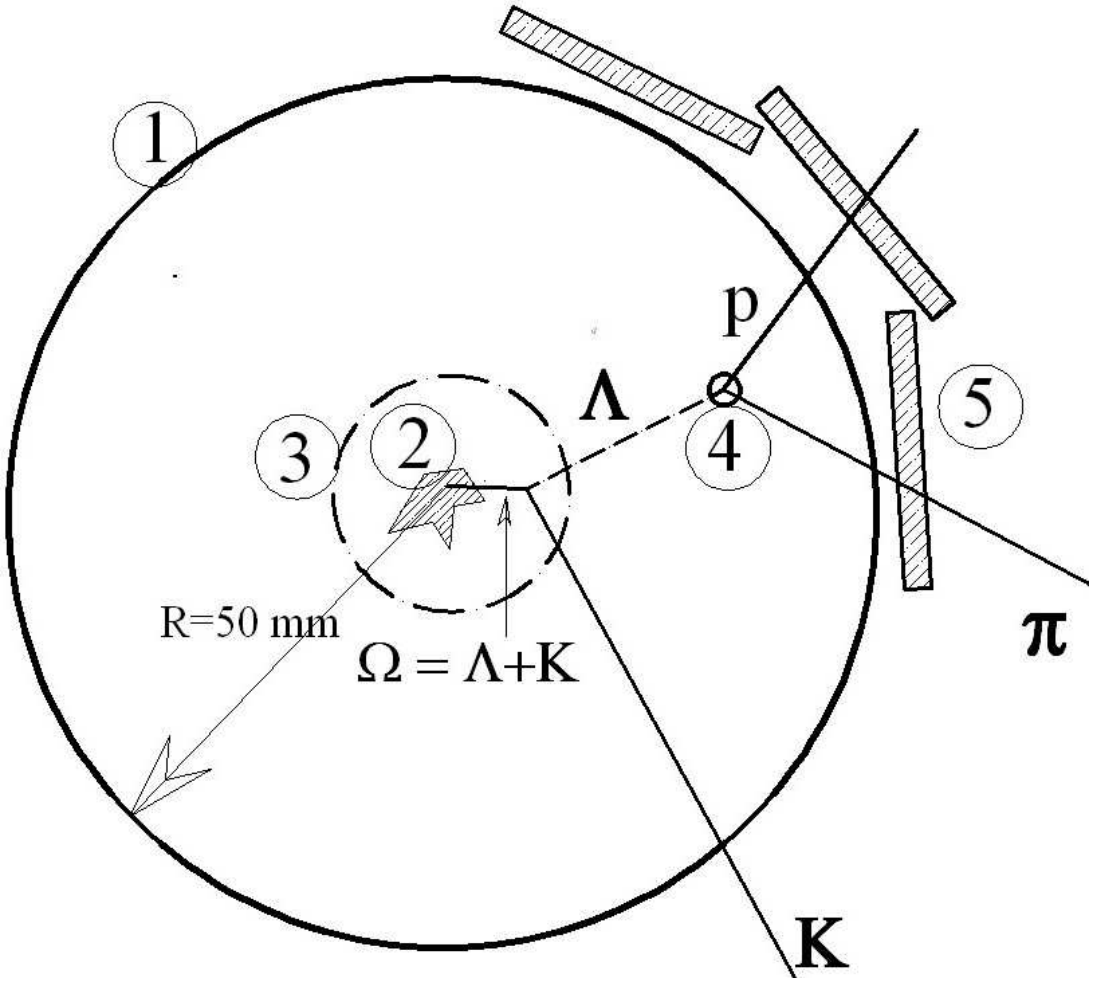

Fig. 2.52: An example of decay of a 0.5 GeV/c multistrange hyperon Ω in the interaction region of MPD. Notations: 1 - collider vacuum chamber; 2 - beams intercept region; 3 - region of uncertainty of tracks extrapolation based on TPC measurements (11 mm); 4 - region of uncertainty of tracks extrapolation obtained with the IT (40 um); 5 - silicon strip detectors of the ITS.

The data presented in Table 2.13 summarizes the information on hyperon decay patterns sutable for experimental tracing. The Σ^0 hyperon (line 2) is practically unaccessible for registration with the IT, since it is difficult to associate a single secondary γ particle with Λ and calculate its effective mass. On the contrary, $\Sigma^0(1385)$ resonance (lines 3, 4) seems to be detectable. The dynamics of interaction of this short life hyperon with the fireball matter may substantially differ from that describing the interaction of other long lived hyperons. Thus, these hyperons could provide essential signatures of the excited and compressed baryonic matter. The same remark is true for other resonances outlined in lines 9 and 12 of Table 2.13. Within this experimental program, the identification of the hyperons Ξ and Ω with strangenesses -2 and -3 stands apart as one of the most challenging problem. At $E_{cms} = 9$ GeV the multiplicity of Ω particles in a central Au+Au collision is $\approx 2 - 0.2$ whereas the multiplicity of the other species is much higher: Λ - 28, K - 70, p - 150, $\pi^{\pm}$ - 350. A typical mean range of Ω hyperon with momentum 0.5 GeV/c is 7 mm and the range of Λ (as a product of Ω decay) is 30 mm. The corresponding decay vertices are located well inside the collider chamber as shown in Fig. 2.52. To identify such hyperons, one should well resolve their decay vertices from the primary interaction

vertices, each of those emitting about 800 charged particles! The plot in Fig. 2.52 shows that it is only the ITS with its superb vertex resolution that can answer the experimental challenge. Preliminary simulations of Au+Au collisions with the LAQGSM event generator indicate that a sample of about 10^7 events with multistrange hyperons could be obtained within a 3 month run of NICA-MPD.

The last but not least, challenging task of hyperon polarization measurements with the ITS should be mentioned. It is well known that Λ particles produced in pp and pA interactions have high polarization - 30 % in the range of longitudinal momentum $x_F \approx 0.4 \div 0.7$. This manifests that the hyperons produced in pA collisions are not thermalized. It seems to be worth examining the hyperon polarization with MPD ITS setup as a function of beam energy and degree of centrality in AA collisions to get a direct answer to the question of the level of the thermal equilibration of nuclear matter under investigation with NICA-MPD.

2.4.1 Concept

The conceptual layout of the NICA-MPD Inner Tracker System (ITS) is shown in Figs. 2.53 - 2.55. The tracker is based on the Silicon Strip Detector (SSD) technology developed for the ALICE, LHC [233], STAR, BNL [234] and D0, FNAL [235] experiments within the last 15 years.

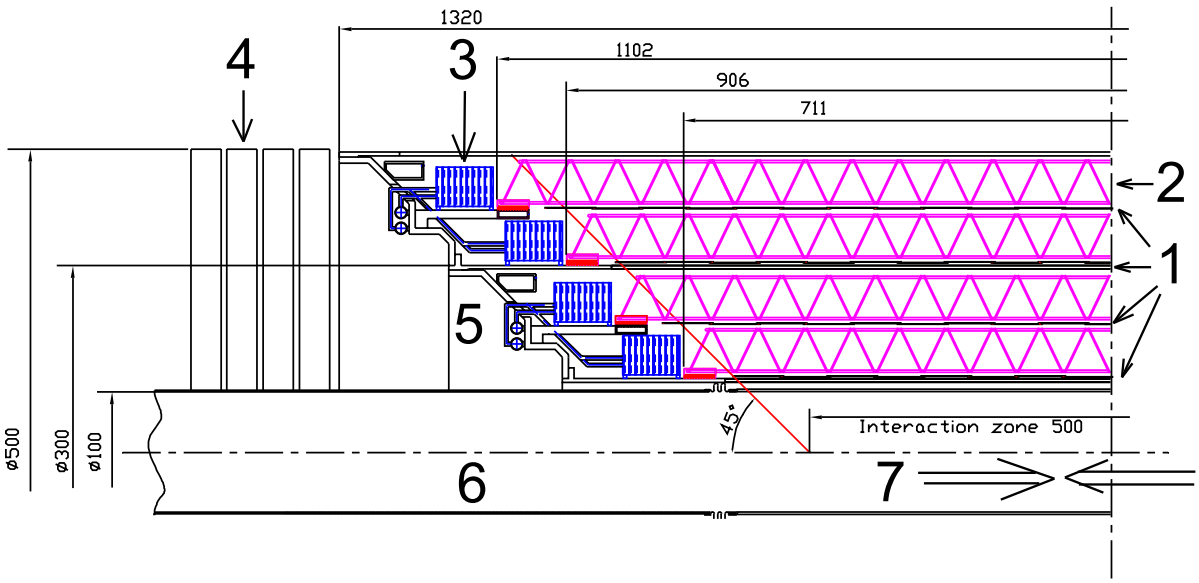

Fig. 2.53: Conceptual layout of ITS with a side view of its quarter. Notations: 1 - silicon strip detectors of the cylindrical part of ITS; 2 - carbon fiber support; 3 - front end electronics; 4 - disc detectors; 5 - cooling system elements; 6 - accelerator chamber; 7 - collider beams.

The ITS schematic is shown in Fig. 2.53. It consists of a silicon barrel and a system of silicon discs. The mechanical support and cooling elements of both the cylinders and the discs are manufactured out of carbon fiber to minimize the material budget of the setup and hence to diminish the impact of the Coulomb multi-scattering on track resolution. The anticipated thickness of each sensitive layer and supporting material is $0.008X_0$ regardless

of its location within the system. The double sided SSDs of the four cylinder-like sensitive layers of the barrel are mounted on the 3-D light Carbon Fiber (CF) space frames similar to those developed for the inner tracker of ALICE (CERN) and STAR (BNL).

The SSDs are 75x42 mm^2 in size most suitable for production on a 4 -inch silicon wafer technology line available in Russia. The 42 mm side is parallel to the beam axis (and to the magnetic field vector). The stereo angle between the strips on the opposite sides of the SSDs is the subject of further optimization in the course of computer simulation of the ITS performance and may be within the range of $\alpha = 5 \div 15^o$. The optimization of the value of stero angle is important for minimizing the number of ambiguities in track reconstruction (see discussion below). From typical strip pitch of h = 100 um yields a space resolution of a track close to $\sigma_\varphi = h/(\sqrt{2} \cdot \sqrt{12})$=20 um in (r, φ) direction, and $\sigma_z = \sqrt{2}h/(\sqrt{12} \cdot \alpha)$=160 $\div$480 um in Z the direction along the beam line. To eliminate the effect of insensitive areas at the edges of the sensors, the ladders are positioned with a small overlap as depicted in Fig. 2.54. All in all, the silicon barrel contains 1012 detectors mounted on 48 CF supports as denoted in Table 2.14.

Particles with large pseudorapidity $|\eta|$ are registered by the silicon discs built out of wedge-like modules shown in Fig. 2.55.

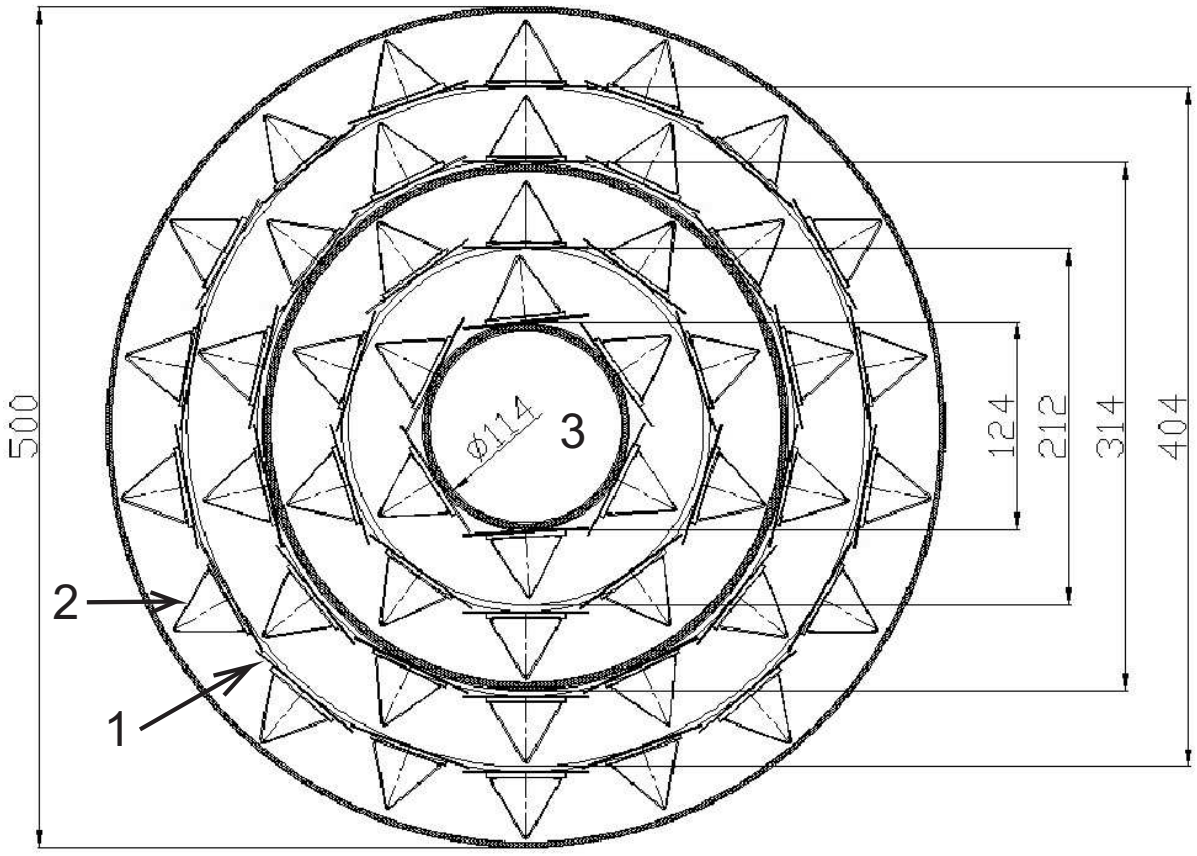

Fig. 2.54: View of the cylinder part of the ITS along the beam direction. Notations: 1 - silicon strip detectors of the cylinder part of the ITS; 2 - carbon fiber support (ladder); 3 - accelerator chamber.

The particles with large absolute values of pseudorapidity (small emission angle) are detected by means of disk modules. The disk system consists of left and right parts, located at the end faces of the ITS cylinders. Each part includes four disks built each

Table 2.14: The number of detectors in cylinder part of ITS.

Layer number	Radius, mm	Number of sectors	Number of detectors
1	62	6	16×6=96
2	110	10	19×10=190
3	160	14	21×14=294
4	202	18	23×18=432
	-	Total 48	1012

of 24 basic wedge modules (sectors). A wedge module with 15^o opening angle is built of three SSDs. The strips are parallel to one side of the detector. The strips on both sides of the SSD make a hit position sensitive network schematically shown in Fig. 2.55. The technique similar to that successfully used in discs of the D0 experiment at FNAL [235] is suggested to be further developed for the disc part of the NICA-MPD ITS. However, additional development of technology is needed here since the sensitive area of the MPD ITS disks is considerably larger than that in the D0 setup.

The space track resolution of the disc system is similar to that of the barrel part discussed above. The distances between the discs shown in Fig. 2.53 are optional and will be eventually determined during the optimization simulations of the tracking performance of the ITS discs together with the End Cups and the Forward Spectrometer.

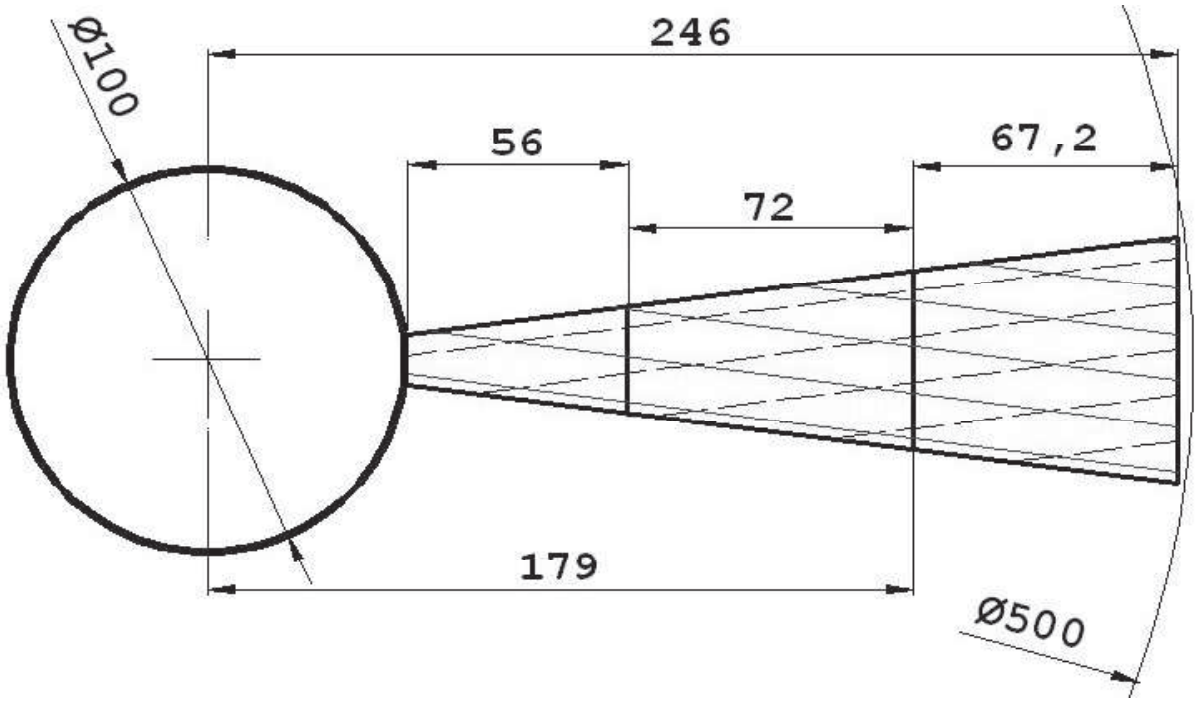

Fig. 2.55: Layout of the wedge-module of the IT disc. 24 modules are needed to build one MPD IT disc.

The full scale electromechanical mockup of wedge module prototype manufactured in 2009 is shown in Fig. 2.56.

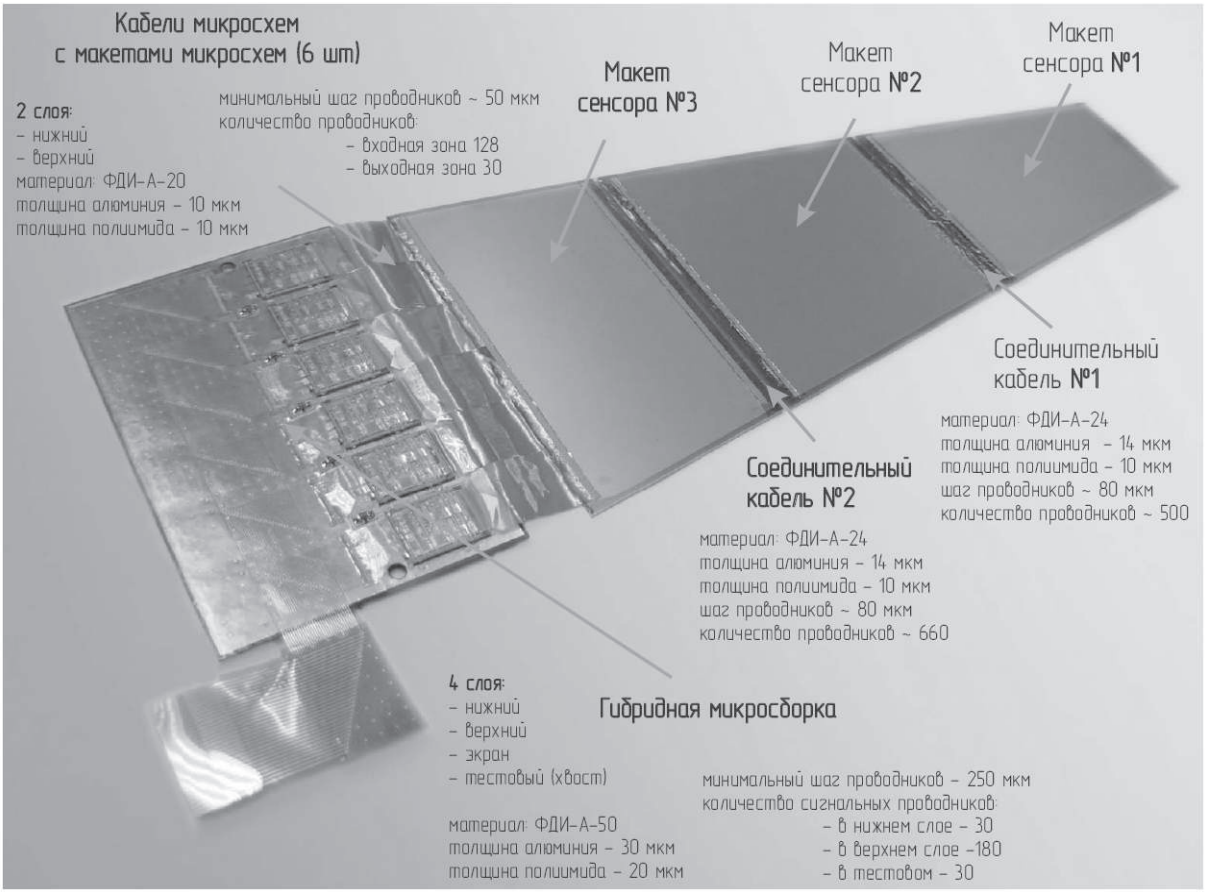

Fig. 2.56: The mockup of the wedge module for disks of the ITS. Each disk consists of 24 such modules.

The design of the assembly of the first layer of the ITS cylinder part is depicted in Fig. 2.57.

2.4.2 Occupancy and false hit rates estimation

Two basic parameters set limits on the performance of the system - the occupancy and the rate of the false hits. To obtain the quantitative estimations of these parameters computer simulations of collisions with the LAQGSM event generator [236] were undertaken to estimate the maximum occupancy of the IT sensors situated at distances closest to the interaction region i.e. 6 cm from the interaction region emits secondary particles at 90^o scattering angle (pseudorapidity η=0). For central collisions of gold ions corresponding to E_{cms}=9 A GeV the charged particles density was found to be 2.6 cm^{-2}, which gives an estimate for the maximum strip occupancy equal to 0.10. It is an acceptable value since the probability of two particles incidence on one strip is 0.5%.

The coordinates of the hit of the particle determined by coordinates of the strips fired on two sensitive layers are known to become ambiguous for the events with high multiplicity of secondary particles. Namely, n secondary particles uniformly spread over the surface of the detector produce n^2 false images (false hits) uniformly spread over the area of the sensor as shown in Fig. 2.58. If a is the detector size and ρ is the density of the real hits, the number of the real hits is $n = \rho \cdot a^2$ while the number of the false hits is $n_f = n(n-1) = \rho^2 \cdot a^4$. Here, we assumed that $n \gg 1$. If one assumes also that

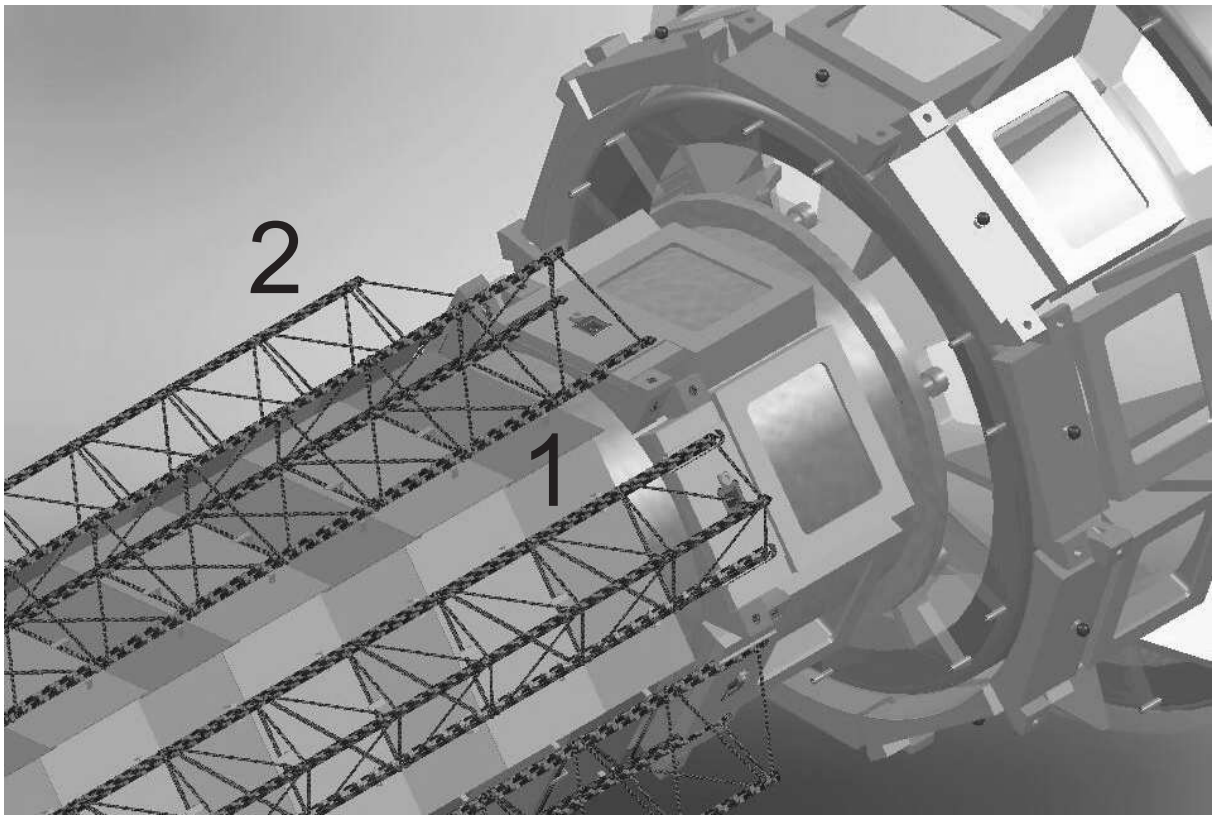

Fig. 2.57: The assembly of the first layer of the ITS cylinder part. Notations: 1 - silicon strip detectors; 2 - carbon fiber support (ladder).

$tg(\alpha) \simeq \alpha$, $(\alpha \ll 1)$ then the area populated by the false hits is $S_f = \frac{a^2}{\alpha} \cdot \frac{1}{2} \cdot 2 + a^2 = \frac{a^2}{\alpha}$. This leads to dependency of the false hits density on the stereo angle $\rho_f = \frac{n_f}{S_f} = \rho^2 a^2 \alpha$. For the ITS, with ρ=2.6 cm^{-2}, a=4 cm, and α=0.25 rad one gets ρ_f=27 cm^{-2}. This value should be compared with the $\rho_f(\alpha = \pi/2)$=105 cm^{-2}. Considerable difference between these numbers indicates that the impact of the false hits on the reconstruction performance of ITS should be relatively small. Real hits are separated from the false ones by comparison of their coordinates determined from any two couples of detectors, for instance, from the ITS barrel layers 1, 2 and 3, 4. Coordinates of the real hits will follow the expected trajectory of the particle while the false ones will not. However, since false hits are distributed quasi randomly, the chance exists of an accidental pileup. The corresponding probability is $\cdot(\sigma_Z \cdot \sigma_{R\varphi}) \cdot \rho_f \simeq 0.10\%$, where σ denotes the uncertainty of the Z and $(R\varphi)$ coordinates. The more exact estimation will be evaluated after computer simulations are finished.

2.4.3 Detector prototype R&D status

The performance of a double-sided strip detector manufactured by CIS, Erfurt, Germany was tested in the 50 GeV proton beam of the U-70 accelerator at IHEP (Protvino) in December 2008. The idea of the experiment was to check the basic features, spacial track resolution and efficiency of the silicon double sided SSD for the track reconstruction of minimum ionizing particles. The detector prototype was the first in a row of the MPD ITS critical elements to be tested in the feasibility studies of technologies relevant to the

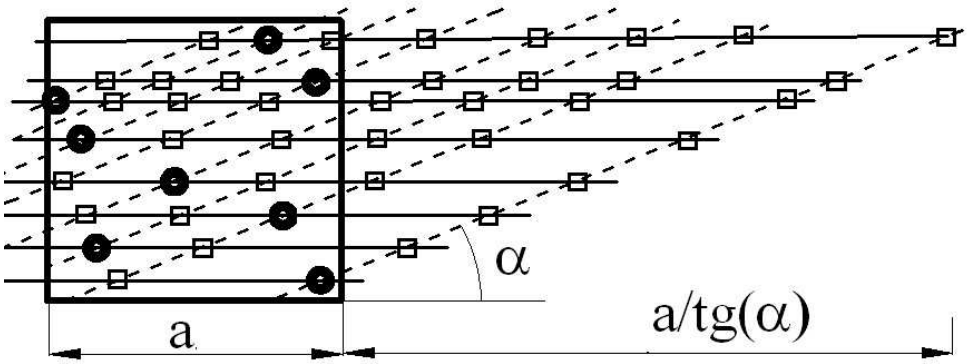

Fig. 2.58: The origin and the explanation of the relation between the real and the false hits density. Notations: ◯ - real hits; □ - False hits. For simplicity, only the right part of crossing strips is shown on the plot which is in fact left - right symmetric.

ITS R&D program. The purpose of this study was also a quality check of the double-sided SSD detectors assembled within the technology of thin aluminum cables anticipated for wide usage in the engineering solution of the ITS.

The project was successfully realized as the joint effort of the CBM-MPD STS Consortium [237] focussing on the problems of design and manufacturing of silicon tracking systems for the MPD (NICA, Dubna) and the CBM (FAIR, Darmstadt) experiments.

The detector was assembled at the SE SRTIIE, Kharkov, Ukraine, and tested electrically for shortcuts and ruptures of strips at the probe stations of SINP MSU, Moscow. The further trial using radioactive source was done at JINR LHEP where the stand to conduct the tuning and testing of the SSD electronics was built up. A photograph of this stand is shown in Fig. 2.60. Then SSD was located at the position of one of the beam-track stations of the SVD-2 setup used by the SVD collaboration [238] to study the high multiplicity events in collisions of 50 GeV protons with a liquid hydrogen target. The vertex coordinates together with the coordinates of the tracks estimated from the high precision 25 um pitch beam-track stations situated before and after the tested SSD made possible position monitoring of the 50 GeV protons on the demonstrator with an accuracy of around 6 um. The beam intensity was $\sim 10^6$/cycle, with 1.5 s spill with and 10 s gap between the spills.

The proton passing through the detector may fire several adjacent strips and form the so called clusters with the number of fired strips distributed as follows: 87 % one-strip, 12% two-strip, and 1% three and more strips. The registration efficiency of the protons is close to 100%. The correlation between the cluster charges measured on the p- and n-sides of the demonstrator is shown in Fig. 2.59. This correlation can be used for suppression of false hits when detecting events with high multiplicity and thus speed up the track reconstruction [239].

The high quality of the TAB-bonded thin aluminum microcables produced by SE SRTIIE, Kharkov, was experimentally confirmed. It was also demonstrated that even with the moderate signal-to-noise ratios achieved in this first test the resulting spacious resolution turned out to be still compatible with the requirements of the experiment.

The creation of ITS is a large scale enterprize and challenging scientific and technical problem. The international consortium is being organized to reach this goal. The Consortium comprises groups from the following institutions.

1. Joint Institute of Nuclear Research (JINR), Dubna, Russia.

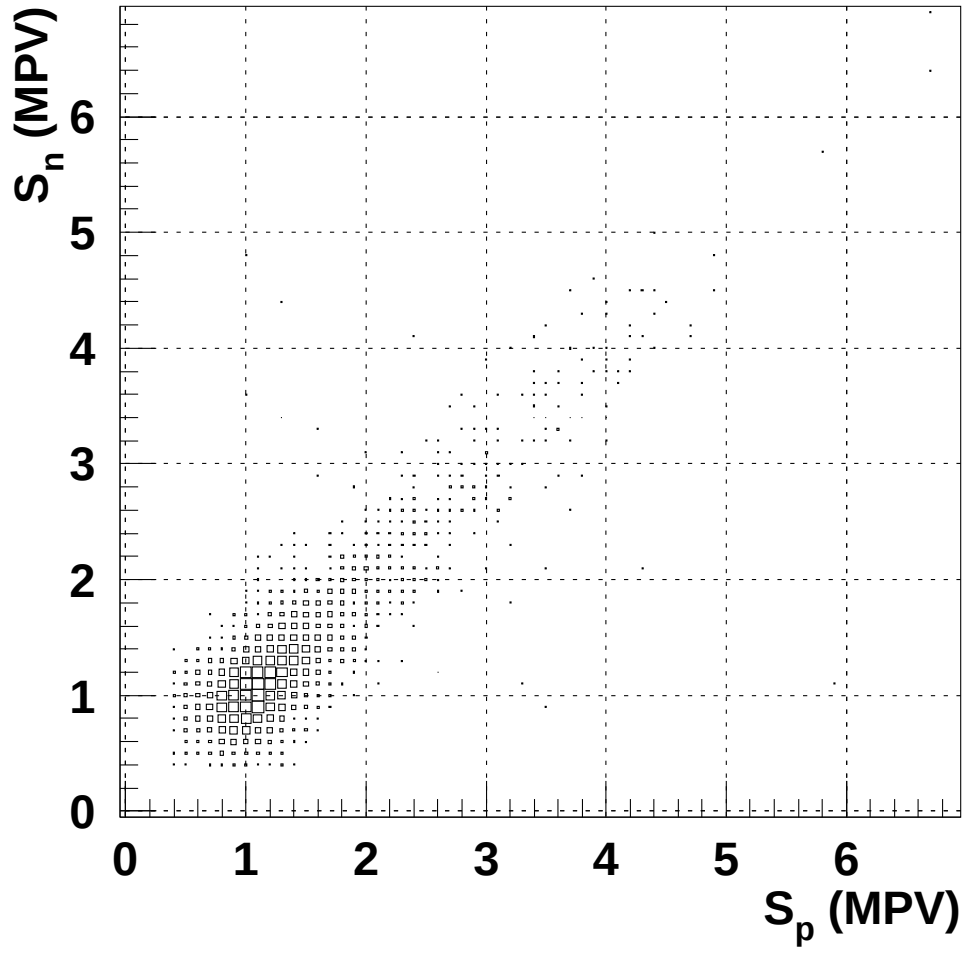

Fig. 2.59: Correlation of cluster charges measured from two sides of a double sided strip detector.

Fig. 2.60: The test stand of the SSD electronics at JINR LHEP.

2. Skobeltsyn Institute of Nuclear Physics of the Moscow State University (SINP-MSU), Moscow, Russia.

3. V.G. Khlopin Radium Institute (KRI), St.Petersburg, Russia.

4. State University of SPb, (SPbSU), St.Petersburg, Russia.

5. Institute of High Energy Physics (IHEP), Protvino, Russia.

6. State Enterprize Scientific Research Technological Institute of Instrument Engineering (SESRTIIE), Kharkov, Ukraine.

7. Gesellschaft für Schwerionenforschung (GSI), Darmstadt, Germany.

8. State Enterprize PLANAR, Minsk, Belarus.

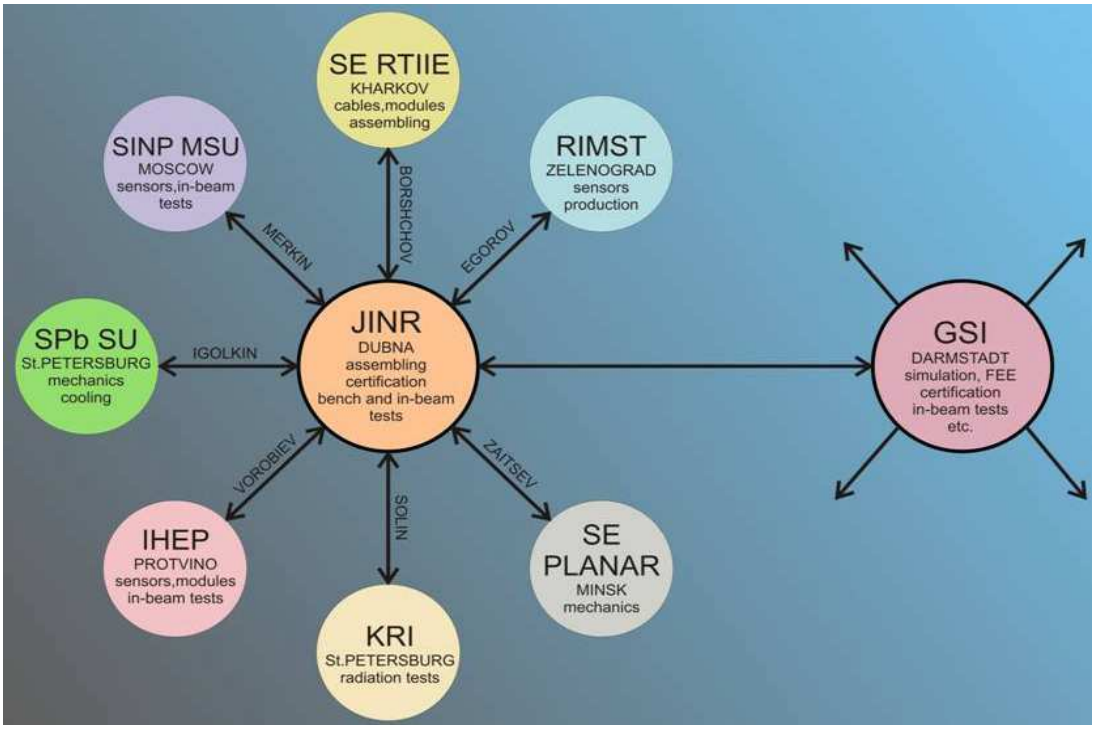

Fig. 2.61: Structure of the CBM - MPD STS Consortium.

9. State Enterprize RIMST, Zelenograd, Russia.

The Consortium is an open organization, and any other institute can join provided it shares the goals of the Consortium, and the member institutes have no objections. Its structure is shown in Fig. 2.61.

2.4.4 Hyperon reconstruction with ITS

To illustrate the importance of the ITS data for hyperons detection, the simulation of the hyperon identification using data from TPC alone and TPC plus cylinder part of ITS was carried out. The analysis was performed with the help of MPDROOT framework and URQMD event generator for central Au+Au collisions at an energy of $\sqrt{(s)} = 9$ GeV. A subset of events with hyperons having decay range exceeding 10 mm was selected. This value is $\sim$ twice as large as a characteristic hyperon range and therefore the efficiency of the system is limited. However, such condition allows most robust analysis of the identification power of the combined TPC+ITS system which demonstrates essential increase of the hyperon identification efficiency for the system with ITS compared to the system without ITS. The identification efficiency of Λs by means of TPC is 4.3%, whereas inclusion of the ITS increases it to value 8.1%. The same for Ωs reads as 1.3% and 2.1% respectively. Figures. 2.62 and 2.63 present invariant mass distribution of the $K^-\Lambda^0$ pairs obtained using TPC alone and TPC + ITS respectively.

In fact, ITS localizes the primary and secondary vertices with an accuracy of $\sim$ 40 um, thus the selection of the hyperons with the decay range $\geq 1 \div 2$ mm, would gain a drastic increase the setup efficiency for hyperon identification.

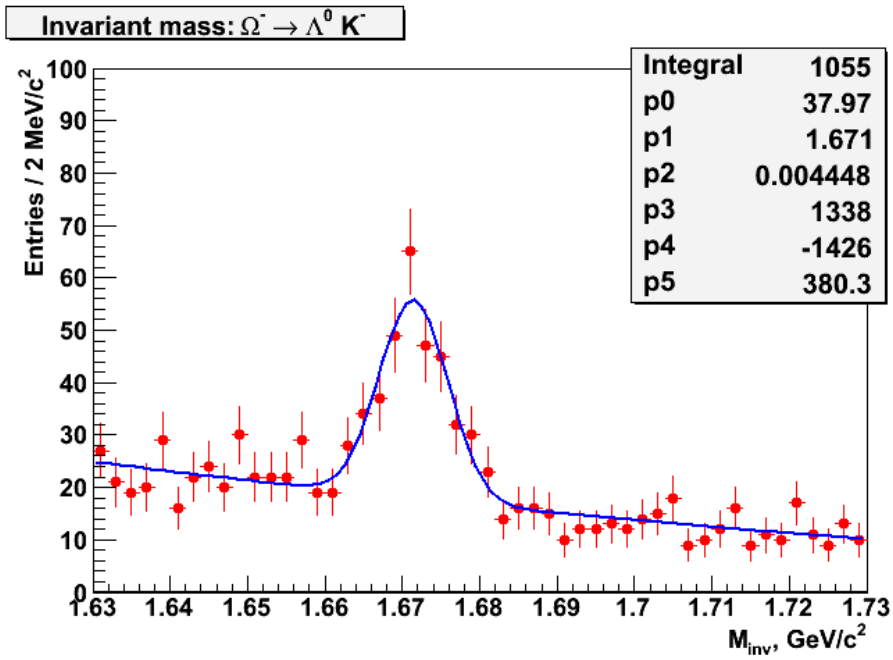

Fig. 2.62: Simulation of the Ω^- hyperon detection using TPC alone - invariant mass spectrum of the $K^-\Lambda^0$ pairs.

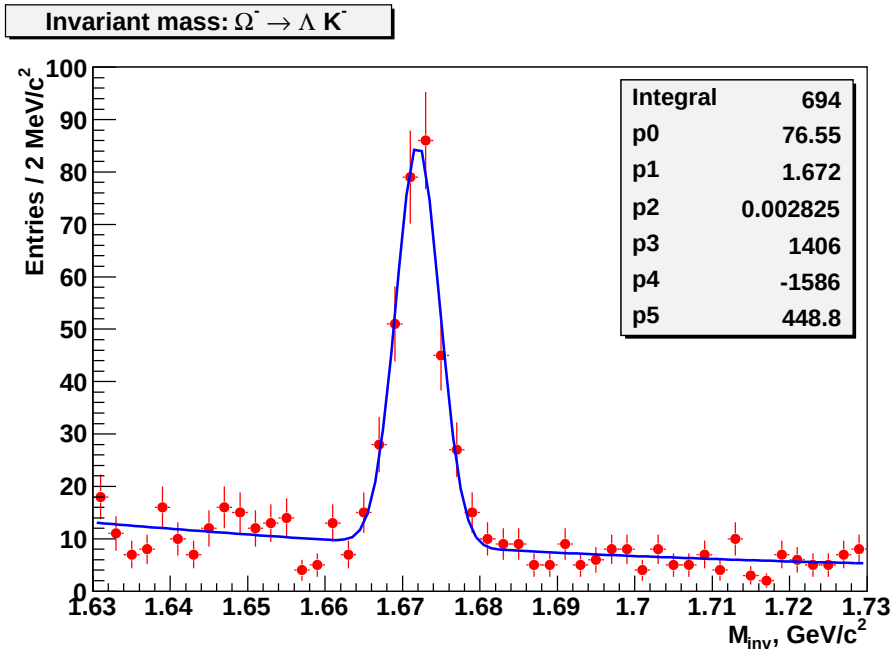

Fig. 2.63: The same as in Fig. 2.62, but using TPC +ITS.

2.5 Time of Flight System

2.5.1 Introduction

Ambitious physics goals of MPD require excellent particle identification capability over as large as possible phase space volume. Identification of charged hadrons (PID) at intermediate momenta (0.1–2 GeV/c) is achieved by the time-of-flight (TOF) measurements which are complemented by the energy loss (dE/dx) information from the TPC and IT detector systems.

The basic requirements to the TOF system are:

– large phase space coverage $|\eta|$ <2;

– high granularity to keep the overall system occupancy below 10–15% and minimize efficiency degradation due to double hits;

– good position resolution to provide effective matching of TOF hits with TPC tracks;

– high combined geometrical and detection efficiency (better than 80%);

– identification of pions and kaons with $0.1 < p_t < 2$ GeV/c;

– identification of (anti)protons with $0.3 < p_t < 3$ GeV/c;

– TOF detector elements must function in a 0.5 T magnetic field.

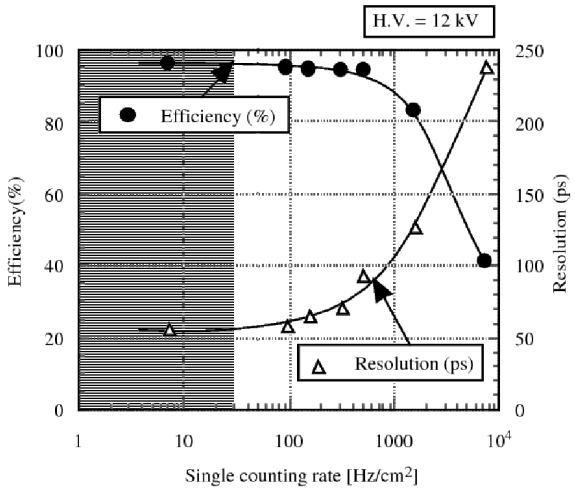

Fig. 2.64: Efficiency and average charge versus counting rate for double stack RPCs [240]. Highlighted is the single counting rate range of TOF MPD.

The UrQMD event generator predicts the charged particles density of about 3×10^{-3}cm^{-2} (η=0, r = 1.3 m) for a 5% central $Au + Au$ collision at $\sqrt{s_{NN}}$ = 9 GeV/c. At an average luminosity of the NICA collider of $L \sim 10^{27}$ cm^{-2}s^{-1}, the expected event rate for a central trigger (5-10% centrality) will not exceed ∼700 Hz. Therefore, the flux of particles which cross the TOF system is about 2 cm^{-2}s^{-1}.

Our choice for the TOF system is the Multigap Resistive Plate Counters (MRPC), which were widely used in such heavy-ion experiments as ALICE[240, 241], CBM[242], PHENIX[243], STAR[244]and HADES[245]. The RPCs have good timing performance and are efficient at particle fluxes up to 10^3 cm^{-2}s^{-1} (see Fig. 2.64)

2.5.2 Estimation of the main parameters of TOF detector

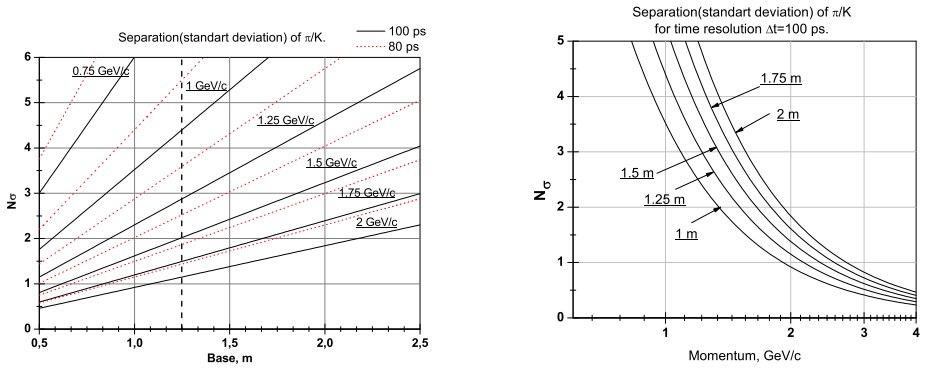

Fig. 2.65: π/K separation as function of TOF base for different momenta of particles and TOF time resolution (left panel) and for fixed bases and 100 ps time resolution as function of particle momentum(right panel).

The TOF barrel system can be represented as a barrel with a 1.3 m radius. From Fig. 2.65 one can estimate that on a 1.3 m base at a 100 ps TOF resolution one can discriminate between π and K at a level of 2 standard deviations of detector time resolution in a momentum range of up to 1.5 GeV/c. In reality, the average flight path of the TOF system is 1.77 m. In this case the system will distinguish pions from kaons with 2 standart deviations up to momentum of 1.8 GeV/c.

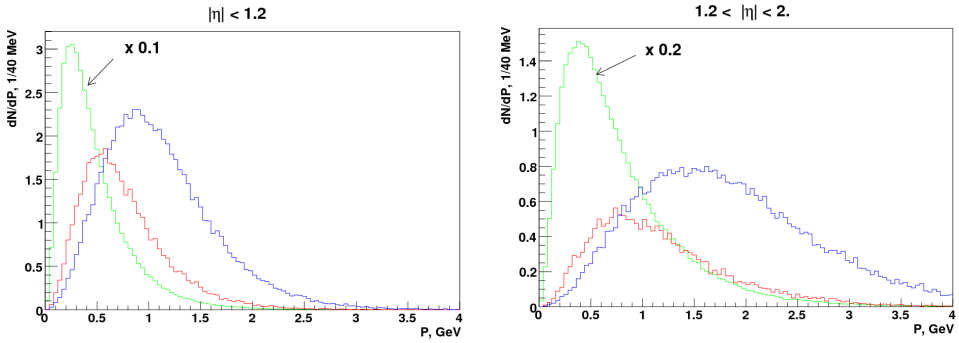

Fig. 2.66: π, K and p total momentum spectra detected in the barrel (left panel) and in the end-cup (right panel) TOFs.

2.5.3 Particle Momentum Spectra

To study the kinematical coverage of the TOF detector for the layout shown in Fig. 2.1 a chain of simulation (RQMD+GEANT) and reconstruction (MPDRoot) programs has been developed (chapter 7). The total momentum spectra of hadrons (π, K, p) registered in the TOF detectors are shown in Fig. 2.66. In the pseudorapidity interval $|\eta| < 1.2$ (left panel) which corresponds to the total TPC+(barrel)TOF coverage, all the pions and most of kaons have total momentum less than 1.5 GeV/c; while more than 95% of protons have $p < 2.5$ GeV/c. For an average track length of 1.8 m and expected overall

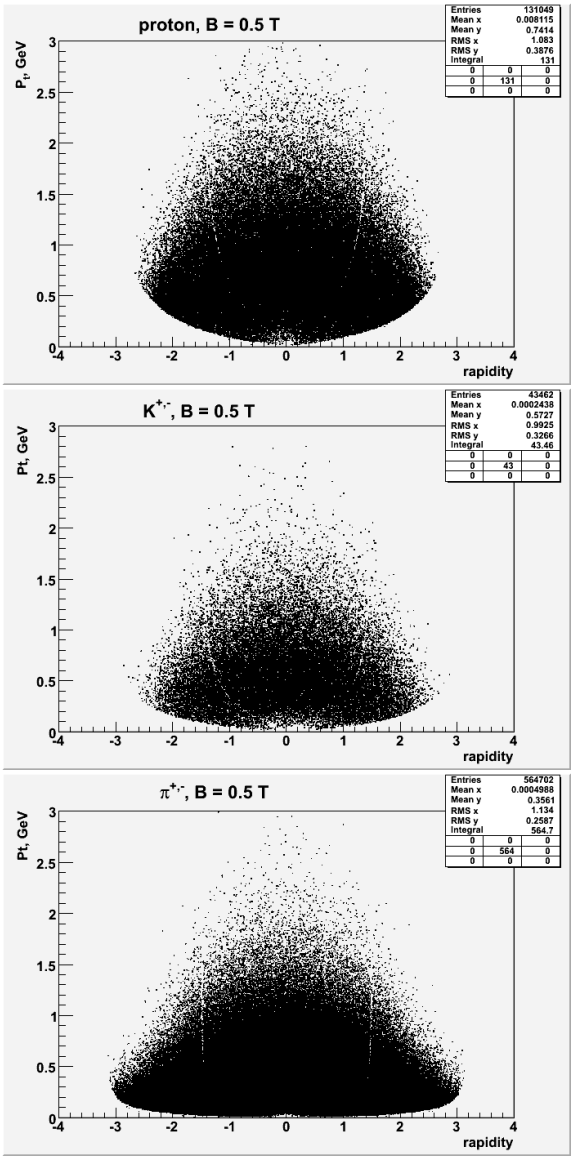

Fig. 2.67: Transverse momentum versus rapidity coverage of the barrel TOF (π, K, p).

time resolution of 100 ps we will be able to identify in the barrel region of the acceptance all hadron species to about 3σ level (see Fig. 2.65). The P_t versus rapidity distributions of the primary hadrons reaching the TOF barrel and the endcap are presented on Fig. 2.67. The forward region ($|\eta| > 1.2$) is covered by the end-cup TOF plus Straw tube system and (partially) by TPC. The momentum distributions for hadrons are broader in this pseudorapidity range, but due to a longer track length (a typical value about 2.4 m) a 2σ π/K separation can be obtained up to $p = 2$ GeV/c.

2.5.4 Particle identification with TOF and ionization losses in TPC

From the plots on Fig. 2.68 one may conclude that information on ionization loss from TPC improves the TOF results for π/K separation in the momentum region of 0.2–1.3 GeV/c.

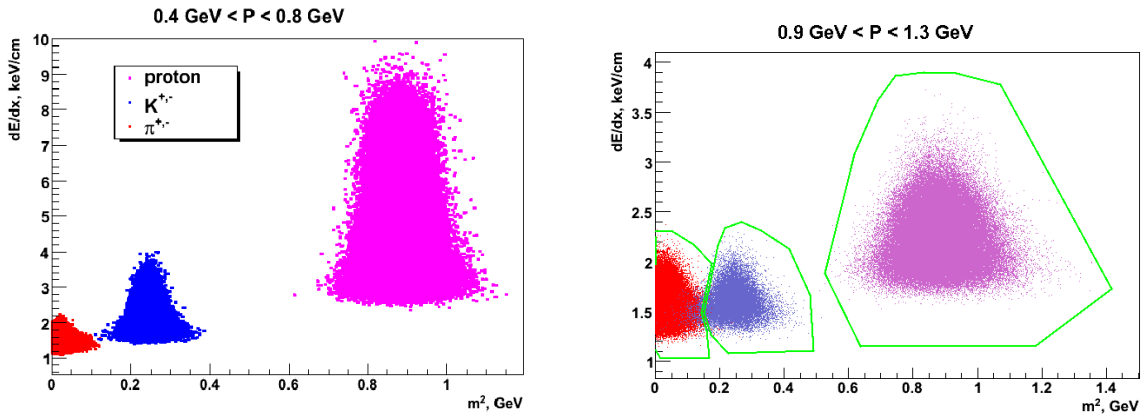

Fig. 2.68: Possible enhance of mass separation power with information on ionization losses measured in the TPC and mass reconstruction with TOF and TPC systems for particles in different momentum range.

The TPC alone provides particles separation in the momentum range 0.1–0.6 GeV/c. It may be of interest for identification of low momentum (below 0.2 GeV/c) particles which do not reach TOF, and for the secondary particles — decay products in the TPC volume.

	π	K	p
Efficiency	0.99	0.96	1.0
Contamination	0.0061	0.01707	0.0

2.5.5 Detector design

Mechanical construction of barrel. The TOF system looks like a barrel with a length of 500 cm and radius of 1.2 m (see Fig. 2.69). Along the beam it covers the region $|\eta| < 1.4$.

The surface of the barrel TOF detector is about 25 m^2. The dimensions of one multigap RPC counter are 7 cm×62 cm, it consists of 48 2.5 cm×3.5 cm pads. The RPC counters are organized in modules. In total, there are 12 modules in the barrel.

The full barrel is covered by 660 counters. The total number of readout channels is 31680. The geometry efficiency in the region $|\eta| < 1.4$ is 97%.

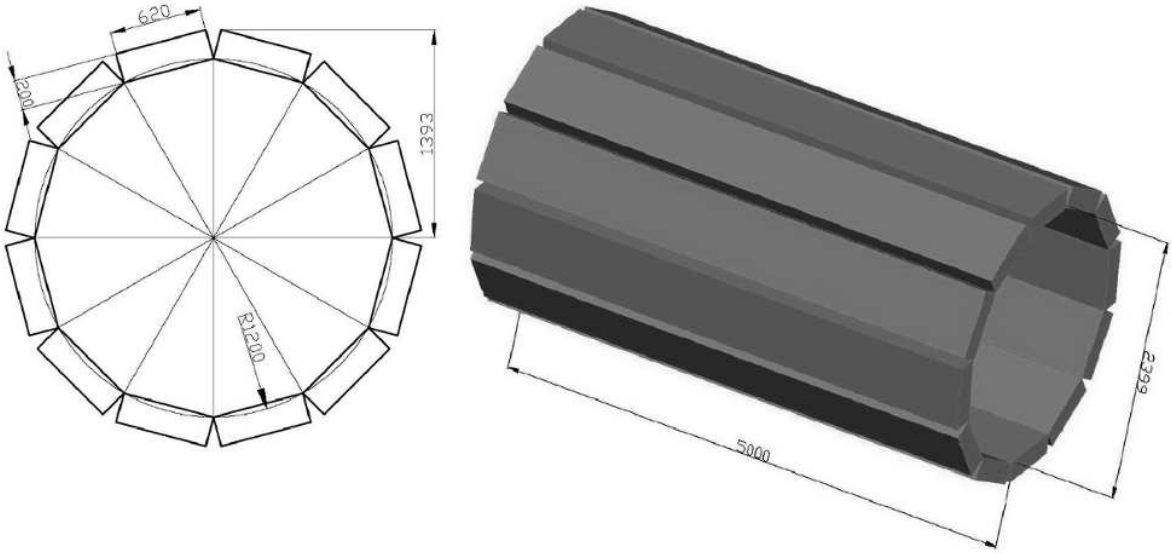

Fig. 2.69: Barrel of TOF system.

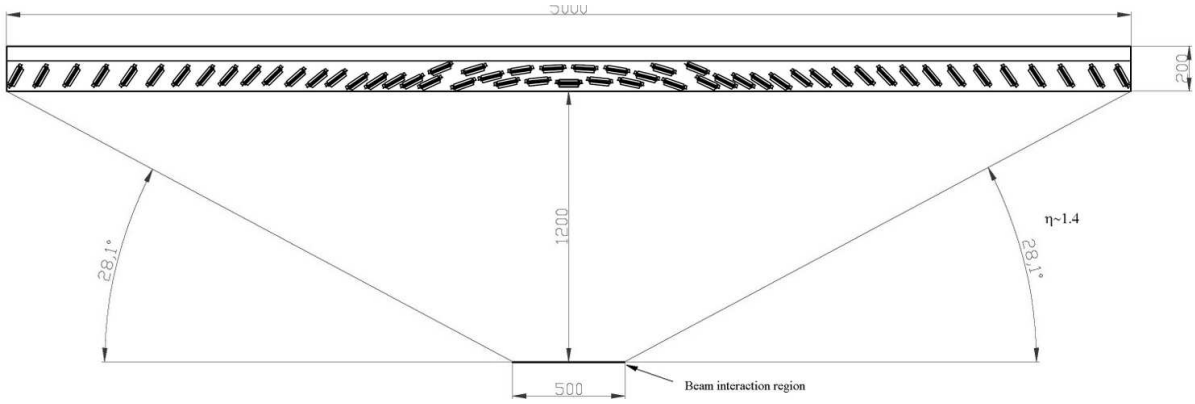

Fig. 2.70: Distribution of RPC elements in the barrel

Design of one module. The arrangement of multigap RPCs in the module is presented in Figs. 2.70 and 2.71. The detectors are placed in the module perpendicular to the beam axes.

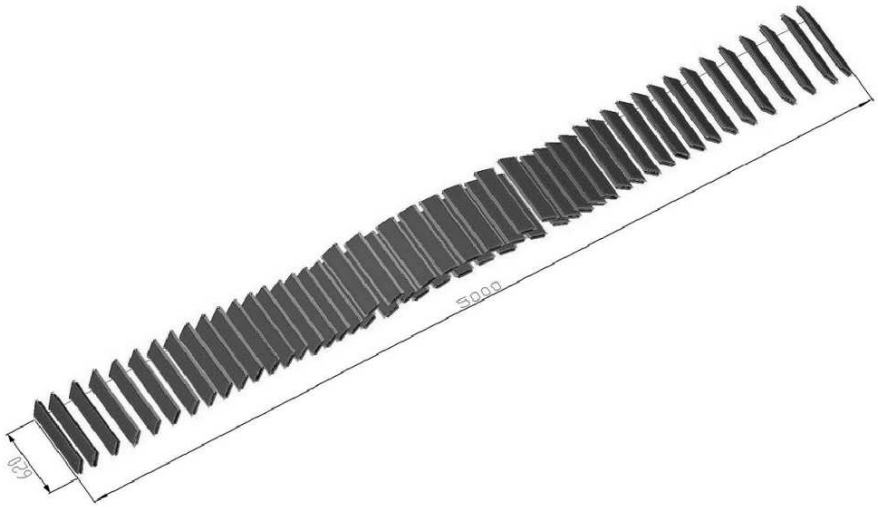

Fig. 2.71: Arrangement of multigap RPCs in the module.

In total there are 55 detectors in each module. The detectors are placed in such a way that the readout pad is perpendicular to the line coming from the interaction point. In order to exclude dead zones, the detectors in the module are designed to overlap.

Design of the multigap RPC module. The multigap Resistive Plate Chamber consists of a stack of 12 plates of glass separated by 220 μm thick spacers forming 10 equal gas gaps. The 10-gap construction was chosen to avoid processing small signals and decrease number of multihit ones.

The ALICE TOF collaboration [241] demonstrated that the RPC made of commercial soda-lime glass with bulk resistivity of $\sim 10^{13}$ Ω·cm can operate at a flux in excess of 1 kHz with no degradation in performance. In case of the NICA MPD the flux is expected to be lower than 20 Hz/cm^2.

The scheme of the detector basic element is presented in Fig. 2.72. The detector consists of two parts of 5 gaps each. The outer glass electrodes have a thickness of 0.8 mm. The internal glass electrodes have a thickness of 0.5 mm.

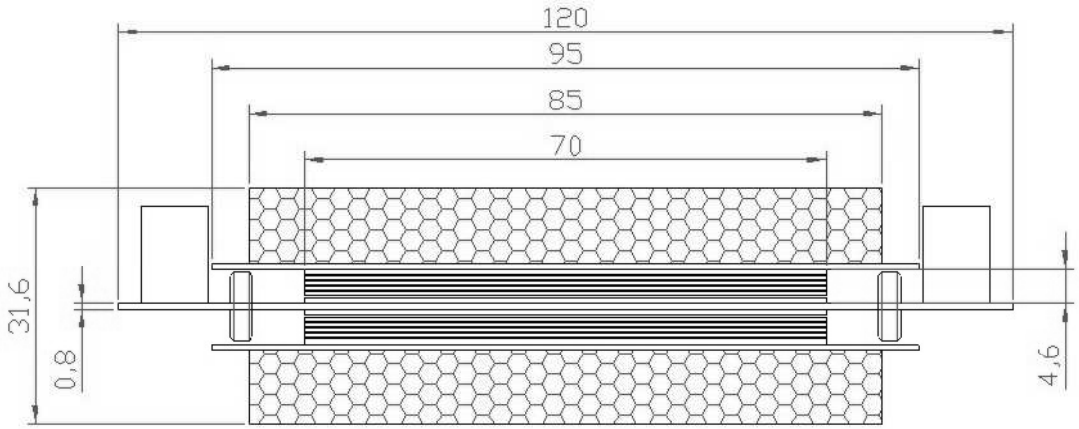

Fig. 2.72: Basic element of the timing RPC.

The fishing line as a spacer defines a 220 μm gap between all electrodes. The outer parts of two external glass electrodes are covered by a conductive tape with a surface resistivity of about 5–10 MΩ/cm^2 to apply high voltage and ground. All internal electrodes are floating. The pick up pads are made on a 0.8–1 mm thick PCB board (Fig. 2.73).

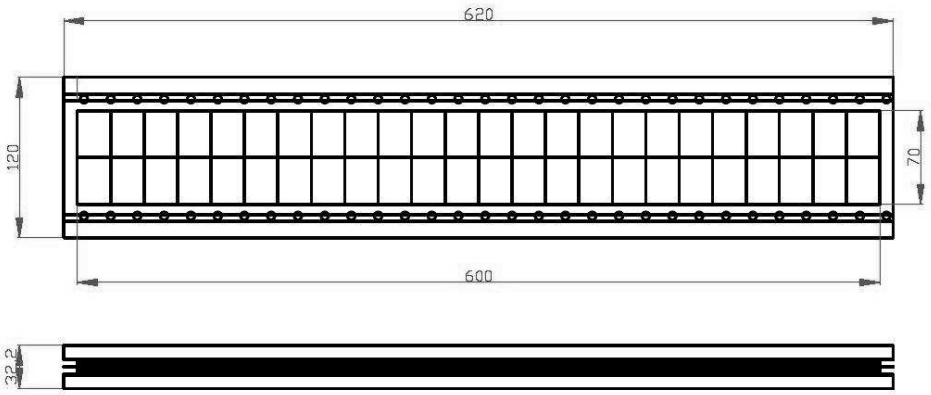

Fig. 2.73: Arrangement of pads on the readout plane and main dimensions of the MRPC element.

It should be noted that the readout pad geometry and dimension is a subject of further study. A final decision will be taken after optimization of tracking capabilities of the whole MPD detector. The coordinate from the TOF could be used as a seed coordinate in the track finding procedure for track reconstruction using the data from TPC and IT.

2.5.6 Mechanical construction of the End cap TOF

The End cap TOF system consists of two plane discs with 250 cm outer diameters placed on both sides of the MPD barrel, behind the Straw tube tracker, 2.3 m from the interaction point. The inner diameter of the disks is 40 cm. They cover the region of the pseudorapidity $1.5 < |\eta| < 2$.

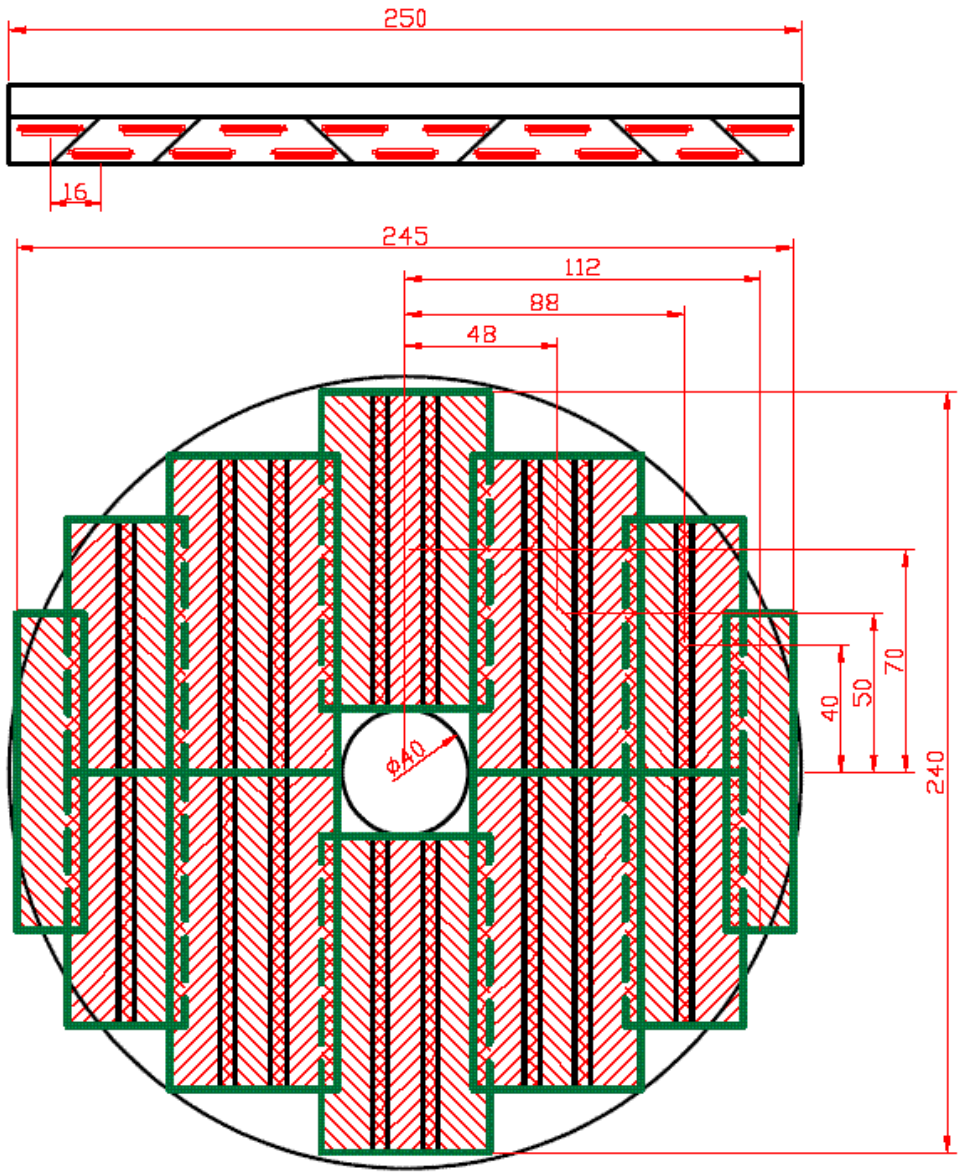

Fig. 2.74: TOF End Cap plane structure.

The End cap Disc assembled of three types of modules is shown in Fig. 2.74. Inside of the module the mRPC strips measuring 100 cm×21 cm or 80 cm×21 cm are placed with an overlap to exclude dead zones Fig. 2.75.

The mRPC readout electrodes are divided into 4 cm square pads.

In total, End cap discs consist of 28 mRPCs with 2640 readout channels. The surface of the End cap TOF detector is about 8.5 m^2.

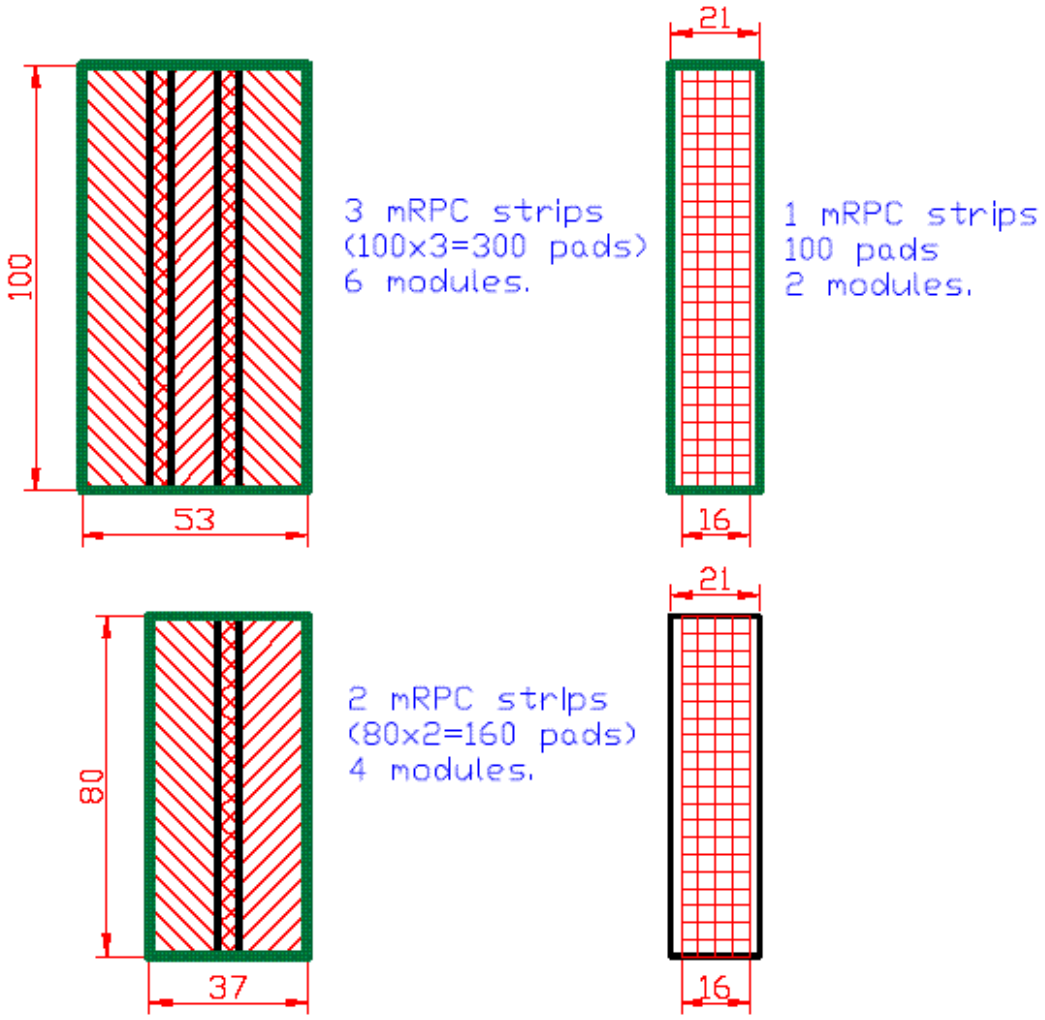

Fig. 2.75: The End Cap TOF will consist of four types of panels with mRPC strips 80 cm and 100 cm long.

2.5.7 Multi-strip mRPC

The results of Monte Carlo simulations of Au+Au collisions at NICA energies demonstrate that the expected occupancy in the phase space covered by the TOF detector is not dramatic even in high multiplicity central heavy-ion collisions. In Fig. 2.76 the particle occupancy in central Au+Au collisions at $\sqrt{s} = 9$ GeV is shown as a function of pseudorapidity η at several positions along the beam line. As a result, the use of strips for mRPC readout looks attractive, since it allows to decrease substantially the number of channels in the TOF electronics without deterioration of the desired time resolution. Moreover, by using timing information from both sides of a strip the expected space resolution of 1 cm is expected for the hits in the TOF detector. In this case the design of the TOF barrel can be much simpler (see Fig. 2.77) A basic structure of the strip readout is shown in Fig. 2.78. Twenty four of 10 mm wide strips with 2.5 mm pitch will be read out from both sides of the plate of 330x660 mm^2 total area.

In 2010 manufacturing of full-scale RPC modules has recently started in VBLHE (Fig.2.79).

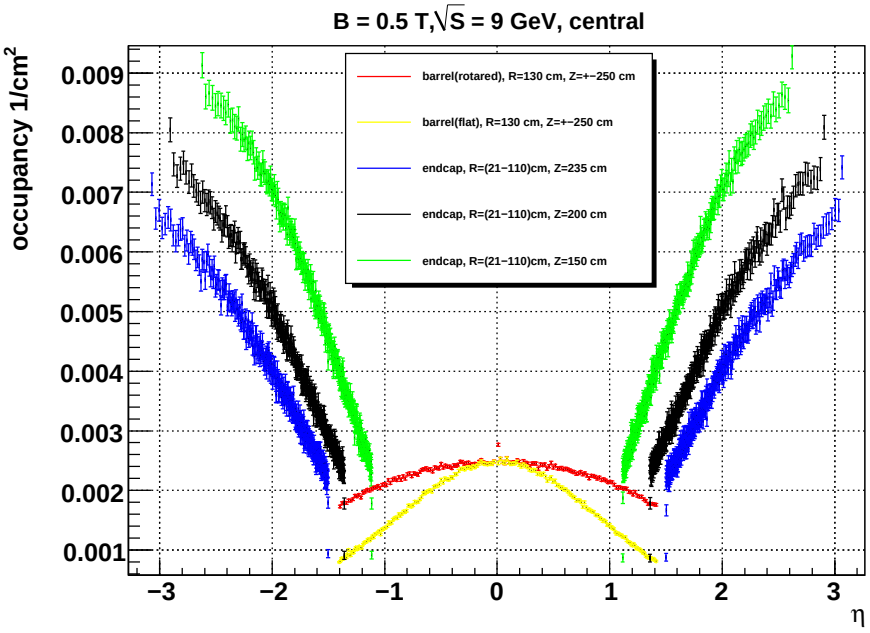

Fig. 2.76: The particle occupancy versus pseudorapidity in central Au+Au collisions at $\sqrt{s}$=9 GeV. The calculations are done at three different positions along the beam axis.

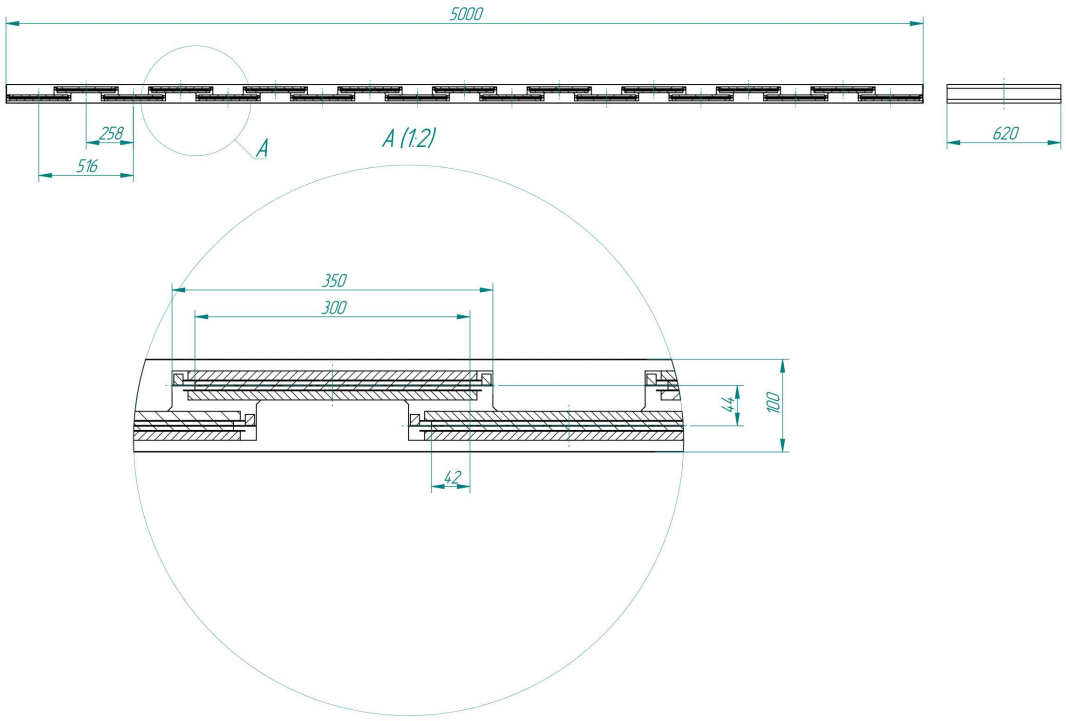

Fig. 2.77: A sketch of a TOF-barrel module with the pixel read-out.

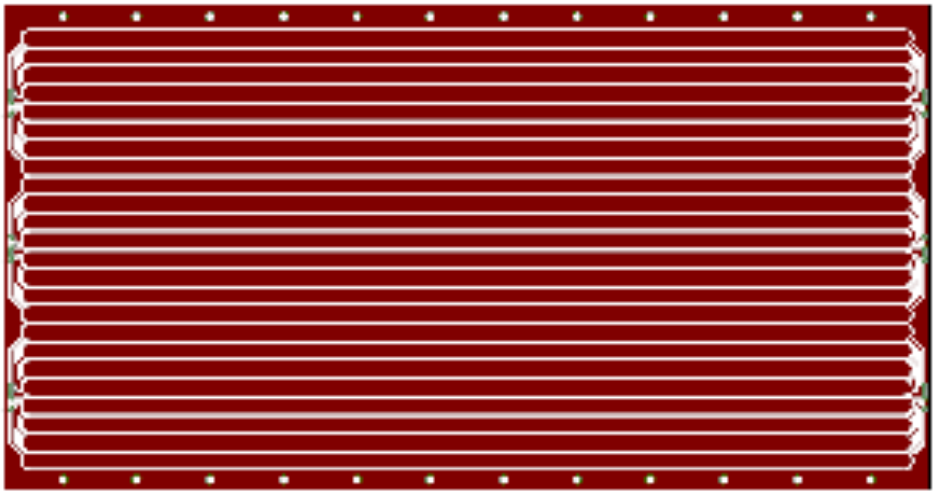

Fig. 2.78: A prototype mRPC plate with the read-out strips.

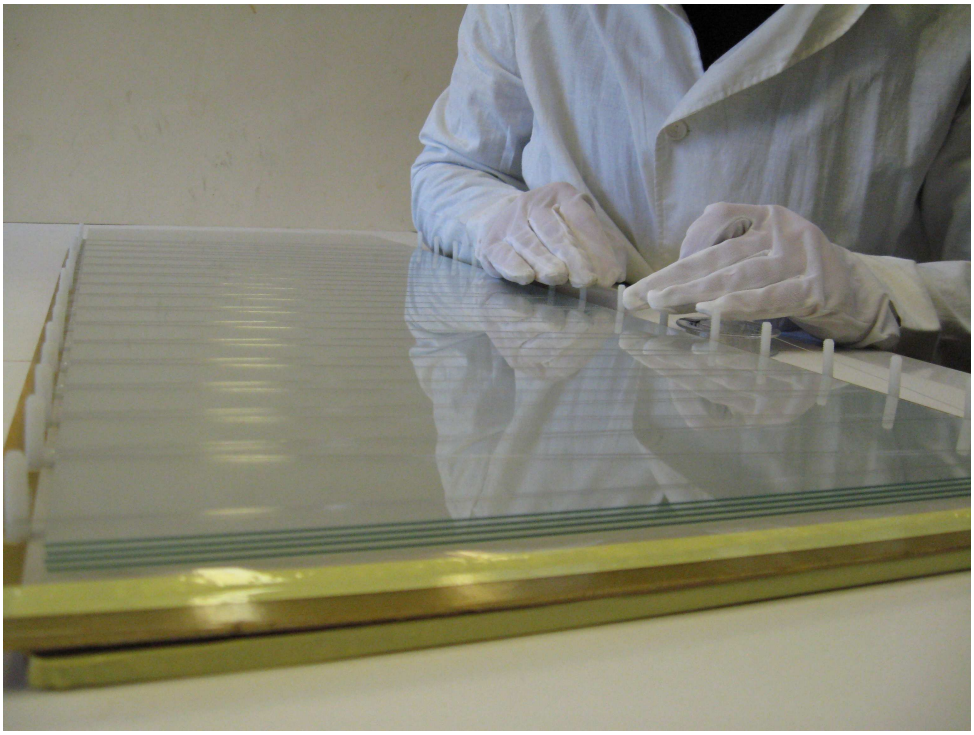

Fig. 2.79: The first full-scale RPC prototype.

2.6 Electromagnetic calorimeter

Electromagnetic probes, such as real and virtual photons (i.e. dileptons), provide key information on temperature, system size at the early stage of collision, and temperature evolution of the system from its formation to thermal freez-out. Created over the course of the entire space-time evolution of the system, once emitted, they escape from the strongly-interacting medium without any final-state interaction. Information on the direct thermal radiation (photons or dileptons) can be used to derive a limit on the initial temperature of the QGP created in heavy-ion collisions.

2.6.1 Design considerations

The primary role of the electromagnetic calorimeter is to measure the spatial position and energy of electrons and photons produced in heavy ion collisions. It also will play a major role in particle identification due to high time resolution. Besides, the photon detector will serve to measure the total energy flow which reflect, to a large extent, the initial conditions reachable in heavy-ion collisions at the NICA. The first step in the event reconstruction will be a search for the π^0 mesons and subtruction of photons assosiated with π^0 mesons from the full photon flux. The remaining photons are labeled as candidates for the prompt photons. The charged tracks with the associated energy deposited in the ECal will be analyzed to be identified as tracks of e, π, K or p. In order to reach the required sensitivity in the π^0 reconstruction, in the high photon flux, photon energies should be measured with the extremely high precision.

The expected high multiplicity environment (Fig.2.80) implies the high segmentation of the calorimeter, large enough distance to the vertex, and use of a dense active medium with the small Moli'ere radius. To have an adequate space resolution and to allow the separation of overlapping showers, the transverse cell size should be of the order of the Moli'ere radius. Reliable reconstruction of photons and mesons is only possible at small shower overlaps. The particle occupancy should not exceed 5% to determine the photon reconstruction efficiency with high accuracy.

The 3 cm squared detector cells will guarantee occupancy below 5% within the whole detector acceptance (Fig.2.81).

The energy resolution of the photon detector is a critical point in the conditions of high photon multiplicity (Fig.2.82, Fig.2.83). Achievement of the energy resolution of about 3% is highly desirable.

Neutral hadrons can be rejected by a cut on the shower width, which is applicable at all energies, and/or by a cut on the time of flight. Indeed, over a distance of 1.5 m, hadrons will reach the detector later than photons, which can be used to reject neutral hadrons in a required energy range. Optional sub-nanosecond time-of-flight measurements are forseen in the proposed photon detector of ECal.

Finally, the photon detector must be able to operate in the full MPD magnetic field of up to 0.5 T, and be compact enough to be integrated into the MPD set-up.

The "shashlyk" type device meets all the above requirements for the MPD electromagnetic calorimeter.

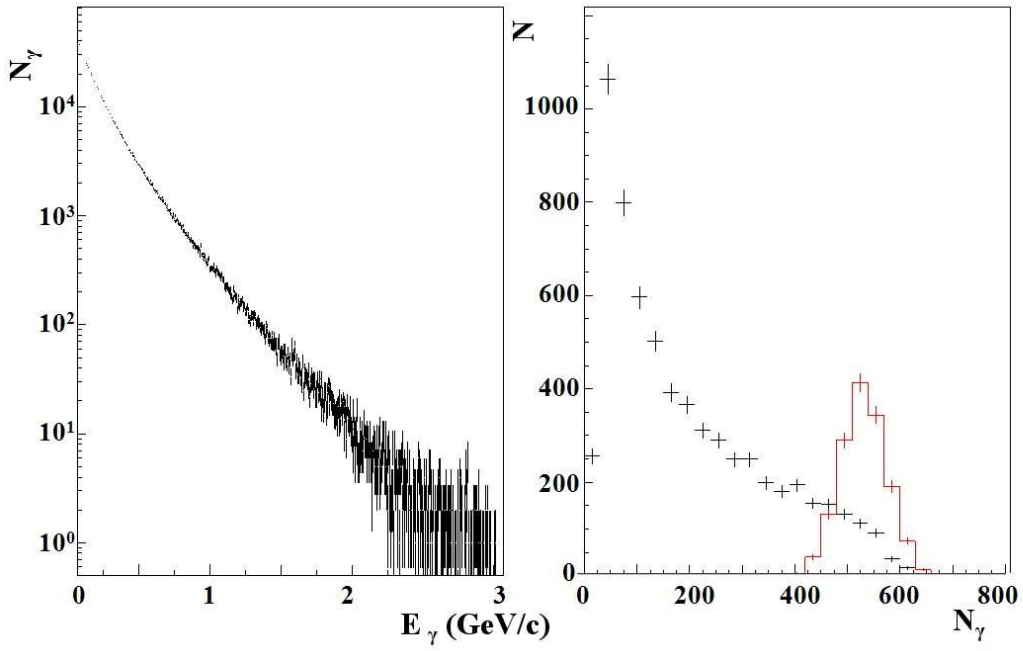

Fig. 2.80: The energy spectrum of photons (left panel) and photon multiplicity distribution (right panel) in the central (red) and minimum bias (black) Au+Au collision (4.5+4.5 AGeV).

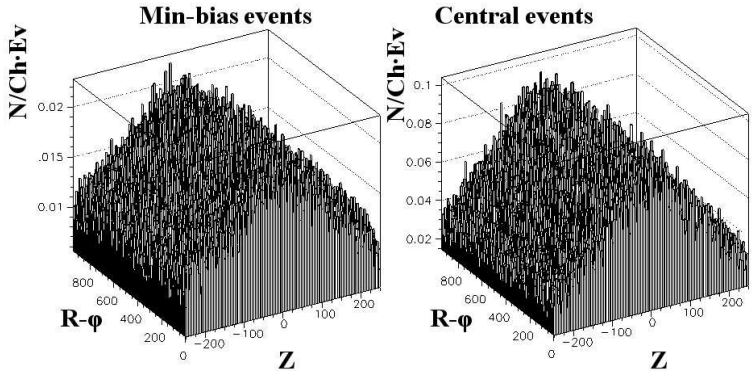

Fig. 2.81: Average occupancy per channel for the barrel part of MPD photon detector with 3×3 cm detector element. Au+Au collision with minimum bias (left panel) and central one (right panel) (at $\sqrt{s_{NN}}$ = 9 GeV).

2.6.2 "Shashlyk" calorimeter

The Pb-scintillator electromagnetic calorimeter of the "shashlyk"-type can be used in the MPD detector. Such calorimeters were used in the PHENIX [246], KOPIO [247], LHCB [248], T2K [249], and some other detectors. Calorimeters of this type are relatively not expensive, radiation hard, robust in design, and provide energy resolution $\sim 3\%/\sqrt{E}$. Spatial resolution of such calorimeters is determined by the optical segmentation and can be easily adjusted to requirements of the experiment. The prototypes of the "shashlyk"

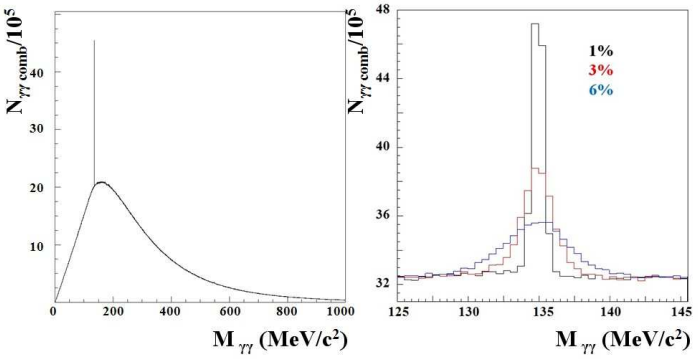

Fig. 2.82: π^0 reconstruction in the intermediate $p_{\pi 0}$ transverse momentum regions for different photon detector energy resolutions. Left panel – ideal detector. Au+Au collision (at $\sqrt{s_{NN}}$ = 9 GeV).

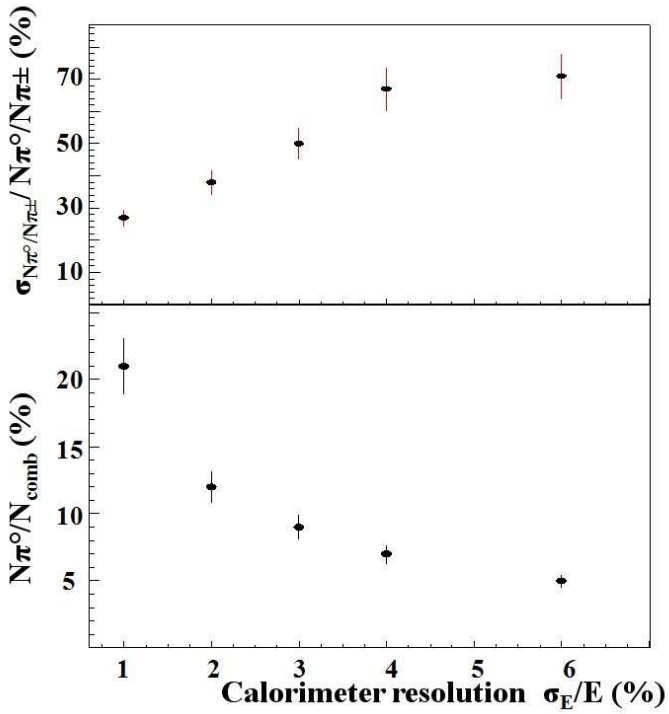

Fig. 2.83: The ratio of number of reconstructed π^0 mesons to a number of events from combinatorial background vs the calorimeter energy resolution.

type calorimeters were extensively studied by several collaborations. As an example, the energy-resolution measured in the KOPIO experiment for various readouts is shown in Fig.2.84. A quadratic fit to these experimental data gives

$$\sigma(E)/E = (1.96 \pm 0.1)\% \otimes (2.74 \pm 0.05)\%/\sqrt{(}E)(GeV),$$

where $\otimes$ means quadratic summation. The relatively large constant term of 2% may be decreased by increasing the length of the module. However, this term is not essential for the photon energy range of 50-1000 MeV.

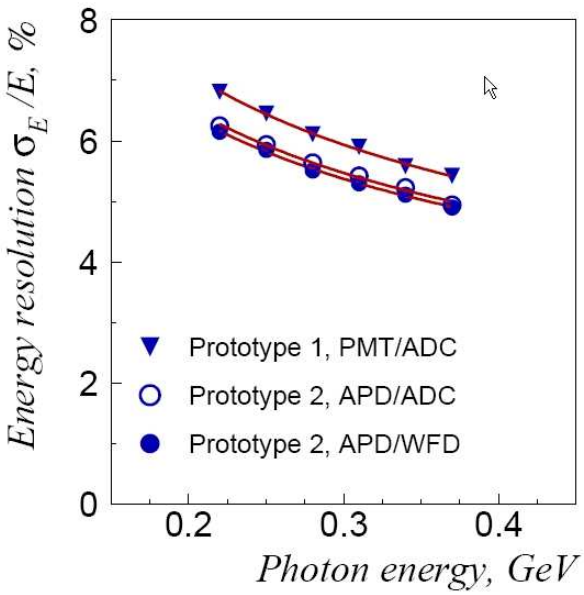

Fig. 2.84: Energy resolution of the "Shashlyk" type calorimeter measured in the in-beam test.

An example of the "shashlyk" calorimeter module is shown in Fig.2.85.

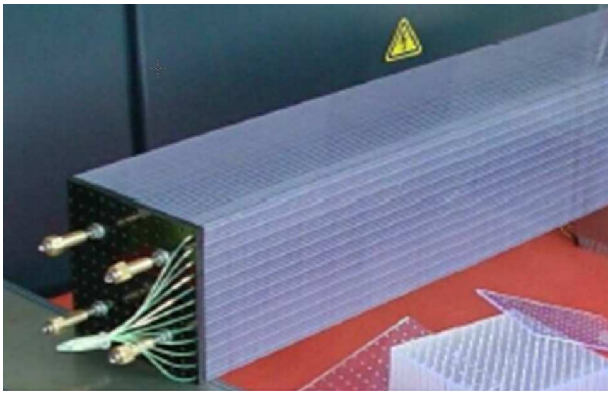

Fig. 2.85: "Shashlyk" module.

The time resolution of a module identical to that of KOPIO was studied by a JINR group at the DESY accelerator. As it was expected, the time resolution in this device has been found to depend on the amplitude of the output signal. There are two reasons for this. The first one is the improved signal-to electronics noise ratio for large signals. The second, and the more important one, is better statistics of light collection for larger energies deposited in the detector. The experimentally measured time resolution of one detector module is shown Fig.2.86.

The ratio of the number of collected photoelectrons to the energy deposited in the calorimeter, experimentally measured by the KOPIO collaboration, was used to simulate the time resolution for different particles crossing MPD (Fig.2.87).

The MPD electromagnetic calorimeter is proposed to be built of towers as basic building elements (e.g., 3 cm squared). Each Pb-scintillator based tower contains sampling

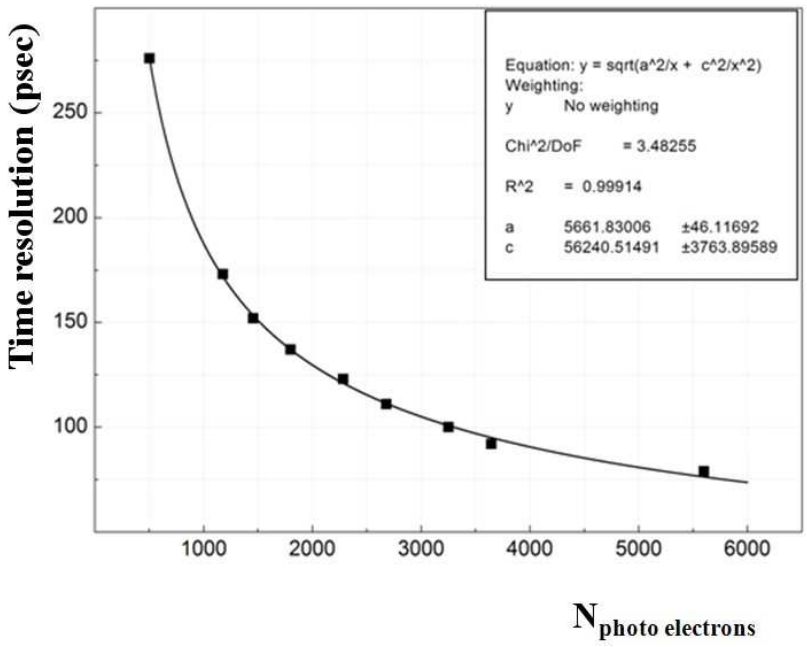

Fig. 2.86: Dependence of time resolution on the number of collected photoelectrons.

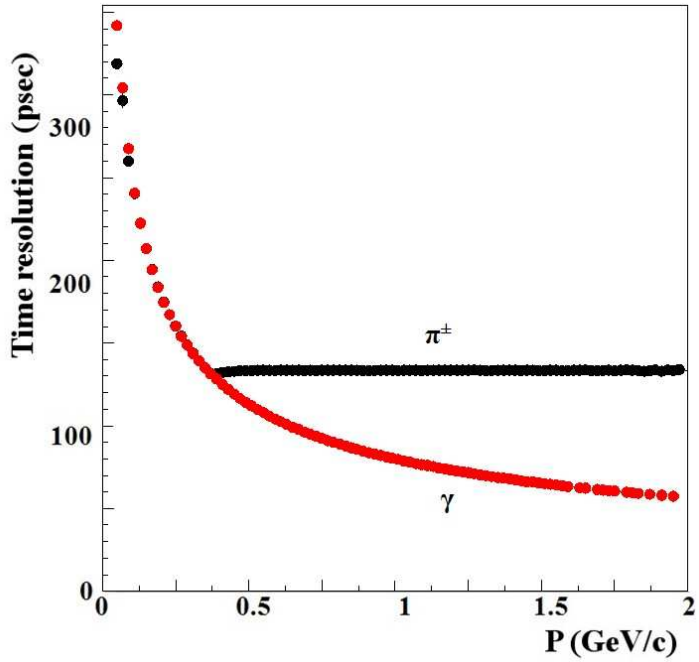

Fig. 2.87: Dependence of time resolution on particle momentum.

cells consisting of 250 alternating tiles of Pb (0.275 mm) and plastic scintillator (1,5 mm). The module with a 18 radiation length thickness will be approximately 40 cm long. The cells of each tower are optically combined by 9 longitudinally penetrating wavelength shifting fibers for light collection. The light collected with 9 fibers is read out by MAPD units with 3×3 mm^2 sensitive areas. The towers, mechanically grouped together, make

a trapezium-shape module. The modules are combined into a detector sector (Fig.2.88) with minimum dead space and projective orientation of each tower.

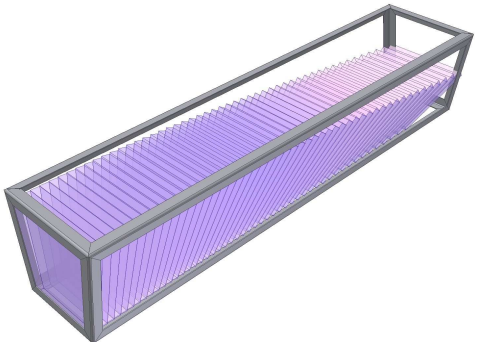

Fig. 2.88: Detector sector.

The whole barrel part of MPD electromagnetic calorimeter will be constructed from 48 sectors (Fig.2.89). The heat-producing electronics will be thus separated from the modules and mounted on the upper parts of sectors.

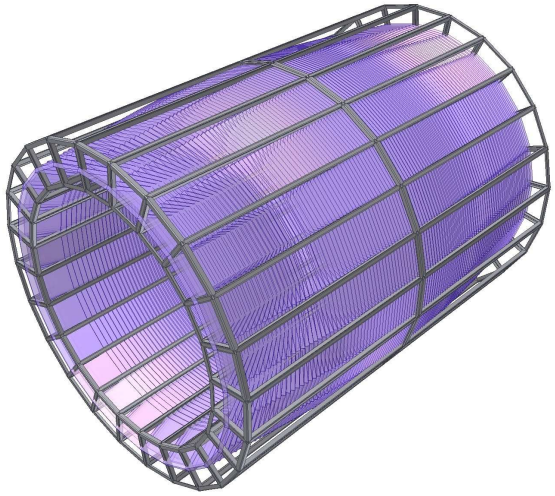

Fig. 2.89: ECAL detector.

The estimated total cost of each module is 100 Euros.

2.6.3 Photodetector

The photon detector is to be operated in a magnetic field of up to 0,5 T. The micropixel avalanche photodiode, which is a novel photodetector with a multipixel intrinsic structure on a common silicon substrate is a best candidate for a photon detector in this case. An advanced version of MAPD with a deep micro-well for charge collection has density of pixels over $10^4/\text{mm}^2$ [250]. Each independent avalanche region (vertical channels) with individual micro-wells for charge trapping/collection is created at a depth of about 3-5 μm using a special distribution of the inner electric field. Charge collection in individual micro-wells provides the local self-quenching of avalanche processes in the MAPD.

Each pixel works as an independent photon micro counter working in the Geiger mode on a common load. Actually, each pixel operates digitally (yes/no) in response to an incident photon, but the MAPD in whole is an analogue device, which can measure light intensity within the dynamic range corresponding to the total number of pixels. Fig.2.90 shows the MAPD design structure, principle of operation and general view.

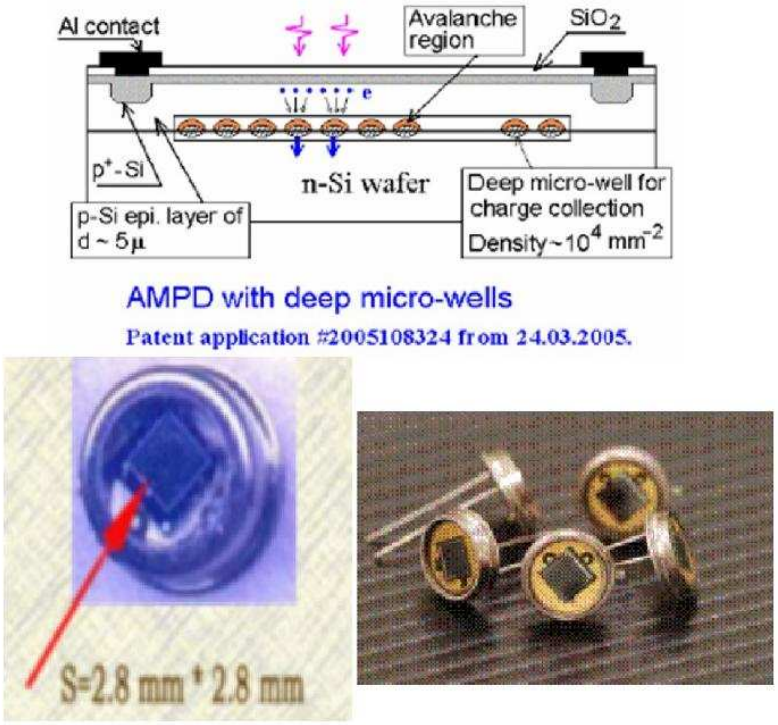

Fig. 2.90: MAPD detector.

The required design parameters of the calorimeter determine requirements also to the photodetectors: they have to be compact, insensitive to magnetic field and have large dynamic range and linearity in measuring particle's energy. Deep Micro-Well MAPD matches these requirements exactly. The present 3×3 mm^2 MAPDs can be easily used for the light detection from 9 fibers of a "shashlyk" calorimeter single tower.

2.6.4 Calibration and monitoring

In order to keep the photon detector energy and space resolution at the required level, the detectors and readout electronics have to be calibrated and monitored. Each detector will be calibrated before installation with a relatively low-energy (hundred MeV) electron test beam at several electron energies. Additional *in situ* calibration will be done during datataking using amplitude spectra from each detector. The truncated mean of the amplitude spectrum of each channel can be used for relative calibration, and the π^0 peak position for absolute calibration. Monitoring will be carried out constantly during datataking. The following values will be monitored:

- The temperature of the MAPD photon detectors with a 0.1^{o}C accuracy. One measurement per module (about 20 detectors).

- The gain of the readout electronics. For this purpose each preamplifier will have a calibration input. One measurement per channel.
- Transparency of the scintillator and their optical contacts with light detectors. This value will be monitored by calculating the truncated mean of the spectrum of each module for a certain time (typically 5-20 minutes) and compared with previous measurements. One value per detector.
- Light emitted by the LED orlaser in each detector will be used for continuous calibration of the full chain.

2.6.5 Read-out electronics

The readout electronics must be capable of measuring energies with a digitization uncertainty of 0.5 MeV in a dynamic range of 50-5000 MeV, and the time of arrival with respect to the common start with an uncertainty of the order of hundred ps. Operation of this readout electronics is required to be completely pipelined with no dead time. To meet these performance requirements for energy and timing resolution, front-end electronics based on the sampling ADCs was built and tested. All the above results were obtained with such electronics. This kind of read-out fully satisfies the needs of the device. Alternatives to the read-out electronics for the calorimeter are under study. Final version of front-end board for the calorimeter will be chosen later on with regard to the fast progress in the development of commercially available electronic components.

2.6.6 Possibility to detect and identify neutrons by electromagnetic calorimeter

Possibility of neutrons registration by electromagnetic calorimeter was studied using MC simulation based on GEANT4 toolkit. Response of the calorimeter with sampling 0.5 mm of lead + 1.5 mm of scintillator (170 layers) on neutrons with kinetic energy in the range 50-1000 MeV has been simulated. Total thickness H of the calorimeter is 34 cm (16 X_0 or 0.8 λ_I). Cell size is 4×4 cm^2 Energy reconstruction has been simulated basing on assumption that energy deposition in the calorimeter is proportional to the energy deposition in the layers of scintillator. All the effects related with scintillation, light collection and transportation, efficiency of photomultipliers and performance of electronics have been neglected. To simulate realistic time shape of the signal (the physical part of it) one has supposed that the effective speed of light in optic fibres is 0.15 m/ns. Particle has been considered as detected if it produced cluster with energy above 30 MeV (corresponding energy deposition in the scintillator is 7.5 MeV).

The efficiency ϵ of neutron registration as function of neutron kinetic energy E_{KIN} is shown in Fig. 2.91. For $E_{KIN} > 100$ MeV it is practically independent on neutron energy and is about 50% that basically corresponds to naive expectation:

$$\epsilon = 1 - e^{-\frac{H}{\lambda_I}} = 0.55. \tag{2.1}$$

Fig. 2.92 represents distribution of total energy deposition in scintillator for neutrons with $E_{KIN} = 200$ MeV and photons with the same energy.

As far as photon and neutron are neutral particles, they can be distinguished only on the base of calorimeter information. Usage of the calorimeter as time of flight detector

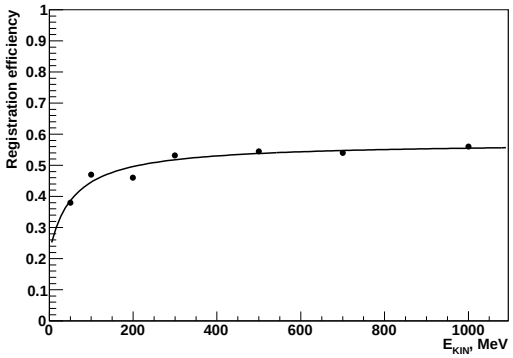

Fig. 2.91: The efficiency ϵ of neutron registration as function of neutron kinetic energy.

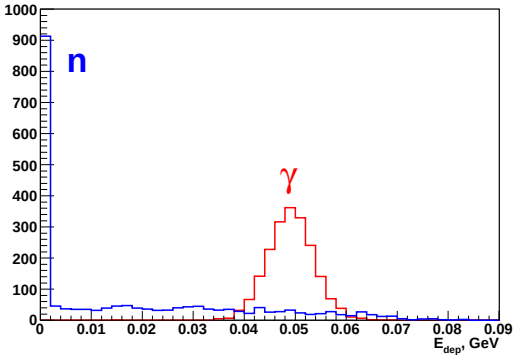

Fig. 2.92: Energy deposition in scintillator produced by photons (red) and neutrons (blue) with E_{KIN}=200 MeV.

provides possibility to separate neutrons and photons (measurement of β) and to measure the momentum of neutrons. In ultrarelativistic case separation of photons and neutrons can be performed using information about cluster shape.

Cluster time t_c is defined as:

$$\int_0^{t_c} \epsilon(t) \ / \ \int_0^{\infty} \epsilon(t) = 0.3 \tag{2.2}$$

where $\epsilon(t)$ is the shape of a signal - number of arriving photons as function of time.

For normal incidence time resolution σ_t of the calorimeter, defined by development of shower and light transportation, for different energies of photon and neutron is presented in Fig. 2.93. It's practically independent on energy and is about 310 ps for neutrons and 190 ps for photons. The main difference can be explained by the fact that geometry of photon shower is quite stable while energy deposition produced by neutron is randomly distributed along depth of the calorimeter. The accuracy of β measurement is

$$\sigma_\beta = \frac{c\beta^2\sigma_t}{L}, \tag{2.3}$$

where $L = L_0/sin\theta$ is the flight distance, $L_0 = 1.5\ m$ is the radius of calorimeter barrel and θ is polar angle of particle momentum in respect to the beam direction. The efficiency and purity of neutron identification should depend on the relative fraction of neutrons and photons in the calorimeter. The described identification procedure is effective only in the case $1 - \beta \gg \sigma_\beta$. For $\theta = \frac{\pi}{2}$ the kinetic energy of a neutron corresponding to the case $1 - \beta = 3\sigma_\beta$ for normal incidence is 900 MeV ($\beta = 0.86$).

Due to the peculiarities of neutron interaction in the calorimeter clusters produced by them have irregular XY-shape while photon clusters are quite symmetric. The value

$$RMS = \sqrt{RMS_x^2 + RMS_y^2}, \tag{2.4}$$

where $RMS_{x,y}$ characterize spatial energy distribution in cluster along X and Y axes correspondingly, can be used as the measure of cluster irregularity. RMS distribution for clusters produced by photons and neutrons with kinetic energy above 1 GeV is shown in Fig. 2.94 .

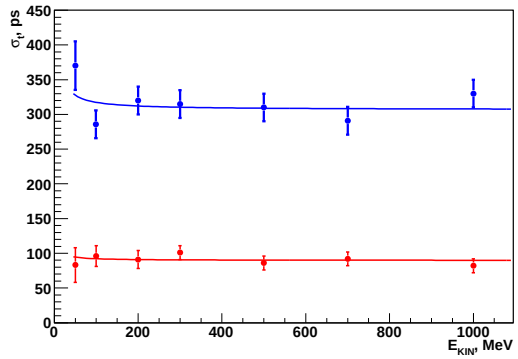

Fig. 2.93: Time resolution for photon (red) and neutron (blue) clusters.

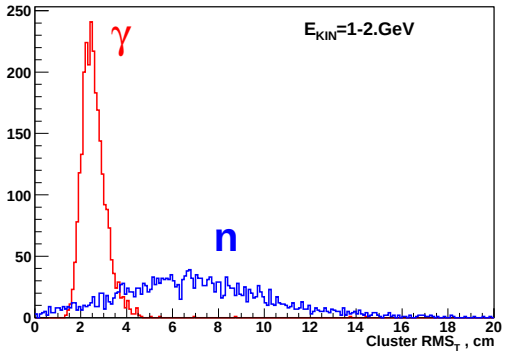

Fig. 2.94: RMS distribution for photon (red) and neutron (blue) clusters, produced by particles with kinetic energy $1\ GeV < E_{KIN} < 2\ GeV$.

Accuracy of neutron momentum measurement is mainly defined by precision of time measurement by calorimeter:

$$dP = \gamma m_n c(\beta^2\gamma^2 + 1)\sigma_\beta = \gamma m_n c^2 \beta^2(\beta^2\gamma^2 + 1)\frac{\sigma_t}{L} \tag{2.5}$$

Relative resolution dP/P is shown in Fig. 2.95 as function of neutron momentum for $\theta = \frac{\pi}{2}$.

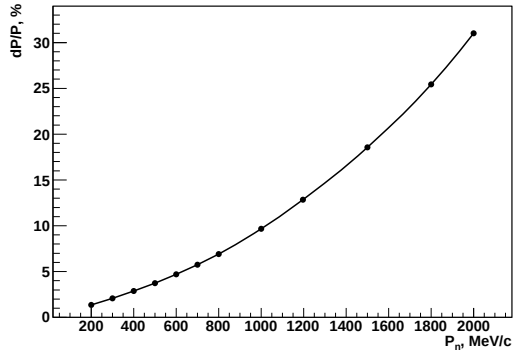

Fig. 2.95: Relative resolution for neutron momentum for .

2.6.7 Crystal option of ECal

Electromagnetic calorimeter on the basis of crystal detectors is considered as backup solution, if a further study of the physics process at MPD will require better parameters from ECAL. Such calorimeter does have some advantages –

- smaller Moli'ere radius increases the two particle separation power and reduce occupancy in each channel of ECAL
- smaller radiation length improves the energy resolution of the ECAL to 1.5 $\%/\sqrt{E}$
- possibility to produce crystals of different shape makes calorimeter more hermetic and may help in further reduction of each channel occupancy.

Lead tungsten (PbW04) and BGO crystals are most promising materials for the photon detector. The PbW04 crystal was chosen by the CMS, ALICE and COSY Collaborations for their electromagnetic calorimeters. However, the requirements of all those experiments are rather different. The possibility of using this crystal for electromagnetic calorimetry has been studied in recent years [251, 252, 253, 254, 255, 256, 257] and very significant progress has been made towards its use in large calorimeters.

A PbWO4- crystal calorimeter, 13.4 cm long (16.8 cm for the BGO crystals) is considered as a possible variant of the electromagnetic calorimeter. The cross section shape of the unit is proposed to be hexagonal. Schematic drawing of the calorimeter is shown in the Fig.2.96.

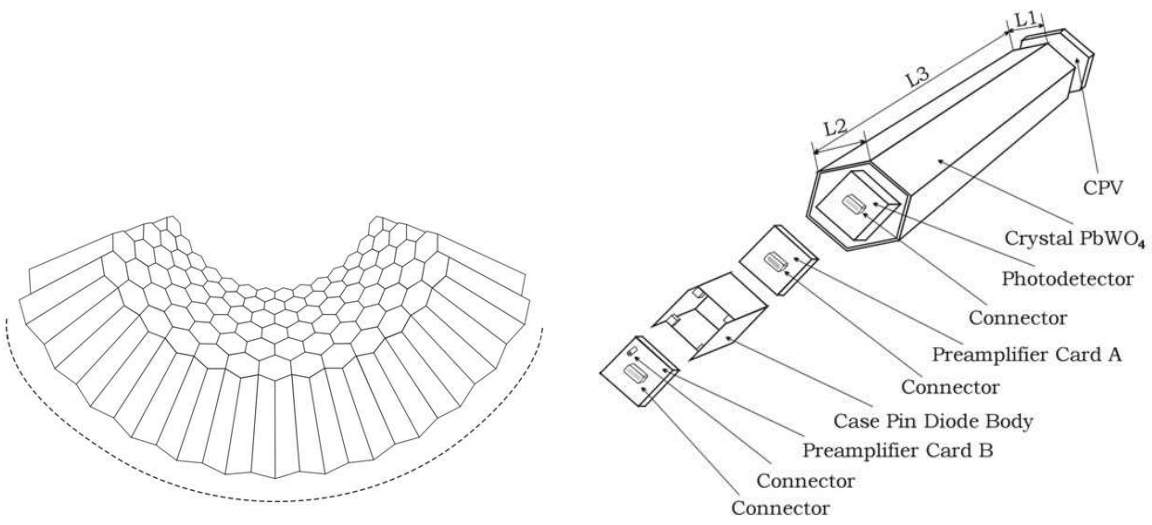

Fig. 2.96: The view of honeycomb shape of hodoscope (left) and the single unit scheme (right).

2.7 Straw end-cap tracker

2.7.1 Technical requirements

The physics objectives of the MPD is detailed in Section 2.1. The MPD TPC and the End-Cap Tracker (ECT) is the main tracking detector in the pseudorapidities $|\eta| \leq 1$ and $1 < |\eta| < 2.2$ (see Fig. 2.3), correspondingly. The ECT together with the TPC and TOF has to provide charged particle momentum measurement, and identification of the π and K. Preliminary simulation shows that for the π and K yields the ratio of data in the ECT to data in the central detector is more 1 for the $Au + Au$ inelastic collisions in the energy range from $\sqrt{s_{NN}}$= 3 GeV to 9 GeV. Moreover the extension of the set-up acceptance is useful on the observation for the collective flows and for registration of strange particles.

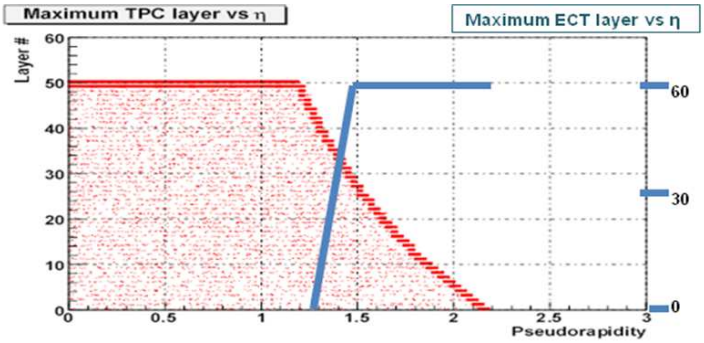

Fig. 2.97: Maximum detector layer number reached by tracks as a function of pseudorapidity in TPC and ECT.

The TPC has good momentum resolution up to $|\eta| < 1.5$, but the resolution deteriorate fast later especially for close particles. Standalone ECT momentum resolution is about 10% (Fig. 2.98), and combined TPC and ECT momentum resolution is better 5% (Fig. 2.99). Rough estimation of the track reconstruction efficiency with straw number of 346 per layer is shown in fig. 2.99. Increasing of the straw density per layer up to 600 pieces will improve these values.

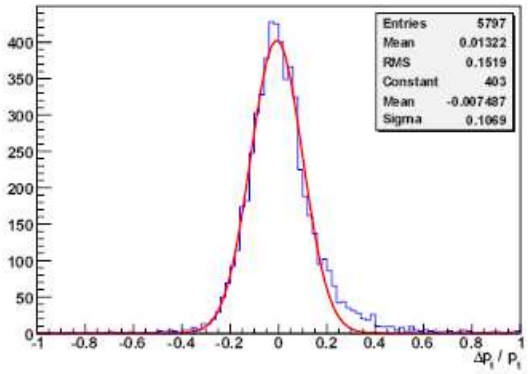

Fig. 2.98: Relative transverse momentum error of primary tracks with $P_t > 0.1$ GeV/c reconstructed in the full acceptance region ($\eta = 1.5 \div 2.0$) of ECT.

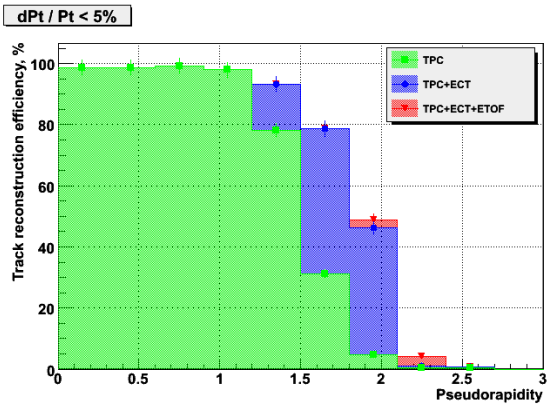

Fig. 2.99: Track reconstruction efficiency vs pseudorapidity. Straw density per layer is understate for the planed value by factor 1.6.

All these requirements need to be fulfilled at the luminosity $L = 10^{27} cm^{-2} s^{-1}$ for $Au+Au$ collisions at NICA at a center-of-mass energy up to $\sqrt{s_{NN}} = 12$ GeV (for ^{197}Au), which corresponds to an interaction rate of the NICA about collider is 10kHz with average particle multiplicities ~500. Differential straw tube occupancy for the central collisions wuth impact parameter $b < 3fm$ is shown in Fig.2.100. The tube occupancy are 0.21, 0.19 and 0.20 for the extreme and middle layers, correspondently. These values come near to the TRT ATLAS LHC occupancy [258]. We will consider the TRT ATLAS experience and the track reconstruction algorithms validation will be studied in more detail, but we consider the possibility to use the segmented straw design of the straw detectors also. It allows to reduce the occupancy up to 9%, but number of the readout channels will be redouble.

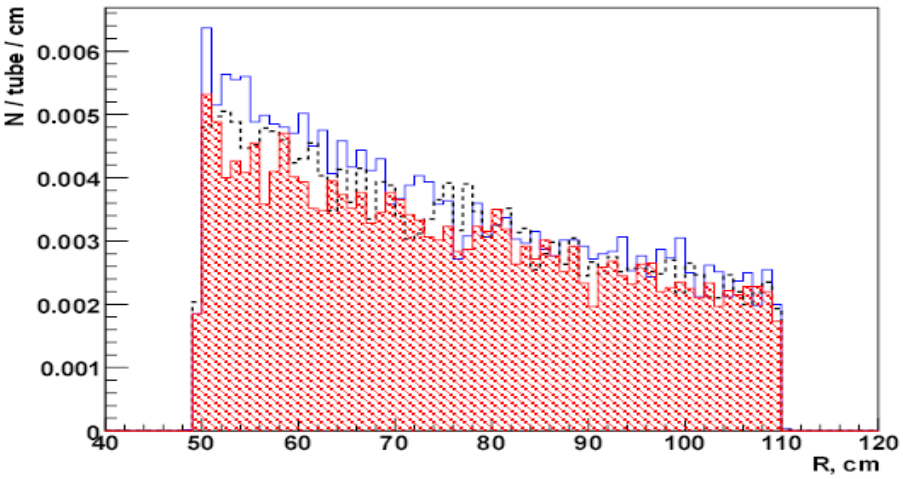

Fig. 2.100: Average number of hits per 1 cm of a straw tube length vs radius of the ring straw detector at 9 AGeV. Solid line: first straw layer, dashed line: central layer and hatched histogram: last layer.

The ECT is required to contribute to the accuracy of the momentum measurement by providing a precise measurement in R-φ. The ECT provides fast and efficient pattern recognition tracks with $p_T > 0.2$ GeV within $0.8 < |\eta| < 2.1$ together with the precision SCT layers and TPC tracking mainly. It also contributes significantly to pion/kaon identification together with the TOF. The using of ECT can allows to fast recognition of the reaction plane for the pseudorapidities within this range.

2.7.2 ECT design consideration

The design of the ECT is similar of the TRT ATLAS End Cap modules, but with many innovation aspects [259, 260, 261]. Each of two end cap parts consists of two sets of identical and independent modules. Each module is divided into five sub modules which will be assembled independently. The sub module contains 6 layers of the 4 mm in diameters straw with 600 straws per layer. The size of the sub module in z-direction is 250 mm, additional 5 mm per side will be need for the Faraday garage. The straws in first and 4-d layers of the sub module will be oriented in radial direction. The straws in second and fifth also in third and sixth layers will be inclined with +7 and -7 degrees to the radial direction, correspondingly (Fig. 2.101). The distance between straws in R-φ

planes varies from 5.2 mm at the innermost radius of 500 mm to about 13.3 mm at the outer radius of 1100 mm. Empty gap between two sub modules has size about 190 mm that can allow to define vector of the tracks for the hard particles. Fig. 2.102 shows the schematic design of radial and incline straw layers of the wheel.

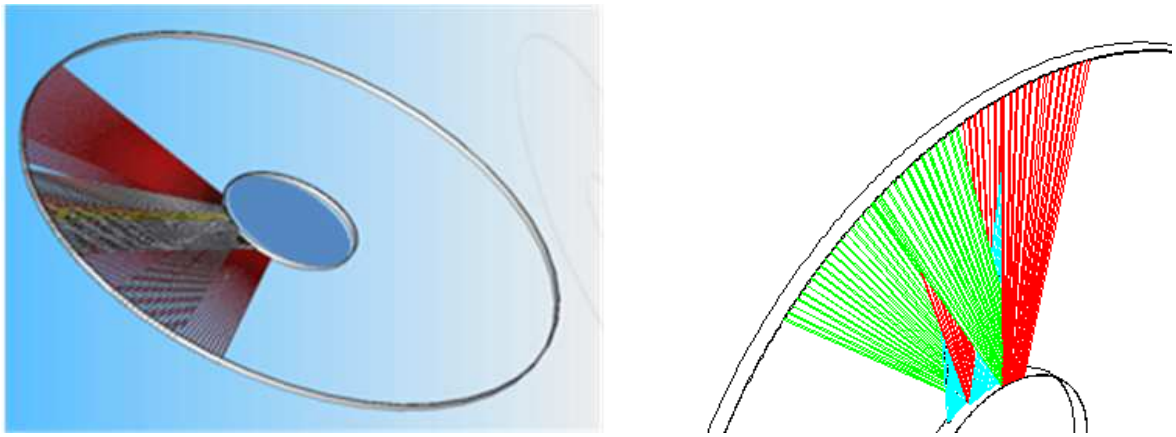

Fig. 2.101: Common view of the ring straw detector with 6 straw layers in radial direction and for ±7 degrees inclined.

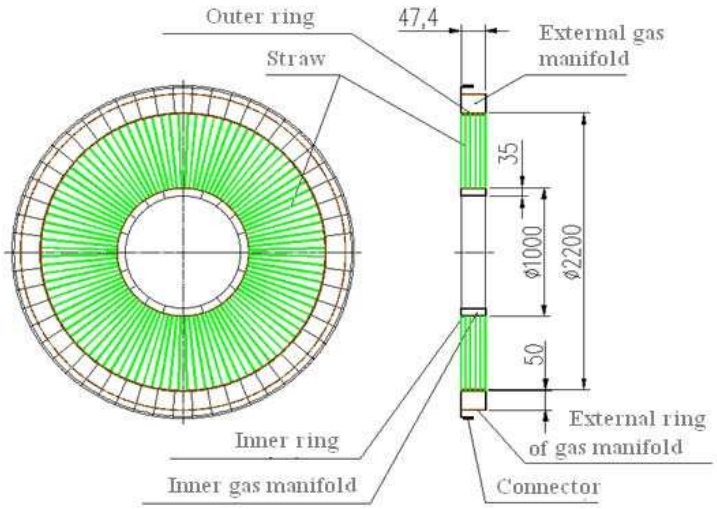

Fig. 2.102: Preliminary design of the ring straw sub module.

The material at the inner radius of the sub modules will be minimizing. All the electronics and high-voltage components will be located at the outer radius. They cover a radial extent of 10 cm, and additional 5-7 cm will be need for the services. The ECT consists mostly of low-Z materials, and contains 2×60 straw layers with 72000 straws long of ∼60 cm. The reinforcing straw diameter is chosen to be 4 mm with granularity of 28 cm^2 or with granularity ∼9 cm^2 and ∼14 cm^2 for two segments of the segmented straws, that provide not very high them occupancy [262, 263]. The sketchy view of the segmented straw is shown in Fig. 2.103. The insensitive length of the central spacer zone is ∼10 mm.

Four mm in diameter straws were chosen as detecting elements as a compromise between value of the granularity, speed of response, and mechanical and operational unifor-

mity and stability. The sensitive time of the straw is about 40 ns, and spatial resolution is 200 μm. The straw anodes are 30 μm diameter gold-plate tungsten wires at high voltage potential and straw front-end electronics inputs directly connected to the anode wires. The tension of the anode wires are in the range of 60-90 grams. A fast low-noise amplifier-shaper circuit is used to process the signals. The discriminator has threshold setting around 0.2-0.3 keV for efficient and accuracy measurement of the drift-time. A low-mass shielded twisted-pair cables are used to removal these signals from located on the detector digital pipeline by the validation from the level-1 trigger.

Fig. 2.103: Common view of the straw with two segments.

2.7.3 Prototype studies

Carbon-coated Kapton straws with an inner and outer graphite cover, similar to those used in the ATLAS TRT [258], have been chosen as the detecting elements for EC. The diameter tolerance for the straws of 4 mm in diameter is specified to be $-0 + 30$ μm, the length of the straws is 607 mm. Thickness of the straw tube wall is 72 ± 10 μm, and the cathode of the straws has a moderated resistance ($\rho_0 \approx 10$ $\Omega/square$). Small prototypes have been used for the investigations of time-amplitude characteristics and the rate capability properties for gas mixture $ArCO_2$ with an addition of CF_4 and O_2. The studies led to the choice of $80\%Ar + 20\%CO_2$ gas mixture as the optimal gas for the EC. Addition of up to 20% of CF_4 or up to 3% of O_2 lead to insignificant change of the time parameters for the straws of 4 mm in diameter [264]. A study of the straw rate capability for the gas mixture based on Ar was carried out using X-Ray tube [265]. It has been shown that the relativistic particles intensity $\approx 5 \times 10^5$ $s^{-1}mm^{-1}$ should be regarded as a maximum rate capability for the straw of 4 mm in diameter (Fig. 2.104).

A separate sector prototype is developed to validate the conceptual design described in Subsection 2.7.2. A schematic design of the prototype is shown in Fig. 2.105 (left sketch). This 30^0-sector prototype will contain 6 layers of radial and inclined at $\pm 7^0$ straws. The common view of the prototype with the installed radial straws is shown on the Fig. 2.105 right part. The straws are reinforced with C-fibres, their length is chosen to be 50 cm.

2.7.4 Material budget

The used straws is like TRT ATLAS straws with high radiation hardness, weight of the nonreinforcing and reinforcing straw is 1.1 gram per one meter of its length and 1.58 g/m, correspondingly. Table 2.15 shown an radiation length for seven different η-bins (R — radial distance from the beam line) for main elements placed in sensitive area of the ring straw module.

Radiation length in % of X_0 for the crimping pins per one layer of the straw and plastic end plugs is 0.657% and 0.23%, correspondingly. These elements are located into the inner gas manifold with length of 40 mm in radial direction.

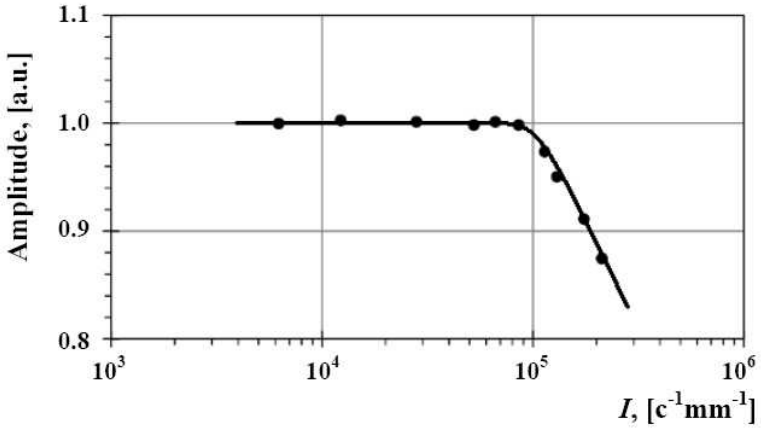

Fig. 2.104: The change of the signal amplitude versus the irradiation of the 1 mm of the anode per second.

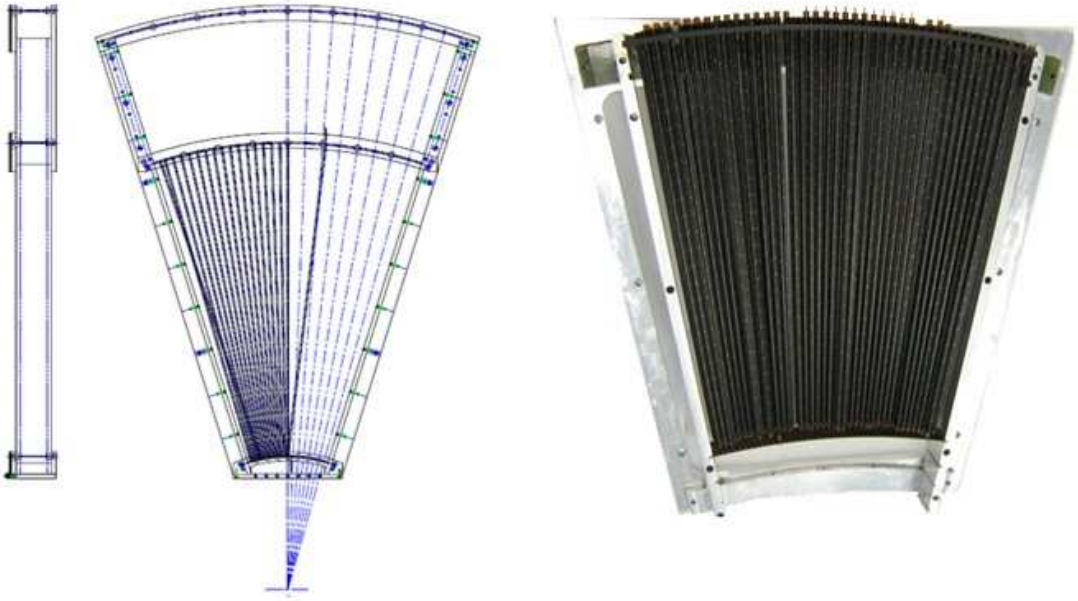

Fig. 2.105: The sketch of the 30^0-sector prototype (left) and the common view of this prototype (right).

Table 2.15: Breakdown of the ECT material budget as a function of a R. The estimation is done assuming particles crossing at normal incidence.

	Radiation length in % of X_0						
R, mm	942	845	760	684	615	554	501
Straw walls, 60 layers	1.1	1.2	1.95	1.51	1.67	1.86	2.06
Reinforcing straw walls, 60 layers	1.6	1.76	1.43	2.18	2.42	2.69	2.97
Anode wire, 60 layers	0.12	0.13	0.14	0.16	0.18	0.20	0.22

2.8 Drift CHambers (DCH) end-cap tracker

MPD physics requires precise momentum measurements in the forward hemisphere. Among the options for the MPD end-cap tracker, use of cylindrical drift chambers has also been considered. As an optimal solution, it was decided to include into the MPD setup several chambers of such type manufactured and employed by the NA48 experiment at CERN [266]. The equipment was transported to Dubna in July 2010 [267] in the framework of the JINR-CERN partnership co-operation program (the agreement was signed in January 2010 [268]).

A proposed setup is shown schematically in Fig. 2.106

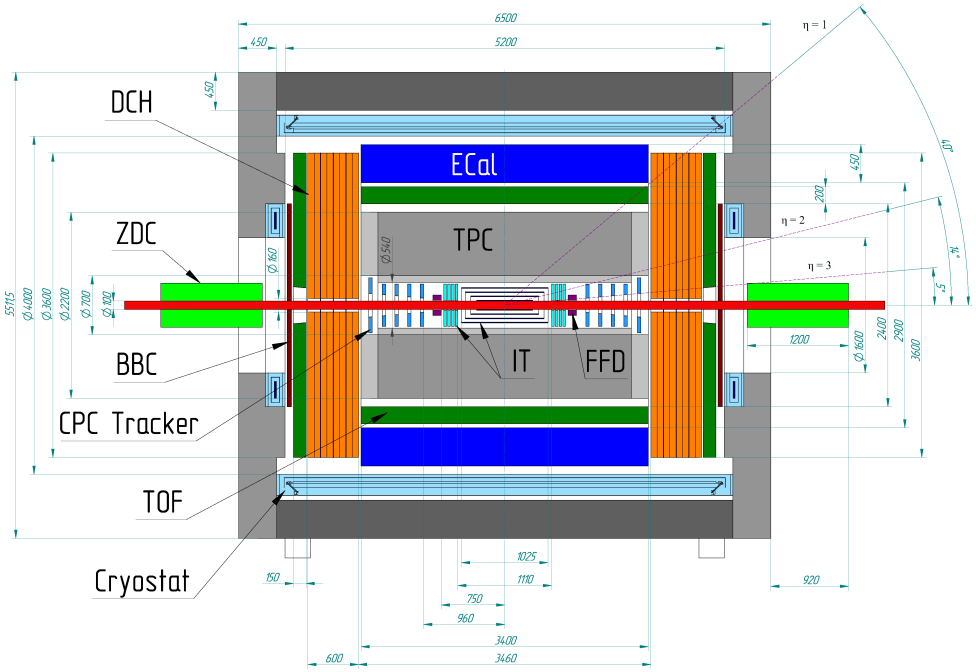

Fig. 2.106: Cross-section of the MPD central detector with the former NA48 drift chambers as the end-cap tracker.

The end-cap tracker (DCH system) consists of 4 drift chambers (see Fig. 2.107) with a diameter of 2.6 m located just behind the TPC ends. Each chamber has four views (X, Y, U and V) to avoid ambiguities in the position measurement. Each view consist of two planes of 256 wires, at a distance of 1 cm from each other. In total, there will be roughly 16 measured points (in addition to the TPC points) for a track segment reconstructed within the DCH system. The spatial resolution of each view (point) is of about 100 microns. Monte Carlo simulations have been performed aimed in studying some basic characteristics of the MPD detector for tracking in the region of pseudorapidities $\eta > 1.4$ for the combined (TPC+DCH) tracker. In Fig. 2.108 the relative transverse momentum resolution ($\Delta p_t/p_t$ at p_t=1 GeV/c) for particles reconstructed in the MPD endcap is plotted as a function of pseudorapidity η. As one can see, the MPD tracking capability for the case of combined TPC+DCH reconstruction is extended well above $\eta = 1.7$. Moreover, the fractional momentum resolution in the forward hemisphere has improved considerably for the combined tracking in comparison with the TPC-only scheme. In the reconstruction algorithm, a track candidate is accepted only if there was more than 8 points found in each tracker (in TPC and DCH). The latter condition brings us to an

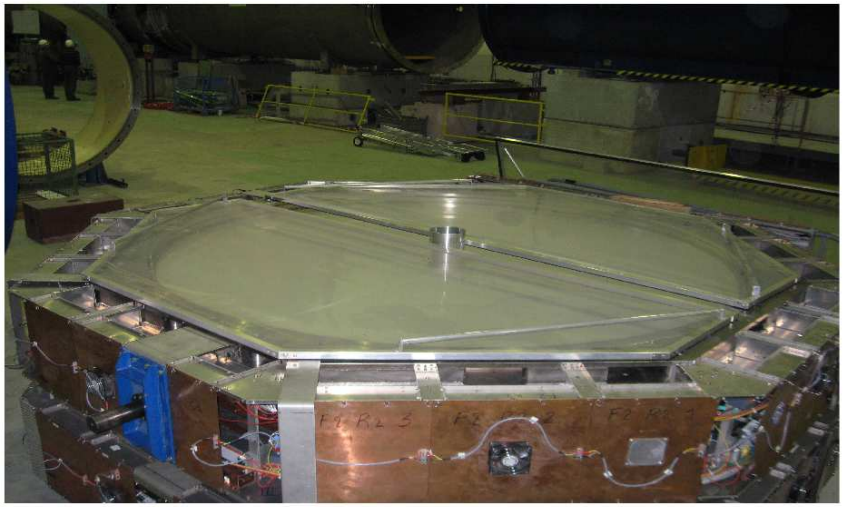

Fig. 2.107: The NA48 drift chambers before the journey to Dubna (see text for details).

additional tracking inefficiency which depends on polar angle or η. Fig. 2.109 demonstrates that the tracking efficiency is above 50% in the interval of pseudorapidities $1.2 < \eta < 2.0$. The efficiency could, in principle, have done better by loosing the cut on the number of points getting the overall momentum resolution somewhat worse, however. In addition to that, two scenarios are considered in calculation of the tracking efficiency. In the first one we assume that for each DCH point the ambiguity on which side of the wire the particle traversed is resolved (method of removing this ambiguity will not be discussed here), while it is not the case in the second scenario. The results of Monte Carlo simulations indicate that in the latter case the fraction of the 'ghost'-tracks does not exceed 8%.

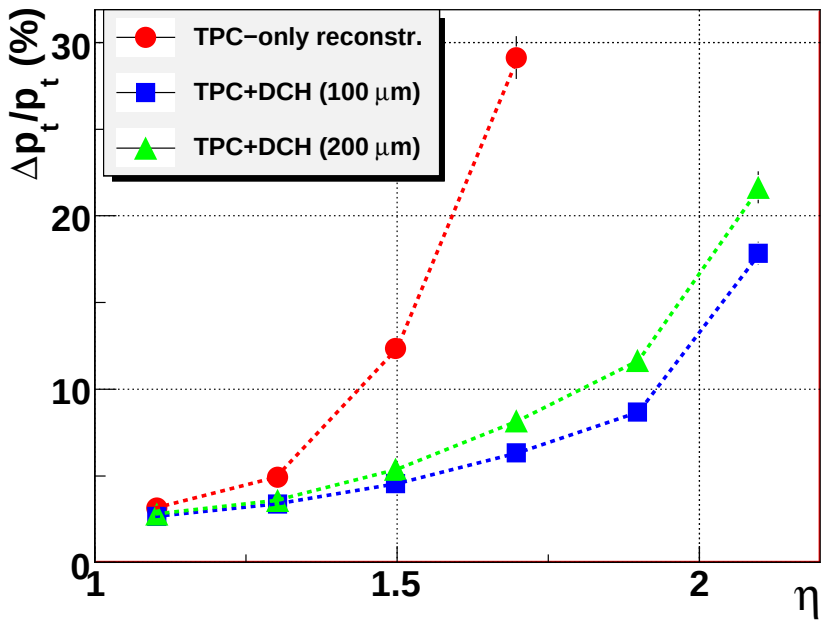

Fig. 2.108: $\Delta p_t/p_t$ (at p_t=1 GeV/c) as a function of η for TPC-only and for combined TPC+DCH reconstruction with the intrinsic space resolution of the DCH system 100 and 200 μm.

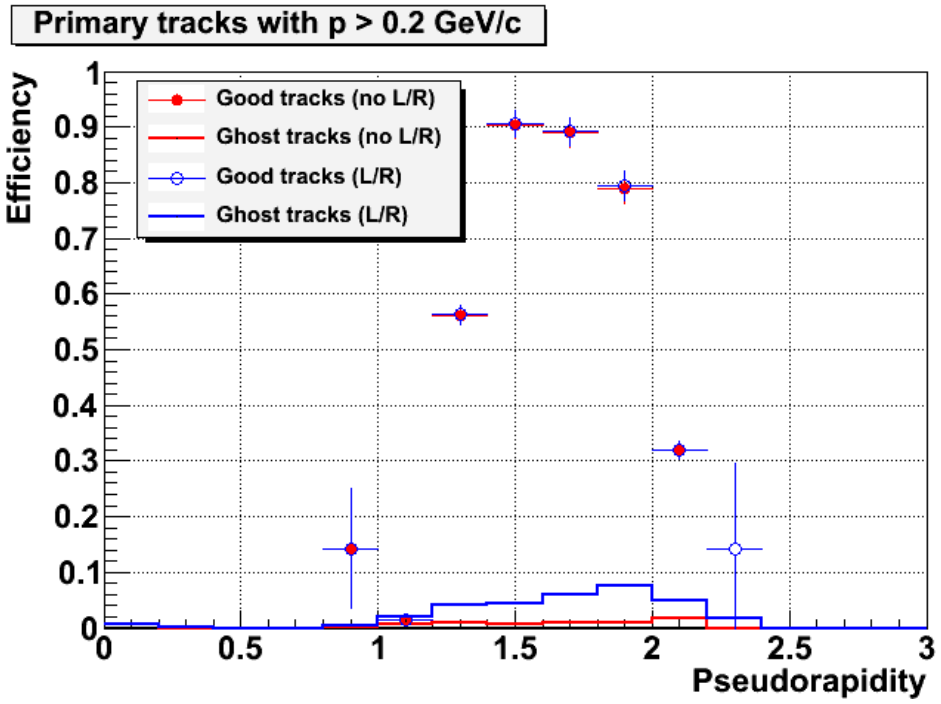

Fig. 2.109: Track reconstruction efficiency and contribution of fake tracks ('ghosts') as a function of pseudorapidity for the case of (not)resolving Left-Right Ambiguity.

2.9 Cathode pad chambers

The Cathode pad chambers (CPC) [269, 270] are part of the tracking system which together with silicon discs and TOF covers the the pseudorapidity interval $2 < |\eta| < 3$. The task of CPC is to provide additional precise space coordinates of the particles in the distance between silicon tracker discs and TOF. In moment when the forward spectrometers will start functioning this additional coordinate information makes the track linking between forward spectrometer and inner tracker more efficient.

2.9.1 CPC Design

A conceptual design of the CPC of EC Tracker is shown in Figs. 2.110,2.111.

The precise coordinate determination is based on the center of gravity measurement of induced on several neighbor pads charge. The inherent precision of the CPC comes from the lithographic process used in the etching of the pad structure. With this technique the pad position can be determined with a precision of about 15 μm.

The basic elements for the CPC construction are a module panels. The procedure of module construction as follow:

— the high modulus skins of Carbon Fiber Composite (CFC) glued on both sides of 10 mm thick core of ROHACELL 31 HF [271] foam;

— to ensure the sealing of the gas box and its electrical shielding and grounding, a thin laminate of Kapton and Aluminium will be added to both sides of the panel;

— the FR-4 printed boards with cathode pad structure will be glued after that to both sides of the panel;

— at each end of the module panel, an insert will be glued, sandwiched between the two CFC.

Precision holes in the insert will permit the alignment of the panels during the detector - module assembly and provide the interface to the support system.

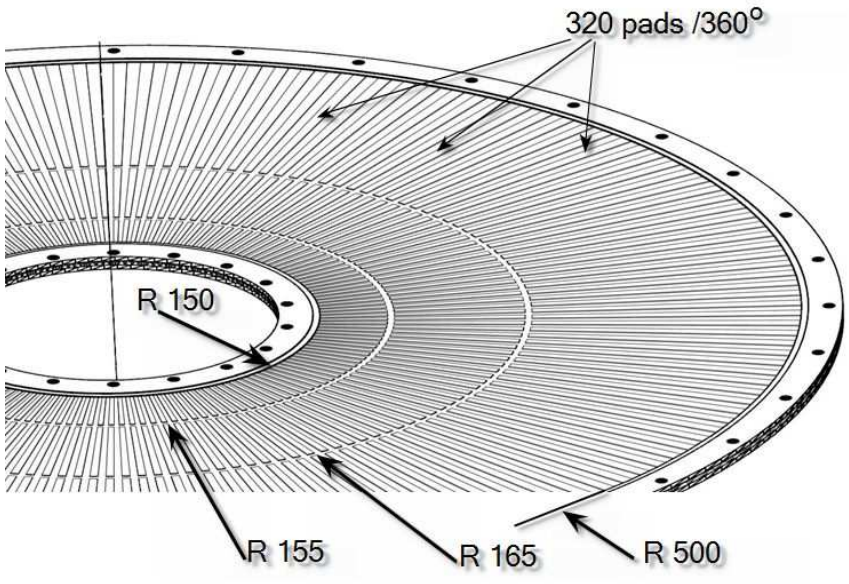

Fig. 2.110: Layout of an CPC cathode pad structure in φ.

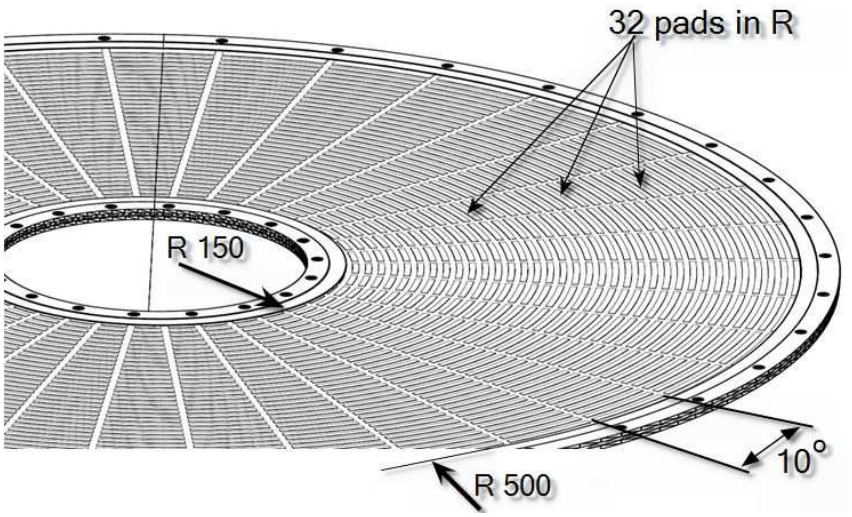

Fig. 2.111: Layout of an CPC cathode pad structure in R.

Table 2.16: Mechanical parameters of CPC

Number of panels per chamber	4 pc
Module panel thickness	10 mm
Number of gaps per chamber	3
Gaps	2 x 5 mm
Maximum outside diameter	1060 mm
Frame width	30 mm
Inner diameter	240 mm
Coordinate planes	6 (3 R,3 φ)
Wires per chamber	400 x 3
Wire diameter	30 mkm
Wire pitch	2.5 mm
Number of pads in R	36 x 32 x 3 = 3456
Number of pads in φ	320 x 3 x 3 = 2880
Chamber thickness	70 mm
Space angle per chamber	0.16
Total material per chamber in active area	0.028 X_0
Maximum number of charge particle per plane	100
Occupancy	less than 6%

2.10 Beam-beam counter

The main role of the MPD Beam-beam counter (BBC) is to produce a signal for the MPD Level-0 trigger. At low energies ($\sqrt{s_{NN}} = 5 \div 11\ GeV\ (Au + Au)$) it is critical to have reliable minimum bias trigger which will work from most of the central events to peripheral ones.

2.10.1 Requirements and detector configuration

The BBC consists of two scintillator annuli, installed around the beam pipe, on the east and west poletips of the MPD magnet. This corresponds to a pseudorapidity range from 1.5 to 4.5 over the full azimuth.

The BBC needs to satisfy the following requirements:

1. Since the BBC is proposed to be placed in a very high-level radiation area around the beam pipe near the interaction region, the BBC should be radiation hard.

2. The BBC is proposed to be installed just in front of the MPD magnet poletip. The expected magnetic field in this area is 0.5 T; therefore, the BBC needs to work in the high magnetic field environment.

To meet all the above requirements, we choose the following configuration. The BBC scintillators will be cut from the 1 cm thick Kuraray SCSN-81 which is radiation resistant. Scintillation light produced within a tile is collected by four 0.83 mm diameter Y-11 doped optical fibers inserted into grooves machined within the depth of the scintillator from both surfaces. The ends of the fibers are aluminized. The grooves ramp down from the scintillator surface and have fiber guides cut to trap the optical fibers. The fibers form a nearly circular loop within a distance of 2 mm from the isolation grooves limited by the 3 cm minimum bend radius of the fiber to ensure response uniformity independent of where an ionizing particle penetrates the tile.

Regular hexagonal tiles are defined by cutting 2 mm wide and 5 mm deep optical isolation grooves in a Mercedes pattern from both sides of the scintillator and then back filling these grooves with MgO2-loaded epoxy. Since grooves are cut on both sides, the optical isolation is complete. After machining, the sides of the hexagons are covered with white reflecting paint to trap scintillation light within each tile. Each scintillator surface is then covered with 0.01 mm thick aluminized mylar, taped to the painted scintillator edges. The reflectors are then covered by 0.05 mm thick black construction paper and black electrician's tape to make the assembly light tight.

The outer radius of the BBC annulus is about 110 cm and the inner radius is just larger than the beam pipe – 5 cm, corresponding to the clearance between the BBC and beam pipe of 1 cm (Fig. 2.112).

2.10.2 Triggering capabilities

The pseudorapidity region proposed for the BBC is $1.5 < \eta < 4.5$, which is outside the TPC acceptance, and therefore will not introduce a trigger bias to physics measurements which mostly rely on the $-1.0 < \eta < +1.0$ pseudorapidity region. A minimum bias trigger will require both the BBCs (east and west) to reduce beam gas background contamination.

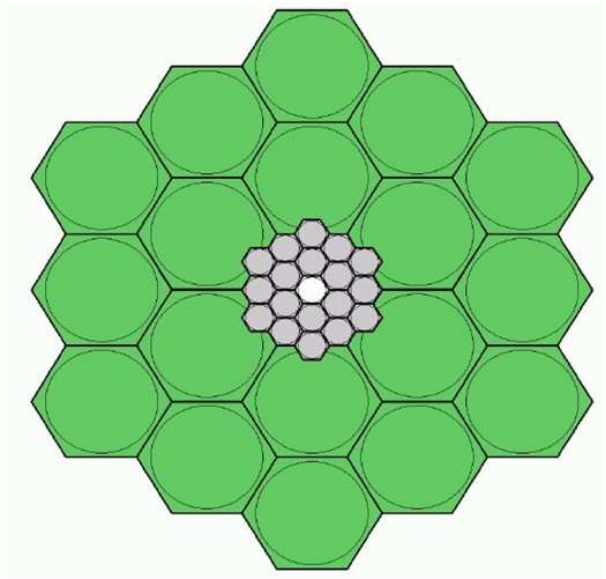

Fig. 2.112: Beam-Beam Counter front view. Small tiles can be inscribed in a circle with 12 cm diameter, large tiles are exactly four times larger. Inner empty space is left for the beam pipe.

Further cuts on the vertex position using timing information from the BBCs and signal amplitude will allow selecting clean minimum bias events.

We estimated the minimum bias trigger inefficiency of the proposed BBC configuration using HIJING generator of relativistic nuclei collision. The number of charge tracks in the BBC acceptance is shown on the Fig. 2.113 as a function of impact parameter for $Au + Au$ collisions at $\sqrt{s_{NN}} = 5 \div 9$ GeV. It can be concluded the BBC will be effective over the full above-mentioned region of pseudorapidity.

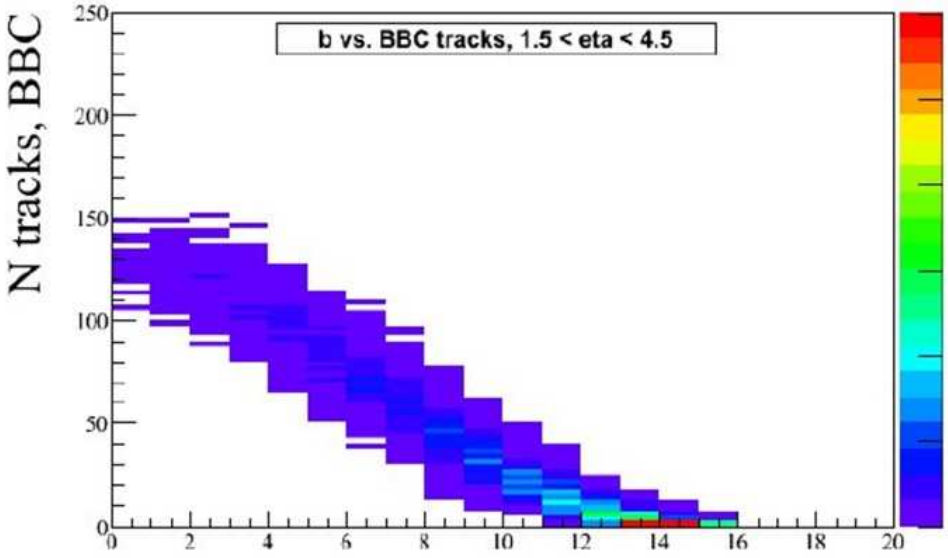

Fig. 2.113: Simulated $Au + Au$ collisions at $\sqrt{s_{NN}} = 9$ GeV. The expected number of charged tracks in the BBC acceptance vs. the impact parameter, HIJING predictions.

2.11 Fast forward detector

2.11.1 Aim, concept and position in MPD setup

The key requirement driving the trigger and timing in the MPD experiment is the efficient detection of Au+Au collisions at any centrality with time resolution of ∼50 ps. A proposed Fast Forward Detector (FFD) is a technical conception to realize these requirement.

It is important to note that such fast detectors with two arms, left and right from a collision point along a beam line, are used in collider experiments at RHIC and LHC for the same purpose.

Main aims of the FFD are (1) fast determination of a nucleus-nucleus interaction in the center of the MPD setup, (2) generation of a start pulse for the TOF detectors, and (3) production of L0-trigger signal together with other fast detectors, ZDC and BBC. The excellent time resolution of the FFD allows as to obtain z-position of the collision point with small error as to reach the required characteristics for the TOF system.

Besides, there are some additional important tasks where FFD is a useful instrument. It can much help in (4) adjustment of beam-beam collisions in the center of the MPD and (5) operative control of the collision rate and interaction point position during a run.

In comparison with experiments at ultra-relativistic energies at RHIC and LHC, there are two essential difficulties at the NICA energies. First, the charged particles produced in collisions mainly are not relativistic, and there is a large spread of spectator velocities which differ from the velocity of light (the beam velocities are in an interval $0.78 \leq \beta \leq 0.98$). Second, the particle multiplicity is much lower than one in the other collider experiments. As a result, for efficient trigger we need to cover a large acceptance and try to detect all particles with β ∼1 to achieve needed timing.

It leads to conclusion that the trigger and timing detectors used in other experiments at higher energies are not an optimal solution in our case and do not allow to reach the requirements mentioned above. So, one has to develop another conception of trigger and timing detectors for the MPD experiment.

There is a well-known fact that central and semi-central collisions of two heavy nuclei at relativistic energies are characterized by multiple pion production. The neutral pions immediately decay with generation of many high energy photons passing the MPD sub-detectors. The main idea of the FDD is to register a part of these photons at small angles to beam axis as the most suitable secondaries with highest and constant velocity.

The proposed FFD design is a granulated Cherenkov detector which has a high efficiency for the high energy photons and for ultra-relativistic charged particles as well.

The FFD consists of two sub-detectors, FFD-L and FFD-R, which are symmetrically placed to the MPD center along the beam line. Each sub-detector array has a hole for the beam pipe and locates at a distance of 75 cm from the center. Its acceptance in pseudo-rapidity is $2.5 \leq \mid \eta \mid \leq 3.2$.

2.11.2 Detector design

Both FFD-L and FFD-R are modular structure arrays where Cherenkov photons produced in fused quartz radiators by electrons and other fast charged particles are registered by multi-anode micro-channel plate photomultipliers (MCP-PMTs). Nowadays one of the most promising MCP-PMTs for a detector design with ps-timing are Burle/Photonis models with large square active area called Planacon.

The new model of Planacon (85012/85022) has excellent characteristics for development of fast modular detectors: a very low-profile package, ideal for close packing into arrays, good spatial resolution, excellent timing, pulse linearity, and immunity to magnetic field. The active area of 53×53 mm covers 80%-fraction of the MCP-PMT square. It has rather small cross talk and good cathode and anode uniformity. The cathode quantum efficiency is 24% and the maximum of spectral response lies in wavelength range from 230 to 580 nm that is important for application in Cherenkov detectors. The typical rise time and pulse width are 0.6 and 1.8 ns respectively.

The tests recently performed in other laboratories have given time resolution of ∼40 ps (sigma) for a single photon and ∼20 ps and even better if the number of photoelectrons exceeds of 30.

A schematic view of the proposed FFD array is shown in Fig. 2.114. It consists of 12 identical modules. Each the module includes a 7-mm lead converter, four $30 \times 30 \times 15$-mm fused quartz bars as Cherenkov photon radiators directly coupled with quartz window of Planacon and front-end electronics with four independent channels as it is shown in the same figure. Thus, total granularity of the detector array is 48 channels.

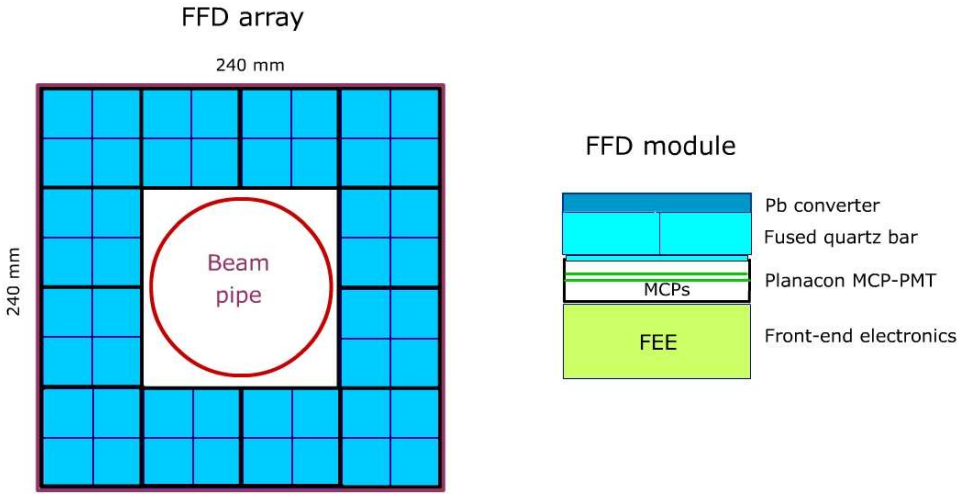

Fig. 2.114: Front view of FFD array (left) and module structure (right).

As the module front dimension is 6×6 cm the X×Y-dimension of the detector array is 24×24 cm.

The Cherenkov photons produced in the radiator induce photoelectrons in Planacon photocathode and after amplification in two MCPs with typical gain of $\sim 6 \times 10^5$ a charge pulse appears in anode pads. The best timing and the largest response are provided with detection of high energy photons by means of its conversion to electrons in the lead plates placed in front of the quartz radiators. To reach perfect timing the detector has to be compact with rather small number of elements and the proposed design follows this statement.

It is important to underline that the FFD is sensitive to high energy photons and charged particles with $\beta > 0.69$ coming from interaction point. It means that only pions with momentum higher than 132 MeV/c and protons with momentum higher than 885 MeV/c can be detected. And one may conclude that background of lower energy particles does not give any essential response in the FFD.

2.11.3 Tests with magnetic field

The performance of Planacon in magnetic field has recently been studied by several groups in a range up to $B = 1.5$ T. The results of test measurements display that a single photon response has three components: prompt signal (∼70%), short delay (∼20%) and long tail (∼10%) [272]. When a magnetic field is perpendicular to faceplate the pulse shape somewhat changes with the field, it becomes shorter and the tail almost disappears at $B = 1.5$ T. Thus, the timing a bit improves in the magnetic field. The same result has been obtained for cross talk between MCP-PMT anodes. It decreases with the field.

Also, the gain has been investigated as function of the magnetic field. The result of the Photonis test measurement with Planacon 85012 is shown in Fig. 2.115. First the gain factor somewhat increases and gets maximum at $B \sim 0.35$ T. Then it begins to fall with the magnetic field and at $B = 0.6$ T it reaches a value obtained without the field. So, one may hope that the gain of the Planacon in magnetic field of MPD will be a little higher of this normal value.

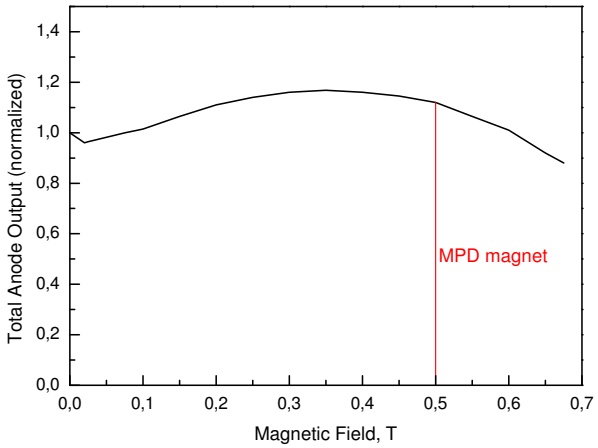

Fig. 2.115: Total anode output for Planacon 85012 as function of magnetic field which is perpendicular to faceplate (Photonis data). The red line shows the MPD magnetic field.

2.11.4 FFD performance

The MC simulation of $Au + Au$ collisions with the code UrQMD NICA plus GEANT3 was used for study of trigger and timing performance of the proposed FFD. Only 1-mm aluminium beam pibe, magnetic field of 0.5 T and the FFD geometry and materials were taken into account. The primary task for investigation was the photon energy spectrum and multiplicity of the high-energy photons and charged particles with $\beta > 0.99$ in the acceptance of FFD array because of its importance to achieve the required timing and vertex.

The obtained yield of the ultra-relativistic charged particles in the angular interval covered by FFD is rather small. The proton-spectators move in a narrow cone along beam axis and do not hit the detector array. Thus, only the high energy photons, mainly produced in decays of neutral pions, with some small contribution of charged particles define the FFD fast response.

The energy spectrum of photons for $Au + Au$ collisions at $\sqrt{s_{NN}}$=5 GeV is given in Fig. 2.116. For the most part of the photons its energy exceeds 100 MeV. These photons produce electrons in the 7-mm lead converter with a high efficiency and are detected by means of this process.

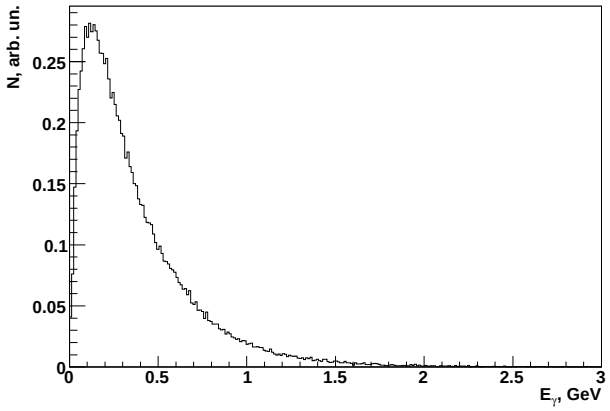

Fig. 2.116: Energy spectra of photons coming to front surface of the FFD array, $Au + Au$ collisions at $\sqrt{s_{NN}}$=5 GeV.

The photon multiplicity distribution as a function of impact parameter is shown in Fig. 2.117 (left). In the central collisions from 1 to 15 photons come to the lead converter of FFD. The mean number of these photons falls with increasing impact parameter. The right figure displays a background of slower charged particles which velocities exceed threshold value for Cherenkov radiation in quartz. Its multiplicity lies between 10 and 30 and its time of flight from a collision point to the detector is less than 5-ns. As the detector granularity is 48, only from 0 to 2 hits per detector cell are induced. It is expected a small influence of these particles on the detector performance due to a delay of the particle arrival in comparison with the photons and a strong dependence of Cherenkov photon multiplicity on a velocity.

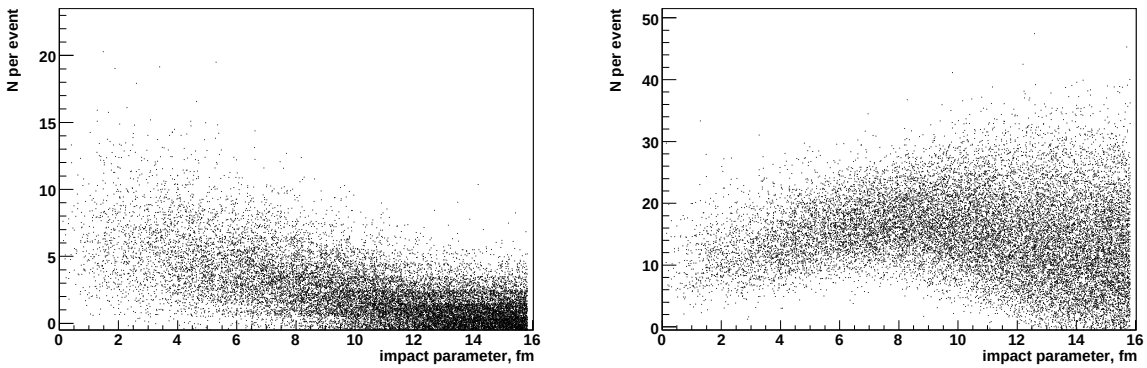

Fig. 2.117: Photon multiplicity distribution in acceptance of the FFD array as a function of impact parameter for $Au + Au$ collisions at $\sqrt{s_{NN}}$=5 GeV (left) and the same for charged particles with velocities above threshold value for Cherenkov radiation in quartz (right).

The same distributions but for the collisions at $\sqrt{s_{NN}}$=9 GeV are shown in the next Fig. 2.118. Here the mean photon multiplicity in central collisions is essential larger and

it falls with impact parameter as for the lower beam energy. But the charged particle multiplicity has already strong dependence on centrality with a maximum value of ∼30 for the central collisions of gold nuclei.

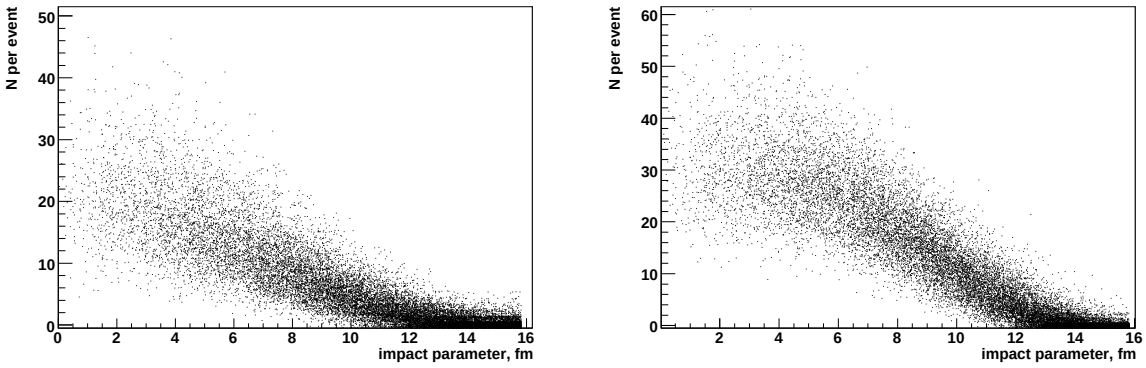

Fig. 2.118: The same as in Fig. 2.117 but for Au + Au collisions at $\sqrt{s_{NN}}$=9 GeV.

The electrons produced by a high energy photon in the Pb converter generate a great number of Cherenkov photons in the quartz radiator and induce many photoelectrons from Planacon photocathode. The MC simulation showed that mean multiplicity of the photoelectrons is larger of 30 pe for the 15-mm quartz radiator. This important result confirms that due to the good statistics of the induced photoelectrons the FFD will provide pulses with characteristics required for ps-timing.

The efficiency of registration of $Au + Au$ collisions with single the FFD array is shown in Fig. 2.119 for four different energies $\sqrt{s_{NN}}$=5, 7, 9 and 11 GeV. The detector bias is 30 pe. For the 5-GeV collisions the efficiency is close to 1 if $b < 6$ fm and it falls to 0.9 with increasing impact parameter to 12 fm. For the higher energies there is ∼100% registration of the collisions with $b < 10$ fm.

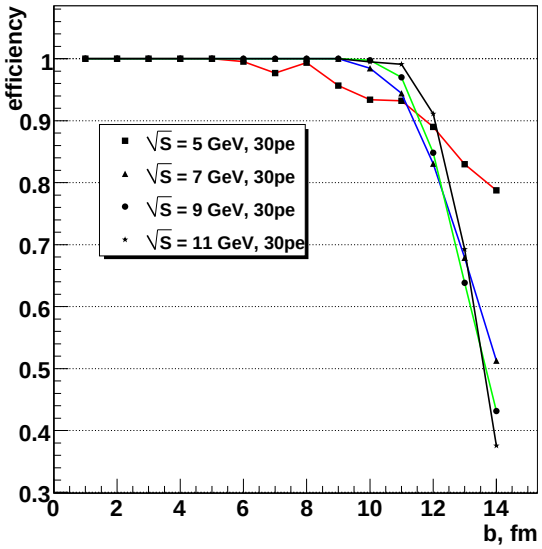

Fig. 2.119: FFD array efficiency for detection of Au + Au collisions at four different energies $\sqrt{s_{NN}}$=5, 7, 9 and 11 GeV with bias of 30 pe.

Thus, the results of study of the FFD performance with the MC simulation leads to the conclusion that the proposed Cherenkov detector array will provide timing and triggering $Au + Au$ collisions according to the requirements.

2.11.5 FFD structure

The FFD structure consists of several parts and systems. The preliminary scheme is shown in Fig. 2.120. First part is the modular detector itself with the Pb converters, the fused quartz radiators and the MCP-PMTs Planacon. The Planacon pulses come to fast amplifiers which outputs are split up in two branches. The first branch is transported to inputs of fast ADCs and the second one comes to fast disriminators. The prototypes of amplifiers and discriminators will be designed and tested in the first stage of project. The signals from the discriminators are also split up for TDC inputs and for fast logic unit with function OR. This units joint all 48 signals for each FFD array and generate fast T0-L and T0-R pulses coming to T0, Vertex and L0-trigger electronics and to inputs of TDC. The concept of this electronics is also a goal of the first stage.

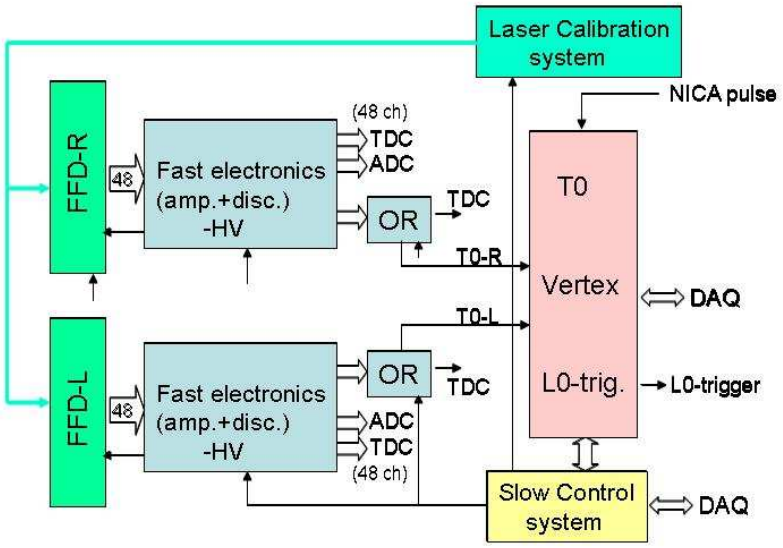

Fig. 2.120: Scheme of FFD structure.

The expected uncertainty of determination of z-position for $Au+Au$ collision is $\sim$2 cm and it is obtained with the vertex trigger using T0-signals of FFD-L and FFD-R arrays. The information written with the fast TDCs and ADCs will be used for off-line corrections to obtain better time resolution, for control and calibration purpose and for data analysis.

As it is expected the system of FFD, ZDC, and BBC will provide L0-trigger for MPD with high efficiency at any centrality of $Au + Au$ collisions.

The high voltage for Planacon operation is generated by HV units in each detector module. We plan that this HV system controlled via a slow control system will be designed and produced by HVSys company in Dubna.

The special calibration system with a ps-laser and fibers transported shot light pulses of the laser to the detector cells is important part of the FFD structure. Such system has been recently developed for T0-detector of the ALICE experiment and it is considered as a good prototype for the FFD system.

2.12 Zero degree calorimeter

The events classification by centrality of the relativistic nuclei collisions is a key topic of the experiments studying a strongly excited (hot and/or dense) hadronic matter properties. Obviously, the selection of central events is a necessary to study the most excited nuclear matter. However centrality classification not only separates central and peripheral events. Observables analysis in different centrality intervals appears very informative and allows to study space–time picture of the nuclear–nuclear collisions as well as hadronic matter properties, both of which impossible without centrality data involving (see for example [93], [95], [92], [94]). The importance of centrality classification can be illustrated by the following examples:

- The ratio of the elliptic flow to the space excentricity of the collision region is a constant for a wide range of the impact parameter, as it obtained at the RHIC experiments [273]. This fact as well as a great value of elliptic flow is a strong experimental indication for a small ($\leq 1fm/c$) thermalization time value. Such measurements are impossible without centrality classification of events, because space excentricity of the collision region is determined by centrality.

- For description of the Jet Quenching and J/Ψ suppression in nuclei–nuclei collisions the nuclear modification factor (R_{AA}) is used. This factor depend from the number of binary collisions, which is determined by centrality.

Many examples of another observables, which requires centrality classification too, can be presented. However lets only note, that many current and planned relativistic nuclei collision experiments are paid essential attention to centrality extraction topics as well as measurements of the observables dependence on centrality (see [274] and references in it).

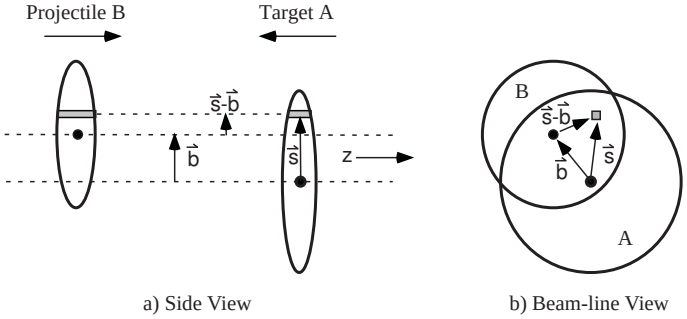

Fig. 2.121: Schematic view of two nuclei collision at the impact parameter $\vec{b}$.

For the centrality definition a simple geometric picture showed on Fig. 2.121 is used. The 2–dimensional vector $\vec{b}$, called an impact parameter, connects the projections of centers of the collided nuclei onto plane perpendicular to collision axis. The length of this vector is used for centrality determination. So knowing an impact parameter b we can (of course, in frame of some model of collision early stage) to calculate the following values, which traditionally used for description of geometric properties of initial state (see [275] and references in it):

- N_{part} – number of participants (it is a number of nucleons from colliding nuclei, which involved into at least one collision);

- N_{coll} – number of binary collisions;
- N_{spect} – number of spectators (it is a number of nucleons from colliding nuclei, which do not involved in any collision).

In the majority of relativistic nuclei collision generators (for example, HIJING [276], VENUS [277], RQMD [278], UrQMD [279], and others) the impact parameter related with values mentioned above by the Glauber Approximation (for detailed discussion see [275] and references in it).

Centrality classified by impact parameter (in fm) range $[b_{min}, b_{max}]$, or by part of full geometric cross section, which corresponds to $[\sqrt{b_{min}/2R_A}, \sqrt{b_{max}/2R_A}]$ range, where R_A is a radius of collided nuclei, which assumed identical. Another approach uses a number of participants N_{part} averaged over some impact parameter range. Relations between these two classifications are discussed in [280]. Here we will use the classification by impact parameter range. Because both impact parameter and participants number can not be measured directly, lets to explain briefly an observables traditionally used for centrality determination.

Two options illustrated on Fig. 2.121 are used usually. First approach determines centrality by energy carried by spectators (nuclei fragments). There are essential experimental arguments to do so namely by energy of nuclei fragments instead of such fragments number (see next subsection). Its clear, that both participants number and number of binary interactions grows with collision centrality increasing during transition from peripheral to central collisions. This fact used by second approach, where the centrality determined by a number of particles produced in region outside of fragmentation regions of collided nuclei. Examples of centrality obtaining schemes used by some current experiments are presented in Table 2.17. Lets note that calorimeters for spectator energy measurement are different by detected spectator's type, and this fact should be accounted during comparison of centrality obtaining schemes in different experiments.

Table 2.17: Examples of centrality obtaining schemes used by some current experiments.

NA49	ZDC Only
STAR	Number of Tracks in TPC
PHENIX	ZDC&BBC

In the next subsections we will discuss the centrality determination for MPD@NICA experiment.

2.12.1 Common requirements to ZDC construction

Below the common requirements for ZDC@MPD construction are discussed. The aims of ZDC are (in combination with another detector subsystems) the classification events by centrality and using it for the triggering purposes. The energy of spectator should be measured in ZDC. The spectators are protons, neutrons or nuclei fragments with different ratio of charge to atomic number, so we should know how the magnetic field changes the spectator's probability to reach ZDC.

According to the MPD project the magnetic field is constant (about $0.5 \div 0.7$ T) and directed along beam (Z axis). In such field a spectator trajectory is spiral. For the

NICA energies the MPD magnetic field do not changes the polar angle of spectator (i.e. the angle between spectator momentum and beam direction). Only difference between zero and nonzero magnetic field is the trajectory rotation in the (X,Y) plane by small azimuthal angle:

$$\Delta\phi = \frac{0.3QBz}{p_z A} \leq 6^o \ . \tag{2.6}$$

So we can conclude that estimation of the front ZDC module's dimensions can be done with zero magnetic field.

Two features of the ZDC geometry, which can change the efficiency of spectator detection, so should be taken into account, are:

- In the center of ZDC should be beam pipe hole, dimensions of which are determined by the collider construction. The number of spectators lost in this hole is estimated in the next subsection by Monte Carlo simulations. It will be shown that beam pipe hole can dramatically decrease spectator detection efficiency for peripheral collisions.

- The external size of the ZDC can be determined from known spectra of spectator nucleons (see, for example, [281]). From such spectra we can conclude, that the majority of spectators have transverse momentum < 300 MeV/c, so at the energy $\sqrt{S_{NN}} = 9$ GeV/c the spectator's polar angle is < 0.07. The distance from interaction point to ZDC is $L_z = 287$ cm. It means that transverse size have to be at about $D_{ZDC} \approx 40$ cm.

The front view of ZDC, which was fixed in agreement with this two requirements is shown in Fig. 2.122. The squares in this picture are the modules of hadron calorimeter. Each module consists of 60 layers of lead–scintillator sandwiches with the sampling ratio 4:1 (the thickness of the lead plates being 16 mm, scintillator plates – 4 mm) to satisfy the compensation condition. The calorimeter construction is discussed in more details in subsection 2.12.3. The energy resolution of this calorimeter was obtained from simulation using GEANT v3.2170 [282] code. We check resolution dependence on energy by simulated dispersions of calorimeter response, which usually has the following form:

$$\frac{\sigma}{T} = \frac{\beta}{\sqrt{T}} + \gamma \ \ , \tag{2.7}$$

where T – spectator kinetic energy. It was obtained $\beta = 67 \pm 12\%\sqrt{\text{GeV}}$ and $\gamma = 0.1 \pm 0.9\%$. The small value of constant term γ is connected with the specific for ZDC in which the deposited energy increase with increasing the number of spectators having kinetic energy close to the beam energy per nucleon.

Let us make comparison of this kind of calorimeter with the requirements coming from experimental data obtained in [283]. This paper states that in the central Pb+Pb collisions ($0 \div 5$ %) in average a 17 nucleons (as 9 neutrons, 7 protons and 0.5 deuteron) are emitted per one colliding nucleus. So for Au+Au collision the total average number of spectators passing through ZDC are:

$$N_s(0-5\%) = 2 \cdot N_s^{exp}(0-5\%) \cdot \varepsilon(ZDC) \ \ , \tag{2.8}$$

where $\varepsilon(ZDC)$ – the efficiency of ZDC for small impact parameters. The efficiency estimated from spectator's spectrum is $\varepsilon(ZDC) \geq 75$ % for the energy $\sqrt{S_{NN}} = 9$ GeV. So

for Au+Au collisions the following average energy is deposited in both ZDC:

$$E_{ZDC}(0-5\%) = (\sqrt{S_{NN}}/2 - m_N) \cdot N_s(0-5\%) \approx 90\ GeV \quad , \tag{2.9}$$

where m_N – nucleon mass. From this equation the fluctuation of ZDC energy caused by the fluctuations of the spectator's number is:

$$\sigma(E_{ZDC}(0-5\%)) = (\sqrt{S_{NN}}/2 - m_N) \cdot \sqrt{N_s(0-5\%)} \approx 18\ GeV \ . \tag{2.10}$$

And for the same collision energy ($\sqrt{S_{NN}} = 9$ GeV) the ZDC resolution according to (2.7) is $\sigma_{ZDC} = 6$ GeV. So for central collisions the spectators energy fluctuation is greater than the proposed ZDC energy resolution $\sigma(E_{ZDC}(0-5\%)) > \sigma_{ZDC}$. This means the energy resolution of proposed calorimeter is quite enough for ZDC purposes.

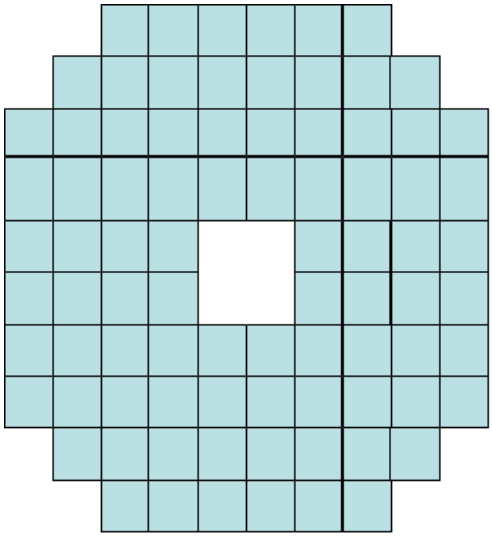

Fig. 2.122: Front view of ZDC. The squares size is $5 \times 5\ cm^2$.

2.12.2 Simulation of ZDC

In order to study the possibility of the collision centrality determination the simulation was made by three event generators: UrQMD [279], SHIELD [284] and LAQGSM [285]. It was generated events for Au+Au collisions at $\sqrt{s_{NN}} = 9$ and 5 GeV. While UrQMD is commonly used as a generator for nucleus–nucleus collisions, however for spectator simulations it has a serious disadvantage: the only definition of a spectator nucleon is that it has no collisions during its passing through nuclear medium and its rapidity is close to the rapidity of the incident nucleon. Therefore UrQMD cannot estimate the number of fragments, which is very important in a peripheral collisions (see subsection 2.12.1 and [283]).

For the definition of spectators in SHIELD we limits the transverse momentum less than 0.3 GeV/c, total momentum between 4 and 7 GeV/c for spectator nucleons protons and neutrons, and larger than 6 GeV/c for nuclei fragments. On Fig. 2.123 the clear identification of the spectators generated by SHIELD is seen for protons, neutrons and nuclei fragments in these limits. For UrQMD there are two areas of generated proton and neutron, and spectator nucleons: near zero rapidity (target fragmentation region) and at 4.5, where the nucleons are identified as the projectile spectators.

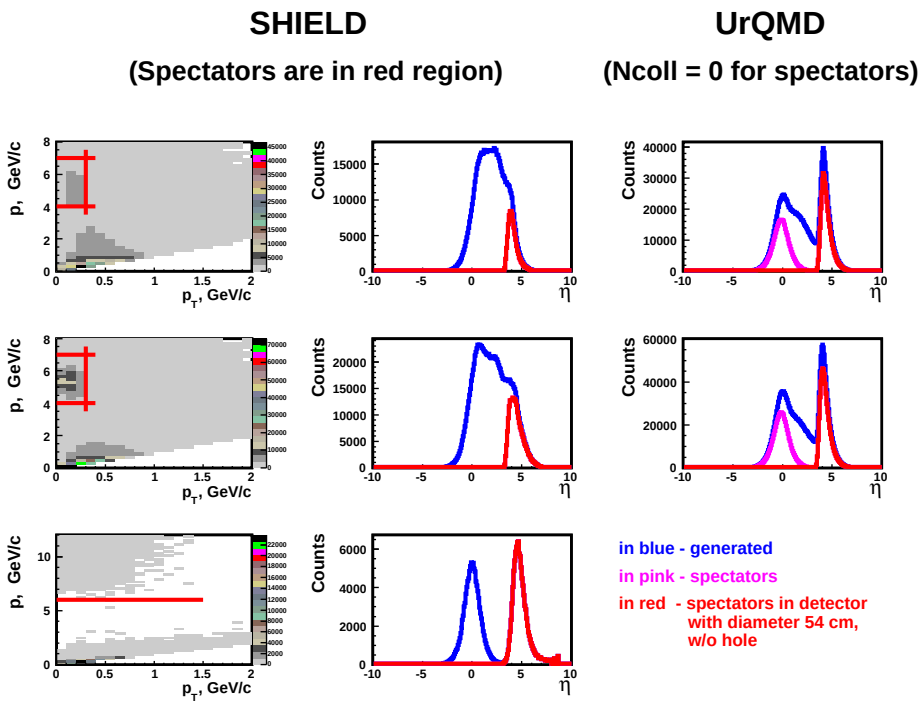

Fig. 2.123: Dependence of generated number of protons, neutrons and fragments in 2D plots on transverse and total momentum and on pseudorapidity.

For the ZDC acceptance determination the spectators transport to the calorimeter has been simulated by means of GEANT (version 4). The calorimeter is 120 cm long, its transverse dimensions are 50×50 cm^2. The cases with the beam pipe hole of 10×10 cm^2 and without it are simulated. The distance from the interaction point to the calorimeter is 287 cm. The number of reconstructed spectators N_{sp} are determined as follows:

$$N_{sp} = \frac{E_d}{\alpha E_0} \quad , \tag{2.11}$$

where E_d – the energy deposited by a spectator in the calorimeter, E_0 – the beam energy per nucleon,

$$\alpha = \frac{E_d}{E_{sp}} \quad , \tag{2.12}$$

E_{sp} – the total spectator energy. Parameter α was determined in the dedicated calculation with 4.5 GeV protons, and is equal to 0.09 ± 0.03. The comparison of generated and reconstructed spectators from UrQMD and SHIELD generators are shown on Fig. 2.124 in dependence on the impact parameter b. The numbers of spectators passing through the hole at the entrance and the exit of ZDC are shown too.

The total acceptance of ZDC is shown in the Table 2.18 for the calorimeter with the beam hole 10×10 cm^2 at the entrance and exit position. The acceptance of the ZDC for spectators at 4.5 $A\cdot$ GeV without a hole is close to 100 %, at 3 $A\cdot$ GeV – about 86 %. However, as it is seen from Fig. 2.124, the number of spectators hitting the calorimeter and calculated with SHIELD generator are decreasing for the impact parameters larger than 8 fm. In order to determine the accuracy of the impact parameter determination the deposited energy in the calorimeter was calculated.

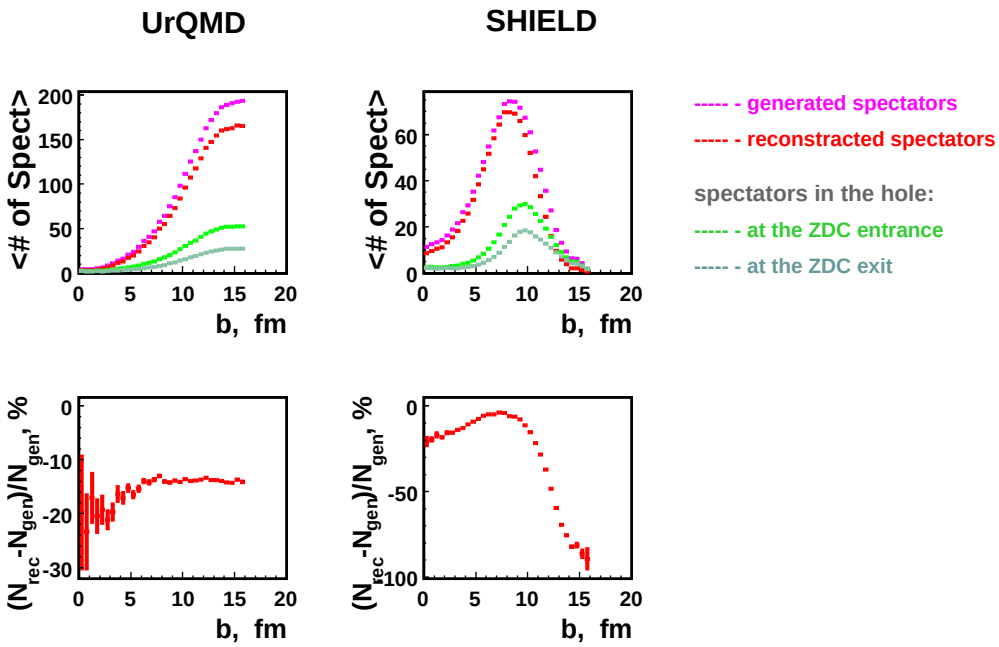

Fig. 2.124: The numbers of generated and reconstructed spectators for a ZDC with a beam hole vs the impact parameter.

Table 2.18: The acceptance of the ZDC with the beam hole at the position of entrance and exit of the calorimeter.

	UrQMD		SHIELD	
	entrance	exit	entrance	exit
protons, neutrons, fragments (%)	72.9	84.3	62.6	77.2
protons (%)	70.2	84.3	84.5	92.3
neutrons,(%)	74.6	87.0	63.6	77.5
fragments (%)	–	–	41.4	62.9

In Fig. 2.125 the total deposited energy dependence on the impact parameter is shown for UrQMD and SHIELD generators. Also the number of events with different centralities of the total 10000 is calculated for several thresholds on the deposited energy. It is seen that for the central events with $b < 8$ fm the results of UrQMD and SHIELD agreed quite well, giving the accuracy of the impact parameter determination about 0.5 fm. However the deposited energy for the peripheral events calculated by SHIELD is decreased in contrast for ones from UrQMD. It is due to the fact that the majority of spectators in the peripheral events are the nuclei fragments, which escapes the calorimeter through the beam hole. This effect was seen in the NA49 experiment, where the energy contribution from spectator nucleons at large impact parameters is more than 5 times lower than one from nuclei fragments (see [283]).

Because ZDC energy deposition dependences on the impact parameter are different so much for UrQMD and SHIELD events, we perform the additional simulations, by which

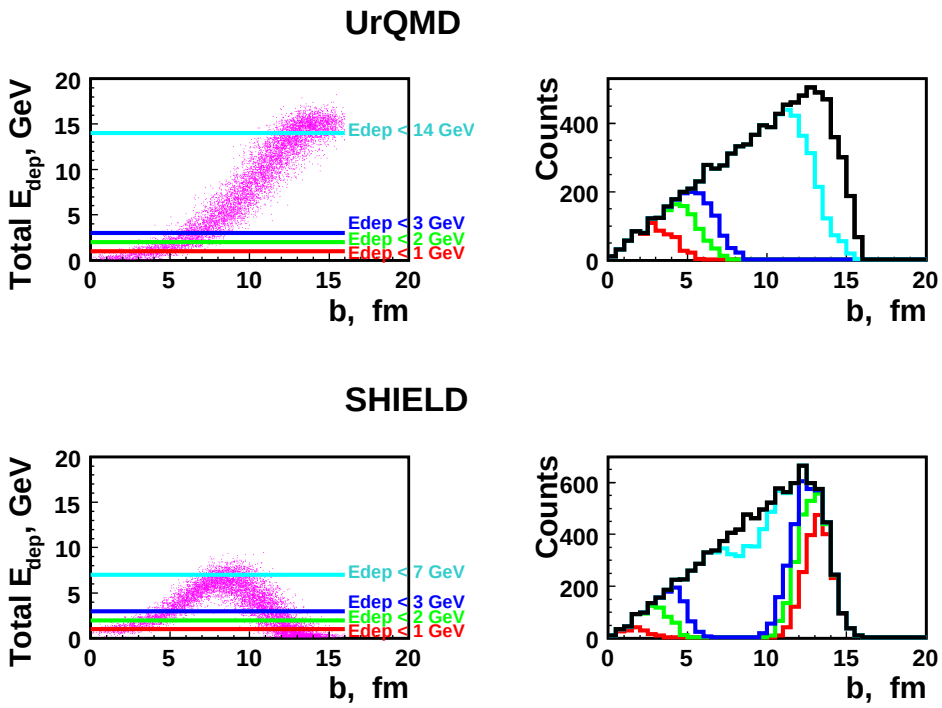

Fig. 2.125: The dependence of the deposited energy and counting rates of spectators with different thresholds on the impact parameter.

we tried to answer the following questions:

- Is a ZDC energy dependence on impact parameter non monotonic behavior a specific feature of the SHIELD generator?
- How such dependence changed with collision energy changes?
- Is it possible to extend monotonic behavior of such dependence by changing the beam hole size?

For this study we used UrQMD and the latest version of LAQGSM generator, which well describes the nuclear fragments production, and geant4_vmc implementation of GEANT v4 transport code in the mpdroot framework. The energy deposited at ZDC at two collision energies $\sqrt{S_{NN}} = 9$ and 5 GeV as a function of the impact parameter is shown on Fig. 2.126 and Fig. 2.127 for the UrQMD and LAQGSM generators. From these pictures one can conclude the following:

1. Both LAQGSM and SHIELD simulations show similar non monotonic dependence of the energy deposited in ZDC from impact parameter, while UrQMD data show monotonic dependence.
2. The maximum in such dependence is shifted to the lower impact parameter values for the smaller collision energy.
3. The maximum in ZDC energy dependence on impact parameter is shifted to the lower impact parameter for higher beam energy. As it was mentioned before,

the UrQMD cannot simulate the spectator fragments but only spectator nucleons. Therefore the results of the simulation with UrQMD for peripheral events are wrong. The explanation of the failure of the correct description of the deposited energy in the calorimeter for peripheral events could be found in the definition of the spectator particle by UrQMD. The spectator is the nucleon (proton or neutron) of the incident nucleus which has experienced no interaction with other nucleons by passing the target nucleus. However since they left the incident nucleus during the collision process they acquire the transverse Fermi momentum and hit the calorimeter even for peripheral collisions. However let us consider the real process. For the ultra peripheral events the colliding nuclei feel only Coulomb potential. Then only electromagnetic dissociation occurs, and very small energy is deposited in the calorimeter mostly by one or two emitted neutrons [286]. For smaller impact parameters the energy deposited in the calorimeter is increased due to nuclear multifragmentation. Some of the fragments and nucleons gain the transverse momentum and hit the calorimeter . Then we see a maximum at some medium impact parameter (Fig. 2.125 for SHIELD and Figs. 2.126,2.127 for LAQGSM). For more central events the number of spectators goes down.

The distribution of the total number of spectator nucleons (including ones bounded in the nuclei fragments) over the beam hole is shown in Fig.2.128 for three centrality regions. One can see that the width of this distribution decreases fast with increase of the impact parameter. The ratio of the number of nucleons passing through the beam hole to the total number of spectator nucleons are presented in the table 2.19 for three regions of centrality. From this table one can see that for the peripheral events practically all spectators directed to the beam hole. And Fig.2.128 shows that these spectators can not be registered by ZDC even if we decrease the beam hole because of very narrow angular distribution of the spectators for the impact parameter > 9 fm.

We plan to study the angular distributions of the fragments experimentally on the extracted Nuclotron–M beams to compare ones with SHIELD and LAQGSM results. From these measurements we hope to obtain an answer to the question, how good the SHIELD and LAQGSM describe the spectator fragments.

If the spectators angular distributions provided by SHIELD and LAQGSM generators will be confirmed experimentally, then for MPD@NICA centrality determination the information from another detector(s) (for example, the number of tracks in TPC) should be used in combination with ZDC data. Our simulations results for this option are shown in Fig. 2.129, from which we can conclude, that the event centrality in Au+Au collision at NICA energies can be determined up to centrality < 70 %, if the ZDC signal will be used together with number of tracks in TPC.

Table 2.19: The number of spectator nucleons detected in different space regions of ZDC for initial energy $\sqrt{S_{NN}} = 9$ GeV by LAQGSM generator. Here N_{ZDC} – total number of spectators in ZDC, N_{hole} – total number of spectators in beam hole for 1000 minimal bias events.

value centrality	< 60 %	$60 - 80$ %	> 80 %
N_{ZDC}	71041	22848	4787
N_{hole}	19707	47826	60431
$N_{tot} = N_{ZDC} + N_{hole}$	90748	70674	65218
$\varepsilon = N_{hole}/N_{tot}$	22 %	68 %	93 %

In conclusion we can note:

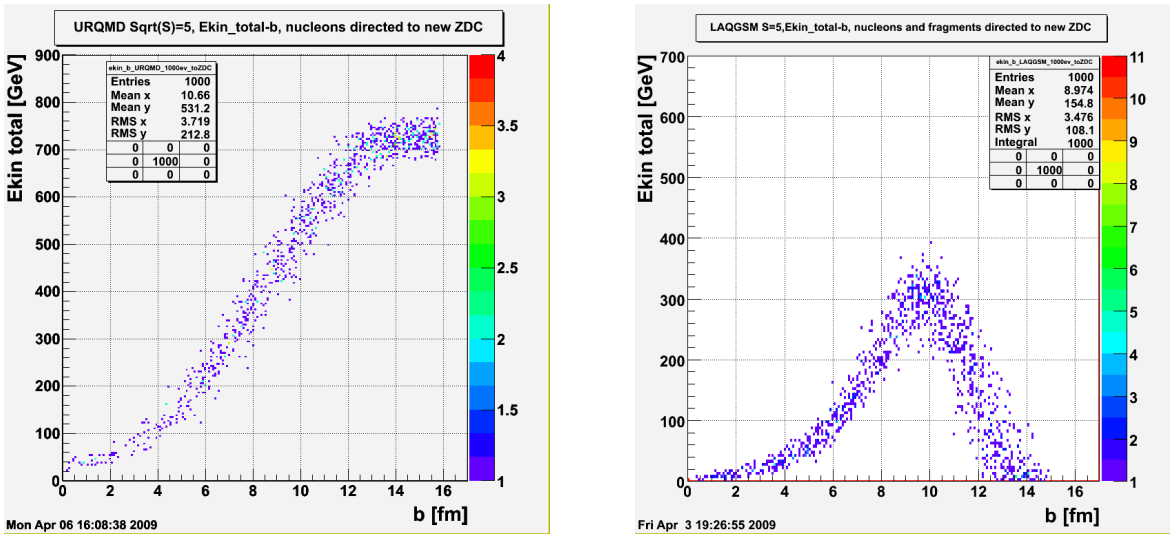

Fig. 2.126: The total kinetic energy of spectators passing through ZDC as a function of impact parameter for Au+Au collisions at $\sqrt{S_{NN}} = 5$ GeV. Left panel – events from UrQMD, right panel – LAQGSM.

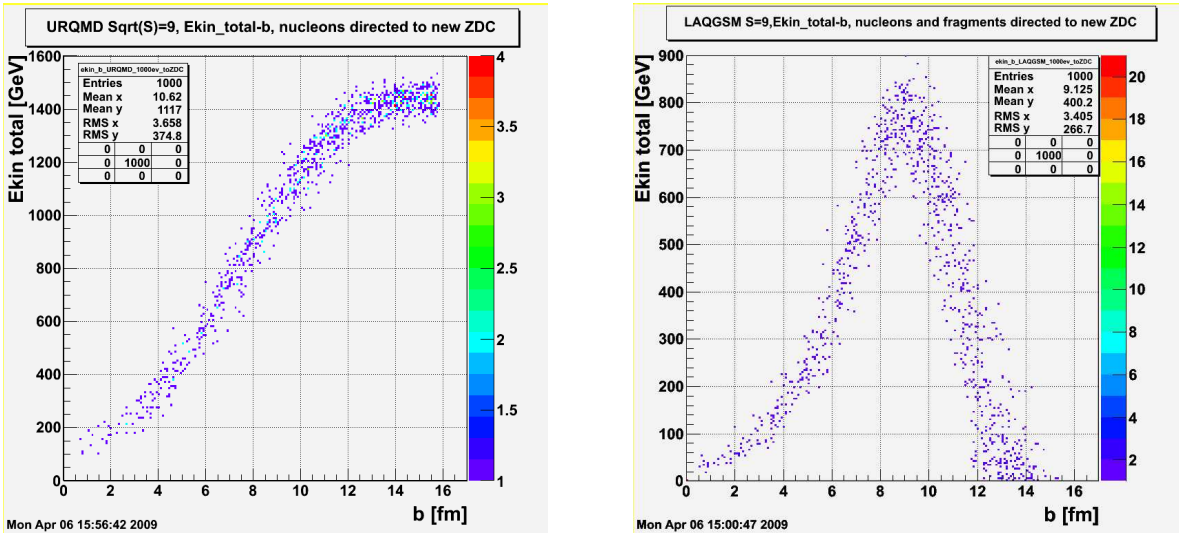

Fig. 2.127: The total kinetic energy of spectators passing through ZDC as a function of impact parameter for Au+Au collisions at $\sqrt{S_{NN}} = 9$ GeV. Left panel – events from UrQMD, right panel – LAQGSM.

1. The proposed ZDC can measure the centrality alone (without data from another detector(s)) for the cases when it is known that the impact parameter is smaller than $8 \div 9$ fm.

2. One of the possible solutions is to use the particles multiplicity measured by TPC detector together with the value of energy deposition in ZDC. The selection of the most central and the most peripheral events in this case can be easy made by the corresponding large and small signal from the TPC.

3. As another solution for the selection of the peripheral events with a small signal in ZDC an additional Zero Degree Neutron (ZDN) calorimeter can be installed after the first dipole magnet of NICA. The amplitude (multiplicity) threshold on ZDN

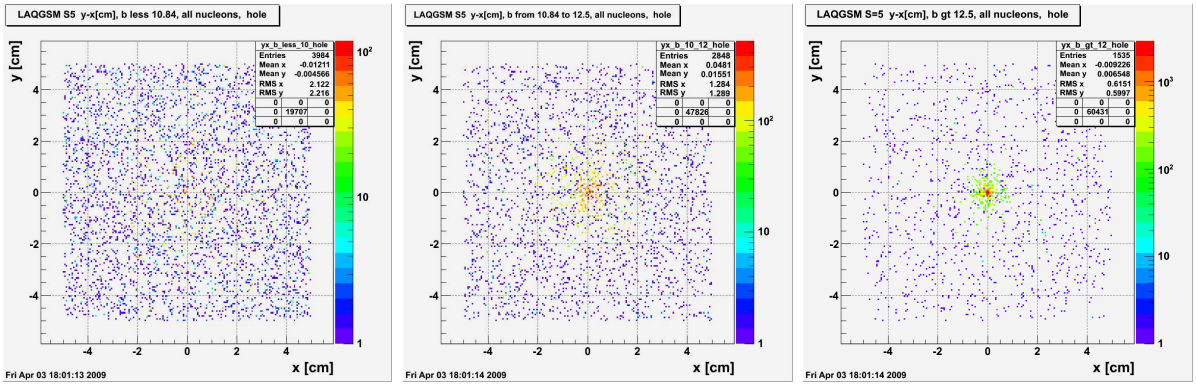

Fig. 2.128: The space distribution of the total number of spectator nucleons (including ones bounded in the nuclei fragments) over the central hole in ZDC for Au+Au collisions at $\sqrt{S_{NN}} =$ *5 GeV. Left distribution – for the centrality* $< 60\%$*, central –* $60 - -80\%$*, right –* $> 80\%$*.*

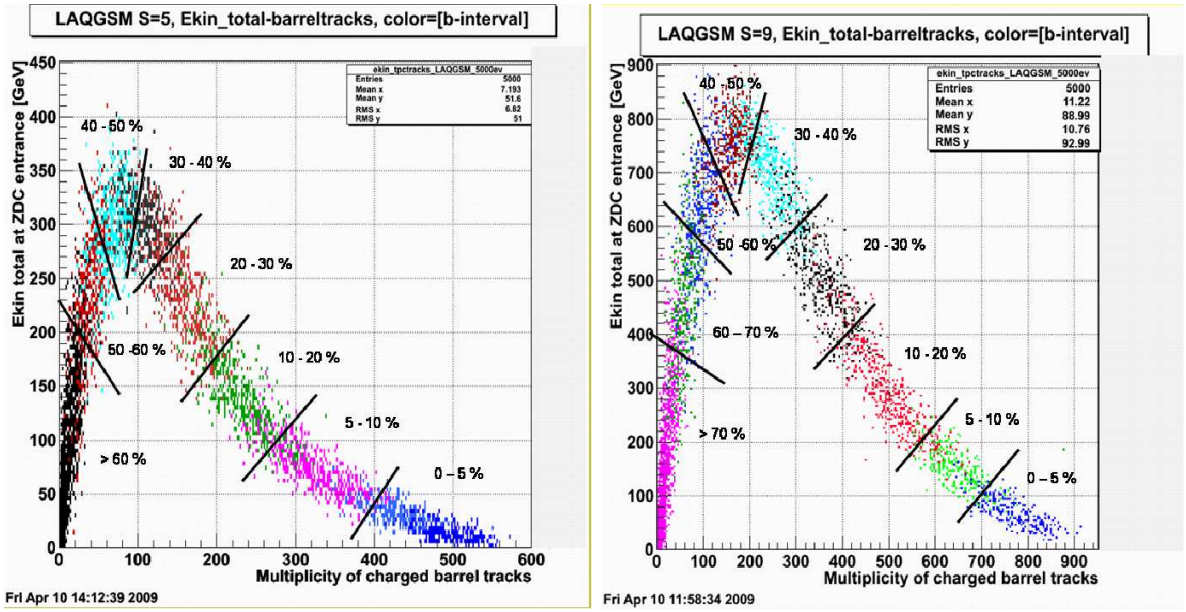

Fig. 2.129: ZDC deposited energy and TPC track numbers distribution for events with different centrality for Au+Au collision. Left pannel – $\sqrt{S_{NN}} = 5$ *GeV, right – 9 GeV. The different colors correspond to the different centrality. The short lines shows the cuts that can be used for selection events on centrality.*

will select the events with the impact parameters of $8 \div 14$ fm, where we have an ambiguity in the amplitude signal of ZDC. Such ZDN calorimeter may be used also for the determination and monitoring of the collider luminosity.

4. The selection of the most central and the most peripheral events can also be made by a small electromagnetic calorimeter placed out of the beam in front of ZDC, as it was made for ALICE experiment.

5. The experimental study of the spectator distributions have to be performed on the extracted beam of Nuclotron–M at the fixed target. For such study the beam energy equals to (or less than) one NICA ring energy ($\sqrt{S_{NN}}/2$) is enough.

2.12.3 Technical design

General consideration

R&D on the design of ZDC modules was performed during last 2 years. Each module of hadron calorimeter consists of 60 lead-scintillator tile "sandwiches" with the sampling ratio 4:1 (thickness of lead and scintillator plates are 16 and 4 mm, respectively) to satisfy the compensation condition. The transverse dimensions of the module are 5x5 cm^2. All 60 layers in each module are tied in one block with length about 120 cm (about 6 nuclear interaction lengths) by a stainless steel tape 0.5 mm thick. Then, this block is loaded into box made of the same steel and covered by another similar box. The two boxes are point welded to each other. The weight of each module is about 120 kg. Main attention was paid to the method of light readout from the scintillator tiles that should provide good efficiency and uniformity of light collection. Proposed light readout scheme of the ZDC module is shown in Fig. 2.130.

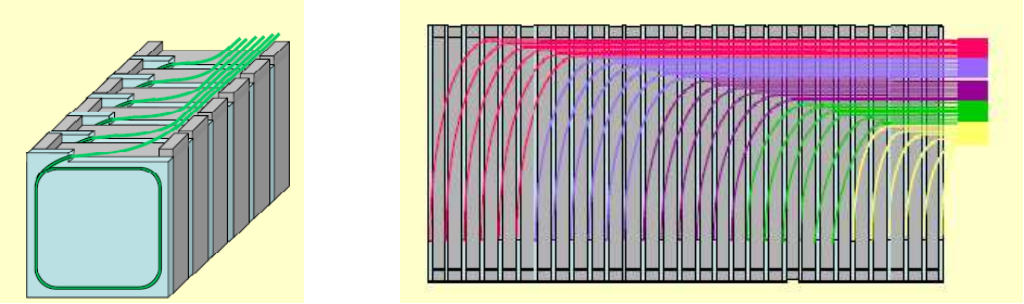

Fig. 2.130: Light readout scheme from the scintillator tiles in ZDC module. Left – front view, right – top view (only half-length of the module is shown). Fibers from each 6 tiles are collected together and viewed by a single MAPD.

Light readout is provided by the WLS-fibers embedded in the round grooves in scintillator plates that ensures high efficiency and uniformity of light collection over the scintillator tile within a very few percent. WLS-fibers from each 6 consecutive scintillator tiles are collected together and viewed by a single photodetector at the end of the module. The longitudinal segmentation in 10 sections ensures the uniformity of the light collection along the module as well as the rejection of secondary particles from interaction in the target. It makes possible also the development of the algorithms for the subsequent improvement of energy resolution based on the measurement of the longitudinal hadron shower profile. The individual calibration of longitudinal sections is essential for the monitoring of the light yield drop caused by the absorbed radiation dose in scintillator tiles at high intensity ion beams. Longitudinal segmentation of the calorimeter modules requires 10 compact photodetector coupled to the end of WLS-fibers at the rear side of the module. The use of micropixel avalanche photodiodes, MAPDs (or silicon photomultipliers, SiPMs) seams to be an optimum choice due to their remarkable properties as high internal gain, compactness, low cost and immunity to the nuclear counter effect. 10 MAPDs per module are placed at the rear side of the module together with the front-end-electronics (amplifiers). Such configuration ensures an easy access to MAPDs.

Scintillator tiles, WLS fibers and lead plates.

The main elements of the module are scintillator tiles with WLS fibers and lead plates. The scintillating tiles with 4 mm thickness were made of polystyrene based scintillator produced in Kharkov (Ukraine). They have 1.1 mm depth grooves for the WLS fiber (Fig. 2.131, left). The shape of the grooves provides parallel exit of WLS fiber from the groove relative the upper side of the scintillator.

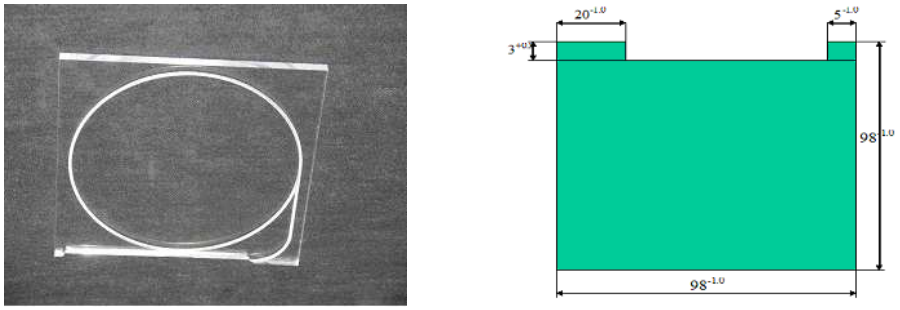

Fig. 2.131: Scinillator tile (left) and lead plate (right) Lead plates have 16 mm thickness and the same shape as scintillator plates. The lead plates contain about 3 % antimony to increase their hardness. WLS fibers Y-11(200) with double cladding and diameter 1 mm produced by Kuraray were used for the ZDC prototype assembling. The light attenuation length of this fiber is about 4.5 m .

Light readout by micropixel APDs

The principal problem in development of ZDC is the choice of the photodetectors for the readout of the light at the end of WLS-fibers. These photodetectors must be compact enough to set 10 pieces at 10x10 cm^2 rear side of the module. Immunity to the nuclear counter effect and the acceptable cost are also key requirements for these readout elements. The avalanche photodiodes, APDs are natural choice in this case. They are successfully used in the electromagnetic calorimeters and have well defined and reliable parameters. At the same time, low (50-100) gain of APD requires a sophisticated amplifier and limits its capability to detect low intensity light at the level of around 40 photons. The hadron calorimeters have light yield one or more orders less comparing to that of electromagnetic calorimeters. This limitation is essentially critical for the calibration with the low energies deposited in the calorimeter from minimum ionizing particles. Among a few modifications of avalanche photodiodes, the diodes with micropixel structure are of special interest because of their remarkable properties . Avalanche micropixel photodiodes, MAPDs are rather novel devices that are intensively developed and applied in modern research projects. Each pixel in MAPD might be regarded as an individual photodiode creating the avalanche in limited Geiger mode with the internal gain up to $\approx 10^6$. MAPDs have very compact dimensions in the scale of a very few millimeters. Due to the pixel structure, MAPDs have no nuclear counting effect, they are sensitive to the single photoelectron signal and have remarkable energy resolution even for a few photoelectrons signal. The technology of MAPD production and their parameters are sharply improved. As a summary, the main advantages of MAPD are: very compact sizes, low bias voltage, gain comparable to PMT, relative low price, insensitivity to magnetic field and absence of nuclear counter effect (due to the pixel structure).The sketches of two different MAPD

types are shown in Fig. 2.132. Main details of first type are group of p-n cells (pixels) connected to metal electrodes via the individual surface resistors. Other name of this MAPD is MRS (metal-resistor-semiconductor) APD indicating the described structure (Fig. 2.132, left). Unfortunately, the standard MAPD technology with individual surface resistors has a strict limit in number of pixels/mm^2 due to the dead areas around each individual pixel. This limitation is principal for the calorimetrical applications, in particularly, for ZDC. A reason is the dynamical range of measured energies. MC simulation shows that the detected energy in single section of PSD module achieves 1 GeV. It would be equivalent to 10000 photoelectrons taking into account the light yield 10 photoelectrons/MeV and the proportionality between the number of fired pixels (photoelectrons) and the number of produced photons (energy). In reality, the limited number of pixels, N_{total} leads to the nonlinear dependence of the number of fired pixels, N_{fired} on the number of photons, $N_{photons}$:

$$N_{fired} = N_{total}(1 - \exp(-\frac{N_{photons}PDE}{N_{total}})) \tag{2.13}$$

Using this formula one might easily estimate the minimum number of pixels requested for measured energy range. In our case the number of pixels must be a few tens of thousands for the linear MAPD response. MRS APDs with surface resistors have pixel density about 500-1500/mm^2, while MAPDs with the pixel density about 10000-20000/mm^2 are required. At present, there exists another advanced technology of MAPD production based on the creation of the pixels with the use of electrical field distribution inside the silicon wafer (Fig. 2.132, right). Produced in such way MAPDs have the pixel density about 10000-20000/mm2. There are a few R&D projects , where similar MAPDs are successfully used. These MAPDs are produced by JINR (Dubna, Russia) in collaboration with the Mikron Company (Zelenograd, Russia). At present, this technology is successfully applied by Zecotek Co.

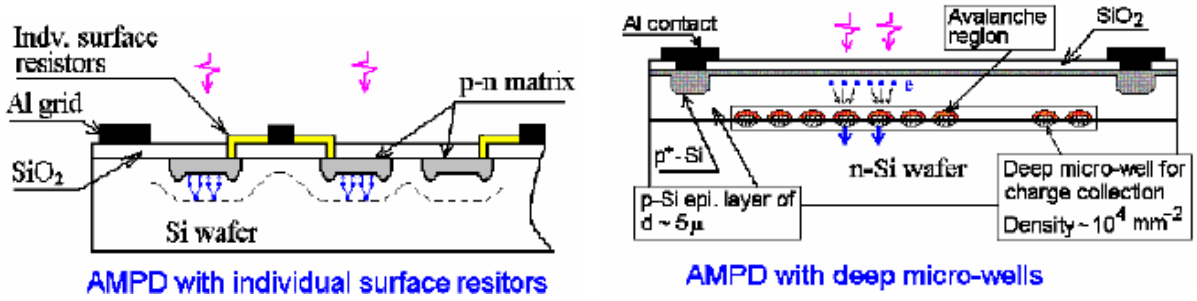

Fig. 2.132: MAPDs with two different structures. Left – MRS (metal-resistor- semiconductor) APD with the individual surface resistors and number of cells (pixels) of about 1000/mm^2. Right – MAPD with deep micro-wells.

2.12.4 Beam tests of ZDC prototype modules

In May 2010 a beam test with ZDC prototype modules was performed at the PS accelerator at CERN (Fig. 2.133 shows the experimental setup). Beams of charged pions were used to measure the calorimeter response function, module linearity and energy resolution in the NICA energy range (2-6 GeV). Beams of charged muons were also used for calibration. New high-sensitivity avalanche photodiods (Zecotek MAPDs, 15000 pixels/mm^2,

Fig. 2.133: Experimental setup in the May'2010 beam test (9 ZDC prototype modules are assembled on the top of the yellow-colored platform).

gain $5 \cdot 10^4$) were used as photodetectors (see Fig. 2.134). Fig.2.135 shows the measured

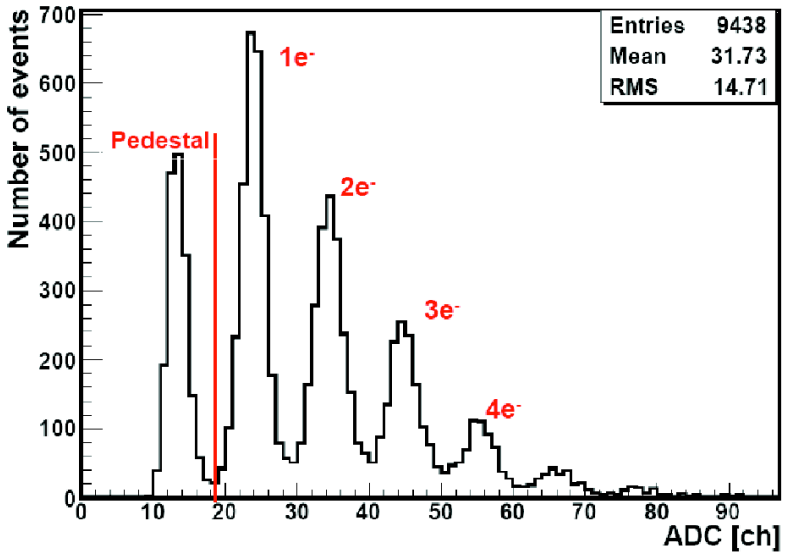

Fig. 2.134: Amplitude spectrum obtained with high-sensitivity Zekotec MAPDs. Labeled by red are well resolved N-photoelectron peaks (N from 1 to 4).

calorimeter response (mean of the signal amplitude in GeV) to 4-158 GeV pions as a function of energy. As one can see, the measured energy deposition in the tested module is linear in a wide range of hadron energies.

Measured relative energy resolution $\sigma(E)/E$ is shown in Fig. 2.136 as a function of hadron energy. The resolution (in percent) is parameterized as:

$$\sigma(E)/E = \frac{a}{\sqrt{E}} + \frac{b}{\sqrt[4]{E}} + c,$$

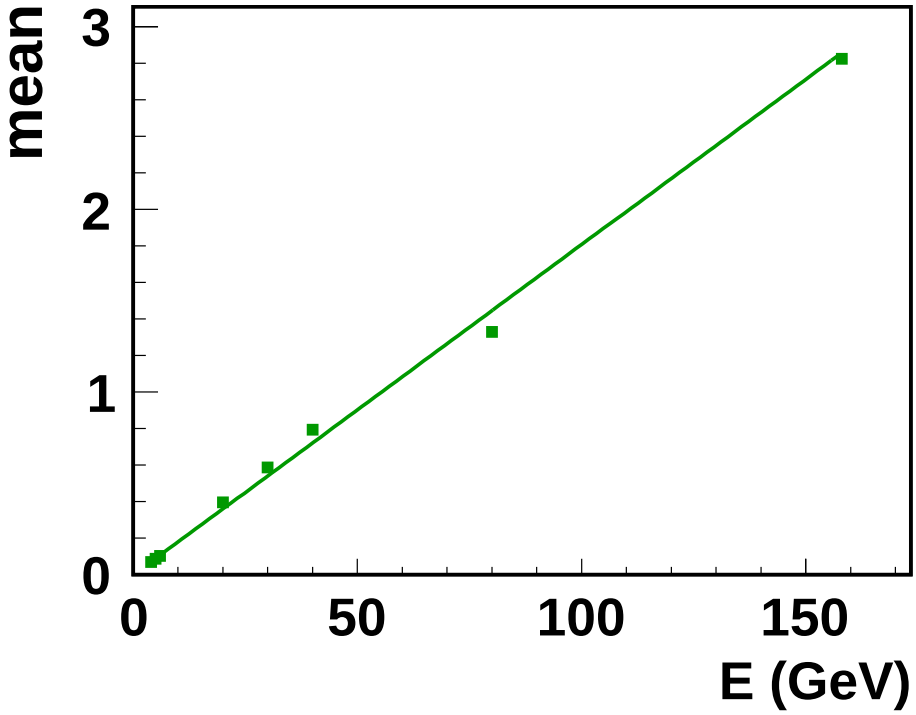

Fig. 2.135: Measured ZDC response to charged pions versus energy

where $a = 48.7\%, b = 16.7\%, c = 1.4\%$. The second term with coefficient b ("leakage"-term) is added in order to take into account fluctuations in energy deposition due to lateral shower leakage (the transversal dimensions of the tested ZDC prototype assemble

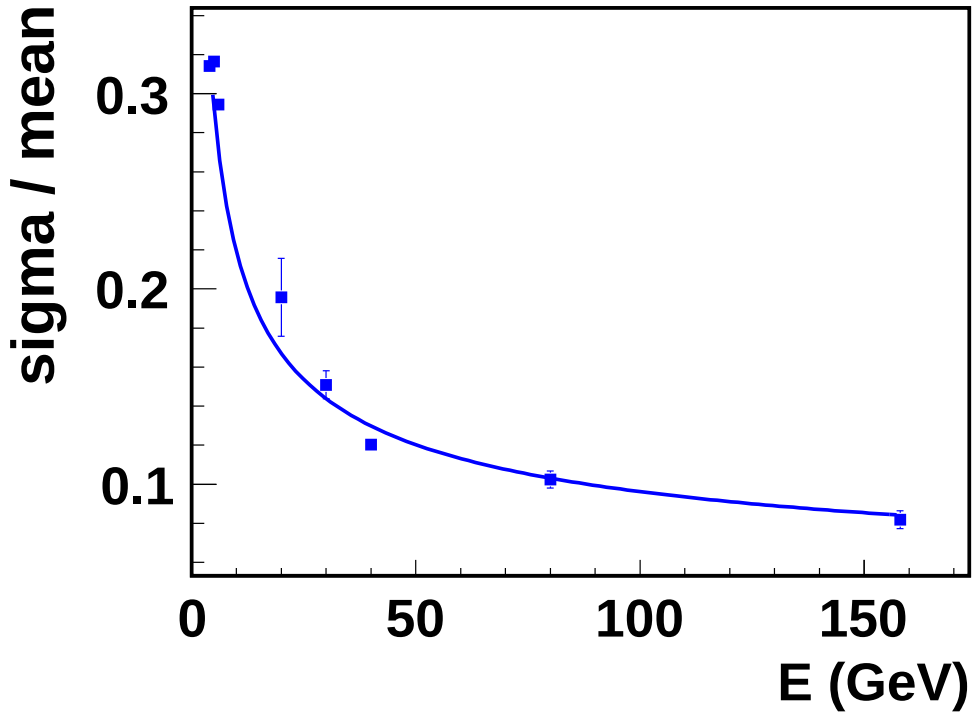

Fig. 2.136: Relative energy resolution of the ZDC prototype unit as a function of energy.

2.13 Forward magnetic spectrometers

The FS's are optional detectors which necessity will be defined after the CD became operational and first physics data are available. Those spectrometers should provide good momentum resolution and particle identification in the intermediate rapidity interval and large momentum region. There are considered two FS's - A and B, allocated symmetrically along the beam line. Below we present some arguments in favor of forward spectrometers.

The particle momentum resolution of stand-alone CD in the region of pseudorapidity of $\eta > 2$ is deteriorated dramatically due to small value of $\int \mathbf{B}dl$. The information on the particle time-of-flight with hypothesis of particle type can allow for momentum reconstruction. It is evident that as longer time-of-flight base as better particle momentum determination. The result of such approach is presented in Fig. 2.137. However for pions the resolution is poor even with long TOF bases. The solution of the problem could come with introduction of magnetic spectrometer. The estimation of the momentum resolution of the magnetic spectrometer shows that if coordinate accuracy of track detectors is about 200 μm and track length in magnetic field is about 1 meter that allow momentum resolution better than 2%:

$$\Delta p/p = (\sigma/L_p^2)(p_p/0.2998B)\sqrt{[720/(m+6)]}.$$

$m = 5$ – number of measurements along the track
$B = 1$ T, $\sigma = 200$ μm, $L = 1$ m, $p = 1$ GeV/c $\quad \frac{\Delta P}{P} \sim 1.7\%$

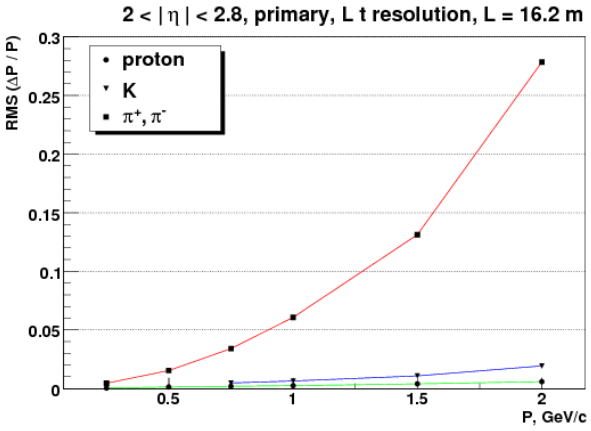

Fig. 2.137: Momentum resolution of protons, kaons and pions defined with the TOF system.

The schematic view of FS-B is shown on the Fig. 2.1. We propse spectrometer based on toroidal magnet (TM) and 5 layers of coordinate detector (DC). TOF will be used for particle identification. Magnetic field has a toroidal shape and is defined by 6 warm coils rotated by 60 degrees with respect to each other. The nominal value of magnetic field is about 1 T. Three layers of the coordinate detector are situated inside the toroid, and two layers are outside it.

Fig. 2.138 shows the momentum resolution of the forward spectrometer with 5 stations of coordinate detectors for particle spectra simulated by GEANT [282] with generator UrQMD [287].

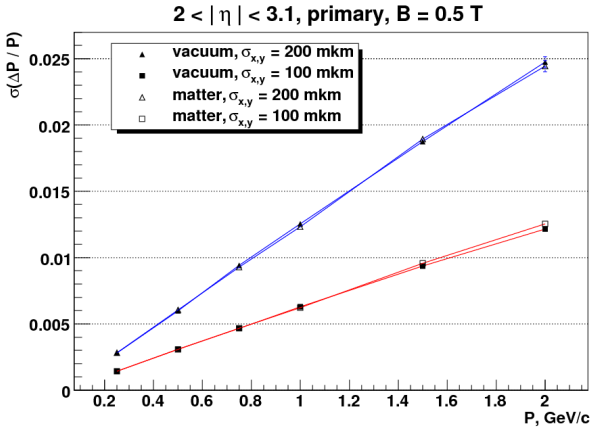

Fig. 2.138: Momentum resolution of Forward Spectrometer as a function of particle momentum. Two lines represent coordinate resolution of tracker 200 μm (top line) and 100 μm (bottom line).

Table 2.20: Requirements to spectrometer

Parameter	Value
etha coverage	(2.0–3.0) or (5–14) degree
magnet type	air toroid
nominal magnetic field	1 T
spectrometer Z position	(7600–9800) mm
$B \times L$	$1\ T \times M$
number of coordinate layers	$10(2 \times 5)$ layers
spatial resolution	$\leq 200\ \mu$m
track efficiency	about 99%
radiation length of layers	less than 5%
particles rate	10^6 (average – 100 Hz/cm^2, near beam pipe up to 1 kHz/cm^2)
sensitive area	about 14 m^2 per layer, 280 m^2 in total

The main requirements to the spectrometer are shown in Table 2.20:
Several approaches could be used to design tracking system of the FS:

- Drift chamber;
- Cathode strip chamber;
- Drift tubes;
- Straw

JINR LHEP has an infrastructure and the experience for the straw mass production. A lot of detectors of such kind were produced in past (TRD ATLAS end-cap [258, 259, 260], straw prototype for NA62 tracker [288]).

Our option of the Forward Spectrometer tracking system is based on the straw tubes. Straw has a spatial resolution better than 200 μm and efficiency about 100%. The total radiation length of 5 layers can be easily made to be less than 5%. Straw rate capability is up to 3 MHz. For the particle identification a TOF system is forseen which is located after the last plane of the track chambers.

2.13.1 Straw tubes production

Machine for straw production has been designed at LHEP (Fig. 2.139). Ultrasonic head and anvil are used for maylar tape welding. Ultrasonic welding seam is parallel to straw axis. Straws with the diameters in the range (6-30) mm and length up to 250 cm can be produced. Maylar thickness is in the range (20-50) μm. Aluminum coating thickness is in the range (0.05-0.15) μm.

Fig. 2.139: New machine for the straw tubes production (left), ultrasound head (right up) and anvil (right down).

Straws with diameter about 10 mm and length 220 cm were produced for straw prototype of CERN NA62 tracker [289]. Mylar thickness is h=36 μm and Al thickness is about 0.150 μm at both sides. Gilded tungsten with rhenium wire with D=30 μm (Luma, type 861) was chosen for the straw anode. The main straw parameters are presented in the Table 2.21.

48-channels straw prototype was tested [288]. Front-end readout electronics was based on chip ASD-8 [290]. Electronic amplification was about k = 5 mV/fC and noise - about 1 fC for the straw capacity C=25 pF. TDC modules are based on HPTDC chip [291]. The TDC scale was 0.1 ns/bin.

A 'slow' gas mixture $CO_2 + isoC_4H_{10} + CF_4(80 : 10 : 10)$ with electron drift velosity about 30 μm/ns was chosen in order to reach a good straw spatial resolution. CF_4 was added to prevent a radiation damage of the straws.

HV was set in the range 2200-2600 V and electronic thresholds were 6 fC and 12 fC during the tests.

Straw spatial resolution (sigma of residuals distribution) versus the straw radius was studied. Comparison of the measurements to the GARFIELD simulation results is presented on Fig. 2.140.

Table 2.21: Straw parameters (L=2350 mm)

Parameter	Value
Inner diameter	(9.75 ± 0.05) μm
Outer diameter	(9.85 ± 0.05) μm
Straw length	(2350 ± 1) mm
Linear elastic elongation (from external force F)	4 μm/gram, $dL = 4mm$ at $F = 1$ kg
Additional elastic elongation (from pressure)	$dL = 1.0mm$ at dP=1 Bar
Radial expansion	(50 ± 10) μm at P=1 Bar
Gas leakage	< 0.003 cm^3/min
Straw rotation	about 30 degrees/Bar
P_{max} (straw damage)	> 5 Bar
Cathode resistance	(35-45) Ohm
Anode wire resistance (d=30 μm, Luma, type 861)	250 Ohm
Anode wire tension	(80 $\pm$ 10) gram
Straw wave resistance	350 Ohm
Signal attenuation	55%

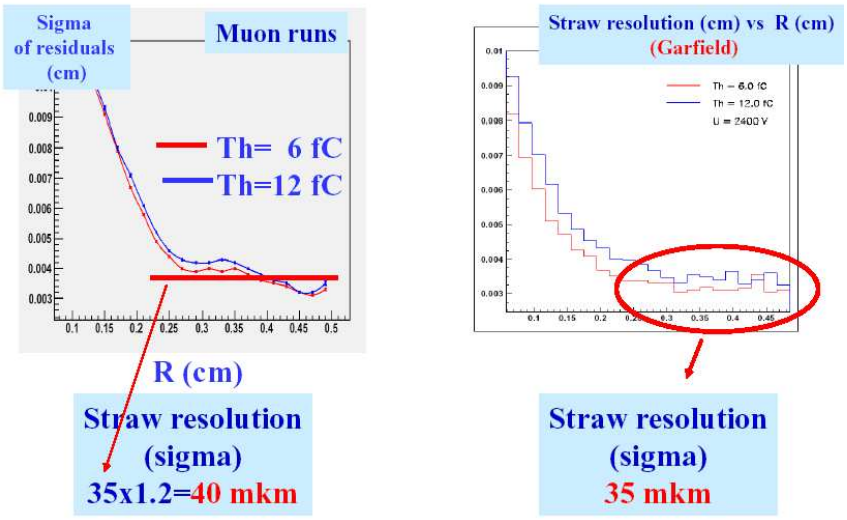

Fig. 2.140: Straw spatial resolution (sigma of the residuals distribution) versus the straw radius R (left – measurements, right – simulation results).

Dependence of straw spatial resolution on high voltage value (for threshold 6 fC) is presented on Fig. 2.141. The spatial resolution archive flat part of curve at the minimum high voltage value about 2.4 kV (gas gain about 2×10^5).

Comparison of the track reconstruction efficiency versus straw radius R agree well with the simulation results (Fig. 2.142). To determine the straw efficiency only first five layers have been used for the track reconstruction. For track in five layers an associated hit in the sixth layer has been required. Efficiency is about 100% up to $R = 4.7$ mm. A lowest efficiency near the straw wall is due to a small number of primary electrons. The measured value of "efficient" straw radius was taken into account for the design of the

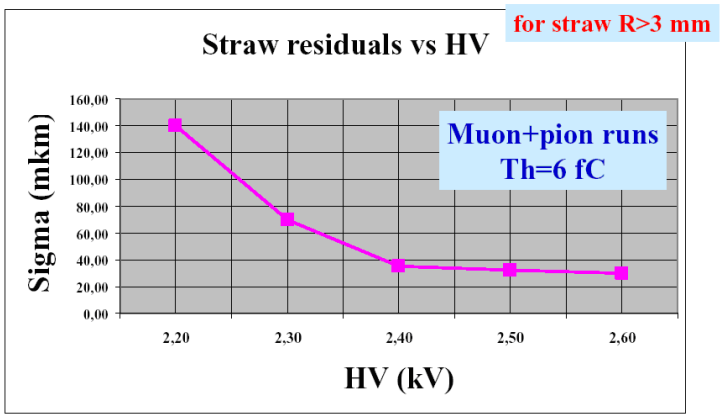

Fig. 2.141: Sigma of residual distributions (for straw $R > 3$ mm) vs HV.

full-scale detector (see below).

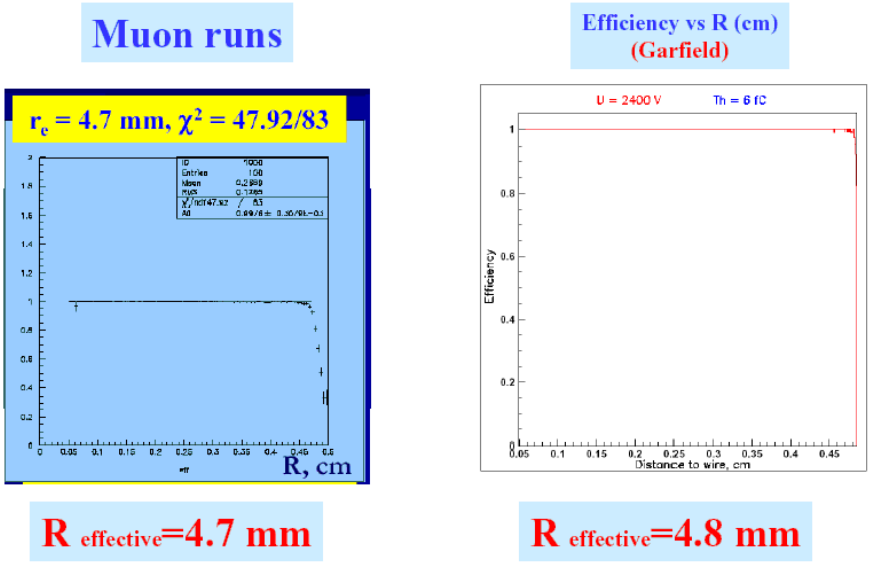

Fig. 2.142: Straw efficiency versus straw radius R.

It was shown, that the straw spatial resolution is about 200 μm near the anode wire, and it is about 50 μm for $R > 2$ mm. 'Slow' gas mixture CO_2+$isoC_4H_{10}$+CF_4(80 : 10 : 10) was used. The straw efficiency is about 100% for R up to 4.7 mm (straw wall is at R=4.9 mm). Optimum gas gain is about 2×10^5 (HV=2.4 kV). Value of the 'plato' is about 200 V. The measurements and the GARFILD simulation results are quite compatible.

Chapter 3

Trigger, DAQ and Computing

3.1 Data acquisition system and trigger

The main tasks of the Data Acquisition (DAQ) and Trigger systems are:

1. maximum readout efficiency with no dead time;
2. data selection and compression;
3. independent operation of subdetectors for testing and calibration.

The general structure of the MPD detector is the same as that used in STAR and ALICE. It allows subdetectors to operate independently.

All subdetectors will be connected to the readout systems that include the local data collectors (LDC) and detector readout electronics (DRE) boards. The central trigger processor (CTP) is common for all detectors; it generates trigger signals and synchronizes the operation of the MPD. The LDC and Global data collector (GDC) are connected together to the DAQ network via 10 Gbit Ethernet links.

The DRE module (Fig. 3.1) consists of front-end cards (FEC) and a read-out card (ROC). The FEC is an electronic module that amplifies and digitizes the analogue signals coming from a subdetector. It has a pipeline structure, which eliminates the subdetector dead time. The module provides zero suppression and data selection initiated by the L1 trigger. The FEC sends data to the readout card by a 2.5 Gbps front-end data link (FEDL). The FEC issues a trigger request signal (TRQ) when it has any nonzero data. The readout card analyzes all TRQ signals and produces a trigger signal $L0 = f(TRQ1...TRQn)$. The DRE boards connected to the subdetectors not included in the trigger decision logic generate no trigger signals TRQ or L0.

The central trigger processor analyzes L0 signals from subdetector readout electronics and generates the L1 trigger signal. The readout cards move the data selected by the L1 trigger to a local data collector.

Complex algorithms of data processing allow further data selection by the L2 trigger generated by the CTP. By L2 signal the data from the local data collector moves to the global data collector.

Fig. 3.2 shows the estimated data rates from subdetectors. The calculation is made assuming that the event rate is 6000 events per second and multiplicity is 500.

The electronics is proposed to be developed on the basis of on the custom ASIC designed for different detector types (PASA, ALTRO, HPTDC, etc.) and advanced data communication protocols. The electronics will contain monitoring functions for temperature, supply voltage and current.

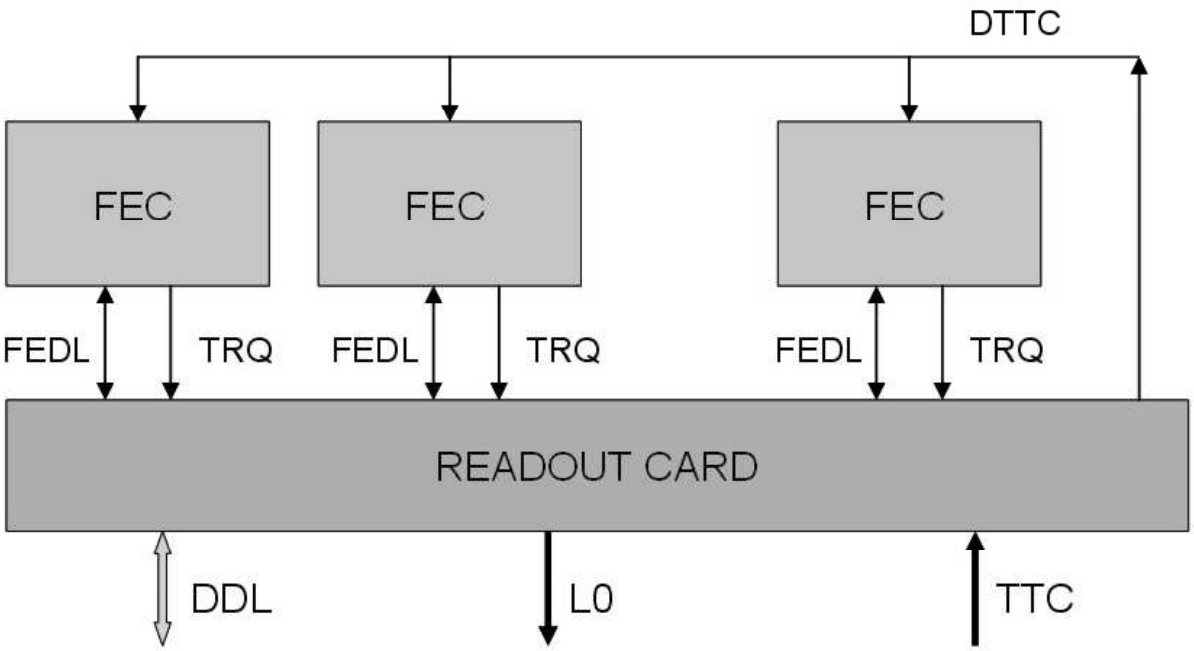

Fig. 3.1: Detector Readout Electronics.

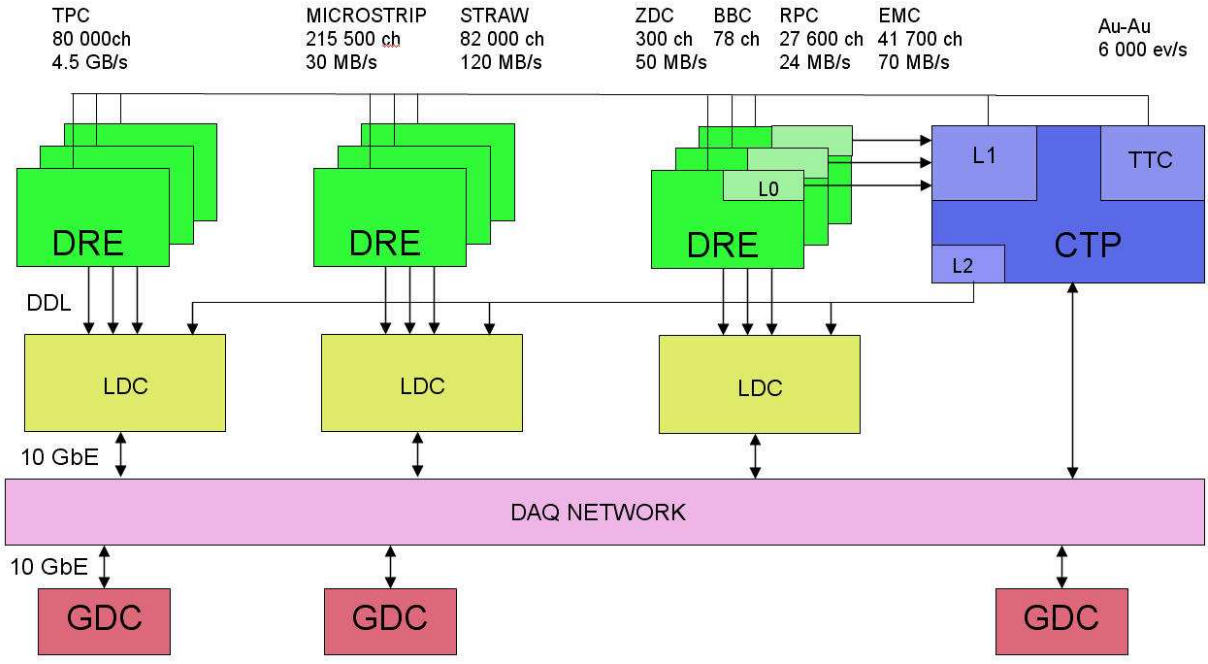

Fig. 3.2: MPD Data Acquisition System.

3.2 Computing

The MPD collaboration plans to detect ion collisions during a minimum of 120 days per year, starting in 2015. Assuming an overall efficiency of 60% and 6 kHz event rate, this would allow collection of about 19 billion raw events per year. Assuming ~ 4.7 GB/s data rate from the detectors, the total raw data volume per year of running can be estimated as 30 PB, and 8.4 PB after compression and zero suppression. The computing resources necessary for handling of so large amount of data are estimated later in this section. The estimations are based on DAQ characteristics, previous experience, and similar estimations performed for the ALICE experiment [292].

3.2.1 Data processing model

The data processing model will correspond to the scheme presented in Fig.3.3. The data coming from the MPD subdetector PCs (directly connected with the experiment readout) are collected by the event builder on-line PC-farm (EB), and written to the disk storage of the offline PC-farm after event formation via a dedicated 10 Gbps optical fiber link. Each EB writes a single "work file" every 1 minute of data taking.

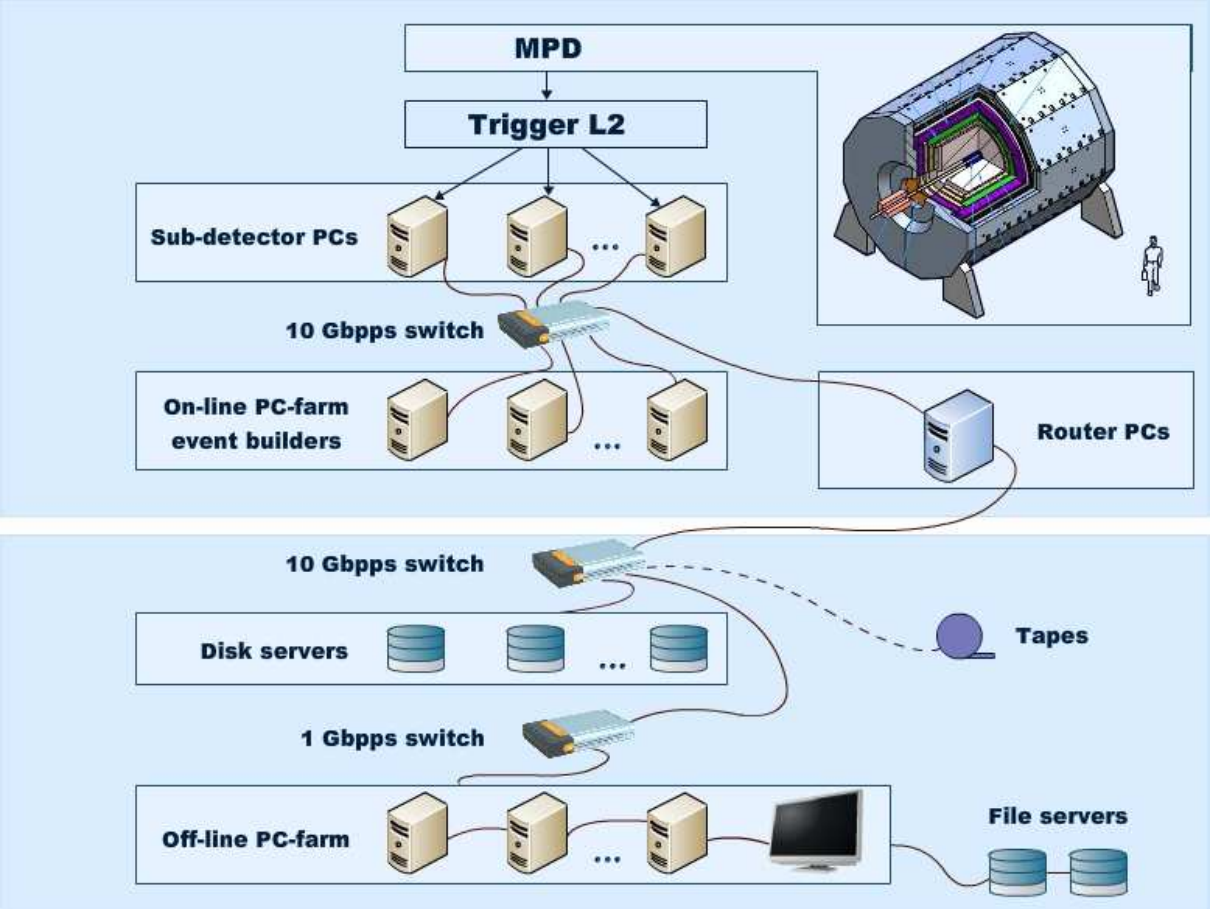

Fig. 3.3: MPD data processing model.

After L3 production, the accepted events are written to the raw data file (one file per 1 minute of data taking), and then fully reconstructed. The fully reconstructed event is written to disk in a special format. At the end of the process the raw data (RAW format)

are copied to the disks (tapes), and finally, the work files and the RAW files are deleted from the disk.

The RAW-format event size is estimated to be about 0.45 MB. The mean CPU time required for event reconstruction is about 2 s.

3.2.2 Computer resources for the experiment

Using the estimates of the data rate, the expected event size, and reconstruction speed, one can calculate the computer resources required for the experiment in terms of disk storage and processing power.

Assuming that no selection is applied during the first production step of L3 (before reconstruction), the expected data rate coming from the experiment is 1.3 GB/s, or about 70 TB/day. From the size of a single event of 0.45 MB, the expected trigger rate (6 kHz), and the reduction factor due to the past-future protection (0.5), the total required data storage is estimated as 8.4 PB/year for RAW data. Taking into account ∼20% of simulated events and the expected sizes of some compact data files produced on special requests of the experts, the total required disk space is estimated as 10 PB/year.

Using the expected CPU time of 2 s/event required for the reconstruction, a total time in 1K SI2K units is estimated as $37.4 \cdot 10^9$ s. This allows on to estimate the number of the offline 1K SI2K PCs as about 1480. Together with the online PC-farm and ∼ 20% processing power for simulation, the total number can be estimated as 1800 1K SI2K PCs. The specific character of events requests a minimum of 2 GB RAM for each CPU.

Full information and calculations for the above estimation is presented in Table 3.1.

Table 3.1: Estimation of the necessary disk space and power of PCs.

Parameter	**Value**	**Unit**
Data rate from L2	4.7	GB/s
Experimental run duration	120	day
Efficiency	60	%
Event rate	6	kHz
Past-future protection	50	%
Total number of events	$\mathbf{1.87 \cdot 10^{10}}$	event
Mean number of tracks per event	500	track
Mean number of hits per particle (TPC + eCAL)	20	hit
Mean number of bytes per hit	45	byte
Total size of RAW data	**8.4**	PB
Total necessary disk space	**10**	PB
Mean reconstruction time per event by 1K SI2K PC	2	s
Total time per year for 1 PC	7000	hour
Number of 1K SI2K PCs for reconstruction	**1480**	
Total number of necessary PCs	**1800**	

Chapter 4

Integration and Services

4.1 Integration and Services

Allocation of MPD in the LHEP experimental building is shown in Fig. 4.1 and Fig. 4.2. The MPD operation position is shown as it is included in the NICA accelerator circuit. To put the MPD longitudinal axis in line with accelerator beam axis, the detector operation position (as well as the assembly area and the transport passage between them) has to be deepened down to 4 m relative the Experimental Building hall floor level.

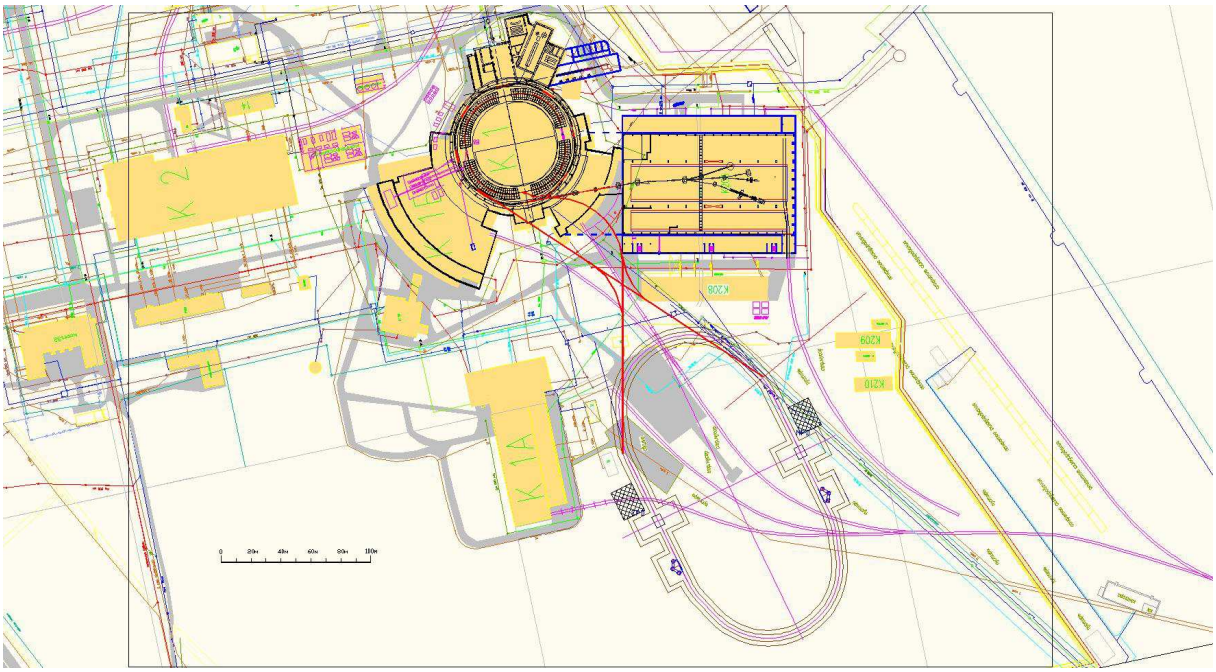

Fig. 4.1: Allocation of MPD in the experimental building of LHEP

4.2 Hall facilities and services

The hall of the reconstructed building will be equipped by the overhead travelling crane with two crane hooks of 50 and 10 ton weight-carrying capacity. Crane service area covers the unloading site of the building and the assembly site of the detector (see Fig. 4.1 and Fig. 4.2). The crane is able to provide bulky cargo transportation from the unloading site of the building to the MPD assembly area. The cargo can be delivered to the hall unloading site trough the main transport entrance gates of 5 in high and of 7 m in width

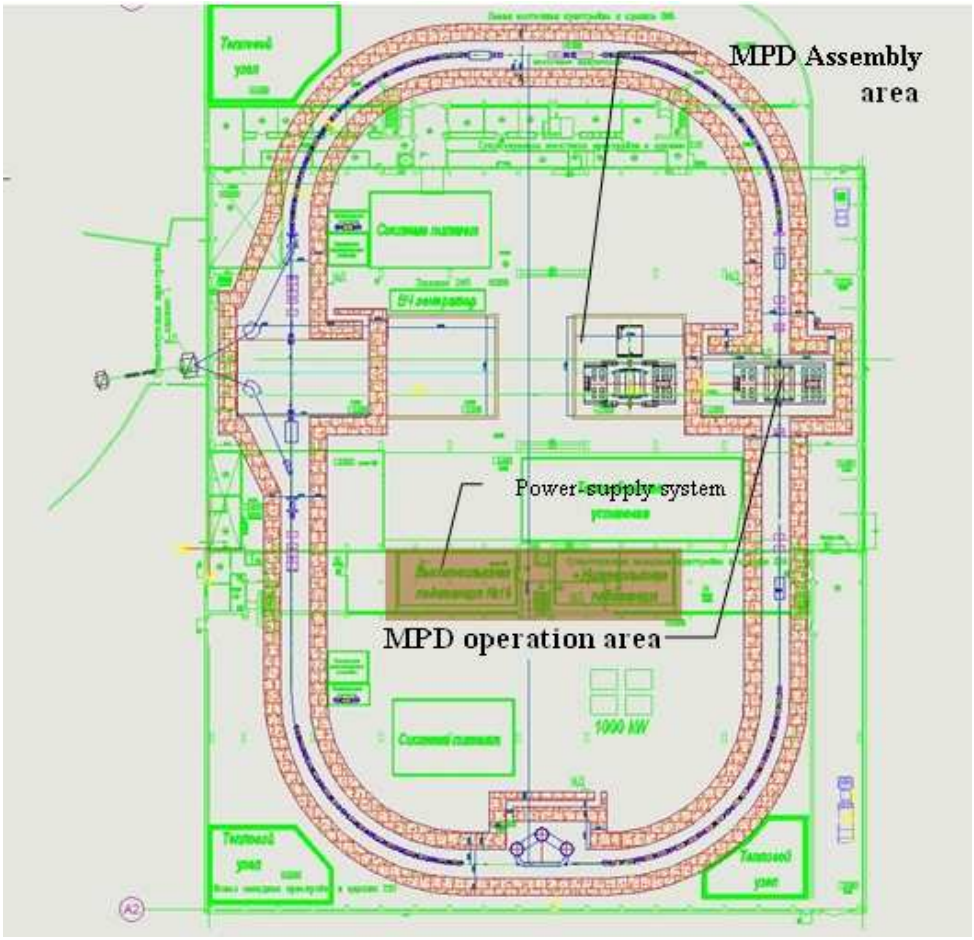

Fig. 4.2: Composition of the building

(the gates are indicated in Fig. 4.1). The crane is able to provide all necessary additional assembly operations when the MPD is in the operation position as well.

The hall solid concrete floor is considered to have the bearing capacity of 40 ton/m^2 (at least) in the operation and assembly areas. It would be quite enough:

- to bear the weight of the assembled detector,
- to keep the integrity of the detector in the process of its transportation on the rail guided carriage,
- to provide a stable detector position during operation cycles.

A satellite helium refrigerator of an adequate capacity will be mounted in close vicinity to the detector magnet to provide cryogenic fluids and gases for magnet operation (see Fig. 4.1).

The concrete shielding blocks of the former TPC experiment will be reused with addition of some new ones to prepare a shielding wall around the MPD and a labyrinth for cables and tubing (see Fig. 4.2).

An integrated design approach to electrical power network for all detector subsystem consumers will include providing of filtered ac network, electrical grounding strips, prop-

erly selected cables, cable terminals, clips and connectors, adequate racks and raceway design.

The essential part of infrastructure systems and detector subsystems require filtered electric power supply.

It is foreseen that emergency power supply of critical infrastructure and detector subsystems and uninterruptible power supply of control units will be provided. The area where the power-supply system is allocated is indicated in Fig. 4.2.

Circulating water supply system has to be mounted for chilling of the detector subsystems and trim coils (the place of water system allocation is not chosen jet).

The crates of the data acquisition systems and power supplies will be placed in close vicinity of the detector on special electronic platforms. It is supposed that the electronics platforms will be transported together with the detector from the operation point to the parking position. This will eliminate the need for future cable disconnections after completing detector subsystem tests. To provide access to the electronic racks when the detector is in operation position and the accelerator is on, between the detector and the electronics platform a special radiation shielding with cable labyrinths will be provided (see Fig. 4.2).

4.3 MPD integration

The integration of the MPD within the accelerator ring is presented in Fig. 4.3 and Fig. 4.4. These pictures specify overall dimensions and mutual position of the accelerator optic units and of the detector relative the hall reference points. The envelope volumes for scaffolding, raceways for electronic and electric cables, passages for service and adequate space for the detector assembly etc are defined in these pictures.

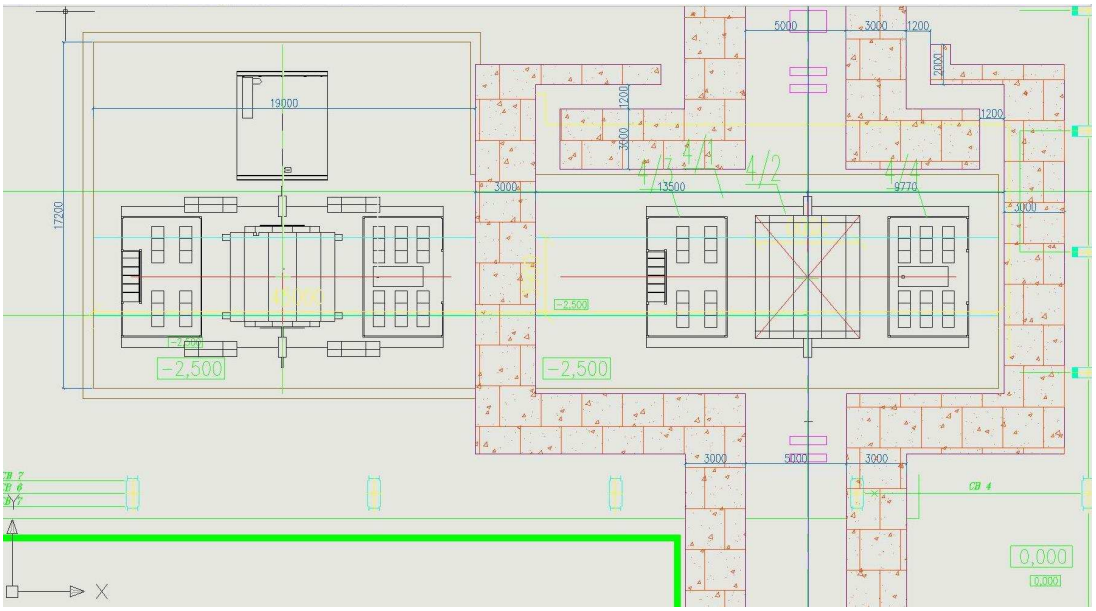

Fig. 4.3: MPD detector layout in the operating (and parking) position

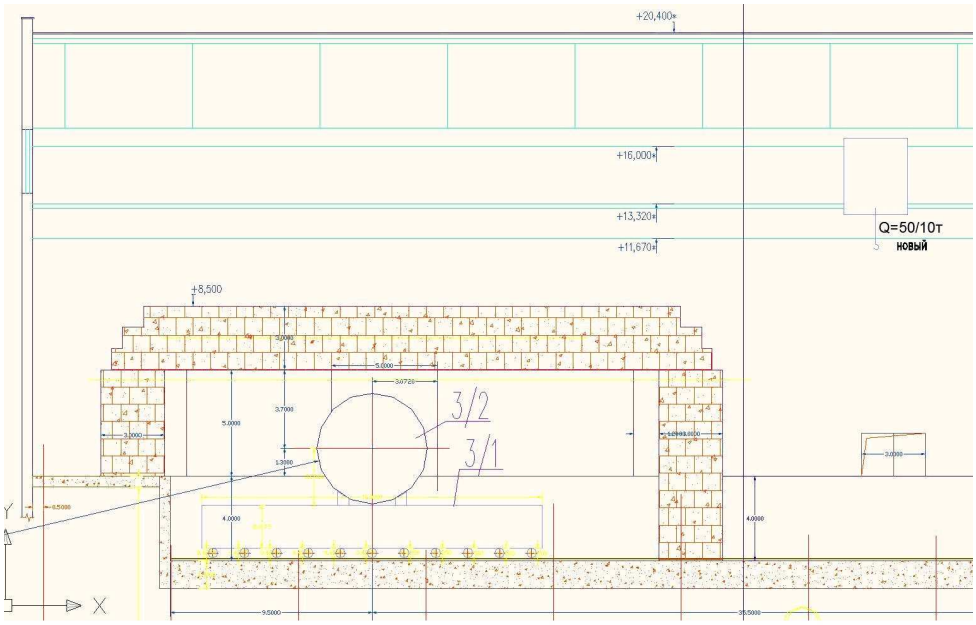

Fig. 4.4: MPD detector layout in the operating position (side view)

4.3.1 Magnet and Inner Detectors Interfaces

Since the magnet is the main component of MPD in terms of size, weight and rigidity it is used as the reference frame for all the detectors placed inside. The MPD layout which covers integration issues between detector subsystems is shown in Fig. 4.5. The inner diameter of the solenoid cryostat and the cryostat length are defined by the arrangement of the central detectors (TPC, TOF, Straw EC Tracker, BBC, EMC, etc). This picture doesn't provide detailed dimensions. It specifies the volumes necessary to allow safe location of all detectors inside the magnet yoke and cryostat, without interference with other subsystems. In other words, it establishes the positions of every subsystem in order to allow the other detector subsystem design to progress.

Access to the faces of the inner detectors for repair requires a substantial amount of time and effort thus causing an unacceptable delay in the physics program. So this procedure has to be facilitated as much as possible. Therefore the end caps of the yoke mounted on the skids should be promptly movable back in axial direction up to 1000-1200 mm to liberate free passage to the inner detectors 400-600 mm (see Fig. 4.6).

4.3.2 Layout of the magnet assembly area

The magnet assembly process is explained in detail in part 2.2 of this paper. So long as for assembly site arrangement it takes allocation of essential space in the Experimental Building, layout of the assembly area has to be considered beforehand. Since the detector assembly activity is planned for the period of accelerator commissioning, a special radiation shield has to be mounted for this period to prevent the radiation hazard for the personal.

Before beginning of the assembly process all magnet component parts have to be stored at the experimental area of the Experimental Building (see Fig. 4.7, Fig. 4.8). Delivery of cargo to the experimental area will be provided by means of the 50 t bridge crane from

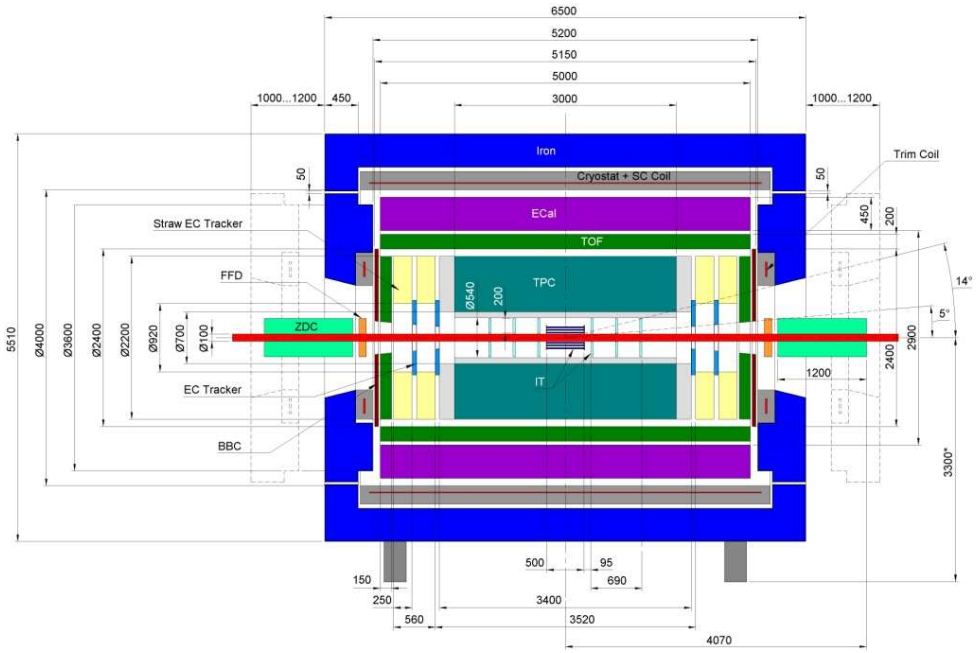

Fig. 4.5: MPD integration

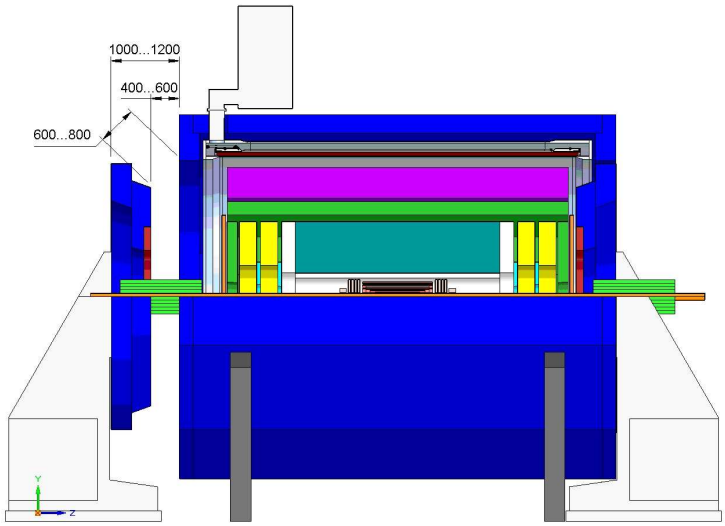

Fig. 4.6: Access to the inner detectors

the unloading site of the Experimental Building. The weights and overall dimensions of the iron yoke pieces and of the cryostat are listed in the Table 2.9. A special area for handling with lifting bridles and turning around by means of tilters is provided.

The magnet assembly begins with the installation of the movable rail-guided carriage on rails running from the assembly area to the experimental area. Then the traveling solenoid section (the magnet without both poles) will be mounted on the carriage and equipped with the main part of inner detectors. The end caps units will be assembled on their rails in the operation area (see Fig. 4.9).

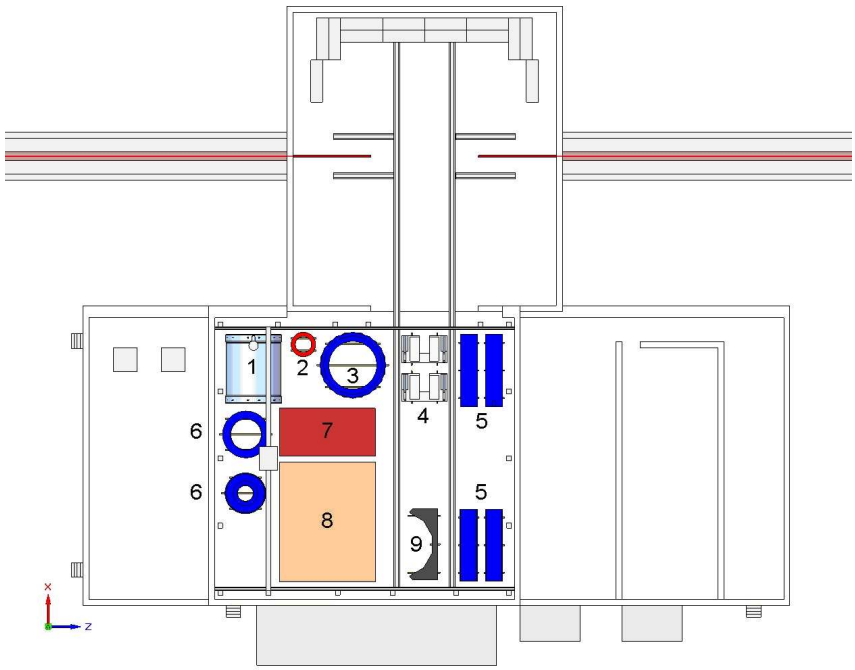

Fig. 4.7: Allocation of the magnet component parts in the assembly area of Bd.205: 1) cryostat; 2) trim coils; 3 support rings; 4) pole supports; 5) barrel beams; 6) end caps components; 7) place for handling jigs; 8) canting place; 9) solenoid supports

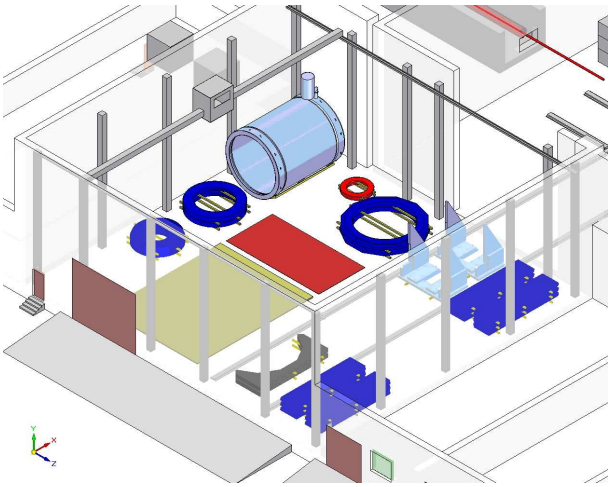

Fig. 4.8: 3D view of the magnet assembly area with allocated component parts

After transportation of the magnet traveling section to its operational position the rest of the inner detectors will be mounted and the end caps installed on their rail guided supports will be inserted to their positions inside the yoke support rings (see Fig. 4.10). Subsequently the end caps remain at their positions during transportation of the traveling solenoid section to the parking position for a solenoid upgrade or repair.

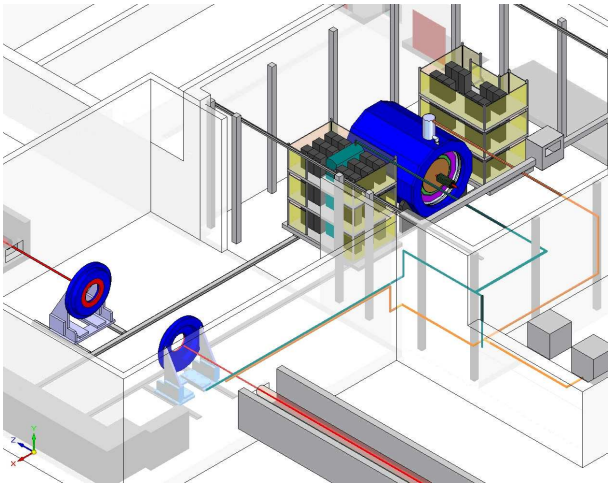

Fig. 4.9: Assembled magnet traveling section equipped by detector subsystems before transportation

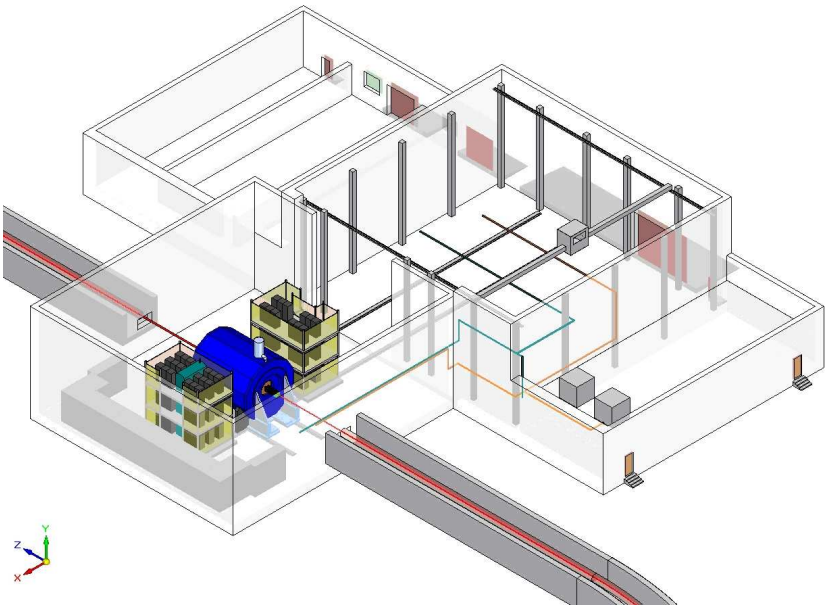

Fig. 4.10: Assembled MPD in its operation position

4.3.3 Magnet services

Electrical circuit and Power supply of the SC coil

The electrical circuit of the MPD superconducting solenoid is shown in Fig. 2.18. At the nominal magnet field 0.5 T, the current through the superconducting coil is 1363 A.

Current supply has to provide the voltage up to 10 V to provide the dynamic regimes of the coil excitation and discharge.

The current supply has to be equipped by a mechanical switch of polarity. The two 2 kA circuit breakers are air cooled and must support an opening voltage of 1000 V. They

are "normally open" type.

The power supply must operate with stability of ±0.01%.

The power supply has to be connected to the solenoid current leads by insulated flexible copper cables. The cables should be air cooled.

The stainless steel dump resistor for the fast discharge of the solenoid is of 0.37 Ohm and has to absorb the total solenoid magnetic energy of 7.8 MJ with a temperature increase of 300 C at its hottest point. It is air cooled through convection cooling.

Power supplies of trim coils

At the nominal magnet field 0.5 T, the currents through the trim coils are 1625 A. It takes two independent power supplies to correct field inhomogeneity due to the axial deviation of the SC coil position. The coils consume 2×65 kW for the zero deviation regime.

The power supplies must operate with stability of ±0.01%

The power supplies have to be connected to the trim coils by insulated flexible copper cables. The cables should be air cooled.

The current supplies have to be equipped by commutated mechanical switches of polarity synchronized with the switch of polarity of the SC solenoid circuit.

Cryogenic supply

The MPD solenoid needs cryogenic supplies: $\sim$ 50 W refrigeration at 4.5 K, $\sim$ 800 W refrigeration at 50 K and 0.16 g/sec liquid helium (liquefaction).

Water supply

The trim coils are cooled by demineralized recirculated water. It takes total water discharge of 2×0.52 liter/sec at the pressure drop 6 Bar.

4.3.4 Cables, utilities routing

4.4 Detector assembly

The assembly of the inner detectors of MPD is a very critical process because of their essential weights and close-packed arrangement within the solenoid aperture (see Table 4.1). Choice of a suitable assembly processes and their sequence is able to prevent a possible future damage of the solenoid cryostat or detectors.

Because of the high weight of the package of all inner detectors ($\sim$ 53 ton) there do not appear to be sufficient the reasons for its assembly by insertion of the whole package into the solenoid aperture in consideration of damage risk.

After solenoid assembly completion the space frame of the Ecal will be inserted into the aperture. The frame holders are to be fixated on the supporting rings of the yoke (Fig. 4.11).

The frame is intended for space fixation of 48 Ecal modules. Every Ecal module is a sector cartridge completed by spatially oriented crystals (see Fig. 4.12). In addition the frame houses rails on its inner surface to support TOF and TPS system (see Fig. 4.13).

All 48 Ecal cartridges will be inserted into their frame cells turn-by-turn on their supporting bearings (see Fig. 4.14). 24 cartridges are to be inserted from one side and the

Table 4.1: Overall dimension and weights of the inner detectors

Part	Inner Radius, mm	Outer Radius, mm	Length, mm	Weight, ton
Solenoid aperture		2000	5200	
ECal	1450	1950	5000	> 50
TOF	1200	1400	5000	~ 1
TPC	350	1100	3000	< 1
IT	70	160	500	~ 0.1
Total weight				~ 53

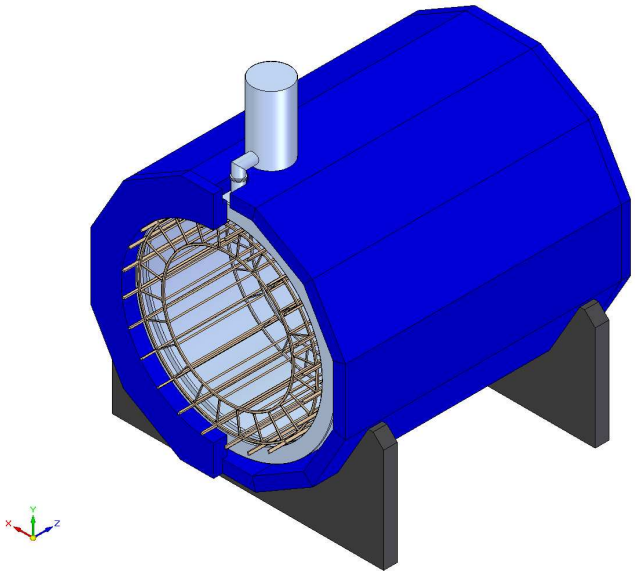

Fig. 4.11: MPD magnet equipped by the space frame for the Ecal

remaining ones - from another side of the magnet. After completion of the Ecall modules installation the TOF unit will be wheeled into the space frame and after installation of additional rails the TPC unit will be rolled in (see Fig. 4.15).

Montage of the ion tube with Internal Tracker (IT) and other inner detectors is to be continued after transportation of the magnet traveling module to the operation position. The IT must not touch with TPC inner surface. Two possible options of the ion tube sag compensation are shown in Fig. 4.16.

Access to the inner detector faces is possible after retracting of the end caps. This procedure can be done without disassembling of the vacuum chamber, disconnecting cables, or removing mechanical support elements. It is expected that an end cap can be extracted and repeatedly inserted for service within one shift during a normal beam down period. Access to the vertex detector is a more complicated procedure because the beam line has to be disassembled. This work can be performed during a longer shutdown period without movement of the whole detector.

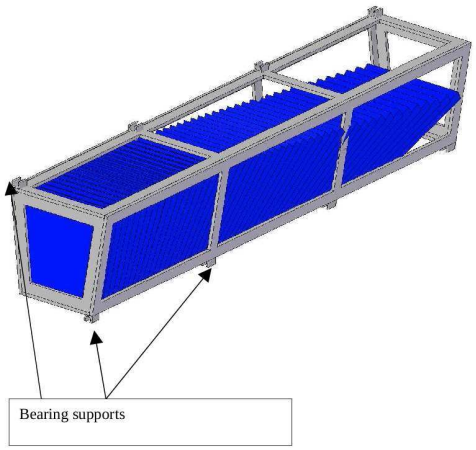

Fig. 4.12: An ECal cartridge equipped by supporting bearings

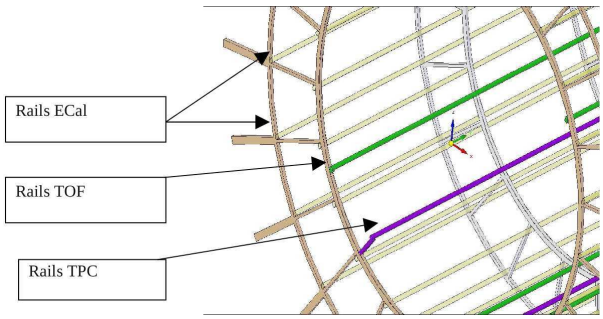

Fig. 4.13: Rail system on inner surface of the Ecal space frame to support TOF and TPS

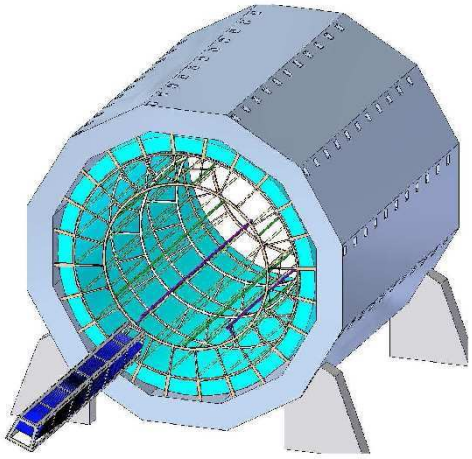

Fig. 4.14: Insertion of ECal cartridges into the supporting frame

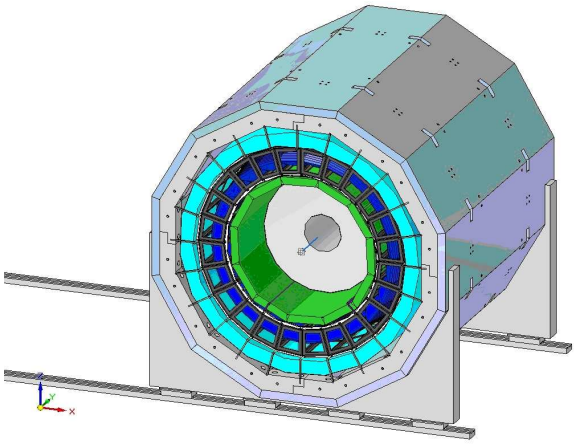

Fig. 4.15: Installed ECal cartridges, TOF, TPC units in the interior of the MPD magnet cryostat

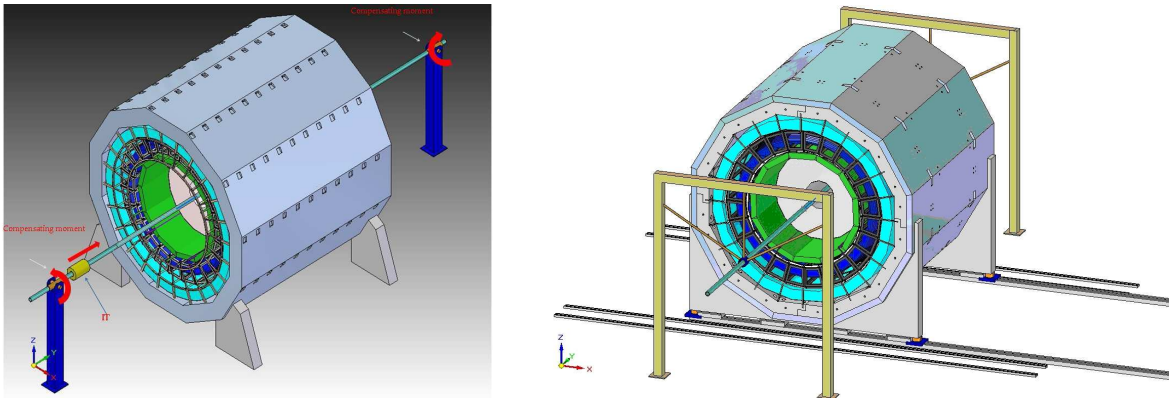

(a) (b)

Fig. 4.16: Options of the Inner Tracker (IT) installation

4.5 Detector control system

The MPD Detector control system (DCS) should provide control and coherent operation of NICA infrastructure and all MPD subsystems including subdetectors and DAQ.

The main parts of all subdetectors are Front End (FE) devices. On one hand at the beginning of a run FEs must be initialized according to the run type. On another hand during a run FEs should be monitored, for example usually subdetector active media and/or FE temperature during the run have very big importance therefore this information should be periodically red-out and stored for the further use during physics analysis.

Another important task is a periodical reading back of FE settings to ensure that due to radiation effects in internal FE memory or registers the required FE settings have not been lost.

Due to the fact that amount of communication links between FEs and second layer of readout system equipment is quite limited, the FEs could belong to two different worlds — a world of DAQ and a world of DCS. These worlds are built with very different concepts.

For the MPD we assume that the FE parameter downloading/reading back and temperature monitoring should be performed by a system (DAQ or DCS) having better communication links to FEs. After information is received by Back Ends it should be distributed to the corresponding channel of processing. For example if a readout of FEs is performed by DAQ then FE settings monitoring should be performed by DAQ and temperature information should be directed to subdetector DCS.

4.5.1 Technical requirements

MPD includes subdetectors having their subsystems as follows

- Magnet
  - Current source
  - Cryogenic system
- IT
  - HV power supply system for silicon detectors
  - LV power supplies for powering of digital and analog electronics
  - Cooling system to provide silicon detector stable working temperature
  - FE temperature monitoring system
  - FE control
- TPC
  - HV power supply system
  - LV power supply system
  - Gas mixing system
  - FE control
- ECT
  - HV power supply system
  - LV power supply system
  - Gas mixing system
  - FE control
- TOF

- HV power supply system
- LV power supply system
- Gas mixing system
- FE control

- ECAL
  - HV power supply system
  - LV power supply system
  - Cooling
  - Thermo-stabilization
  - FE control
  - UV laser calibration/monitoring system
- BBC
  - HV
  - LV
  - FE control
- FFD
  - HV
  - LV
  - FE thermostabilization (to be discussed)
  - Laser calibration/monitoring system (to be discussed)
  - FE control
- ZDC
  - HV
  - LV
  - Cooling
  - FE control

A control of some of these subsystems is mission-critical. For example magnet current source and cryogenic system could be seriously damaged in case if corresponding control system fails.

For mission-critical tasks we plan to use Programmable Logical Controllers (PLCs) or/and home-made microcontroller-based microcomputer boards similar to ATLAS ELMBs built with modern components. As a replacement for PLCs for subsystems which are not so crucial we could use industrial PC with incorporated hardware watch-dog timer which will restart PC in case of program hanging.

For other subsystem we will use PC running both Windows and Linux operating systems.

4.5.2 MPD DCS architecture

To minimize the cost of the DCS development we plan to reuse software developed at CERN for LHC experiments. Therefore as the main Control And Data Acquisition (SCADA) toolkit we plan to use PVSS II together with the JCOP framework components.

In case if PVSS using is too expensive we assume to replace the PVSS-based software with own developments based on modern Rapid Application Development (RAD) tools like Borland Development Studio for Windows and Borland Kylix for Linux. There tools provide cross-platform compatibility at level of source code and contain both Delphi and C++ languages.

Due to very limited funding and very limited manpower we plan to use only essential modules of the JCOP framework. These elements are

- PVSS itself
- Alarm handling subsystem
- Final State Machine
- JCOP tools for configuring of LV and HV systems
- Gas mixing system framework components
- Access control (to be discussed)
- DB recording (to be discussed)

The MPD DCS has three-layer hierarchical structure, see Fig. 4.17

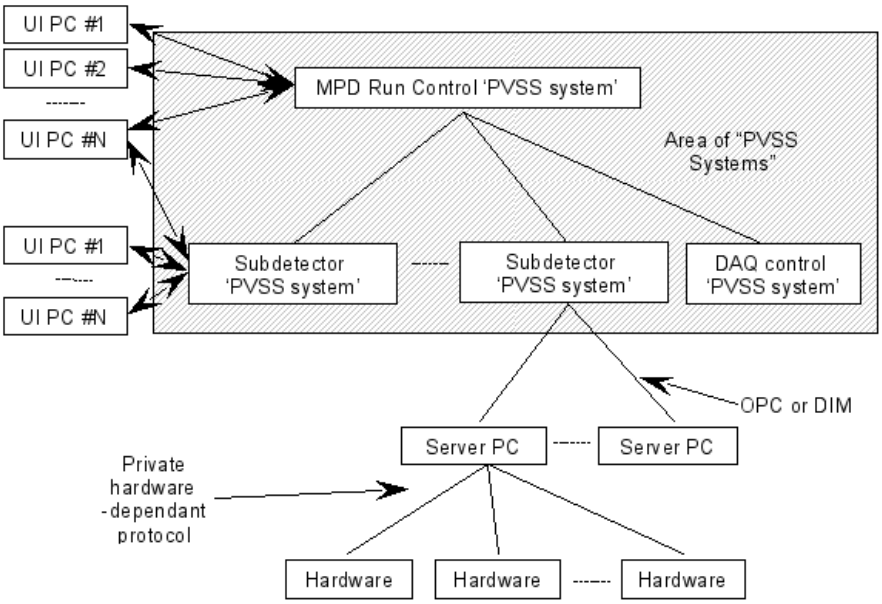

Fig. 4.17: Structure of the MPD DCS.

Two upper layers are based on PVSS. To minimize the cost of PVSS licenses these layers contain only one so called 'PVSS system' per subdetector or a root node.

To provide convenient operation of all PVSS-based DCS nodes including the DCS root we propose to use multiple User Interfaces (UIs) connected to "PVSS systems" and running on additional computers which do not have "PVSS system" installed. Therefore each node of two upper DCS layers could contain more than one PC. Each of these UI PCs could run PVSS panels from more than one "PVSS system".

For example during hardware debugging the TPC could run one PVSS system at the main TPC DCS node with couple PCs running Gas Mixer panels and HV control panels used by a groups working with the gas system and the HV system in parallel.

The global control of MPD including Run control is performed at the first layer by a main node. This node being the root of the hierarchical tree of MPD DCS receives states and alarms from all subdetectors, the magnet and the DAQ. This node also communicates to the NICA and infrastructure control systems.

The root also provides the distribution of commands to subdetectors according to the selected run mode and commands to change operation state like set "On", "Off" etc. states of MDP DCS.

Second layer consists of subdetector control nodes. As it was mentioned above this node runs one PVSS system and provides control only of its own subdetector.

The hardware, logical and FSM trees presenting segmentation of subdetector should run at this computer.

The bottom DCS layer consists of server PCs providing communication to subdetectors hardware. These computers should unload PVSS PCs from execution of CPU-time consuming polling procedures providing execution of low-level communication protocol. PVSS should receive only filtered resulting information containing only useful information.

The routines providing communication to hardware should run in compiled executables, so called "hardware servers". Moving of these algorithms to PVSS drastically decreases system performance due to the fact that PVSS is an interpretive system and as show measurements performed at ATLAS the difference in performance between PVSS and compiled program could achieve tens of thousands times.

Second reason to move low-level communication algorithms to compiled modules is very poor set of PVSS debugging tools. Typically debugging of programs communicating to hardware is very complicated process and using of modern Rapid Application Development (RAD) tools allows to work in much more user-friendly environment. Typically development of polling algorithms in PVSS takes much longer time in comparison with development and debugging performed with using of RAD tools.

We plan to use as much industrial equipment as possible. Typically manufacturer of equipment provides interface to industrial SCADA. At the present moment de-facto industry uses the OPC protocol to interface devices to SCADA.

OPC (OLE for Process Control, OLE stands for Object Linking and Embedding) is based on top of Microsoft COM/DCOM technology (Component Object Model/Distributed Component Object Model). Therefore OPC servers could run only on Windows-based computers.

Typically an OPC server is quite bulky and resource-consuming program. In the case if a hardware of a system allows to run more that one OPC server then we would recommend to run these servers on different PCs to load server PC CPU not more than 20–40%. For example in case if a subdetector uses the CAEN power supply system consisting of many crates we would recommend to run more then one OPC server having few crates in a logical branch to achieve short refresh period and low response time.

For interfacing of home-made hardware to PVSS we will use protocol DIM (Distributed Information Manager). The DIM has been developed at CERN and it will be supported during whole life-time of all LHC experiments. CERN provides the DIM PVSS API manager having both DIM server and DIM client.

The DIM performs addressing of items by items names. We plan to build independent domains of names presenting independent subsystems. We expect that each subdetector will have its own DIM name domain to provide internal data inter-exchange between servers and clients including both testing/debugging clients and PVSS DIM client without disturbing work of other subdetectors.

The FSM tree should have its own name domain. The corresponding DIM Name Server should run at the root DCS PC.

For home-made servers we recommend to use following scheme, see Fig. 4.18.

Server should provide reading of hardware state and should send commands to change this state. The reading is performed by a polling algorithm which should send to DIM server module only changed data.

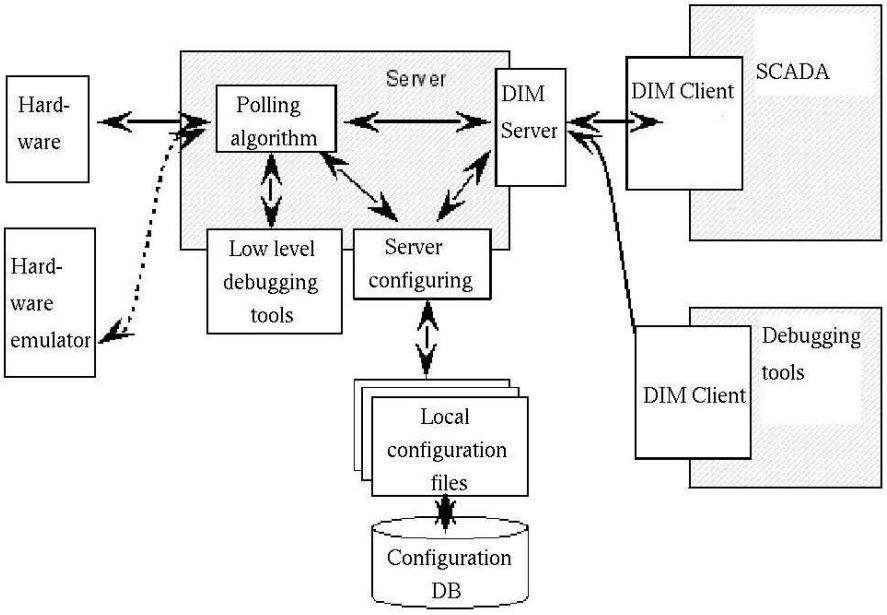

Fig. 4.18: Recommended template for server development.

It would be useful if server contains incorporated low-level debugging tools to allow browsing of I/O traffic.

The configuration information which defines communication hardware settings, DIM item names should be stored in a local configuration file. There should be a possibility to store these files in the MPD configuration DB.

In the case if a communication protocol is quite complicated we recommend to develop a hardware emulator to simplify fault diagnostics and troubleshooting.

To monitor data published by server a set of diagnostic tools should be used. This could be general purpose DIM browsing tools being a part of JCOP framework or a dedicated engineering or debugging tool. As shows experience of LHC projects, this tool might be very useful to run a subdetector system in stand-alone mode in the case if some central services like subdetector head node are down.

Servers should be able to run in the case when no user is logged in to the server PC. For that the servers should be developed as a Windows service application or "daemon" for Linux.

Second possibility to start appropriate servers for the Windows operating system is to use a "WatchDog" system starting standard windowed or console-type applications at the operating system startup.

As it was mentioned above, the MPD DCS has hierarchical structure. To navigate through this structure we plan to use a toolkit developed at CERN and being a part of the JCOP Framework. It contains a set of panels to present, to edit and to navigate through three trees: hardware tree, logical tree and FSM tree.

The hardware tree represents an addressing scheme of subdetector hardware. It should reflect the hardware hierarchy of a subdetector in terms of racks-crates-modules. This tree is used to create or to modify current hardware configuration.

The logical tree presents the logical segmentation of subdetector in terms of components and subcomponents.

For example the hardware tree represents the location of HV connector providing HV

power to a chamber. The logical tree presents the name of a chamber HV cable being plugged to this connector.

The FSM tree represents a scheme of a command propagation between nodes of logical tree from top to bottom and a state propagation from bottom to top. The FSM tree allows to partition the MPD hardware. For example a part of the DCS system could be disconnected from the root node and then connected to a local temporary root to perform hardware debugging and adjustment in local mode.

The FSM tree nodes could have following states:

• **SWITCHED_OFF** — a stable state when all power supplies are off.

• **OFF** — transient state when some LV power supplies are on and some are off.

• **STANDBY** — all LV power supplies are on and HV power supplies are off.

• **RAMPING** — transient state, all LV power supplies are on, some HV power supplies are on and some are off.

• **READY** — all power supplies are on, all infrastructure components are ready for data taking.

• **INITIALIZING** — transient state, all power supplies are on, all infrastructure components are ready for data taking and FEs initialization is in progress.

• **RUNNING** — data taking is going on.

• **PAUSED** — data taking is paused.

• **ERROR** — at least one of power supplies is tripper or at least one of DCS subsystems or infrastructure components is in ERROR state.

FE parameter downloading should follow a scheme shown in Fig. 4.19.

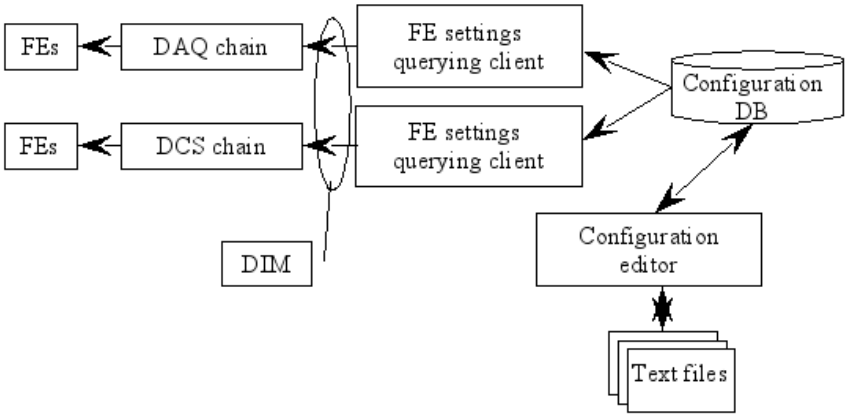

Fig. 4.19: FE parameter downloading.

Parameter retrieval from the Conditions DB is performed by the DB Client which executes query to DB according to the run type. This client is build according common template and does not distinguish if FE of a subdetector is controlled by the DAQ or DCS. The data are sent to a corresponding chain using the DIM protocol.

The set of run configurations should be edited by the configuration editor being common for all subdetectors.

To have a possibility to use convenient editors the Configuration editor should have possibility to import local text files containing a description of FE settings.

After configuration is edited and tested, it is permanently stored at the Configuration DB and could not be deleted or edited any more without changing of configuration name or version number.

We expect that DCS PCs are installed into racks and do not have their own keyboards and screens. The access to DCS PCs should be performed from user's PCs with Remote Desktop utility.

Unfortunately at least at the beginning of the work we will not have automatic software installation facilities like CERN CMF. Therefore for the maintenance and installation of the DCS software the subdetector DCS groups should provide installation packages stored in the Configuration DB. This package should contain all drivers and executables needed for the installation of the DCS software to a brand new PC having only operation system installed. The package also should contain the installation manual and, if possible, a setup program which should install all DCS modules required for a normal run of node PC.

We expect that DCS PCs are installed into racks and do not have their own keyboards and screens. The access to DCS PCs should be performed from user's PCs with Remote Desktop utility.

Chapter 5

Simulation and Detector Performance

The software and computing parts of MPD project is responsible for the activities including the design, evaluation and calibration of the detector; the storage, access, reconstruction and analysis of the data; and the support of a distributed computing infrastructure for physicists engaged in these tasks.

5.1 Detector simulation software packages

The software framework for the MPD experiment (MpdRoot) is based on the object-oriented framework FairRoot [293] and provides a powerful tool for detector performance studies, development of algorithms for reconstruction and physics analysis of the data.

Recently, this framework has already been used by many experiments planned to work at FAIR project at GSI (e.g. CBM [294], PANDA [295]). The flexibility of the framework is gained through it's modularity. The physics and detector modules could be written by different groups. The modules can be plugged into the application framework at run time, independently of the computing environment. One can easily choose between different versions of various modules. The modules do not communicate with each other directly but only through the data access protocols that are part of the framework itself.

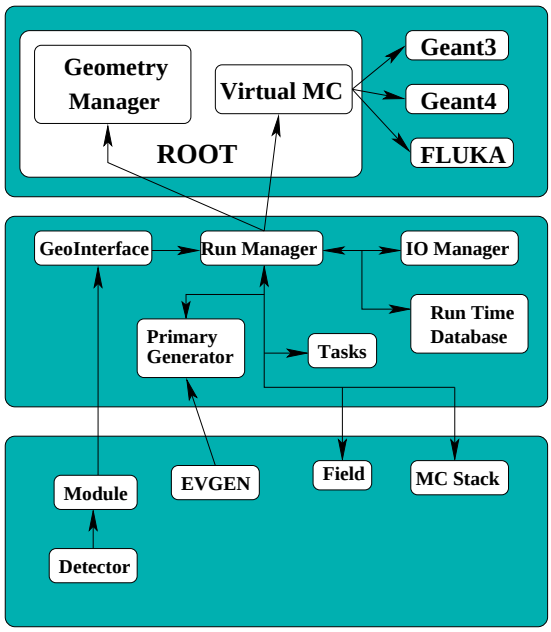

Fig. 5.1: Schematic view of the general part of MpdRoot framework.

In the applied framework the detector response simulated by a package currently based on the Virtual Monte Carlo concept [296] allows performing simulation using Geant3, Geant4 or Fluka without changing the user code. The same framework is used for simulation and data analysis. The schematic design of the MpdRoot framework is shown in Fig. 5.1.

A useful advantage of the framework is that a new geometry reader was developed for it. The input of this reader is in the form of TGeoVolumes (Root Geometry format). This reader is used by the PANDA collaboration to read the detector geometries which are converted from the STEP file format (CAD system) to the Root format. After importing geometry data the database (MySQL) can be used to efficiently store the detector geometry, materials and parameters. The view of the MPD detector geometry implemented in the framework is shown in Fig. 5.2.

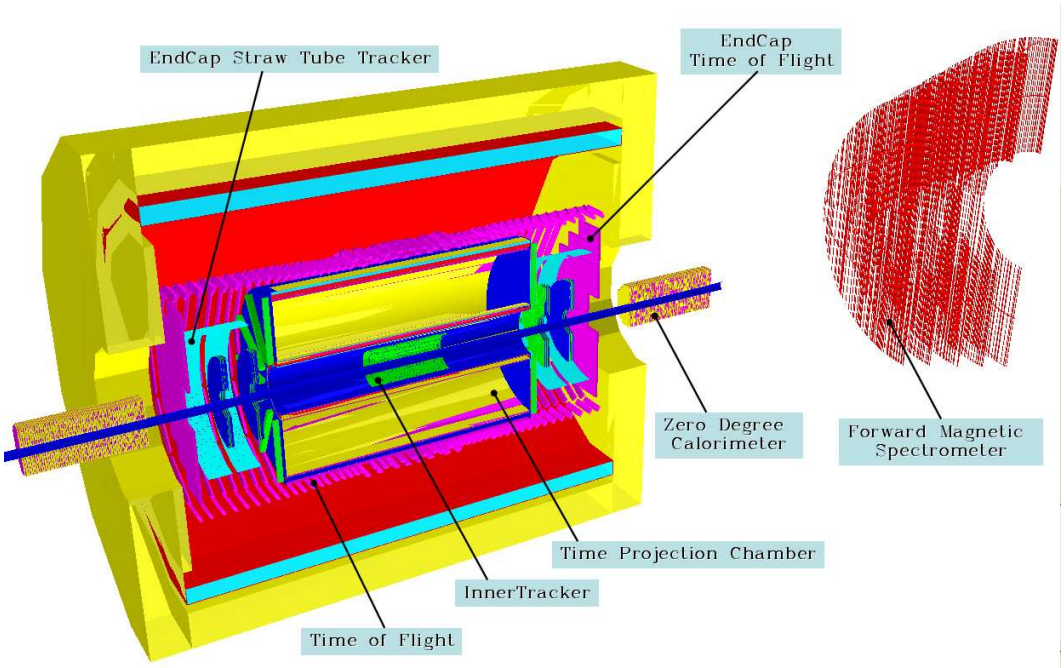

Fig. 5.2: A view of MPD geometry from the simulation package.

The event display in Mpd(Fair)Root is based on the EVE (Event Visualization Environment) package in ROOT [297]. Combined with trajectory visualization in the framework, the event display can be used directly from the macro to display TGeoTracks (MC Tracks), Monte Carlo points, and hits, together with the detector geometry. The EventManager implemented in framework delivers an easy way to navigate through the event tree and to make cuts on e. g. energy, p_t , or particle PDG in user events. An example of an event for the $Au + Au$ collision at $\sqrt{s_{NN}} = 9$ GeV is shown in Fig. 5.3.

For a realistic simulation of various physics processes an interface to the Monte Carlo event generators for nuclear collisions (UrQMD [287] and FastMC [18]) was provided. To study the production of nuclear fragments from nucleus-nucleus collisions the LAQGSM [298] generator was used also. Superposition of minimum-bias events can also be generated with the programme.

The detector performances given in the following chapters was obtained with a current version of the detector geometry. A more detailed detector description and careful cross

checks with the program described above will be made in future.

5.2 Event reconstruction

The event of central $Au + Au$ collision at energies of the NICA collider contains up to 1000 charged particles. The challenge is to reconstruct all these particles from the particle hits measured in various subdetectors of the MPD experiment.

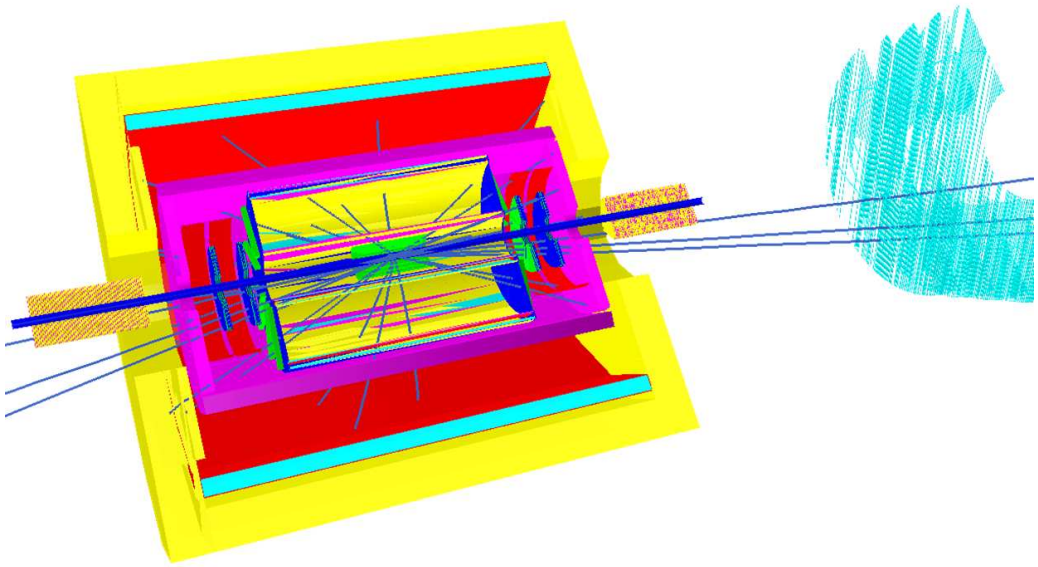

Fig. 5.3: Event of $Au + Au$ interaction at $\sqrt{s_{NN}} = 9$ GeV generated with the UrQMD model and simulated in the mpdroot framework.

The data produced by the event generators contain the full information about the generated particles: particle identification (PID) and momentum. As these events are processed via the simulation chain, the information is disintegrated and reduced to that generated by particles when crossing a detector. The reconstruction algorithms restore the information about the particle trajectory and identity from the information contained in the raw detector data. In order to evaluate the software and detector performance, simulated events are processed through the whole cycle and finally the reconstructed information about particles is compared with the information taken directly from the Monte Carlo generation.

The tasks for charged-track reconstruction in experimental high-energy physics are pattern recognition (i.e. track finding) and track fitting. The current approach to the track reconstruction problem is based on the Kalman filtering technique [299, 300]. The Kalman filtering method provides a mean to do pattern recognition and track fitting simultaneously. The multiple scattering can also be handled properly by the method.

The Kalman filter is a set of mathematical equations that provides an efficient computational (recursive) solution of the least-squares method. The algorithm starts from track candidates ("seeds"), for which vectors of initial parameters and covariance matrices are evaluated. Then each track is propagated to some surface (detector or intermediate point). The new covariance matrix can be obtained using the Jacobian matrix of the transforma-

tion, i.e. the matrix of derivatives of propagated track parameters with respect to current parameters.

If there is a new measurement in a certain window around the extrapolated point with its vector of local measured parameters and covariance matrix it can be added to the track, and the Kalman filter updates the vector of parameters, covariance matrix and χ^2-value of the track.

The MPD reconstruction strategy is the following. For TPC, a two-pass method has been developed. During the first pass, track seeding is done using hits from the outer detector layers. Namely, hits from the layers 50 and 49 are combined with the ones from the layers 44 and 43 to form track candidates under the assumption that the track comes from the primary vertex. The criteria for the track to be accepted include cuts on the longitudinal projected distance from the primary vertex ($|z - z_{vertex}| < 10$ cm) and transverse momentum ($0.05 < p_t < 10$ GeV/c). The usage of several layers (50, 49) allows to take into account possible detector inefficiency.

After propagation of the track candidates through TPC toward the innermost layer, hits assigned to the tracks are removed from the consideration during the second pass. Here, track seeds are built using hits from two consecutive innermost layers with the relaxed cut on longitudinal projected distance ($|z - z_{vertex}| < 30$ cm) in order to preserve reconstruction efficiency. The found seeds are propagated outward. Then double tracks (tracks having more than 50% of the same hits) are found and the ones with a higher quality (with larger number of hits or smaller χ^2) are accepted. Such a two-pass procedure allows to achieve a high efficiency as for high-p$_t$ and low-rapidity as for low-p$_t$ or high-rapidity tracks.

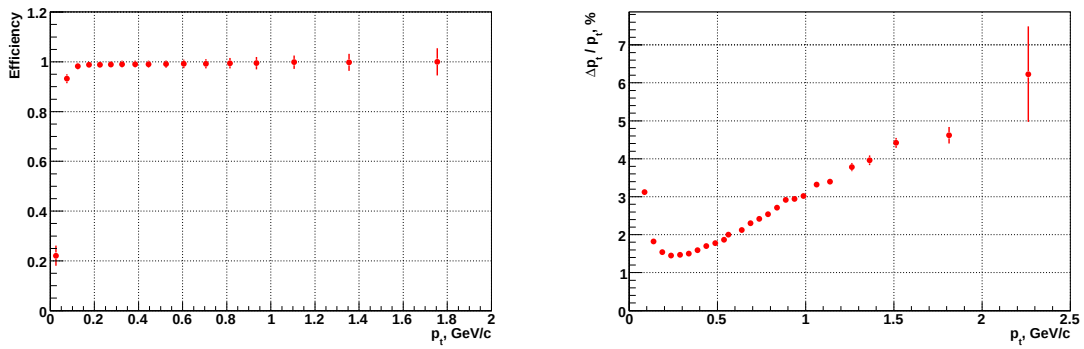

Fig. 5.4: Efficiency of track finding in TPC (left) and relative transverse momentum errors for charged particles (right) within the pseudorapidity $|\eta| \leq 1.2$.

For the End-cap straw tube tracker (ECT), the most obvious approach is to follow high-rapidity tracks from TPC through ECT. But, due to relatively low single layer efficiency and high tube occupancy, the following track propagation procedure has been proposed. For each TPC track going into ECT aperture, multiple track hypotheses are built, i.e. track continuations are searched starting from the ECT layer No.1, then starting from No.2,..., No.10. Then the best branch is selected among them. This procedure allows to have a reliable track propagation in the conditions of relatively high ECT detector occupancy.

Since the TPC performance is expected to somewhat deteriorate for tracks going in the forward direction, an alternative track finding approach has been developed where the track seeds are built from ECT and endcap TOF-detector hits. A similar to the

mentioned above procedure of making track seeds using hits from different ECT layers is implemented here as well. The seeds are then propagated through TPC towards the interaction region.

At the current stage of simulation of the detector responses we study only the feasibility of event reconstruction with the TPC detector as the main tracking device, TOF, endcap TOF and End-Cap tracker. The track finding efficiency was evaluated for all charged particles entering the TPC acceptance with the transverse momentum $p_t \geq 100$ MeV/c.

As it is shown in the Fig. 5.4, this method gives a good efficiency for track finding in high multiplicity events. Relative momentum errors of $\Delta p/p \approx 2 \div 3\%$ can be achieved for particles in the considered momentum range, as shown in Fig. 5.4.

In the future, the reconstruction algorithms should be optimised with more realistic detector response. It will allow to better perform the detector configuration optimization task as well as to do more realistic physics analyses.

Vertex resolution Precise knowing of the primary events vertex position essentially improves the momentum resolution and secondary vertices finding efficiency. The primary vertex is found by extrapolating all primary tracks reconstructed in the TPC back to the origin. The primary vertex resolution is found as the RMS of the distribution of the primary tracks extrapolation at the origin. The global average of this distribution is the vertex position. The primary vertex resolution along the beam direction is shown in Fig. 5.5 as a function of reconstructed primary tracks multiplicity. The precision of finding the primary vertex position in the azimuthal direction is better than that along the beam axis. A resolution of 100 μm along the beam direction is expected to be achieved for central events.

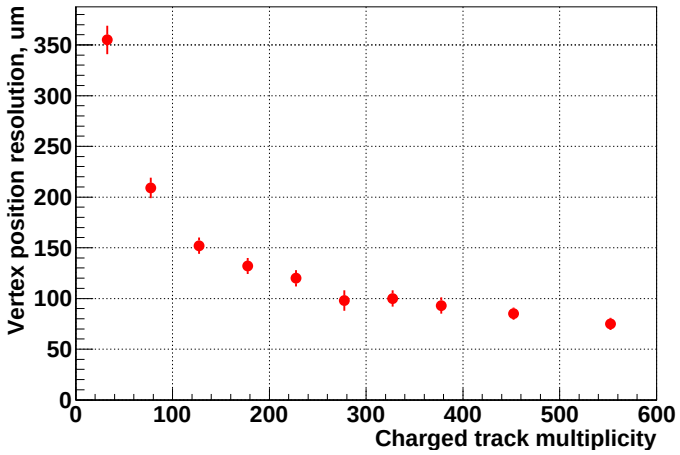

Fig. 5.5: The primary vertex position resolution along the beam axis versus the reconstructed primary track multiplicity in the TPC for $|\eta| < 1.2$

5.3 TPC-TOF matching procedure.

In the reconstruction chain the simulation of hits in the TOF detector is based on the information about propagation of charged particles through the MPD detector from GEANT. The position of the interaction point(s) of a track in the TOF detector material, energy

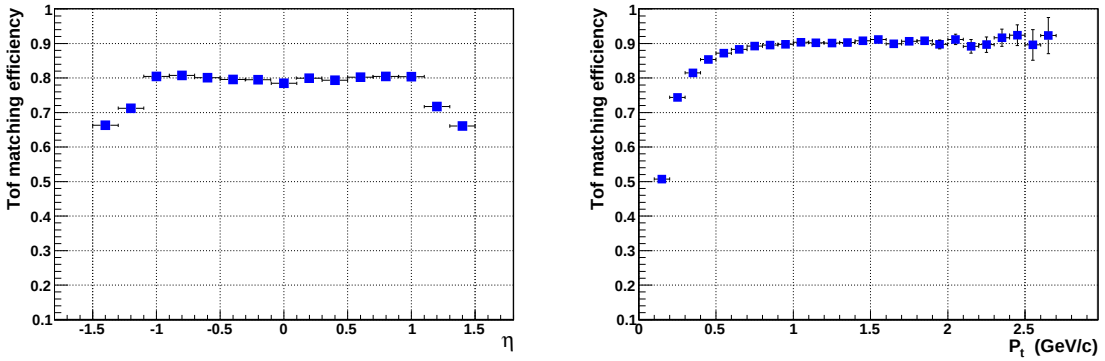

Fig. 5.6: TPC-TOF matching efficiency as a function of η (left panel) and p_t (right panel).

loss within a TOF module, as well as time of flight from the primary collision vertex is used to simulate a detector response, i.e. charge collected from the pads in the module, thresholded ADC distribution and timing signal of the hit. The array of the TOF hits produced (each containing the hit coordinates, timing and ADC information) is then processed together with the reconstructed in the TPC tracks to find all the matches between tracks and TOF hits. The matching procedure is based on extrapolation of the TPC tracks to the TOF using a Kalman-filter algorithm. The matching is processed in two steps. First, we extrapolate the TPC track on the cylinder of radius **R** (R=1.3 m) and determine the interval in polar angle ϕ for the TOF hit-candidate (TOF-barrel consists of 12 regions in ϕ of $\Delta\phi = \pi/6$). After that we scan through the ordered list of the modules within the region-candidate and find the module with the minimum distance between the position of the extrapolation on the module's pad plane and the module's center. Finally, new track parameters (momentum p and length from the vertex to the pad plane L) are determined by re-fitting of the TPC track adding the coordinates of the track extrapolation to the TOF. The results for the transverse momentum and pseudorapidity dependence of the matching efficiency are presented in Fig. 5.6. The efficiency in a $p_t(\eta)$-bin is determined as the ratio of the number of matches of the TPC track projections with TOF hits to the number of reconstructed in the TPC tracks having at least one GEANT point in any among TOF modules. The integrated over p_t matching efficiency is flat over $\eta < 1$ and drops down at the edges of the TOF-barrel acceptance. The correct matching is about 90% efficient at $p_t > 0.6$ GeV/c; the averaged over η efficiency decreases to roughly 50% at low p_t due to multiple scattering in the detector material.

5.4 Particles identification with TOF

The squared mass m^2 for a detected track is calculated using the information about the reconstructed momentum (p), flight path length (l) and time-of-flight (t) measured as

$$m^2 = p^2 \left(\frac{ct^2}{l^2} - 1 \right) \tag{5.1}$$

Assuming the overall time resolution of 100 ps, the calculated mass for the particles detected in the barrel TOF system was smeared and the result plotted in Fig. 5.7. The green lines shown in the figure indicate the regions of particle species selection that were

used to estimate the loss due to PID and corrections for particle misidentification. The estimated PID efficiency and contamination of misidentified hadrons are shown in Fig. 5.8.

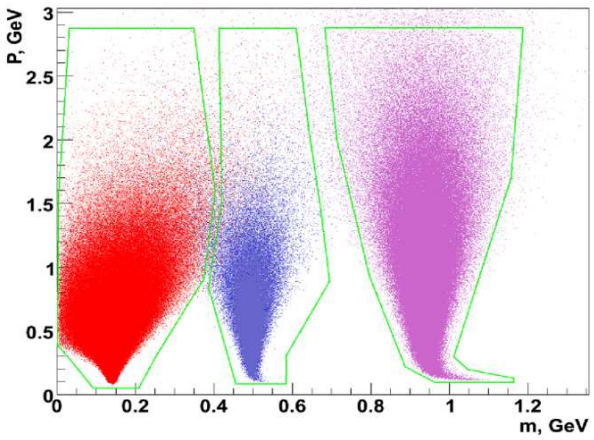

Fig. 5.7: Mass separation with TOF (100 ps resolution) and TPC in the region of pseudorapidity $|\eta| < 1.2$ of primary particles created in the $Au-Au$ interaction at $\sqrt{s_{NN}}$= 9GeV/c. The green lines show the boundaries for efficiency and contamination estimation.

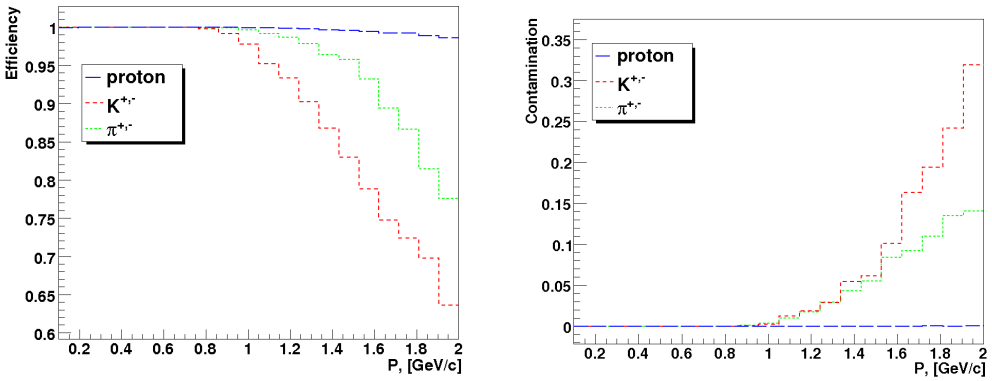

Fig. 5.8: Particle identification efficiency and contamination of mis-identified hadrons versus total momentum (|η|)

To make an estimation of particles loss one has to take into account the TOF TPC acceptance and detector efficiency (table 5.1) prior to identification.

Track reconstruction efficiency in TPC in the region of $|\eta| < 1.2$ and for transverse momentum range $p_t = 0.1$–2.0 GeV/c is $\varepsilon = 100\%$

End Cap One of the advantages of the MPD is that it covers a wide solid angle. As it was pointed out earlier, the acceptance of TOF and TPC is $|\eta| < 1.2$. The region of $1.2 < |\eta| < 2.0$ is also covered by the End cap TOF system situated at a distance of 2.4 m from the interaction point. For track (momentum) reconstruction in this region Straw tube tracker is used. The momentum resolution and track length determination accuracy are presented on Fig. 5.9(a,b).

To make a final estimation of the loss of particles of each type, one has to take into account the TOF TPC acceptance and detector efficiency (table 5.2) prior to identifica-

Table 5.1: MPD barrel (TPC+TOF) geometrical coverage and different contributions to the acceptance loss.

	π		**K**		**p**	
Produced in 4π	693		65.6		153.8	
$\|\eta\| < 1.2$	423.1	1.0	37.9	1.0	67.4	1.0
Reached TOF $B = 0$ T (decay, interaction losses)	360.1	0.85	34.7	0.92	60.4	0.9
Reached TOF $B = 0.5$ T	334	0.79	25.3	0.67	60.4	0.9
TOF geometry efficiency 0.93	310.5	0.73	23.5	0.62	56.2	0.83
TOF registration efficiency 0.95	295	0.69	22.3	0.59	53.4	0.79

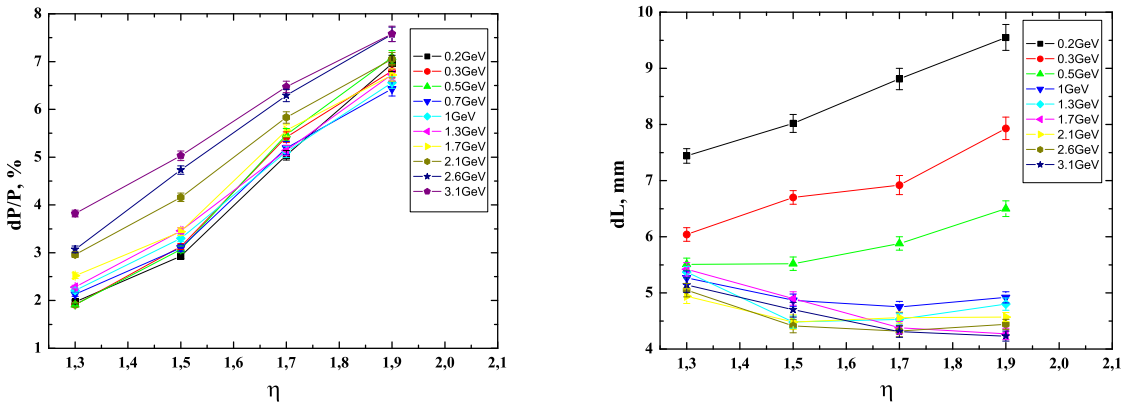

Fig. 5.9: Particle momentum (left-a) and track length (right-b) reconstruction accuracy with TPC and Straw tube tracker in the forward region at a magnetic field of B =0.5 T.

tion. The identification capability of the TOF with End Cap and TPC trackers in the forward direction presented on figs 5.10, 5.11.

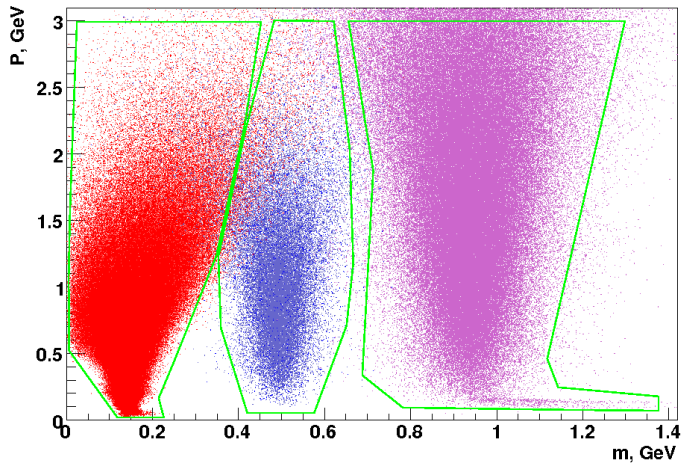

Fig. 5.10: Mass separation with the TOF (momenta reconstructed in the End Cap Straw Tracker) as a function of momentum.

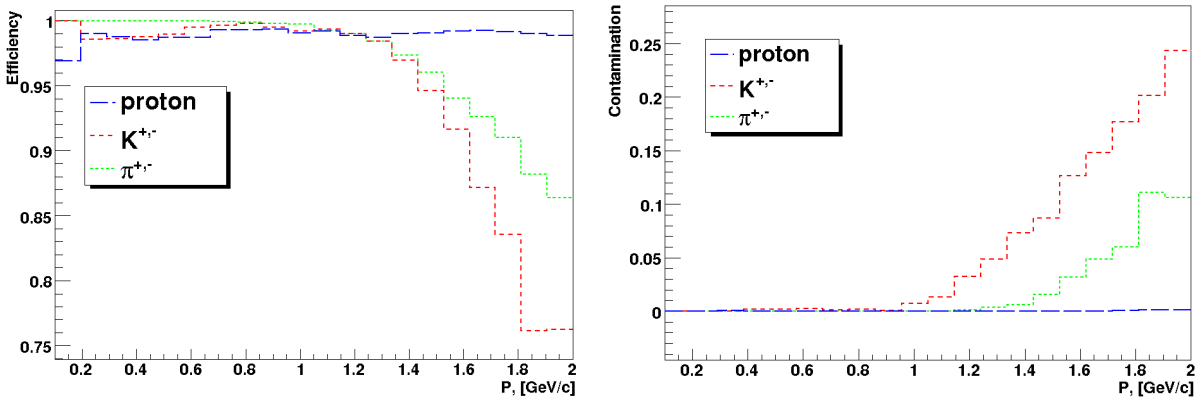

Fig. 5.11: Particle identification efficiency and contamination as a function of momentum for central collisions, primary particles. B =0.5 T, $1.2 < |\eta| < 2$.

Table 5.2: Loss of different particles in the region of $1.2 < |\eta| < 2$. Central $Au - Au$ collision at $\sqrt{s_{NN}}$=9 GeV/c

	π		**K**		**p**	
Produced in 4π	693		65.6		153.8	
$1.2 < \|\eta\| < 2$	173.4	1.0	17.8	1.0	41.6	1.0
Reached TOF $B = 0$ T (onlydecay)	154.6	0.89	16.5	0.93	37.1	0.89
Reached TOF $B = 0.5$ T	140.7	0.81	11.5	0.65	37.1	0.89
TOF geometry efficiency 0.93	130.9	0.75	10.7	0.6	34.5	0.83
TOF registration efficiency 0.95	124.3	0.71	10.2	0.57	32.8	0.79

5.5 Detector performance studies

At this stage of the CDR preparation the TPC (Time Projection Chamber) and TOF (Time of Flight) only serve as the tracking devices of the MPD. They should meet the requirements of the multipurpose detector having capabilities of measuring of wide spectrum of observables. Among the most promising observables which could serve as sensitive diagnostic probes in the energy range under study are the strangeness-to-entropy ratio which can be presented by the kaon-to-pion and/or Lambda-to-pion ratios, as well as fluctuations, HBT correlations, and collective flows of identified hadrons. One more interesting effect, which was possibly observed at RHIC, is the Chiral Magnetic Effect implying a charge separation along the magnetic field, created in non-central heavy-ion collisions. Aiming the search for these effects, one should estimate beforehand the kinematical characteristics of the produced particles, their tracking, and particle identification performance of the detecting system (TPC-TOF). The TPC pursues the object to analyze and identify charged particles $\pi^+, \pi^-, K^+, K^-, p$, pbar directly, as well as various neutral and charged strange particles ${K_s}^0, \Lambda, \Xi^-, \Omega^-$ via charged-particle decay modes. Yield and kinematical characteristics of the produced particles for Au+Au in central collisions, with the impact parameter $b < 3$ fm, are simulated by the UrQMD [17] and FastMC [18] codes in an energy range $\sqrt{s_{NN}} = 4 - 11$ GeV. The pseudorapidity range and transverse momenta of particle emission covered by the TPC and TOF are $-1.2 < \eta < 1.2$ and $p_T > 100\ MeV$, respectively.

In order to evaluate the algorithms for event reconstruction, events simulated by URQMD generator are processed through the TPC and TOF, and finally the reconstructed information about particles is compared with the information taken directly from the Monte Carlo generation. Charged particles were tracked by GEANT through the magnetic field of 0.5 T. Reconstruction of tracks was performed by the dedicated MPD software (MPDRoot). Efficiency of event reconstruction depends on the tracking efficiency, momentum measurement resolution, two track resolution for close tracks, and pion-kaon misidentification. In turn, the tracking efficiency depends on the acceptance of the detector, on the electronics detection efficiency, as well as on the two-hit separation capability of the system. Details of track reconstruction procedure and particle identification are given in sections "Event Reconstruction" and "Time of Flight System". Comparison of kaon, pion and proton spectra for Monte Carlo (MC) and reconstructed (RE) events are given on Figs. 5.12, 5.13 and 5.14. As seen from figures the kaon reconstruction efficiency decreases significantly at small ($p_t < 0.5 GeV/c$) and high ($p_t > 0.8 GeV/c$). Losses of kaons at high transverse momenta caused by misidentification with pions. As for pions, track losses takes place uniformly in the whole range of p_t.

Event-by-event fluctuations The next step is to extract the strength of non-statistical event-by-event fluctuations of kaon to pion ratio, which are superimposed on the background of statistical and experimental fluctuations. In general, the fluctuations of the ratio of the numbers of particle species A and B, N_A/N_B, is characterised by

$$\sigma^2 \backsimeq \omega_A + \omega_B - 2\rho_{AB}[\omega_A \omega_B]^2, \tag{5.2}$$

where ω_i are scaled variances for species A and B, and ρ_{AB} is the correlation coefficient. The relative width σ^2 can be decomposed into three contributions:

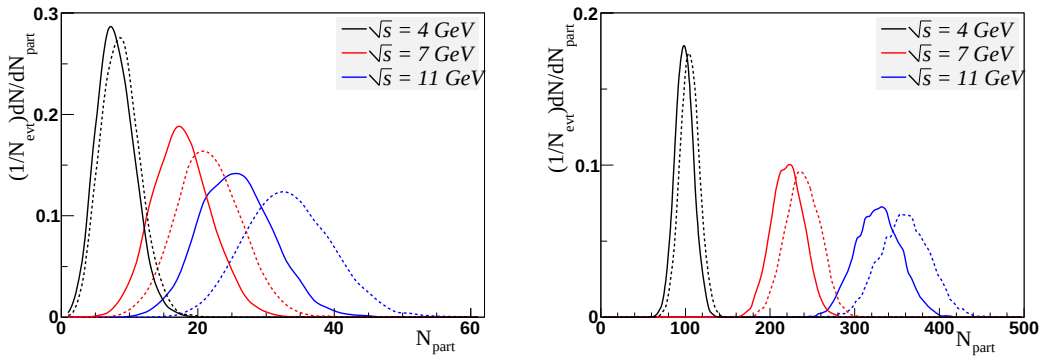

Fig. 5.12: Comparison of multiplicity distributions of charged kaons (left) and pions (right) for MC (dashed curves) and RE (solid curves) events in central Au + Au collisions.

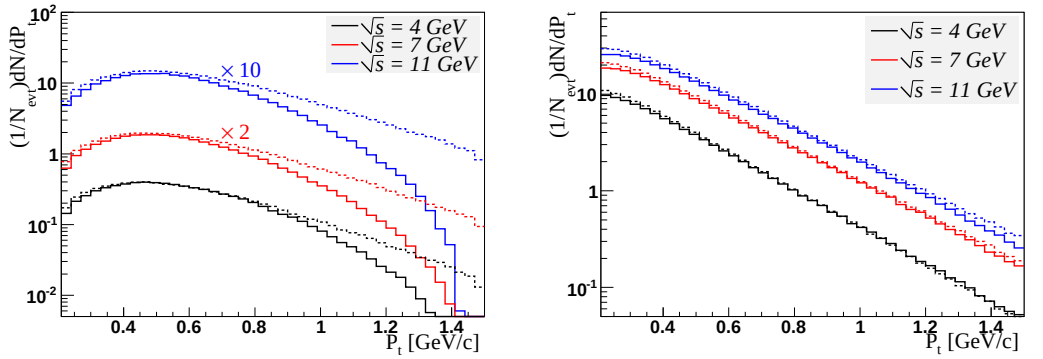

Fig. 5.13: Comparison of transverse momentum distributions of charged kaons (left) and pions (right) for MC (dashed curves) and RE (solid curves) events in central Au + Au collisions.

1. statistical fluctuations due to the finite number of particles produced per event with a width dictated by the individual particle multiplicities within the acceptance,

2. these statistical fluctuations are smeared by non-ideal particle identification,

3. genuine non-statistical fluctuations (if they exist).

These non-statistical, or dynamical fluctuations are estimated by using a mixed event technique [301]. In creating the mixed events, one takes a large number of nucleus-nucleus collision events and measures the numbers of N_A and N_B in each event. Then all A and B particles from all events are combined into one set. The construction of mixed events is done as follows: one fixes a random number $N = N_A + N_B$ according to the experimental probability distribution P(N), takes randomly N particles (A and/or B) from the whole set, fixes the values of N_A and N_B, and returns these N particles into the set. This is the mixed event number one. Then one constructs event number 2, number 3, etc. The experimental data for kaon to pion fluctuations are usually presented in terms of dynamical fluctuations

$$\sigma_{dyn} = sign(\sigma^2 - \sigma^2_{mix})|\sigma^2 - \sigma^2_{mix}|^{1/2}, \tag{5.3}$$

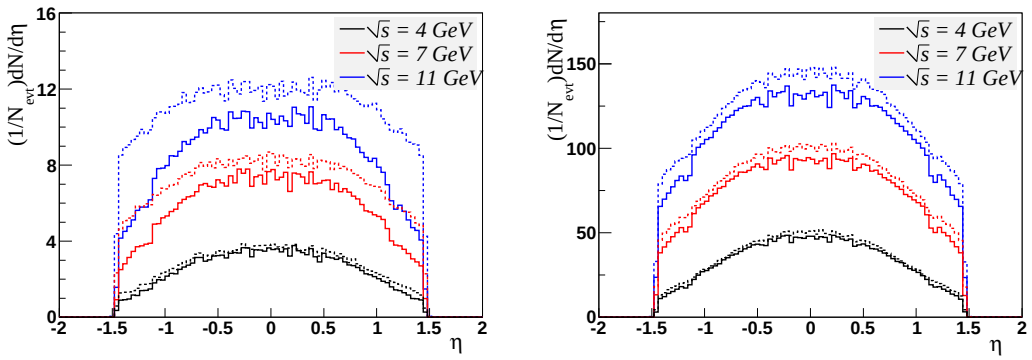

Fig. 5.14: Comparison of pseudorapidity distributions of charged kaons (left) and pions (right) for MC (dashed curves) and RE (solid curves) events in central Au + Au collisions.

where σ^2 corresponding to 'real' events is defined by Eq. (5.2), and σ^2_{mix} corresponds to mixed events. Results of estimated dynamical fluctuations of the charged kaon to charged pion ratio for NICA energy range taking into account corrections on detector efficiencies (which are evaluated in the Chapter "Physics Performance") are shown in Fig. 5.15. Accounting for the experimental acceptance the centrality selection has a relatively small influence on σ_{dyn} and does not change the shape of the σ_{dyn} excitation function.

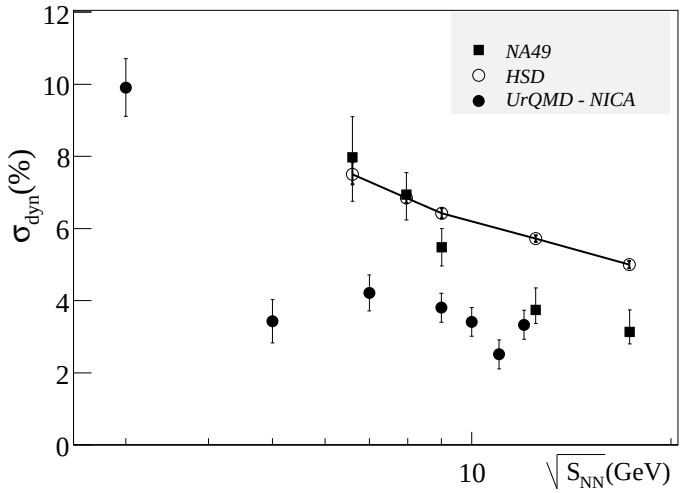

Fig. 5.15: Collision energy dependence of dynamical fluctuations of the $(K^+ + K^-)/(\pi^+ + \pi^-)$ ratio. Filled circles relate to RE events.

Event centrality determination In high-energy heavy-ion collisions at a finite impact parameter b one encounters the vector orientation of b that breaks cylinder symmetry of the hadron emission pattern. After fixing this orientation (the event plane) , the first harmonic in the emission angle ψ with respect to this plane essentially gives the direct flow v_1, whereas the weight coefficient v_2 of the second harmonic quantifies the elliptic flow (see (1.7) and (1.8)). An unambiguous experimental measurement of the azimuthal anisotropic flow is not a trivial task due to the unknown orientation of the reaction plane.

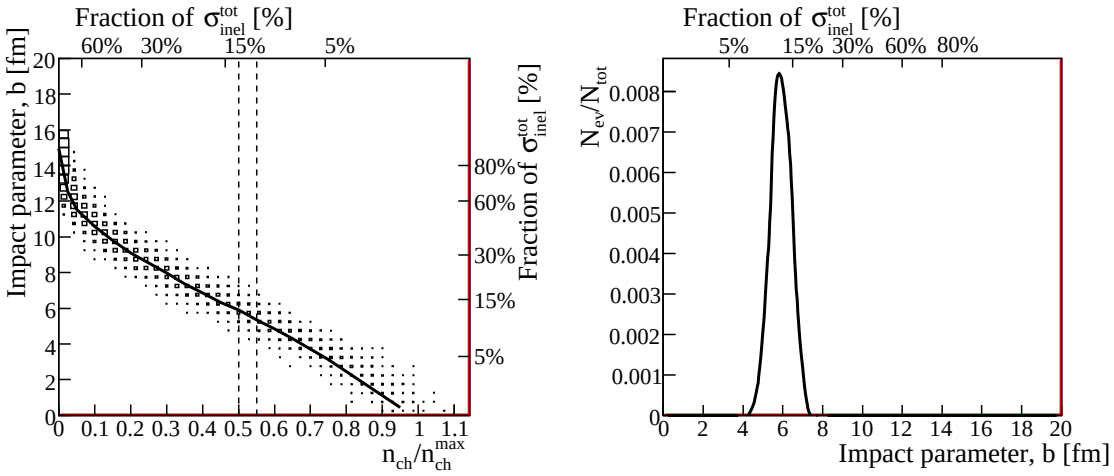

Fig. 5.16: Left: Two dimensional plot of events demonstrating interrelation between centrality, impact parameter and multiplicity. Right: Impact parameter distribution for the selected (on the left plot) band of multiplicities.

There are different methods of estimation of particle azimuthal asymmetry in experimental measurements. For calculations of the azimuthal anisotropy coefficients we use the event plane method. In the UrQMD model calculation of flows, the exact azimuthal angle of the reaction plane Φ_{RP} is known by definition. Analyzing the real data, an experimentalist selects events by centrality and should be able to calculate the orientation of the event plane. Using UrQMD simulations for interrelation between centrality, finite impact parameter and multiplicity one can estimate an impact parameter in the real event during measurements. Fig. 5.16 demonstrates the correspondence between the multiplicity registered by TPC and the values of impact parameter that can be derived during the preliminary fast analysis of the events. The number of events falling into the selected band of multiplicity is approximated by the gaussian distribution in impact parameter representation.

Event plane reconstruction The event plane angle Ψ_2 can be determined by the second harmonic, according to the Eq. (1.9), where n equals 2. Fixing the angle Ψ_2 for all simulated events, i.e. knowing the 'true' event or reaction plane orientation we calculated directed and elliptic flows relatively to this orientation. Since the resolution of the event plane reconstruction is maximal at the impact parameter range $6 \div 9$ fm, samples of events at that impact parameter range were simulated at fixed event plane orientation. Then, using Eq. (1.9) we can reconstruct the 'observed' event plane, which is an estimation of the true reaction plane. The observed value of v_2^{obs} is calculated using the event plane (EP) method as

$$v_2^{\rm obs}\{EP\} = \langle \cos 2(\varphi - \Psi_2) \rangle, \tag{5.4}$$

where the event plane angle Ψ_2 is the estimate of the true reaction plane angle Ψ_{RP}, the mean is taken over all charged particles in a given event and then over all events. The true elliptic flow can be evaluated by dividing the observed one, (5.4), the correction

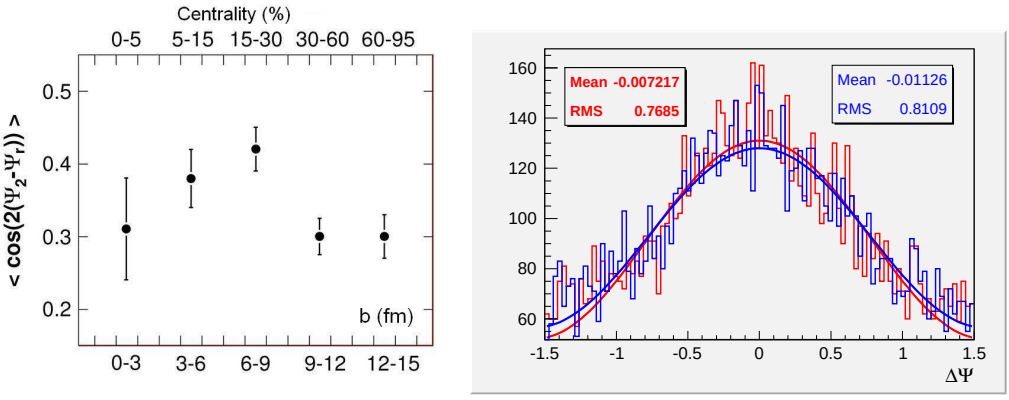

Fig. 5.17: Variation of the event plane resolution with collision centrality and impact parameter (left). The distribution $\Delta\Psi = \Psi_2 - \Psi_{RP}$ at $\sqrt{s_{NN}} = 9$ GeV and impact parameter range $b = 6 \div 9$ fm (right); red histogram relates to MC events, and blue histogram - to reconstructed events. The curves are approximations by the formula (5.6).

factor or the event plane resolution, R:

$$v_2 = \frac{v_2^{\rm obs}\{EP\}}{R} = \frac{v_2^{\rm obs}\{EP\}}{\langle \cos 2(\Psi_2 - \Psi_{RP})\rangle}. \tag{5.5}$$

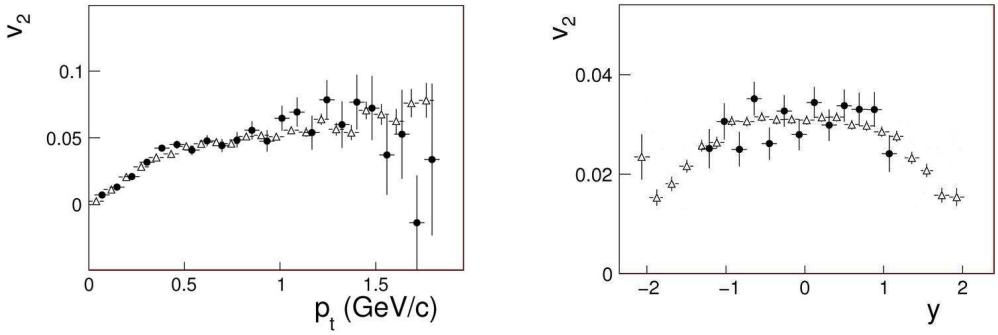

Fig. 5.18: Transverse momentum (left) and rapidity (right) dependence of the elliptic flow in Au+Au collisions at $\sqrt{s_{NN}} = 9$ GeV. Filled circles are simulated and open triangles - reconstructed values.

To exclude the trivial particle autocorrelation the event plane angle, Ψ_2, and elliptic flow coefficient, v_2, are calculated in different samples of the events, namely, in two regions of pseudorapidity, $\eta > 0$ and $\eta < 0$. The event plane resolution depends on the impact parameter or centrality of collisions and multiplicity. The variation of event plane resolution with collision centrality is shown in Fig. 5.17 (left panel). The values of resolution reach maximum at 15-30% centralities or collision impact parameter values in the range 6 - 9 fm. The distribution of the difference between the reconstructed event plane and 'true' event (reaction) plane, $\Delta\Psi = \Psi_2 - \Psi_{RP}$, characterizing variation of the event plane reconstruction is shown in Fig. 5.17 (right panel). This distribution can be approximated

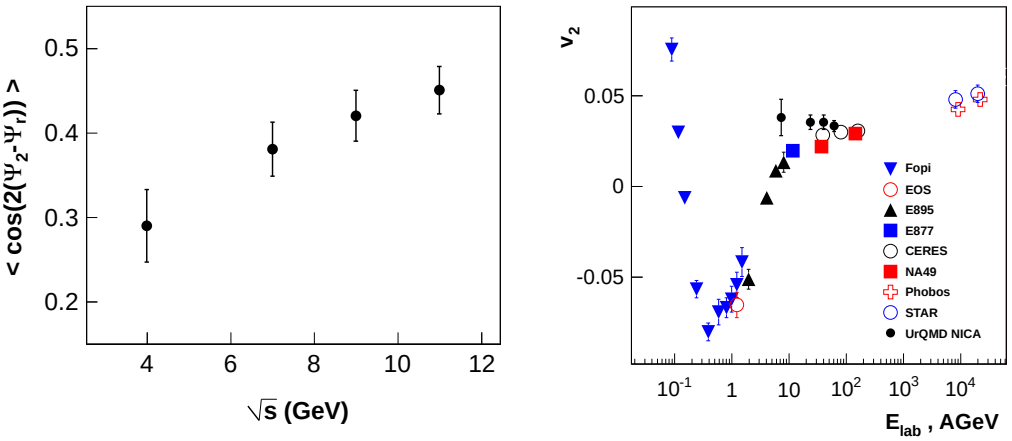

Fig. 5.19: Collision energy dependence of the event plane resolution (left) and the elliptic flow (right) in Au+Au collisions.

by the analytical formula [54, 55]

$$\frac{dw}{d(2\Delta\Psi_2)} = \frac{1}{2\pi}\left[e^{-\frac{\xi^2}{2}} + \xi\sqrt{\frac{\pi}{2}}\cos(2\Delta\Psi_2)\left[e^{-\frac{\xi^2\sin^2(2\Delta\Psi_2)}{2}}\left(1+\mathrm{erf}\left(\frac{\xi\cos(2\Delta\Psi_2)}{\sqrt{2}}\right)\right)\right]\right], \tag{5.6}$$

where w is the weighting variable. Adjusting the dimensionless parameter ξ, one can estimate the resolution of the event plane reconstruction, the correction factor R in (5.5). Relation between ξ and R is given in Fig. 1.15, where $v_2(\xi)/v_2(\xi \to \infty)$ is equivalent to R. For the procedure of the event plane and elliptic flow reconstruction 10^4 events were simulated for Au+Au collision at energies $\sqrt{s_{NN}} = 5, 7, 9, 11$ GeV and the impact parameter range $6 \div 9$ fm. All charged pions falling within the pseudorapidity interval $-1 < \eta < 1$ were analyzed. As seen in Fig. 5.18, the reconstructed values of elliptic flow reproduce well the the simulated transverse momentum (left) and rapidity (right) dependence of selected particles. Dependencies of the event plane resolution (left panel) and the integrated elliptic flow (right panel) on the collision energy are shown in Fig. 5.19. Selected centralities correspond to the maximal values of the resolution at each collision energy. Although TPC-TOF detector system will allow one to perform the measurements of the event plane and anisotropy, some supplimentary detectors are required to develop the precision of these measurements.

V0 Reconstruction To estimate the ability of the TPC to register the strange mesons and hadrons via their decay, 1000 of central Au+Au events (impact parameter $b < 3$) were generated using the UrQMD model and traced through the MPD. The strange $({K_s}^0, \Lambda, \overline{\Lambda})$ and multi-strange (Ξ^-, Ω^-) particles known as V0 are reconstructed from the daughter particles, whose paths are recorded by the TPC. Neutral kaons are reconstructed via their decay ${K_s}^0 \to \pi^+\pi^-$, and Λ - via proton–pion channel. To reconstruct the V0, all oppositely charged tracks in each event are paired and extrapolated towards the primary vertex. Then a cut is placed on their distance of closest approach (DCA) which determines whether they originated from a common interacting point. For candidates passing the

DCA cut the momentum of the parent can be calculated, and a final check is made to see that the momentum of the parent is consistent with that originated from the primary vertex. A pair of the tracks forms a decay-candidate if their DCA is less than 0.5 cm. The tracks originated from the primary vertex may randomly cross with each other and form a fake of secondary vertices known as combinatorial background. The majority of this background is eliminated by requiring that the daughter tracks miss the primary vertex by at least 1.0 cm, and the decay vertex had to be separated from the primary vertex by more than 6 cm. The daughter particles are identified by the MC particles ID. The final cuts applied to V0 reconstruction are listed in Table 5.3.

Table 5.3: The final cuts applied to ${K_s}^0$ and Λ candidates.

Cut Description	${K_s}^0$	Λ
DCA of positive daughter to primary vertex, cm	< 1.0	> 0.5
DCA of negative daughter to primary vertex, cm	> 1.0	> 1.0
DCA between daughters, cm	< 0.5	< 0.5
Particle identification on daughters	MC	MC

Fig 5.20 shows the efficiency of V0 finding as a function of pseudorapidity for ${K_s}^0$ and Λ, respectively. The V0 reconstruction efficiency is defined as the ratio of a number of reconstructed particles to that in the TPC acceptance which is a priori known from MC–simulation. The efficiency depends on the transverse momentum as is shown in Fig 5.21. After applying all cuts listed in the table 5.3, the invariant mass of daughters is calculated. The invariant mass distributions are shown in Fig 5.23. The signal-to-background ratio is 5.0 for ${K_s}^0$, and 7.6 for Λ. These results allow us to conclude that it is possible to reconstruct strange mesons and baryons through their weak decay topology in the TPC. The obtained efficiency is better than 10% in the TPC acceptance and in the momentum range $p_t > 0.2\ GeV/c$. To reconstruct the multiple strange particles Ξ^- and Ω^- which decay into a Λ and either into a $\pi^-(\pi^+)$ or a $K^-(K^+)$, the Cascade finder has to be applied. After the V0 reconstruction has been finished, the Cascade finder begins to operate in essentially the same way as the V0 finder, where one of the decay particles is a V0. The calculated invariant mass distributions of Ξ^- and Ω^- are shown in Fig 5.23.

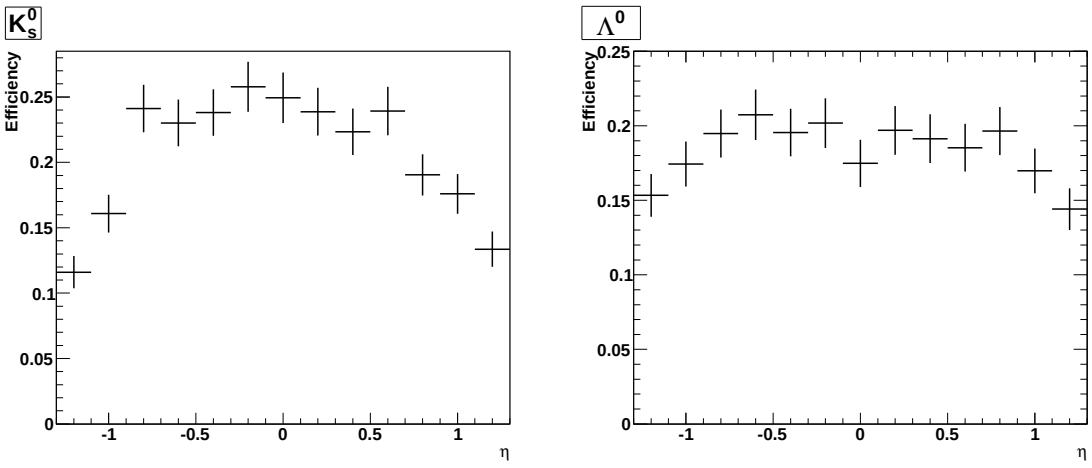

Fig. 5.20: The $K_s{}^0$ and Λ finding efficiency as a function of pseudorapidity.

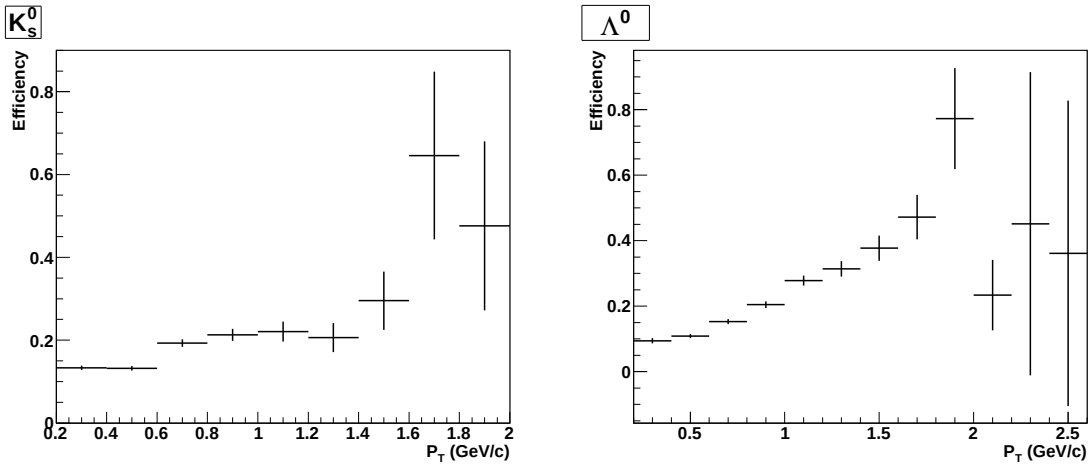

Fig. 5.21: $K_s{}^0$ and Λ finding efficiency as a function of transverse momentum.

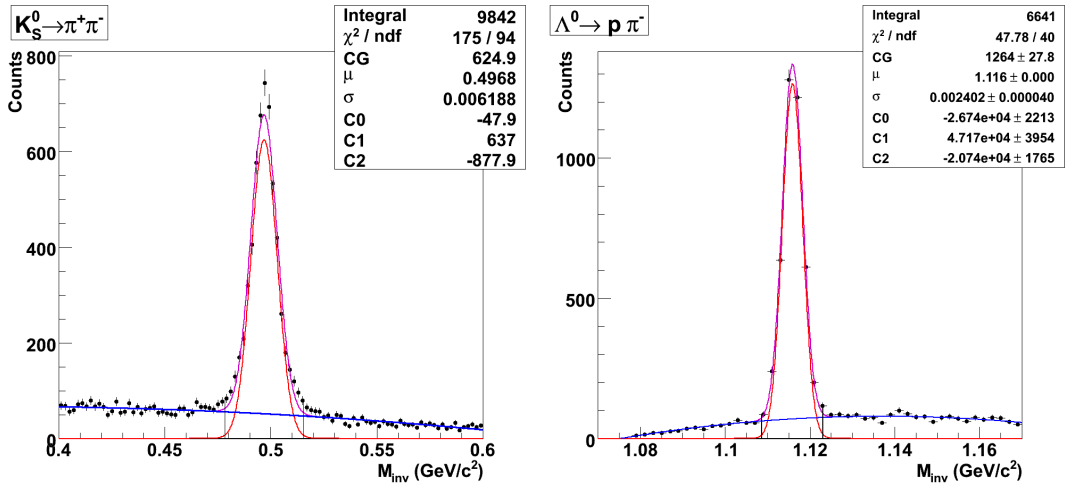

Fig. 5.22: Invariant mass distribution of daughters for $K_s{}^0$ and Λ decays.

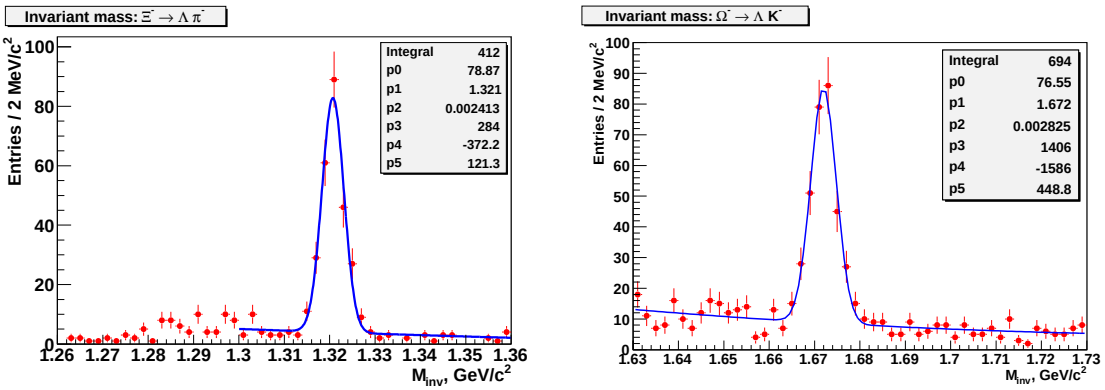

Fig. 5.23: Reconstructed invariant mass distribution of Ξ^- and Ω decays.

5.6 Particle identification with electromagnetic calorimeter

High time resolution of "Shaslyk" calorimeter makes this device appropriate for the effective particle identification. To estimate efficiency of identification and background contamination level we have took into account time resolution performance of the ECAL, the accuracy of particle momentum measurement by the whole detector MPD and track length measurement accuracy by the tracking system. The momentum resolution $dp/p = 2.5\%$ and time resolution $\sim$80 ps/$\sqrt{E_{cal}}$ were used for this test. The accuracy of the track length reconstruction was taken 1 mm. Selection criteria are defined as simple bound on the reconstructed particle mass distributions. Counting particles of a given type (N_i) inside the mass region we define as a right identified sample and a number of cases with particles of other types in this region ($N_{j,k,l}$) as a background contamination. As a result, identification efficiency we define as N_i/N_i^{tot} and background contamination as — $N_{j,k,l...}/N_i^{tot}$, where N_i^{tot} total (generated) number of particles of a given type.Results for electrons are presented in Fig. 5.24 and for pions, kaons and protons in Fig. 5.25.

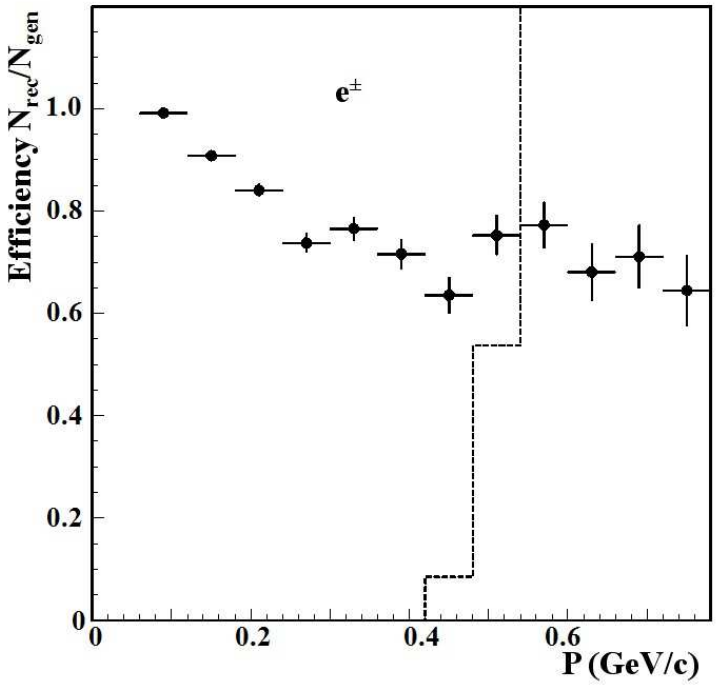

Fig. 5.24: Electron identification efficiency and background contamination level (line) as a function of electron momentum for the barrel region.

As it is seen from Fig. 5.24, on the basis of time-of-flight method electrons can be effectively identified only in the narrow low momentum region. From Fig.5.25 one can see that contamination level to the identified kaons is steeply increased for the momentum of particles more than $\sim$1.2 GeV/c and the momentum region where clean sample of kaons can be selected is restricted by this limit.

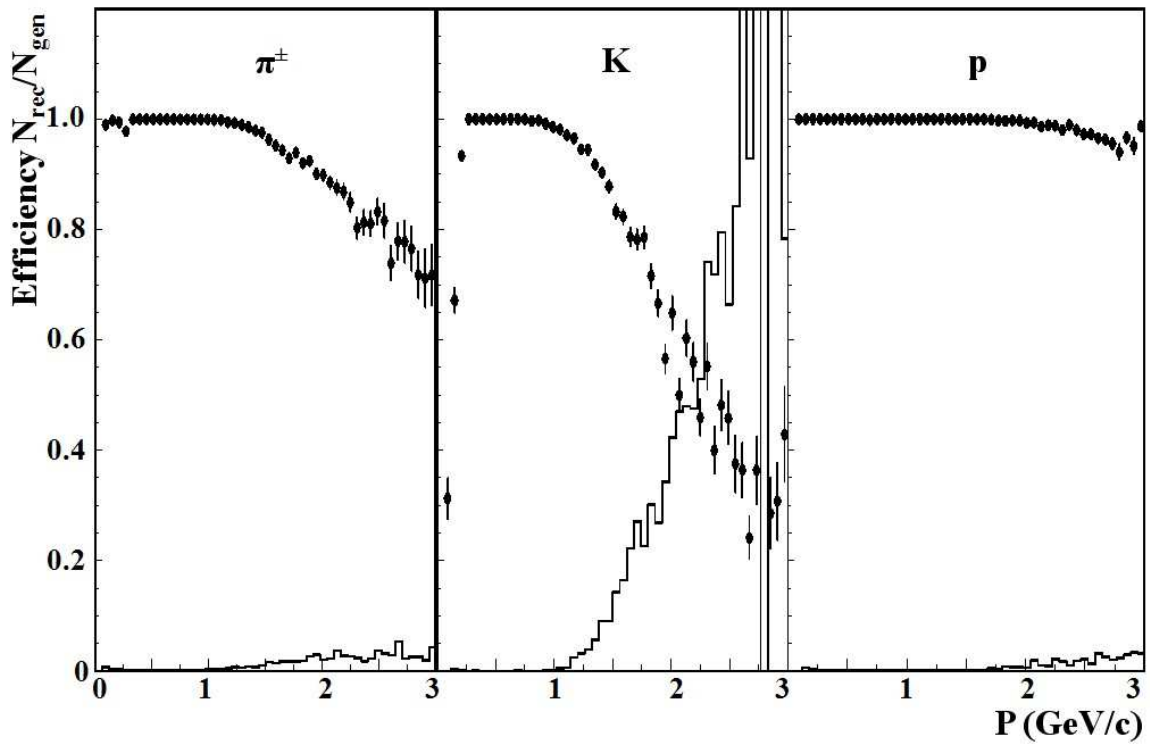

Fig. 5.25: Particle identification efficiency and background contamination level (red) as a function of particle momentum for barrel region.

Chapter 6

Physics Performance

6.1 Analysis of hadron spectra and yields in the MPD experiment

6.1.1 Introduction

Study of inclusive hadron production allows the extraction of the key properties of the system created in heavy-ion collisions. Thermodynamic quantities of the source such as kinetic and chemical freeze-out temperatures, collective flow velocity and the baryon chemical potential μ_B can be derived analyzing the invariant yields, ratios and transverse mass spectra of hadrons. Thus the accuracy with which the position on the phase diagram can be experimentally determined strongly depends on number of particle species precisely identified.

The key feature of the MPD detector that allows studying of hadron production (including the excitation function of the strangeness-to-entropy K/π-ratio) with the highest precision are:

- High event rate (up to 6 KHz) allows minimum bias trigger, so that we will be able to make very subtle measurements of the centrality dependence of any phenomenon under interest.
- MPD has full azimuthal coverage and will measure most of the momentum range in the pseudo-rapidity interval $-2 < \eta < 2$. This provides exceptional capabilities for hadron multiplicity studies.
- TPC for energy loss plus TOF for time-of-flight measurements with excellent parameters ($\sigma_{dE/dx} = 6 - 8\%,\ \sigma_{TOF} = 100$ ps) allow to select pure samples of particle species ($K,\ \pi,\ \bar{p}$ up to $p_t = 2$ GeV/c) and calculate their misidentification rates to highest accuracy.
- The combined tracking of the TPC and the silicon IT tracker provides precise primary vertex reconstruction leading to effective finding of secondary vertexes and tracks capabilities. IT gives a significant gain in efficiency at low p_t; its capabilities in V0-reconstruction are essential in corrections of hadron yields for the contribution from weak decays of hyperons.
- Electromagnetic calorimeter with good time and energy resolution gives extra opportunities — time-of-flight measurements of ECAL will increase efficiency of particle identification.

In the MPD experiment identification of hadrons is achieved via time-of-flight measurements in the barrel and end-cap TOF detectors. The TOF-barrel covers the pseudo-rapidity range of $|\eta| < 1.2$ (see Fig. 2.67) and the TOF identification capability allows

for 2.5σ π/K separation up to $p_t \approx 1.5$ GeV/c (see Fig. 2.65). The contamination of the misidentified particle species in kaons at $p_t < 1.5$ GeV/c is estimated to be less than 6% (see Fig. 5.8).

6.1.2 Analysis procedure

In this section, first results of Monte Carlo simulations aimed at studing of the overall MPD efficiency for hadron measurements and preliminary inclusive spectra of identified $\pi^{\pm}, K^{\pm}$ and p are presented. The analysis is based on 300 central $Au + Au$ collisions ($b < 5$ fm) at $\sqrt{s_{NN}} = 9$ GeV from the UrQMD event generator [302]. All the particles produced were tracked by GEANT3 through the 0.5 T magnetic field of the detector with all the important physical processes included. The interaction point was taken to be at the center of the MPD. The track reconstruction and momentum fitting method for the MPD TPC based on a Kalman-filter algorithm. All the reconstructed in the TPC tracks were then extrapolated to the TOF using the same (Kalman-fit based) method. The TPC-TOF matching efficiency does not vary within the pseudorapidity range $|\eta| < 1.2$ and is typically above 90% at $p_t > 0.5$ GeV/c (see Fig. 5.6). At low p_t, it drops down due to multiple Coulomb scattering in the detector material. The TOF response was simulated by smearing of the true (Monte-Carlo) time of flight with a Gaussian of 100 ps width. The following contributions to the TOF efficiency were considered:

- TPC track reconstruction efficiency
- occupancy effect (multihits in TOF)
- TOF geometrical acceptance
- TPC-TOF matching efficiency
- losses due to decay-in-flight
- secondary interactions in the detector material
- efficiency of the identification procedure

Mass-squared for each track candidate is calculated from reconstructed momentum (p), track length (L) and time-of-flight (T) as follows:

$$m^2 = p^2 \left(\frac{c^2 T^2}{L^2} - 1 \right) \tag{6.1}$$

where c denotes the speed of light.

Fig. 6.1 shows a mass-squared versus total momentum distribution for all the TPC tracks matched with the hits in the TOF-barrel. Particle identification (PID) method is based on a 2-dimensional function $F(p, m^2)$ which fits the distribution in Fig. 6.1 (F - parameterization-function). In order to get an appropriate functional form for the F, we assume that for each particle specie (i.e. π, K, p) the distribution in m^2 ($F(m^2)$) at a particular momentum p is Gaussian (with a momentum-dependent width), while for the $F(p)$ a Boltzmann distribution is a good choice. A typical m^2-distribution for one momentum slice ($p = 0.8 - 1.2$ GeV/c) is show in Fig. 6.2 (positively charged hadrons) together with the fit functions (shown by color dashed lines).

Fig. 6.3 (left panel) shows the Gaussian sigma for protons as a function of the total momentum. A polynomial fit to the data points is plotted by dashed line. The right panel in Fig. 6.3 demonstrates the momentum dependence of the Gaussian amplitude for protons (triangles) for which we used a Boltzmann function in p as a fit (shown by dashed line). Once that is done and the mixture of hadron species can be parametrized (in terms

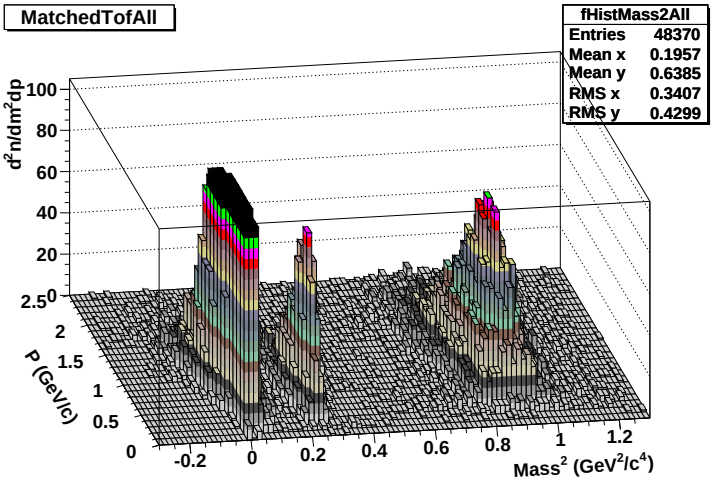

Fig. 6.1: Mass-squared for positive particles as a function of p. The top of the pion peak is cropped for clarity.

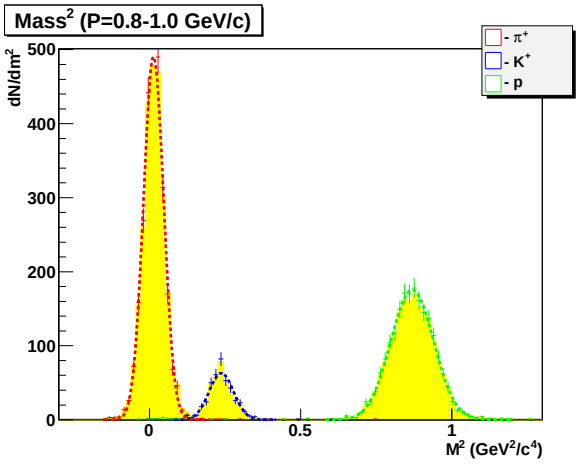

Fig. 6.2: Mass-squared for positive particles in the momentum slice $p = 0.8 - 1.2$ GeV/c. Gaussian fits are drawn by dashed lines.

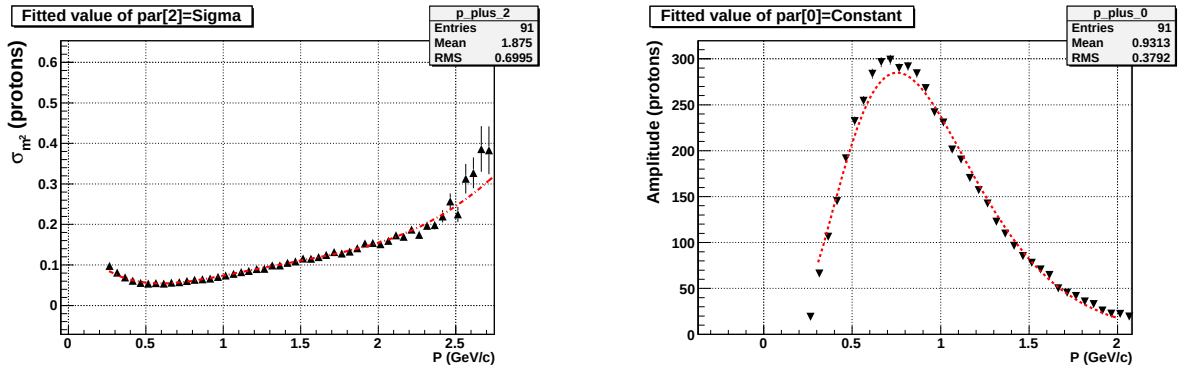

Fig. 6.3: Parameter σ (left panel) and amplitude (right panel) for protons as a function of p. Dashed lines demonstrate parameterizations used for the fit parameters (symbols).

of m^2 and p), we determine a set of probabilities p_i for a track gaining momentum p and mass-squared m^2 to be a particle of specie i ($i = \pi, K, p$) as the ratio:

$$p_i = \frac{F_i(m^2, p)}{\sum_{i=1}^{3} F_i(m^2, p)}, \tag{6.2}$$

where F_i is a function-parameterization for a specie.

Particles are selected using a 3σ momentum-dependent cut around the nominal m^2 position plus a requirement for a track to have a probability of particular particle specie p_i larger than 0.9. The losses due to this cut as well as contamination of misidentified particles are determined on the probability basis.

6.1.3 Corrections

The raw hadron yields are corrected for geometrical acceptance, decay in flight (for π- and K-mesons) and overall reconstruction efficiency (tracking, TOF matching and PID). The correction factors for the finite geometrical coverage of the TOF-barrel detector were obtained from the GEANT-based simulation of the MPD spectrometer. An uniform (box-like) phase space distribution of single hadron species was used as an input and all physics processes were taken into account, i.e. energy loss, multiple scattering and secondary interactions. Fig. 6.4 shows a geometrical acceptance (including decay in flight) of the MPD TOF detector for pions and kaons in terms of rapidity y and transverse momentum p_t. The corrections for decay in flight for pions and kaons exhibit strong dependence on p_t at low transverse momenta. The result of the simulation demonstrates that more than half of the kaons at $p_t < 0.5$ GeV/c decay inside the MPD spectrometer (Fig. 6.5). Track reconstruction efficiency was estimated to be above 99% for all phase space bins; the corrections for the TOF matching efficiency were obtained in bins of y and p_t and applied bin-by-bin.

In the low-p_t region secondaries from hadronic interactions with the material as well as from weak decays are the main source of the background contribution for pions and protons. Using TPC information alone, this background contamination can not be effectively eliminated. Reconstruction of secondary interactions or decay vertexes requires information from the silicon inner tracker (IT) which provide tracks with few very precisely measured points near this interaction (or decay) vertex. For this study, the contribution to

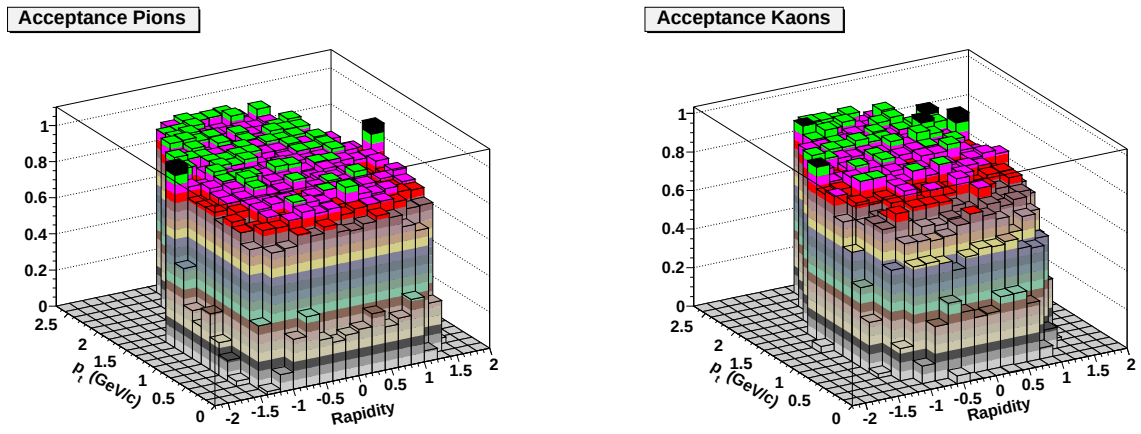

Fig. 6.4: Geometrical acceptance of the MPD TOF-barrel in terms of y and p_t for pions (left panel) and kaons(right panel). Magnetic field B=0.5 T. Decay in flight is taken into account.

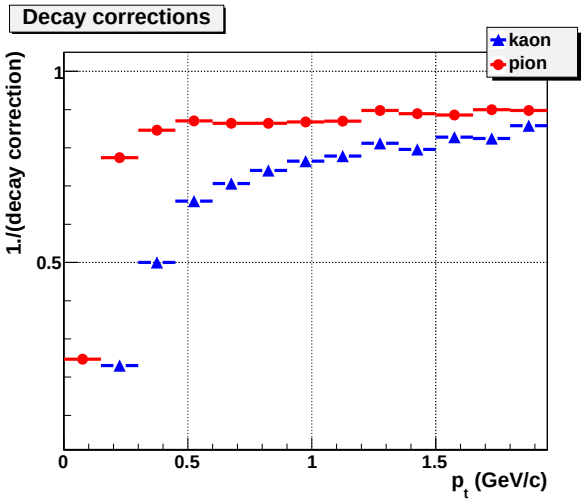

Fig. 6.5: Inverse corrections for decay for pions and kaons as a function of p_t.

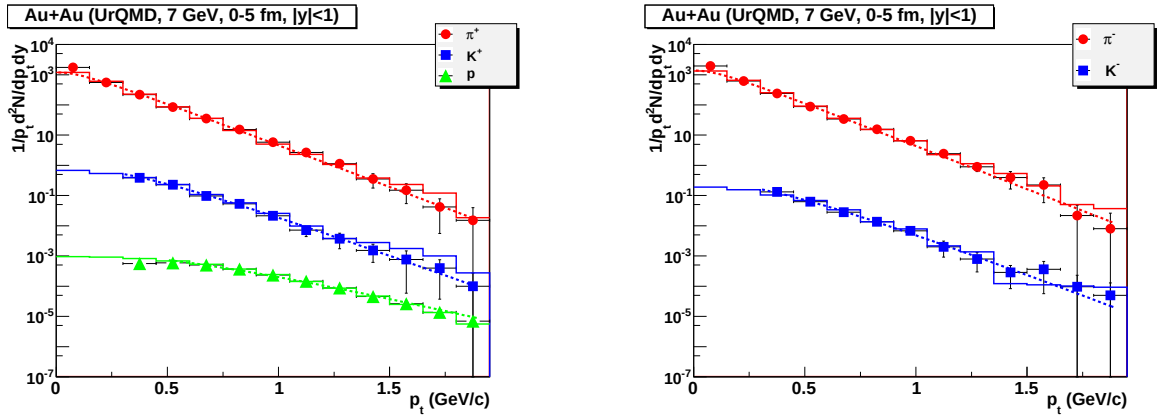

Fig. 6.6: Transverse momentum spectra of $\pi^{\pm}$, $K^{\pm}$ and p in 5% central Au+Au collisions at $\sqrt{s} = 9$ GeV (UrQMD). The reconstructed spectra are depicted by symbols, the input (UrQMD) spectra are plotted as solid lines. The error bars are statistical only. Exponential fits are shown by dashed lines.

the pion and proton yields from weak decays and secondary interactions (about 10%) was subtracted using information from GEANT. Primary and secondary electrons, positrons and muons reconstructed in the TPC can not be identified by TOF measurements only. The contamination of these particle species (as estimated from Monte-Carlo simulations) was found to be of the order of 5%.

6.1.4 Hadron spectra

Fig. 6.6 shows the invariant spectra of charged hadrons ($\pi^{\pm}$, $K^{\pm}$ and p) as a function of transverse momentum p_t for the central rapidity bin ($|y| < 1$). Reconstructed p_t-distributions are depicted by symbols, while the input (UrQMD) spectra are plotted as solid-line histograms. The reconstructed invariant distributions are fitted to an exponential in m_t function ($m_t = \sqrt{p_t^2 + m^2}$):

$$\frac{1}{p_t}\frac{d^2n}{dp_t dy} = A \cdot exp(-m_t/T), \tag{6.3}$$

where m is the rest mass. The exponentials have two parameters labeled A and T. The extracted slope parameter T ("effective" temperature) is tabulated in Table 6.1 for all the analyzed hadron species. The difference between the parameters for the reconstructed and UrQMD spectra ("true slope") is found to be 4, 9 and 8 MeV for π, K and p, respectively. Using the extracted values of the fit parameters, the hadron yield per unit of rapidity dn/dy was calculated as follows:

$$dn/dy = AT(m + T) \tag{6.4}$$

The yields are also tabulated in Table 6.1; the quoted errors for dn/dy are obtained by propagating the errors of the fit parameters A and T.

The K/π-ratio at midrapidity was estimated to be 0.17 ± 0.02. A direct comparison of the model predictions with the experimental data was not among the goals of this study. Nevertheless, a qualitative agreement with the data shown in Fig. 1.12 demonstrates a very good performance of the MPD for hadron measurements as well as a reliability of the developed reconstruction and analyses methods.

Table 6.1: Slope parameters (T) and midrapidity yields (dn/dy) for hadrons.

hadron specie	T	dn/dy
π^+	157 ± 4	55.5 ± 1.5
K^+	160 ± 9	9.3 ± 0.7
p	237 ± 7	34.6 ± 1.1
π^-	151 ± 4	60 ± 1.5
K^-	153 ± 11	2.8 ± 0.4

6.1.5 K/π-ratio

As it was argued in Section 1.3, study of the relative strangeness yield via the K/π-ratio is a valuable diagnostic tool for investigating the strongly interacting matter. The results of the analysis described in the previous section demonstrates that even for a data set of 300 central $Au + Au$ collisions the acceptance and PID performance of the MPD detector allow us to measure hadron spectra up to $p_t = 1.5$ GeV/c. A rough estimate of the event sample volume required to accomplish the goal of the systematic study of K/π ratio as a function of collisions energy, rapidity, transverse momentum and rapidity has been performed. We use as a base for the estimate an event sample of $2 \cdot 10^6$ 1% central $Au + Au$ collisions, which allow sufficient counting statistics for both integrated hadron yield measurements and event-by-event studies. Assuming the luminosity of $10^{27}\ cm^{-2}c^{-1}$ and the event rate of 6 kHz, we will be able to collect the desired event sample within a day of beam time (considering 50% duty period). A program which include measurements at several energies (8-10 points) in the center-of-mass energy range from 4 to 11 GeV takes about 240-250 hours of beam time. Comprehensive exploration of the strangeness production mechanism (in particular, K/π ratio) is planned to be carried out by varying not only collision energy and centrality, but also extending the system-size dependence by colliding nuclei with different atomic numbers A. These studies of evolution of the K/π "horn" and "plateau' observables with the size of colliding system (such a possibility and a nomenclature of the beams available at the NICA collider is under discussion), and, probably, direct observation at some energy-system combination of the onset of these effects will stimulate the theory of strong interactions.

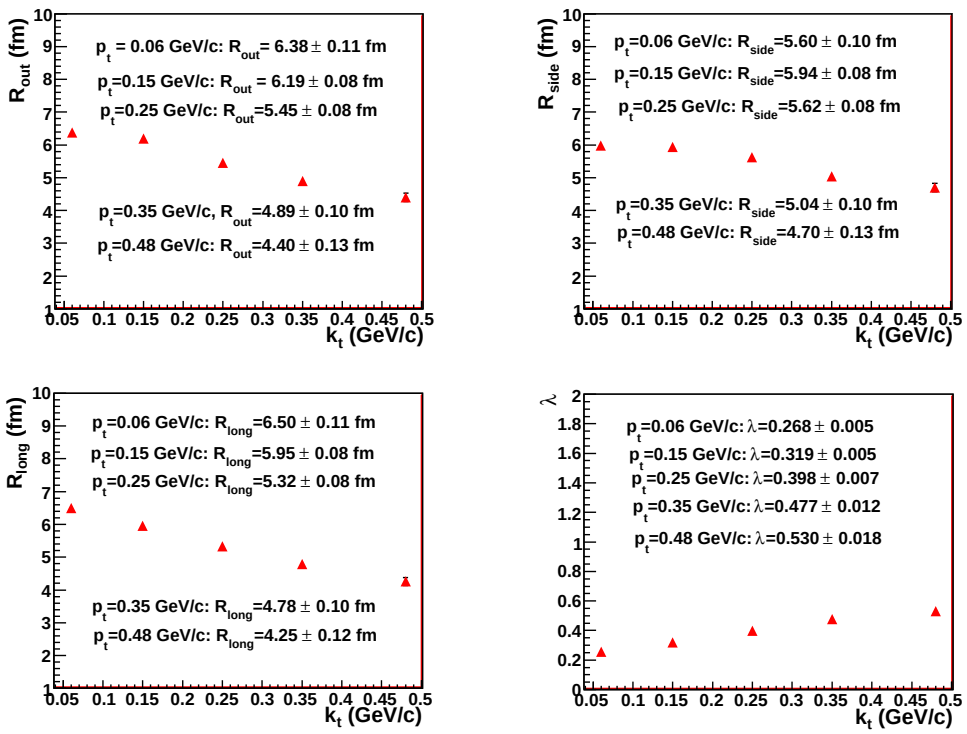

Fig. 6.7: The $\pi^-\pi^-$ correlation radii and the suppression parameter λ at mid-rapidity in central 0−7% Pb+Pb collisions at $\sqrt{s_{NN}} = 6.3$ GeV calculated with FASTMC [18] in different intervals of the pair transverse momentum k_t, 10^5 events, STAR-like procedure of fitting the correlation function is used.

6.2 Study of femtoscopy

6.2.1 Estimation of the exposition time for a study of femtoscopy correlations.

The event generator of heavy ion collisions based on a parametrization of a hadron freeze-out hyper-surface and statistical approach FASTMC [18]-[303] was used to simulate 10^5 PbPb events at $\sqrt{s_{NN}} = 6.3$ GeV with centrality $0-7\%$. The data of NA49 collaboration on particle yields, m_t spectra and $dN/d\eta$ were used for tuning the model parameters. The STAR (ALICE) collaboration procedure [106, 107] for the 3D fit of the correlation functions was applied in the analysis of simulated data to determine the three correlation radii and correlation strength parameter λ in several intervals of k_t (Fig. 6.7). The obtained statistical errors of the correlation radii are $\sim 10\%$. In Fig. 6.8, the projections of 3D $\pi^-\pi^-$ correlation function integrated over all k_t bins and the corresponding radii $R_{out}, R_{side}, R_{long}$ are shown.

One may see that $\sim 1 \times 10^5$ events is enough for measurement of the three $\pi^-\pi^-$ correlation radii in five points at k_t at $\sqrt{s_{NN}} = 6.3$ GeV with statistical errors less 10 %. Note that NA49 collaboration analyzed $\sim 3.6 \times 10^5$ events (0-7% centrality, Pb+Pb interactions) at $\sqrt{s_{NN}} = 6.3, 7.7, 8.8$ GeV in order to measure the $\pi^-\pi^-$ 3D-correlation functions at 5 k_t points with statistical error $\sim 10\%$ [101].

We estimate the overall MPD efficiency to be about $\sim 50\%$. The data sample as large

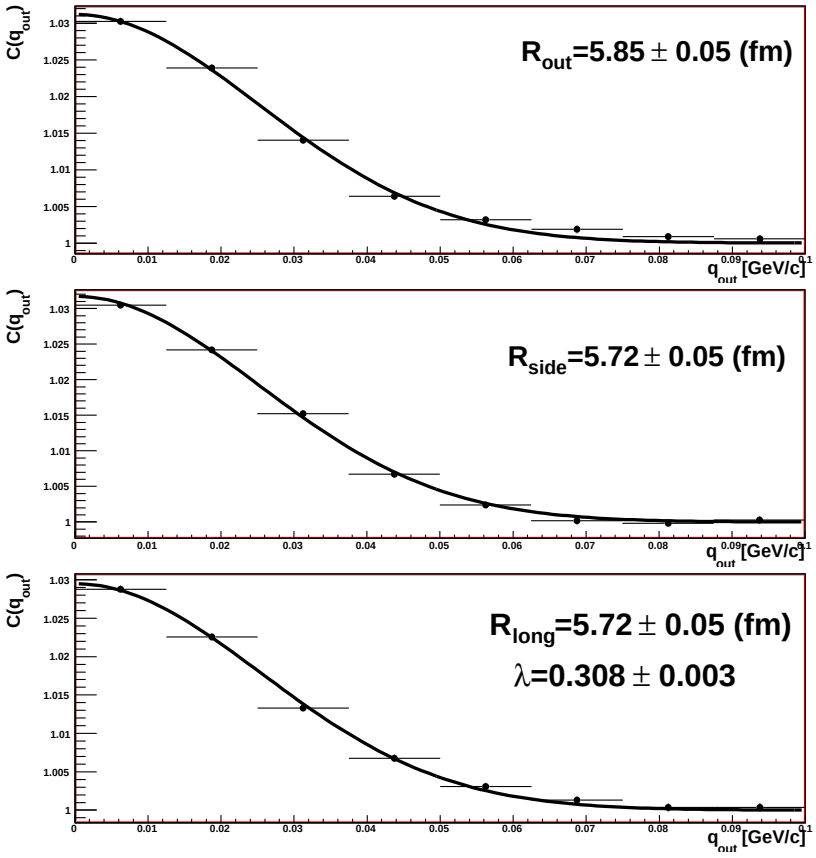

Fig. 6.8: The projections of 3D $\pi^-\pi^-$ correlation function shown in figure 6.7 on $Q_{inv}, Q_{out}, Q_{side}, Q_{long}$, integrated over all k_t bins.

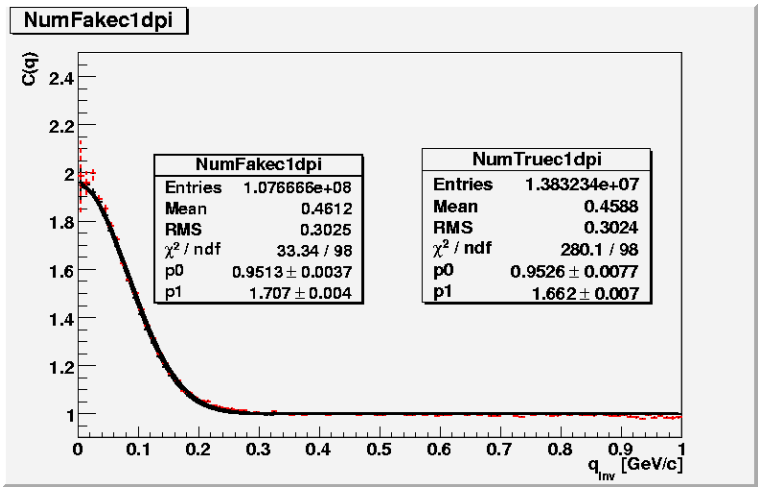

Fig. 6.9: The $\pi^-\pi^-$ CF simulated (NumFake1dpi) and reconstructed (NumTrue1dp) with Gaussian distributed coordinate in Pair Reference Frame(PRF) with r_0= 2 fm.

as 200kEv is enough for measurement of 3D $\pi\pi$ CFs with the statistical errors $\sim 10\%$ at 5 points in k_t at $\sqrt{s}_{NN} = 6.3$ GeV. We suppose for NICA:
Luminosity (Au beam): $L = 10^{27} cm^{-2} c^{-1}$
σ_{tot} (Au+Au) = 6.8 b
Trigger centrality: 10 % (ϵ=0.1)
Collision rate for central events = $(\sigma \times L \times \epsilon) = 700$ Hz (events/s)
It is possible to get $\sim 2 \times 10^5$ events during hours ! One week is enough for a study of the $\pi\pi$ correlation function with respect to the reaction plane.

Such a fast data taking opens a good perspective for a study of rare processes. Various particle systems which can in principle be studied in NICA are listed in Table 1.3. The yields of corresponding particle species are listed in Table 1.2. The correlations of multistrange baryons Ξ, Ω with π can be studied during the reasonable time of several mounths.

6.2.2 Momentum correlations in MPD enviroment.

The most of femtoscopy observables will be measured in the main part of the MPD tracking system: the Time Projection Chamber (TPC) and the Inner Tracker (IT) of silicon strip detectors. Particle identification (PID) will be done by the energy loss measurements in TPC (TPC+IT) and the time of flight measurements in TOF.

The simulated and reconstructed correlation functions with Gaussian distributed coordinates in the Pair Reference Frame(PRF) with all radii $\sim$ 2 fm for $\pi\pi$ are show in Fig. 6.9. The momentum resolution is taken as $\Delta p/p = 1\%$.

The effects of hit clustering, track overlapping, track splitting are especially dangerous for the analysis of femtoscopy correlations of *identical* particles at small relative momenta. A detailed simulations are necessary to eliminate the influence of systematic distortions; the statistical errors will be negligible in most cases ($\pi\pi$, KK...). The non-identical particles with close velocities are well separated in the detector magnetic field and the systematic errors due to the close tracks are absent here.

Track splitting causes an enhancement of pair rate at low relative momentum q. False

pair is created by single tracks reconstructed as two with similar momenta. To remove effect of split tracks STAR collaboration compare the location of the hits for each track in the pair along the pad rows in the TPC and assign a quantity to each pair, called splitting level (SL) calculated as follows [106, 107]:

$$SL = \frac{\sum S_i}{N_{hits1} + N_{hits2}} \tag{6.5}$$

where $S_i = +1$ if only one track has a hit on pad-row, $S_i = -1$ if both tracks have hits on pad-row, $S_i = 0$ neither track has a hit on pad-raw.

Every pair is required to have SL smaller than a certain value determined in a study of the influence of the cut on the one-dimensional correlation function.

After removing split tracks, they studied the effects of two particles reconstructed as one track. These merged tracks cause a reduction of the pair rate at low relative momentum because the particles that have higher probability of being merged are those with similar momenta. To eliminate the effect of track merging, they required that all pairs entering numerator and denominator of the correlation function had a fraction of merged hits no larger than 10%.

One should mention that STAR did not use IT. The MPD setup is supposed to be equipped with IT. The strip pitch of double side silicon detector is 100 nm, so the two track resolution should be ≈ 200 nm and the effect of splitting or merging will be an order of magnitude less.

There is a similar special set of cuts removing the double track resolution effects used by ALICE collaboration [304]. Besides the above mentioned cuts, a cut on the particle separation at the entrance to the TPC is used to remove the "merging" effects.

The effective particle identification (PID) is especially important for kaon femtoscopy.

6.3 Electromagnetic probe estimations

6.3.1 Thermal photons

The thermal photon yield is relatively small in comparison to the inclusive (π^0 and η decays) photon yield, but the spectral characteristics of this photons are different at low collision energy. This behavior arises from the softer π^0 spectra. In contrast with study at a high collision energy, photons with 1 GeV/c $< p_T <$ 3 GeV/c at the NICA energies much more background free (Fig. 6.10) and careful study of real photons with $p_T >$ 1 GeV/c is rather challenging.

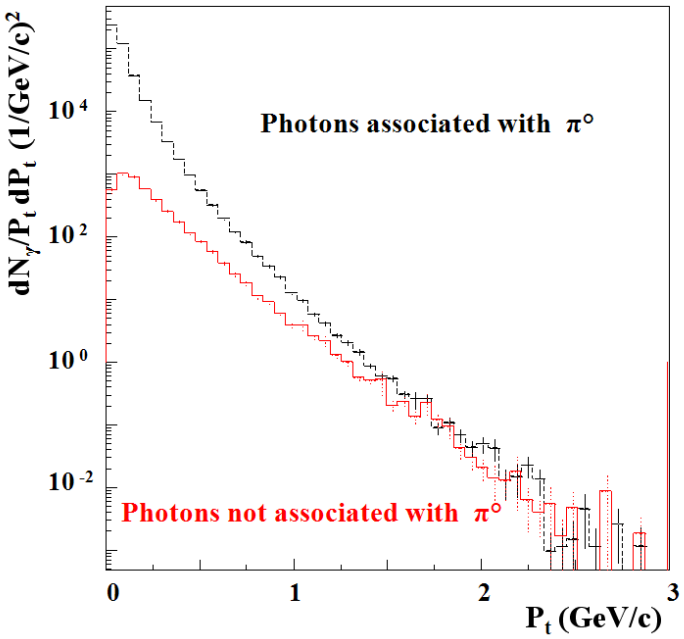

Fig. 6.10: Au+Au events are generated by UrQMD generator at $\sqrt{s_{NN}} = 9$ GeV p_T spectra of the photons detected by MPD electromagnetic callorimeter. Photons creating object with invariant mass close to the π^0 mass are associated to π^0 and plotted in black. The rest of photons are plotted in red.

Monte-Carlo study at the NICA energy shows that the slope and cross-section of the p_T spectra of real photons can be reconstructed with high precision down to a very low intensity (Fig. 6.11).

After subtraction of photons associated with π^0 and application of the selection efficiency, parameters of extra spectra are calculated and plotted with error bars which include statistics and efficiency corrections uncertainties.

These tests confirm, that this region of p_T for the photons, noted as an interesting region for both theoretical and experimental studies (Fig. 1.20), can be well investigated at the NICA energies by the MPD detector.

6.3.2 Low-mass e^+e^- continuum in nuclear collisions

Dielectron production in heavy ion reactions is an ideal tool for probing the fireball interior as electrons do not undergo strong interactions in the medium. Theory predicts that the

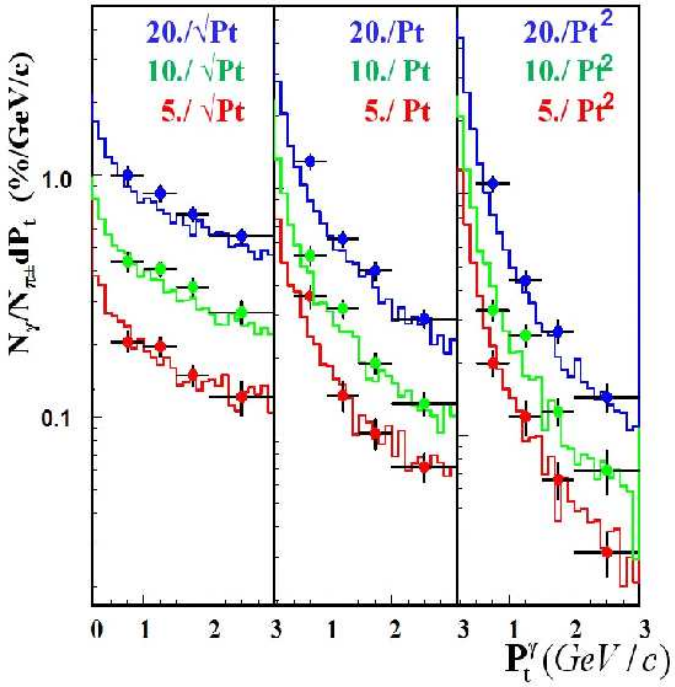

Fig. 6.11: Extra photons have been generated with different p_T dependent intensity for the extra source and were added to the generated by the UrQMD Au+Au events ($\sqrt{s_{NN}}$ = 9 GeV). Slope and intensity of these photons are plotted by solid lines.

masses or/and widths of light vector mesons might be affected by the strongly compressed nuclear matter, in this respect experimental observation of possible modifications of the dielectron mass spectrum in heavy-ion collisions relative to that from elementary nucleon-nucleon interactions are of particular interest (see Section **??**). The low mass region of the e^+e^- spectrum ($M_{e^+e^-} < 1$ GeV/c^2) will be explored extensively at NICA/MPD at energies $\sqrt{s_{NN}} = 4 - 11$ GeV, thus detailed information about possible in-medium modifications of the hadron properties can be obtained. However, extraction of dilepton signal in a high multiplicity environment is a challenging experimental task. Since pions are the most abundant final-state hadron species, ability of the particle identification (PID) system to strong pion suppression is of crucial importance. Moreover, a large combinatorial background comes from 3-body Dalitz decays of π,η-mesons as well as from γ conversion in the detector material. Thus, an additional optimization of the design of the apparatus aimed at minimization of the material budget is required. Also, further development of the reconstruction algorithms for finding of secondary vertices is important.

The MPD design setup does not include a sub-detector for an exclusive electron selection (as RICH Cherenkov counters). Instead, a combination of standard identification techniques used for hadron identification in MPD, namely: time-of-flight (TOF) and ionization loss (dE/dx) measurements complemented by electromagnetic calorimetry will allow us to identify electrons.

Generation of the Monte Carlo dielectron data set. The simulation analysis is based on 20M events for 5% the most central Au+Au collisions at $\sqrt{s_{NN}} = 7$ GeV. An input for the Monte Carlo was provided by the Pluto simulation package [305]. This gen-

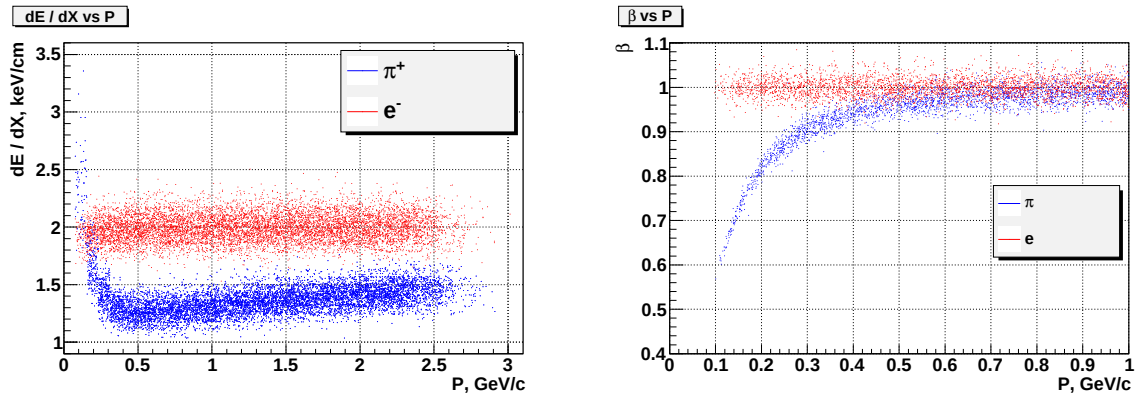

Fig. 6.12: (Left) Energy losses dE/dx in the TPC gas as a function of the total momentum for electrons and pions. (Right) Momentum dependence of β ($\beta = \frac{v}{c}$) for e and π

.

erator has been developed to properly describe e^+e^- spectra originated from electromagnetic decays of hadrons produced in elementary (p+p, p+A) as well as central heavy-ion collisions. A final-state hadron composition, (i.e. 'cocktail' of $\pi, \eta, \eta', \rho, \omega$ and ϕ mesons) was simulated using experimental data on meson production (if available) or a parameterization from the hadron string (or thermal) models. The respective decay properties of each species are described in accordance to decay kinematics and the known branching ratios, here only the direct decays to e^+e^- or Dalitz decays (for example, $\pi^0 \to \gamma e^+e^-$ or $\omega \to \pi^0 e^+e^-$) were simulated. The output from the Pluto generator was mixed with 10k of Au+Au events from the UrQMD generator using proper weighting procedure. The prepared in such a way Monte Carlo data were propagated through the MPD experimental set-up by GEANT and reconstructed within the MpdRoot framework.

Track selection criteria. Electrons were analyzed within the momentum range $0 < p < 2.5$ GeV/c and the pseudorapidity interval $|\eta| < 1.2$. It is required that each track has more than 20 reconstructed in the TPC points. Also, the distance of closest approach (DCA) to the reconstructed collision vertex in the transverse plane (x, y coordinates) was required to be less than $3\sigma_{x,y}$, where $\sigma_{x,y}$ are the RMS of the DCA x, y-distributions.

Electron identification. Identification of electrons was done using combined dE/dx (in the TPC gas) and TOF measurements. A distribution of the dE/dx energy losses in the TPC gas for electrons and pions is shown in Fig. 6.12 (left panel) as a function of the total momentum p. At $p > 0.3$ GeV/c the dE/dx-losses for electrons saturate at $dE/dx \approx 2$ (plateau Fermi), so a low-limit dE/dx-cut cut ($dE/dx > 1.7$) is used for $e^{\pm}$ selection. A designed MPD TPC performance (dE/dx resolution of about 8%) allows for more than 3σ e/π separation for such a cut.

At low momenta ($p < 0.3$ GeV/c) electrons are identified using time-of-flight information. The MPD TOF system with the overall time resolution of about $\sigma_{TOF} \approx 100$ ps will provide a good e/π-separation at $p < 0.3$ GeV/c (Fig. 6.12, right panel).

Figure 6.13 (left panel) demonstrates electron identification efficiency as a function of total momentum p. The observed drop in the efficiency at low momenta is explained by a large fraction of the spiral electron tracks having the inverse curvature smaller than the

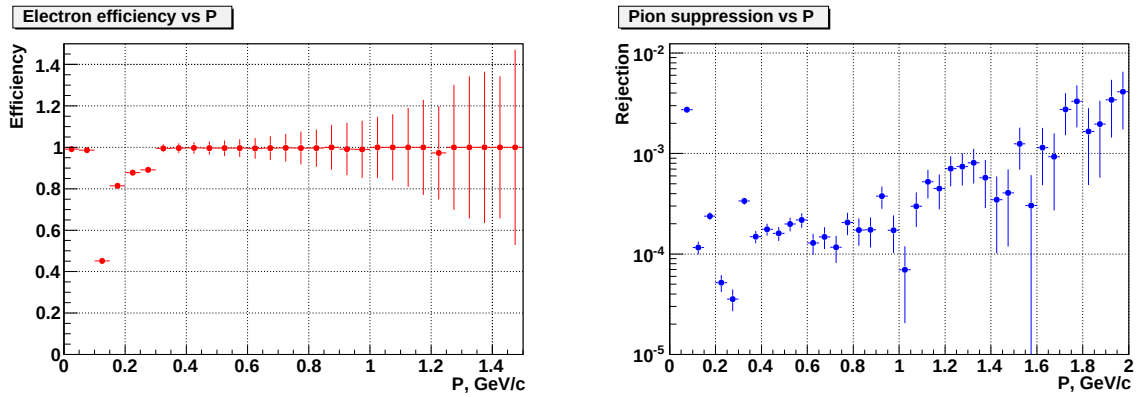

Fig. 6.13: (Left) Efficiency of electron identification by dE/dx-TOF information as a function of the total momentum p. (Right) Pion suppression factor versus p for the electron identification cuts (see text for detail)

radius of the TOF barrel (no TOF hits). It is obvious that the TOF efficiency for electrons at low p might be increased by decreasing the magnetic field inside the MPD solenoid; the optimal value will eventually come out after detailed Monte Carlo simulations.

A momentum dependence of the pion suppression factor (number of pions survived the electron PID cuts relative to the total number of pions in a particular momentum bin) is shown in Fig. 6.13 (right panel). Pion suppression up to the level of 10^{-4} is achieved at $p < 1$ GeV/c using only the dE/dx and TOF information, some extra suppression factor is expected exploiting the information from the electromagnetic calorimeter ECAL.

Inclusive $M_{e^+e^-}$ mass spectra. Invariant mass spectrum of e^+e^- pairs was reconstructed for the sample of tracks survived after all the quality cuts and identified as electron candidates. In each event all possible pair combinations are constructed for the unlike-sign tracks. For each pair $M_{e^+e^-}$ is calculated (neglecting the electron mass) as

$$M_{e^+e^-} = \sqrt{2 \cdot p_{e^+} \cdot p_{e^-} \cdot (1 - \cos\theta_{e^+e^-})},$$

where p_e is the electron momentum and $\theta_{e^+e^-}$ is the angle between the tracks in a pair. In order to remove dielectron pairs from γ conversions which occur in the detector material, two additional kinematic and topology constrains were applied to the pair candidates, namely: an upper-limit cut on the radial position of the reconstructed V0 pair vertex ($R_{V0} < 4$ cm) and a low-limit cut on the angle ψ between the vector normal to the plane of the pair momenta and the direction of the magnetic field $\cos\psi < 0.5$. The inclusive mass spectra for the unlike-sign electron pairs N_{+-} is shown in Fig. 6.14 (left panel). The combinatorial background from the uncorrelated electron pairs was determined by twice of the geometrical mean for like-sign pairs (assuming the Poisson probability distribution for e^{+-} multiplicities)

$$N_{Bkb.} = 2 \cdot \sqrt{N_{++} \cdot N_{--}},$$

where N_{++}, N_{--} are the numbers of the like-sign pairs. The resulting net dielectron mass spectrum after subtraction of the background normalized to the number of events (physics signal) is shown in Fig. 6.14 (right panel). Here the reconstructed mass spectrum shown by symbols and the integral contribution from the hadronic decay cocktail from

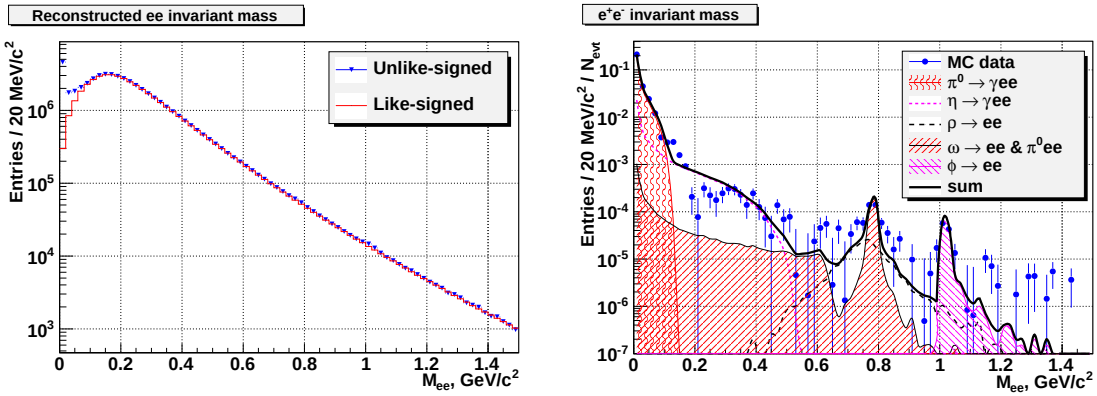

Fig. 6.14: (Left) Invariant mass spectrum of unlike-sign pairs (blue symbols) and the combinatorial background (red histogram). (Right) Background subtracted dielectron mass distribution with individual contributions from meson decays.

the Pluto generator is depicted by the solid black line. Also shown are the individual mass distributions from all the sources which contribute to the spectrum.

The reconstructed mass spectrum requires corrections for the geometrical acceptance, reconstruction and identification efficiencies. The process of determination of these correction factors is in progress. A rough estimate of a mass resolution which might be achieved in MPD was made by a fit (a Gaussian for the signal plus a polynomial function for the background) in the M_{ee} window at the ω-meson mass. The fit gives a result for the $\sigma_{M_{ee}}$ of about 13 MeV.

6.3.3 Conclusion

At the NICA energy both electromagnetic probes, virtual and real photons, can be effectively studied. Due to the high luminosity, right collision energy choice, 4π detector acceptance and high detector efficiency, data with statistical uncertainty below few percent can be collected during about one week run. Systematical errors will become the main source of uncertainty and should be carefully studied. But the simultaneous study of two different channels (l^+l^-, γ) carrying similar information concerning fundamental properties of hot and compressed matter will enable to reduce remaining systematic uncertainty and make an uncertainty cross-checks.

Chapter 7

MPD Project Cost and Timelines

Timetable of the MPD works of is shown in table 7.1. The timetable includes only the global milestones such as: Technical Design Report preparation, R & D of all subdetector elements, their full scales prototypes tests, subdetector construction and installation. The detailed timetables from each subdetector group available. The global approach of the MPD Collaboration is to start experiment as soon as beam collision available. The minimal set of instrumentation includes TPC, TOF barrel and ZDC with FFD. With these detectors we are able to start solving many of our physical tasks. The first group detectors which start experimental program MPD are those which are included in the barrel part.

A preliminary cost of the first stage program is presented in table 7.2. The presented numbers are calculated as sums of the subdetetector element cost. However, those estimations are based on different approaches taking into account different stages of R & D, which are either already available or just staring from scratch. We include the inner tracking system in the first stage due to MPD capability motivation. However we did not evaluate its cost. The group has well progressed strong collaboration which as we expect will share responsibility for its construction in the future.

Timetable of MPD construction and commissioning

	Stage/Year	1	2	3	4	5	Total
	Budget profile for MPD ----→	1080	12500	15500	9300	2560	**40940**
1	**Experimental Hall**						
	NICA Hall Construction						
	Electricity,water & infrastructure						
	Crane(construction & certification)						
2	**Superconducting Magnet**						
	Magnet TDR and Tender						
	Call for Tender-Yoke,SC,trim coils						
	Contracts signing						
	Construction of Iron York & SC						
	Transportation						
	Cryogenics for Solenoid						
	Assembling & Commiss. of Solenoid						
	Field measurements						
3	**TPC**						
	TPC Assembling workshop						
	TPC Construction						
	TPC tests						
	TPC installation and Commissioning						
4	**TOF**						
	TOF Assembling area						
	Test area of TOF mRPC						
	TOF Mass Production and test						
	TOF installation & Commissioning						
5	**ECal modules production**						
	ECal Assembling in sectors						
	ECal installation & Commissioning						
6	**ZDC construction and installation**						
7	**Electronics, Network and**						
	DAQ production &implementation						
	Control Room construction						
	Slow Control system implementation						
	Computing for Data taking & network						
8	**Detector Assembling**						
9	**Commissioning and Cosmic Tests**						

Start up minimum

Table 7.1: Timetable of the MPD works

Subdetector	Cost of the start up minimum (k$)
Magnet yoke and solenoid	9800
Time-projection chamber (TPC)	8600
Time-of-flight detector (TOF barrel)	4000
Data acquisition and control system	5300
Electromagnetic calorimeter	7000
Zero-Degree calorimeter (ZDC)	940
Fast Forward Detector (FFD and BBC)	1300
Infrastructure and computing	4000
Silicon Inner Tracker (IT)	
Total:	40940

Table 7.2: First stage cost estimation

Acknowledgements

We are grateful to M.N.Chubarov for the help in preparation of the present document and to I.V.Shpak and L.G.Ignatova for technical assistance.

Bibliography

[1] A. N. Sissakian, A. S. Sorin, M. K. Suleimanov, V. D. Toneev, and G. M. Zinovjev, Proceedings of the 8th International Workshop 'Relativistic Nuclear Physics: From Hundreds MeV to TeV', Dubna 2005, Russia, 306 (2006), nucl-th/0511018.

[2] A. N. Sissakian, A. S. Sorin, M. K. Suleimanov, V. D. Toneev, and G. M. Zinovjev, *Bogoliubov Laboratory 50 years* (JINR, 2006), pp. 73 – 95, nucl-ex/0601034.

[3] A. N. Sissakian, A. S. Sorin, M. K. Suleimanov, V. D. Toneev, and G. M. Zinovjev, Part. Nucl. Lett. **5**, 1 (2008), nucl-ex/0511018.

[4] A. N. Sissakian, A. S. Sorin, and V. D. Toneev, Proceedings of the 33rd International High Energy Physics conference, ICHEP'06, Moscow, Russia **1**, 421 (2006), nucl-th/0608032.

[5] A. Sissakian *et al.*, *Design and Construction of Nuclotron-based Ion Collider fAcility (NICA), Conceptual design report* (JINR, Dubna, 2008).

[6] N. Bogolubov, B. Struminsky, and A. Tavkhelidze, JINR D-1968, Dubna (1965).

[7] A. Tavkhelidze, High Energy Physics and Elementary Particles, Vienna , 753 (1965).

[8] Z. Fodor and S. D. Katz, JHEP **04**, 050 (2004), hep-lat/0402006.

[9] M. A. Stephanov, PoS **LAT2006**, 024 (2006), hep-lat/0701002.

[10] G. S. F. Stephans, J. Phys. **G32**, S447 (2006), nucl-ex/0607030.

[11] P. Senger, J. Phys. **G30**, S1087 (2004).

[12] A. Sissakian *et al.*, *The MultiPurpose Detector (MPD) to study Heavy Ion Collisions at NICA. Letter of Intent* (JINR, Dubna, 2008).

[13] NA49, B. Lungwitz *et al.*, PoS **CPOD07**, 023 (2007), 0709.1646.

[14] A. S. Khvorostukin, V. V. Skokov, V. D. Toneev, and K. Redlich, Eur. Phys. J. **C48**, 531 (2006), nucl-th/0605069.

[15] V. A. Matveev, R. M. Muradian, and A. N. Tavkhelidze, Nuovo Cim. Lett. **7**, 719 (1973).

[16] M. Strikman, (2007), 0711.1625.

[17] M. Bleicher *et al.*, J. Phys. **G25**, 1859 (1999), hep-ph/9909407.

[18] N. S. Amelin *et al.*, Phys. Rev. **C74**, 064901 (2006), nucl-th/0608057.

[19] J. L. Klay *et al.*, J. Phys. ReV. **C 68**, 054905 (2003).

[20] NA49, C. Alt *et al.*, Phys. Rev. **C77**, 024903 (2008), 0710.0118.

[21] E. L. Bratkovskaya *et al.*, Phys. Rev. **C69**, 054907 (2004), nucl-th/0402026.

[22] M. Stephanov, K. Rajagopal, and E. V. Shuryak, Phys. Rev. **D60**, 114028 (1999).

[23] J. Kapusta and A. Mekjan, Phys. Rev. **D33**, 1304 (1986).

[24] M. Gazdzicki, M. Gorenstein, and S. Mrowczynski, Phys. Lett. **B585**, 115 (2004).

[25] M. A. Stephanov, Prog. Theor. Phys. Suppl. **153**, 139 (2004), hep-ph/0402115.

[26] C. Alt *et al.*, (2008), nucl-ex/0808.1237v2.

[27] M. Stephanov, Nucl. Phys. **A698**, 523c (2002).

[28] NA49, C. Alt *et al.*, Phys. Rev. **C 78**, 034914 (2008).

[29] NA49, K. Grebieszkow, (2008), nucl-ex/07074608v2.

[30] D. E. Kharzeev, L. D. McLerran, and H. J. Warringa, Nucl. Phys. **A 803**, 227 (2008), arXiv:0711.0950.

[31] K. Fukushima, D. E. Kharzeev, and H. J. Warringa, Phys. Rev. **D 78**, 074033 (2008), arXiv:0906.2808.

[32] D. Kharzeev, R. Pisarski, and M. Tytgat, Phys. Rev. Lett. **81**, 512 (1998).

[33] D. Kharzeev, Phys. Lett. **B 633**, 260 (2006), arXiv:0406125.

[34] S. Voloshin, Phys. Rev. **C70**, 057901 (2004).

[35] STAR, S. Voloshin, arXiv:0806.0029.

[36] P. Buividovich, M. Chernodub, E. Luschevskaya, and M. Polikarpov, arXiv:0907.0494v2.

[37] D. Kharzeev and R. Pisarski, Phys. Rev. **D61**, 111901 (2000).

[38] J. Rafelski and B. Muller, Phys. Rev. Lett. **48**, 1066 (1982).

[39] M. Gazdzicki and M. Gorenstein, Acta Phys. Polon. **B30**, 2705 (1999).

[40] M. Gorenstein *et al.*, Phys. Lett. **B567**, 175 (2003).

[41] NA49 Collaboration, C. Alt *et al.*, Phys. Rev. **C77** (2008), 064908.

[42] A. Andronic *et al.*, Phys. Lett. B **673**, 142 (2009).

[43] R. Hagedorn, 1985, CERN-TH-4100/85.

[44] J.-Y. Ollitrault, Phys.Rev. **D46**, 229 (1992).

[45] H. Sorge, Phys. Rev. Lett. **82**, 2048 (1999).

[46] H. Petersen *et al.*, Phys. Rev. **C74**, 064908 (2006), hep-ph/0608189v2.

[47] Q. Li *et al.*, J. Phys. G: Nucl. Part. Phys. **32**, 151 (2006).

[48] C. Alt *et al.*, Phys. Rev. **C68**, 034903 (2003), nucl-ex/0303001.

[49] P. Kolb, J. Solfrank, and H. U., Phys.Rev. **C62**, 054909 (2000).

[50] S. Voloshin, J.Phys.Conf.Ser. **9**, 276 (2005).

[51] H. Stoecker, Nucl.Phys. **A750**, 121 (2005).

[52] E. Shuryak, (2005), hep-ph/0504048.

[53] W. Zajc, Talk given at 21st International Conference on Ultra-Relativistic Nucleus-Nucleus Collisions "Quark Matter 2009" (March 30 - April 4, Knoxville, USA). (2009).

[54] S. Voloshin and Y. Zhang, Z.Phys. **C70**, 665 (1996).

[55] A. M. Poskanzer and S. A. Voloshin, Phys.Rev. **C58**, 1671 (1998).

[56] S. Wang *et al.*, Phys.Rev. **C44**, 1091 (1991).

[57] N. Borghini, P. M. Dinh, and J.-Y. Ollitrault, Phys. Rev. **C64**, 054901 (2001).

[58] A. Bilandzic, N. van der Kolk, J.-Y. Ollitrault, and R. Snellings, (2008), 0801.3915.

[59] R. Bhalerao, N. Borghini, and J.-Y. Ollitrault, Nucl.Phys. **A727**, 373 (2003).

[60] I. Lokhtin *et al.*, Comput.Phys.Commun. **180**, 779 (2009).

[61] M. I. Podgoretsky, Fiz. Elem. Chast. Atom. Yadra **20**, 628 (1989).

[62] M. I. Podgoretsky, Sov. J. Part. Nucl. **20**, 266 (1989).

[63] B. Lorstad, Int. J. Mod. Phys. **A4**, 2861 (1989).

[64] D. H. Boal, C. K. Gelbke, and B. K. Jennings, Rev. Mod. Phys. **62**, 553 (1990).

[65] U. A. Wiedemann and U. W. Heinz, Phys. Rept. **319**, 145 (1999), nucl-th/9901094.

[66] T. Csorgo, Heavy Ion Phys. **15**, 1 (2002).

[67] L. R., Phys. of Atomic Nuclei **67**, 71 (2004).

[68] M. A. Lisa, S. Pratt, R. Soltz, and U. Wiedemann, Ann. Rev. Nucl. Part. Sci. **55**, 357 (2005), nucl-ex/0505014.

[69] R. Lednicky, Braz. J. Phys. **37**, 939 (2007), nucl-th/0702063.

[70] R. Lednicky, V. L. Lyuboshits, B. Erazmus, and D. Nouais, Nucl. Phys. **A583**, 395 (1995).

[71] L. Martin *et al.*, Nucl. Phys. **A604**, 69 (1996).

[72] R. Lednicky, Nukleonika **43**, 345 (1998).

[73] R. Lednicky and V. L. Lyuboshitz, Sov. J. Nucl. Phys. **35**, 770 (1982).

[74] R. Lednicky and V. L. Lyuboshits, In *Nantes 1990, Proceedings, Particle correlations and interferometry in nuclear collisions* 42-54.

[75] R. Lednicky, (2005), nucl-th/0501065.

[76] R. Lednicky, J. Phys. G: Nucl. Part. Phys **35**, 125109 (2008).

[77] Y. Sinyukov, R. Lednicky, S. V. Akkelin, J. Pluta, and B. Erazmus, Phys. Lett. **B432**, 248 (1998).

[78] M. I. Podgoretsky, Sov. J. Nucl. Phys. **37**, 272 (1983).

[79] R. Lednicky, JINR-B2-3-11460, Dubna (1978).

[80] P. Grassberger, Nucl. Phys. **B120**, 231 (1977).

[81] G. F. Bertsch, P. Danielewicz, and M. Herrmann, Phys. Rev. **C49**, 442 (1994).

[82] S. Pratt, In *Hwa, R.C. (ed.): Quark-gluon plasma, vol.2* 700-748.

[83] S. Chapman, P. Scotto, and U. Heinz, Phys. Rev. Lett. **74**, 4400 (1995).

[84] T. Csorgo and S. Pratt, Prepared for International Workshop on Relativistic Heavy Ion Collisions at Present and Future Accelerators, Budapest, Hungary, 17-21 Jun 1991.

[85] B. Erazmus, R. Lednicky, L. Martin, D. Nouais, and J. Pluta, Invited talk at 34th International Winter Meeting on Nuclear Physics, Bormio, Italy, 22-27 Jan 1996.

[86] B. Erazmus *et al.*, SUBATECH-98-03, Nantes (1998).

[87] P. Danielewicz and S. Pratt, Phys. Rev. **C75**, 034907 (2007).

[88] S. Pratt, Braz. J. Phys. **37**, 871 (2007).

[89] STAR, J. Adams *et al.*, Phys. Rev. Lett. **91**, 262302 (2003), nucl-ex/0307025.

[90] M. Gmitro, J. Kvasil, R. Lednicky, and V. L. Lyuboshits, Czech. J. Phys. **B36**, 1281 (1986).

[91] STAR, J. Adams *et al.*, Phys. Rev. **C74**, 064906 (2006).

[92] BRAHMS, I. Arsene *et al.*, Nucl. Phys. **A757**, 1 (2005), nucl-ex/0410020.

[93] B. B. Back *et al.*, Nucl. Phys. **A757**, 28 (2005), nucl-ex/0410022.

[94] STAR, J. Adams *et al.*, Nucl. Phys. **A757**, 102 (2005), nucl-ex/0501009.

[95] PHENIX, K. Adcox *et al.*, Nucl. Phys. **A757**, 184 (2005), nucl-ex/0410003.

[96] Y. M. Sinyukov, S. V. Akkelin, and Y. Hama, Phys. Rev. Lett. **89**, 052301 (2002), nucl-th/0201015.

[97] D. H. Rischke and M. Gyulassy, Nucl. Phys. **A608**, 479 (1996), nucl-th/9606039.

[98] WA97, F. Antinori *et al.*, J. Phys. **G27**, 2325 (2001), hep-ex/0108049.

[99] E895, M. A. Lisa *et al.*, Phys. Rev. Lett. **84**, 2798 (2000).

[100] E802, L. Ahle *et al.*, Phys. Rev. **C66**, 054906 (2002), nucl-ex/0204001.

[101] NA49, S. Kniege *et al.*, J. Phys. **G30**, S1073 (2004), nucl-ex/0403034.

[102] CERES, D. Adamova *et al.*, Nucl. Phys. **A714**, 124 (2003), nucl-ex/0207005.

[103] PHENIX, S. S. Adler *et al.*, Phys. Rev. Lett. **93**, 152302 (2004), nucl-ex/0401003.

[104] PHENIX, K. Adcox *et al.*, Phys. Rev. Lett. **88**, 192302 (2002), nucl-ex/0201008.

[105] PHOBOS, B. B. Back *et al.*, Phys. Rev. **C73**, 031901 (2006).

[106] STAR, C. Adler *et al.*, Phys. Rev. Lett. **87**, 082301 (2001).

[107] STAR, J. Adams *et al.*, Phys. Rev. **C71**, 044906 (2005).

[108] W. Florkowski, W. Broniowski, M. Chojnacki, and A. Kisiel, (2008), 0811.3761.

[109] S. Pratt, (2008), 0811.3363.

[110] Y. M. Sinyukov, S. V. Akkelin, I. A. Karpenko, and Y. Hama, Acta Phys. Polon. **B40**, 1025 (2009), 0901.1576.

[111] J. Berges and K. Rajagopal, Nucl. Phys. **B538**, 215 (1999).

[112] A. M. Halasz, A. D. Jackson, R. E. Shrock, M. A. Stephanov, and J. J. M. Verbaarschot, Phys. Rev. **D58**, 096007 (1998), hep-ph/9804290.

[113] O. Scavenius, A. Mocsy, I. N. Mishustin, and D. H. Rischke, Phys. Rev. **C64**, 045202 (2001).

[114] M. A. Stephanov, Int. J. Mod. Phys. **A20**, 4387 (2005).

[115] D. A. Brown and P. Danielewicz, Phys. Rev. **C57**, 2474 (1998), nucl-th/9712066.

[116] STAR, Z. Chajecki, T. D. Gutierrez, M. A. Lisa, and M. Lopez-Noriega, (2005), nucl-ex/0505009.

[117] NA49, M. Gazdzicki *et al.*, J. Phys. **G30**, S701 (2004), nucl-ex/0403023.

[118] The NA49, C. Alt *et al.*, J. Phys. **G30**, S119 (2004), nucl-ex/0305017.

[119] The NA49, S. V. Afanasiev *et al.*, Phys. Rev. **C66**, 054902 (2002), nucl-ex/0205002.

[120] NA49, M. K. Mitrovski *et al.*, J. Phys. **G32**, S43 (2006), nucl-ex/0606004.

[121] NA49, T. Anticic *et al.*, Phys. Rev. **C69**, 024902 (2004).

[122] S. V. Afanasiev *et al.*, Nucl. Phys. **A715**, 161 (2003), nucl-ex/0208014.

[123] NA49, A. Richard, J. Phys. **G31**, S155 (2005).

[124] NA49, T. Anticic *et al.*, Phys. Rev. Lett. **93**, 022302 (2004), nucl-ex/0311024.

[125] NA49, C. Blume, J. Phys. **G31**, S685 (2005), nucl-ex/0411039.

[126] NA49, C. Meurer, J. Phys. **G30**, S1325 (2004), nucl-ex/0406016.

[127] NA49, M. Mitrovski, Acta Phys. Hung. **A24**, 157 (2005), nucl-ex/0406011.

[128] NA49, C. Alt *et al.*, Phys. Rev. Lett. **94**, 192301 (2005), nucl-ex/0409004.

[129] M. Lombardo, J. Phys **G35**, 104018 (2008).

[130] K. Fukushima, J. Phys **G35**, 104019 (2008).

[131] I. Tserruya, J. Phys **G35**, 104020 (2008), arXiv:0903.0415v1 [nucl-ex] 3 Mar 2009.

[132] W. Cassing and E. Bratkovskaya, Phys. Rep. **308**, 65 (1999).

[133] R. Rapp and J. Wambach, Adv. Nucl. Phys. **25**, 1 (2000).

[134] E. Shuryak, Phys. Lett. **B78**, 150 (1978).

[135] P. Ruuskanen, Nucl. Phys. **A544**, 169c (1992).

[136] K. Kajantie *et al.*, Phys. Rev. **D34**, 2746 (1986).

[137] CERES Collaboration, G. Agakachiev *et al.*, Phys. Rev. Lett. **75**, 1272 (1995).

[138] HELIOS-3 Collaboration, A. Angelis *et al.*, Eur. Phys. J. **C13**, 433 (2000).

[139] S. Turbide, R. Rapp, and C. Gale, Phys. Rev. **C69**, 5351 (2004).

[140] S. Turbide, R. Rapp, and C. Gale, Int. J. Mod. Phys **A19**, 014903 (2004).

[141] P. Arnold, G. Moore, and L. Yae, JHEP **0112**, 009 (2001).

[142] L. Gordon and W. Vogelsang, Phys. Rev. **D 48**, 3136 (1993).

[143] L. V. Bravina *et al.*, Nucl. Phys. **A566**, 461c (1994).

[144] I. Tserruya, Nucl. Phys. **A590**, 127c (1995).

[145] PHENIX Collaboration, S. Afanasiev *et al.*, arXiv:0706.3034.

[146] E. Shuryak, in *Proceeding of Int.Conf.modern developments in nuclear physics*, p. 157, Novosibirsk, 1987.

[147] *Critical Point and Onset of Deconfinement - 4th International Workshop*, Darmstadt, Germany, 2007.

[148] B.Barrois, Nucl. Phys. **B129**, 390 (1977).

[149] A. Baldin *et al.*, Preprint JINR-P1-5819(1971); Yad. Fiz. **18**, 79 (1973), (cumulative effect).

[150] D. Blokhintsev, GETF **6**, 995 (1958), (flucton).

[151] D. Seibert, Phys. Rev. Lett. **63**, 136 (1989).

[152] S. Averichev *et al.*, JINR communication-P1-85-512(1985).

[153] Y. Bayukov *et al.*, Yad. Fiz. **42**, 185 (1985).

[154] V. Stavinskiy, JINR communication, P2-80-767.

[155] A. Baldin and S. Gerasimov, JINR communication E2-11804(1978).

[156] R. Lednicky *et al.*, Phys. Rev. **C61** (2000), 034901.

[157] R. L. Jaffe, Phys. Rev. Lett. **38**, 195 (1977).

[158] R. L. Jaffe, Phys. Rev. **D15**, 281 (1977).

[159] A. T. M. Aerts, P. J. G. Mulders, and J. J. de Swart, Phys. Rev. **D17**, 260 (1978).

[160] P. J. Mulders, A. T. M. Aerts, and J. J. De Swart, Phys. Rev. **D21**, 2653 (1980).

[161] V. B. Kopeliovich, B. Schwesinger, and B. E. Stern, Nucl. Phys. **A549**, 485 (1992).

[162] T. Yamazaki and Y. Akaishi, Phys. Lett. **B535**, 70 (2002).

[163] P. Kienle, Y. Akaishi, and T. Yamazaki, Phys. Lett. **B632**, 187 (2006).

[164] T. Suzuki *et al.*, Phys. Lett. **B597**, 263 (2004).

[165] KEK-PS E549, T. Suzuki *et al.*, Mod. Phys. Lett. **A23**, 2520 (2008), 0711.4943.

[166] S. Wycech, Nucl. Phys. **A450**, 399c (1986).

[167] A. Gal, Nucl. Phys. **A790**, 143 (2007), nucl-th/0610090.

[168] J. Rafelski, Phys. Lett. **B91**, 281 (1980).

[169] J. Rafelski, Phys. Lett. **B207**, 371 (1988).

[170] P. Aslanyan and othres, JINR Commun **4 No. 1**, 99 (2005).

[171] M. Iwasaki, HYP06,Mainz, October 2006 (2006).

[172] DISTO, T. Yamazaki *et al.*, Proc. LEAP/EXA conference, Vienna, 15-19 September, 2008 (2008).

[173] N. Herrmann, Proceedings EXA05,2006 (2006).

[174] FINUDA, M. Agnello *et al.*, Phys. Rev. Lett. **94**, 212303 (2005).

[175] FINUDA, M. Agnello *et al.*, Phys. Lett. **B654**, 80 (2007), 0708.3614.

[176] G. Bendiscioli *et al.*, Nucl. Phys. **A789**, 222 (2007).

[177] P. Buehler *et al.*, The AMADEUS Collaboration, INFN, Frascati, LNF-07/24(IR), November 8,2007 (2007).

[178] P. Salvini *et al.*, Proc. Int. conference LEAP08,Vienna, 16-19 September, 2008 (2008).

[179] M. Balandin and othres, Nucl.Instr. and Meth. **20**, 110 (1963).

[180] T. Nguen-Din, V. Penev, and othres, JINR Commun **13-5942** (1971).

[181] B. Shahbazian *et al.*, Nucl. Phys. **A374**, 73 (1982).

[182] P. Z. Aslanyan, Proc. XVI ISHEPP, Dubna, June 10-15, 2002, JINR **2** (2004).

[183] P. Aslanyan, Proc. I.Ya.Pomeranchuk and Physics at the Turn of Centuries, River Edge, World Scientific , 247 (2003).

[184] P. Z. Aslanyan, AIP Conf. Proc. **796**, 197 (2005), hep-ex/0507105.

[185] P. Aslanyan and V. Emelyanenko, Proc. XVIII ISHEPP, Dubna, October 29-4,2008 (2008).

[186] P. Z. Aslanyan, Fizika **B17**, 207 (2008).

[187] P. Z. Aslanyan, PEPAN **4** (2009).

[188] P. Z. Aslanyan, (2007), 0710.4322.

[189] A. Zinchenko, Proc. XVIII ISHEPP, Dubna, October 29-4,2008 (2008).

[190] K. U. Abraamyan *et al.*, (2008), 0806.2790.

[191] K. U. Abraamian, V. M. Izyurov, M. N. Khachaturian, M. A. Kozhin, and A. G. Khudaverdian, Phys. Lett. **B323**, 1 (1994).

[192] K. U. Abraamian *et al.*, Phys. Atom. Nucl. **59**, 252 (1996).

[193] K. U. Abraamian *et al.*, Phys. Atom. Nucl. **60**, 1843 (1997).

[194] K. U. Abraamian, M. A. Kozhin, G. L. Melkumov, M. N. Khachaturian, and A. G. Khudaverdian, Phys. Atom. Nucl. **68**, 982 (2005).

[195] R.O.Arsey *et al.*, IEEE Trans. Magn. MAG-21 **2**, 490 (1985).

[196] J.M.Baze *et al.*, IEEE Trans. Magn. MAG-24 **2**, 1260 (1988).

[197] P.Fabbricatore *et al.*, IEEE Trans. Magn. MAG-32 **4**, 2210 (1996).

[198] H.Minemura *et al.*, Nuclear Instruments and Methods in Physics Research **A238**, 18 (1985).

[199] R. Brown *et al.*, The star detector magnet subsystem, in *1997 Particle Accelerator Conference*, Vancouver, BC, 1997, BNL-64461.

[200] E.Baynham, Evolution of detector magnets from cello to atlas and cms and toward future developments, Applied Science Division Rutherford Appelton Laboratory, CCRLC.

[201] System Research and Analysis Corp., Los Angeles, *COSMOS M v 2.95 User's Guide*, 2005.

[202] Ami helium vapor cooled current leads, http://www.americanmagnetics.com/currentleads.php.

[203] Safety requirements of strength analysis of the equipment and pipe lines of nuclear power plants, RF Regulation, PNAE G-7-002-86.

[204] M. Anderson *et al.*, Nucl. Instrum. Meth. **A499**, 659 (2003), nucl-ex/0301015.

[205] The STAR Collaboration, *"Conceptual Design Report for the Solenoidal Tracker at RHIC"* , June 1992, Pub-5347.

[206] ALICE Collaboration, *ALICE TDR 7 "Time projection chamber"* , CERN/LHCC 2000-001, January 2000.

[207] ALEPH Collaboration, Nucl. Instr. and Meth. **A294**, 121 (1990).

[208] W. Atwood *et al.*, Nucl. Instr. and Meth. **A306**, 446 (1991).

[209] A. Andronic *et al.*, Nucl. Instr. and Meth. **A523**, 302 (2004).

[210] T. Lohse and W. Witzeling, Internal Note CERN-ALEPH-91-95.

[211] W. Allison and J. Cobb, Ann. Rev. Nucl. Part Sci. **30**, 253 (1980).

[212] A. Lebedev, Nucl. Instr. and Meth. **A478**, 163 (2002).

[213] J. Abele *et al.*, Nucl. Instr. and Meth. **A499**, 692 (2003).

[214] B. Nilsen *et al.*, Nucl. Instr. and Meth. **A599**, 176 (2009).

[215] L. Kotchenta *et al.*, Nucl. Instr. and Meth. **A499**, 703 (2003).

[216] A. Jain *et al.*, Data clustering: A Review, ASM Computing Surveys **Vol.31** (1999).

[217] W. Blum and L. Ronaldi, *Particle Detection with Drift Chamber* (Springer, Berlin, 2008).

[218] S. Amendola *et al.*, Nucl. Instr. and Meth. **A283**, 573 (1989).

[219] A. Handbook, ALEPH 89-77.

[220] I. Lehraus, Nucl.Instr.Meth. **217**, 43 (1983).

[221] S. Palestini *et al.*, Nucl. Instr. and Meth. **A421**, 75 (1999).

[222] S. Palestini and K. McDonald, *Space charge in ionization detectors* , CERN, March 2007.

[223] L. Kumar, *First results from Au+Au collisions at* $\sqrt{s_{NN}}$*=9.2 GeV/c* , for STAR collaboration, Penjab University, 2008.

[224] G. Van Buren *et al.*, Nucl. Instr. and Meth. **A566**, 22 (2006).

[225] L. Musa, *"CERN participation to EUDET for TPC electronics"* , CERN, 31 August 2006.

[226] T. Matsuda, *"TPC for ILC"* , Special Focus Workshop on Micro-Pattern Gas and Silicon Detectors for Tracking, IEEE 2008, Dresden, 18 Oct., 2008.

[227] R. Campagnolo, *"Performance of the ALICE TPC Front End Electronics"* , 9-th Workshop on Electronics for LHC Experiments, Amsterdam, 29 Sept.-3 Oct. 2003.

[228] *ADS5287*, Texas Instruments, SBAS428C-January 2008.

[229] XILINX, *Spartan-6 Family Overview*, DS160(v. 1.0), February 2, 2009.

[230] R. Esteve Bosch, A. Jimenez, B. Mota, and L. Musa, IEEE Transaction on Nuclear Science **Vol. 50, No. 6** (2003).

[231] Y. Zanevsky *et al.*, Preprint JINR P13-2006-168, Dubna 2006.

[232] S. Chernenko *et al.*, CBM Progress Report 2008, GSI Report 2009-03, 36.

[233] Alice, P. Kuijer, Nucl. Instrum. Meth. **A530**, 28 (2004).

[234] STAR, http://wwwstar-sbg.in2p3.fr/index.php.

[235] D0, W. E. Cooper, Nucl. Instrum. Meth. **A598**, 41 (2009).

[236] S. G. Mashnik, K. K. Gudima, N. V. Mokhov, and R. E. Prael, (2007), 0709.1736.

[237] SVD, (2008), http://sunse.jinr.ru/cdsagenda/displayLevel.php?fid=45.

[238] SVD, http://sunse.jinr.ru/cdsagenda/displayLevel.php?fid=45.

[239] CBM, (2009), http://www.gsi.de/documents/DOC-2009-Feb-233.html.

[240] ALICE, (2000), CERN-LHCC-2000-012, ALICE TDR 8.

[241] ALICE, P. Cortese *et al.*, (2002), CERN-LHCC-2002-016, Addendum to the ALICE TDR 8.

[242] *CBM Technical Status Report 2006* .

[243] K. Ikematsu *et al.*, (1998), arXiv:physics/9802024 v1.

[244] F. Geurts *et al.*, Nucl.Instr.Meth. **A508**, 60 (2003).

[245] H. Alvarez-Pol *et al.*, Nucl.Instr.Meth. **A535**, 277 (2004).

[246] L. Aphecetche *et al.*, NIM **A499**, 521 (2003).

[247] G. Atoian *et al.*, Nucl.Instrum.Meth. **A531**, 467 (2004).

[248] S. Barsuk, in *XI Int.Conf. Calorimetry in High Energy Physics*, Italy, 2004.

[249] D. Karlen *et al.*, Nuclear Physics **B 159**, 91 (2006).

[250] Z. Sadygov, Nucl.Instr.Meth. **A567**, 70 (2005).

[251] W. van Loo, Phys. Stat. Sol. **28**, 227 (1975).

[252] W. Moses and S. E. Derenzo, IEEE Trans. Nucl. Sci. **36**, 173 (1989).

[253] M. Kobayashi *et al.*, Nucl. Instrum. Methods **A333**, 429 (1993).

[254] V. Baryshevsky *et al.*, Nucl. Instrum. Methods **A322**, 231 (1992).

[255] P. Lecoq *et al.*, CMS TN/94-308.

[256] Y. Borodenko *et al.*, (1995), in Int. Conf. on Nuclear Tracking and Radiation Measurements, Amsterdam.

[257] M. N. Khachaturian, Particles and Nuclei **34**, 1316 (2003).

[258] ATLAS, (1997), ATLAS Inner Detector: Technical design report. Vol. 2 CERN-LHCC-97-17.

[259] Y. Gousakov *et al.*, JINR preprint. **P13-2008-85** (2008).

[260] V. N. Bychkov *et al.*, Nucl.Instr. and Meth. in Phys.Res. **A556**, 66 (2006).

[261] S. G. Basiladze *et al.*, Nucl.Eksp.Tekh. **51-3**, 336 (2008).

[262] V. Davkov *et al.*, Part.Nucl.Lett. **4(140)**, 545 (2007).

[263] K. Davkov *et al.*, Nucl.Instr. and Meth. in Phys.Res **A584**, 285 (2008).

[264] V. M. Lutsenko, V. V. Myalkovsky, and V. D. Peshekhonov, Phys. Part. Nucl. Lett. **3**, 273 (2006).

[265] I. Zhukov *et al.*, JINR P13-2005-126 (on Russian) (2005).

[266] D. Bederede *et al.*, Nucl.Instr. and Meth. in Phys.Res **A367**, 88 (1995).

[267] CERN Courier **October**, 8 (2010).

[268] CERN Courier **April**, 13 (2010).

[269] Wire Pad chambers and Cathode Pad chambers for the LHCb muon system.LHCb internal note. LHCb internal note.

[270] CMS Muon TDR, CERN/LHCC 97-32,CMS TDR 3, 15 December 1997.

[271] http://www.rohacell.de.

[272] S. Korpar, MCP-PMT Status, Super KEKB – 1^{st} Open Meeting, Dec. 2008.

[273] K. Adcox *et al.*, Phys. Rev. Lett. **89**, 212301 (2002).

[274] R. L. Ray and M. Daugherity, nucl-ex/0702039v2 (2008).

[275] L. M. Miller *et al.*, nucl-ex/0701025v1 (2007).

[276] X. Wang and M. Gyulassy, Phys. Rev. **D44**, 3501 (1991).

[277] K. Werner, Phys. Lett. **B208**, 520 (1988).

[278] H. Sorge, H. Stoecker, and W. Greiner, Nucl. Phys. **A498**, 567C (1989).

[279] UrQMD, http://th.physik.uni-frankfurt.de/ urqmd/ .

[280] C. Aguiar *et al.*, Brazilian Journal of Physics **34**, 319 (2004).

[281] Y. D. Bajukov *et al.*, NP **35**, 960 (1982).

[282] R.Brun *et al.*, *GEANT Users Guide.*, CERN Program Library Vol. Entry W5013 (CERN, Geneva, Switzerland, 1994).

[283] NA49, Eur. Phys. J. **A2**, 383 (1998).

[284] http://www.nea.fr/abs/html/iaea1287.html .

[285] S. G. Mashnik, K. K. Gudima, I.V.Moskalenko, R.E.Prael, and A.J.Sierk, arXiv:nucl-th/0210065v2 .

[286] M. Golubeva *et al.*, Phys.Rev. **2005**, 024905 (2005).

[287] S. Bass *et al.*, Prog. Part. Nucl. Phys. **41**, 225 (1998), nucl-th/9803035.

[288] S. Movchan, Nucl.Instr. and Meth. **A604**, 307 (2009).

[289] G. Anelli *et al.*, CERN-SPSC-2005-013, SPSC-P-326 (2005).

[290] F. Newcomer *et al.*, IEE Trans. on Nucl. Science **v.40 (4)**, 630 (1993).

[291] M. Mota *et al.*, Nuclear Science Symposium, Lyon, France, October 2000 (2000).

[292] ALICE, P. Cortese *et al.*, (2005), CERN-LHCC-2005-018.

[293] D. Bertini *et al.*, J. Phys. Conf. Ser. **119**, 032011 (2008), http://cbmroot.gsi.de.

[294] http://www.gsi.de/fair/experiments/CBM.

[295] http://www-panda.gsi.de.

[296] http://alisoft.cern.ch/.

[297] http://root.cern.ch.

[298] S. G. Mashnik, K. K. Gudima, I. V. Moskalenko, R. E. Prael, and A. J. Sierk, Advances in Space Research **34**, 1288 (2004).

[299] R. Fruhwirth, Nucl. Instr. and Meth. **A262**, 444 (1987).

[300] P. Billoir and Q. Qian, Nucl. Instr. and Meth. **A294**, 219 (1990).

[301] M. Gorenstein, M. Hauer, V. Konchakovski, and E. Bratkovskaya, arXiv:0811.3089v2.

[302] H. Sorge, H. Stocker, and W. Greiner, **192**, 266 (1989).

[303] N. S. Amelin *et al.*, Phys. Rev. **C77**, 014903 (2008), 0711.0835.

[304] ALICE-FEMTO group software.

[305] I. Froghlich *et al.*, PoS ASAT (2007), arXiv:0708.2382, [nucl-ex] .